# Vertical Motion Structure in Tropical Mesoscale Convection Systems

by
Robert Cifelli

Steven A. Rutledge, P.I.

Department of Atmospheric Science
Colorado State University
Fort Collins, Colorado

NOAA Grant NA37J0202
National Oceanic and Atmospheric Administration

Colorado State University

Department of Atmospheric Science

Paper No. 597

# VERTICAL MOTION STRUCTURE IN TROPICAL MESOSCALE CONVECTIVE SYSTEMS

by

**Robert Cifelli**

Department of Atmospheric Science

Colorado State University

Fort Collins, CO 80523-1371

**Research Supported by**

**National Oceanic and Atmospheric Administration**

under Grant NA37J0202

December, 1995

Atmospheric Science Paper No. 597

## ABSTRACT

### VERTICAL MOTION STRUCTURE IN TROPICAL MESOSCALE CONVECTIVE SYSTEMS

VHF wind profiler data were used to study the vertical draft structure within 13 tropical Mesoscale Convective Systems (MCSs) near Darwin, Australia during the wet season of 1989-1990 and 1990-1991. Single-Doppler radar and surface rainfall data were also utilized in order to correlate the reflectivity and surface rainfall patterns with the structure of the vertical air motion measured by the wind profiler during the passage of each system. Because of Darwin's unique location at the southern tip of the Maritime Continent, the wind profiler was able to observe vertical drafts in both the monsoon (maritime) and monsoon break (continental) convective regimes.

The break regime MCSs (6 total) were all squall lines, characterized by a leading line of convection with intense precipitation and sharp horizontal reflectivity gradients. A prominent zone of weaker reflectivities and very light precipitation was observed to the rear of the convective line (transition zone) in most cases, as well as a region with relatively small horizontal reflectivity gradients, light rainfall and a characteristic bright band marking the trailing stratiform region. In contrast, the monsoon systems (7 total) were characterized as relatively unorganized regions of stratiform cloud with embedded convective bands which moved on-shore in the monsoon flow. Results from the Darwin rain gauge network indicated that the vast majority of the total rainfall in

each monsoon and break MCS was associated with the convective portion of the system, in contrast to previous studies of MCSs in other tropical locations.

The break regime MCSs were all characterized by a consistent low-level (4 km) updraft peak associated with convective cells on the leading edge of each squall line, trailed by deeper convective updrafts in the upper troposphere. A significant fraction of the convective rainfall was associated with the low-level updraft indicating that warm rain collision-coalescence processes were as important to precipitation production as mixed phase processes involving both ice and supercooled liquid water (associated with the upper level peak updraft). In the monsoon regime, the convective region vertical air motions were typically less than the squall lines in the lower troposphere but larger in the upper troposphere. The low-level differences are consistent with the smaller virtual temperature excess in the monsoon soundings, as well as the larger vertical radar reflectivity gradients observed in monsoon convection.

Consistent with the differences in vertical air motion patterns, diabatic heating and moistening profiles showed that the monsoon MCSs were characterized by a higher level peak heating and drying compared to the break MCSs. The results have important implications for cumulus parameterizations in numerical models since the large scale circulation is sensitive to the vertical distribution of diabatic heating in tropical MCSs. The vertical air motion and diabatic heating profiles are compared with similar studies from other tropical and middle latitude locations, including TOGA COARE.

Robert Cifelli
Atmospheric Science Department
Colorado State University
Fort Collins, CO 80523
Spring 1996

## ACKNOWLEDGMENTS

I would like to thank Prof. Steve Rutledge for his guidance, sharing of ideas, and encouragement over the last five years. Committee members Profs. Richard Johnson, Tom McKee, and V. Bringi provided helpful comments related to this work. Special thanks are also extended to Prof. Bill Gray who encouraged me to return to graduate school at CSU. This work would not have been possible without the patience and support of my wife Nancy.

Many others assisted in this research at different points over the last five years. Walt Petersen and Charlotte DeMott of CSU are acknowledged for their many insightful comments concerning this work. Doug Burks (formerly of CSU) and Paul Hein provided invaluable help in computer programming and debugging of the PLTGKS software package. Drs. K. Gage, W. Ecklund, and A. Riddle of the NOAA AL assisted in the interpretation of wind profiler spectra. Dave Wolff of Applied Research Corporation was helpful in making TOGA radar data available in a timely fashion. Drs. B. Smull and D. Jorgensen of NOAA NSSL provided much of the COARE multiple Doppler data. Dr. T. Matejka of NOAA NSSL and Mr. D. Boccippio of MIT are gratefully acknowledged for their help in explaining the subtle aspects of Doppler radar retrievals. Drs. T. Keenan and P. May of the BMRC also made important contributions to this research. DUNDEE was enhanced by facilities deployed for NASA's TRMM Ground Truth Program in Darwin under the direction of Otto Thiele. This work was supported by the contract NA37RJ0202 from NOAA (Office of Global Programs - TOGA/COARE).

## TABLE OF CONTENTS

## LIST OF FIGURES

## LIST OF TABLES

# Chapter I

# INTRODUCTION

## 1.1 Motivation for research

The global circulation is largely dependent on deep convection occurring in the tropics. This deep convection often occurs in association with Mesoscale Convective Systems (MCSs), which consist of not only deep convection, but regions of stratiform precipitation, with the latter being characterized by important mesoscale circulations. Both the deep convection and mesoscale circulations act to couple the ocean, planetary boundary layer and free troposphere through heat, moisture and momentum transports. Riehl and Malkus (1958) focused on deep convection (hot towers) and identified their role in transporting heat from the boundary layer to the upper troposphere. Since this early work, other studies have identified the important contributions of mesoscale vertical motions to heating and cooling the troposphere (Houze 1982; Johnson and Young 1983; Johnson 1984, Houze 1989; and others). Indeed, numerical model simulations have shown that the global scale circulations (e.g., Walker circulation and 30-60 day Intraseasonal oscillation) are sensitive to the vertical distribution of heating associated with tropical MCSs involving both convective and mesoscale processes (Hartmann et al. 1984; DeMaria 1985; Lau and Peng 1987; Houze 1989; Hack and Schubert 1990; Johnson 1992). Since the vertical distribution of heating in an MCS is dominated by contributions involving phase changes of water (Houze 1989) which are in turn proportional to vertical air motion profiles (convective and

stratiform), it is important to continue to document these vertical motion profiles and to identify differences with geographic location.

To a first approximation, the diabatic heating and moistening in an MCS can be characterized by the convective system vertical air velocity profile (Johnson and Young 1983) according to:

$$Q_1 \equiv \frac{\partial \bar{s}}{\partial t} + \bar{v}\cdot\nabla\bar{s} + \bar{\omega}\frac{\partial \bar{s}}{\partial p} \cong \bar{\omega}\frac{\partial \bar{s}}{\partial p}, \tag{1.1}$$

$$Q_2 \equiv \frac{\partial \bar{q}}{\partial t} + \bar{v}\cdot\nabla\bar{q} + \bar{\omega}\frac{\partial \bar{q}}{\partial p} \cong \bar{\omega}\frac{\partial \bar{q}}{\partial p}, \tag{1.2}$$

where $Q_1$ is the apparent heat source, $Q_2$ is the apparent moisture sink (Yanai et al. 1973), $s$ represents dry static energy( $C_pT + gz$), $q$ is specific humidity, $\omega$ is the vertical air velocity measured in the isobaric coordinate system and the overbars represent horizontal averages.

Although there is general agreement on the vertical heating distribution in the stratiform portion of tropical and middle latitude MCSs, previous results suggest a relatively wide range of variability in the convective region (Houze 1989; Johnson 1992). Convective region vertical air motion and heating profiles have been empirically diagnosed as a residual of rawindsonde analyses (Johnson, 1984), using a simple entrainment cumulus model with an assumed vertical air motion profile (Houze, 1982), or more recently, using thermodynamic and microphysical retrievals in concert with dual-Doppler radar analyses (Chong and Hauser 1990). The results of these studies have shown significant variation in regard to the location of the peak heating rate (lower vs middle troposphere). Given the fact that these previous studies have diagnosed the convective region heating indirectly, it is difficult to determine how much of the difference in the location of the heating peak is due to natural variability and how much is due to assumptions implicit in the

analysis methods. This apparent disparity indicates the need for more research to determine the global variability of the kinematic structure and diabatic heating patterns within MCSs.

Typically, MCS vertical air motion profiles have been diagnosed indirectly following mass continuity considerations. Data sources such as a rawinsonde network, aircraft, and Doppler radar measure horizontal (radial) wind velocity and calculate horizontal divergence across a specified domain, and then determine the corresponding profile of vertical air motion by integration of the mass continuity equation (i.e. the kinematic method: O'Brien 1970; Ray et al. 1980). In order to extract the profile of vertical air motion using the mass continuity equation, boundary condition assumptions are necessary and a value of vertical air velocity must be assigned to at least one of the boundaries in the integration column. These boundary condition assumptions can be subject to large error, especially in situations where data collection is restricted in height. In such instances, the particular observing platform may not measure the entire depth of divergence occurring in the column and an upper boundary constraint on vertical air velocity may be improperly assigned (i.e., $w = 0$ at the top of the column may not be correct). This effect would clearly corrupt the integration and resulting profile of vertical air velocity in the column. Such an effect would result, for example, when Doppler radar data are subject to significant attenuation or when vertical air motion extends above cloud top into echo-free regions.

Recently, the introduction of wind profilers to the study of MCSs has provided an opportunity to sample the vertical air motion field nearly continuously without boundary condition assumptions. Specifically, wind profilers operating at VHF can directly measure vertical air motions from the lower troposphere to the lower stratosphere assuming that the spectral power returns from hydrometeors and air motions can be reliably separated in cloudy regions (Carter et al. 1991). Of course, in clear air the wind profiler continues to provide direct measurement of

vertical motions, something that is not possible with a scanning Doppler radar operating at microwave frequencies.

This study describes the structure of vertical motion in 13 tropical MCSs using VHF wind profiler data. The data were acquired during the DUNDEE [Down Under Doppler and Electricity Experiment; Rutledge et al. (1992)] and therefore represent MCS vertical air motion in the Maritime Continent region. Since the tropical MCSs examined are approximately equally divided between continental and oceanic in origin (i.e., 6 continental and 7 oceanic), the results compliment similar results from both AMEX and EMEX, which focused on oceanic systems near Darwin.

In addition to wind profiler data, radar reflectivity data from 5-cm Doppler radars and surface rainfall data (from a network of rain gauges) are used to correlate the vertical air motion field with the vertical structure and precipitation features of the MCSs. The vertical air velocity profiles are also composited to construct representative profiles of the vertical motion field in the convective and stratiform components of the MCS. Using the approximation that the apparent heat source ($Q_1$) and moisture sink ($Q_2$) variables are determined solely by the vertical advection of dry static energy and specific humidity, respectively, composite profiles of $Q_1$ and $Q_2$ are constructed using the vertical air motion data. The resultant profiles are compared to vertical air motion and heating-drying profiles from other tropical and middle latitude regions, including TOGA COARE (Tropical Ocean Global Atmosphere Coupled Ocean Atmospheric Response Experiment; hereafter referred to as COARE), in order to identify possible similarities and differences.

Determination of vertical air motion profiles derived from MCSs in the northern Australia region [southern tip of the Maritime Continent, Ramage (1968)] is important for the following reasons:

1) the results are based on the direct observation of MCS vertical air motion structure occurring in the Maritime Continent region and provide additional data from a largely undocumented region to compare with previously studied areas;
2) the location of the DUNDEE field program (discussed in Chapter 2) provided a unique opportunity to study both tropical monsoon (oceanic) and monsoon-break (continental) convection and therefore to compare the vertical air motion within these convective regimes; and
3) convection in this region is situated in the major upwelling branch of the zonal Walker circulation and is therefore a major contributor to global diabatic heat production (i.e., the "global heat engine").

## 1.2 Partitioning MCSs into convective and stratiform components

It has been recognized for some time that MCSs often contain identifiable substructures (e.g., convective and stratiform components; Hamilton and Archbold 1945; Newton 1950; Zipser 1969). As discussed in Sec. 1.1, these substructures play distinct roles in affecting the large scale circulation through heat, moisture, and momentum transports within an MCS and it is therefore important to identify their individual contributions.

Traditionally, convective and stratiform substructures have been classified based on satellite, radar reflectivity, surface precipitation, hydrometeor, or vertical air motion characteristics. The separation of components is fairly distinct in propagating squall line-type systems where a line of

convective cloud is trailed by a relatively homogeneous region of stratiform precipitation with the characteristic radar bright band signature (Houze et al. 1989). Such features have been identified in many tropical and middle latitude MCSs (e.g., Newton 1950; Hamilton and Archbold 1945; Zipser 1969; Gamache and Houze 1982; Smull and Houze 1985; Rutledge et al. 1988; Houze et al. 1990; and others) and have led to the development of conceptual models portraying important aspects of the squall line-type MCS structure and organization (e.g., Houze et al. 1989). However, observational studies have also shown that there are many MCSs which do not fit the conceptual model of squall line structure and appear to have no preferred mesoscale organization (Houze et al. 1990). Indeed, Houze et al. studied 69 middle latitude MCSs in Oklahoma and found that about one third of the heavy rain events studied were not classifiable. The results suggest that there may be a continuous spectrum of mesoscale organization in MCS precipitating clouds (Rutledge 1991).

In the non-squall type MCSs (e.g., many tropical oceanic MCSs), the organization of precipitation features can be much less distinct compared to their squall line counterparts (Houze 1989). For example, widespread stratiform precipitation regions of MCSs occurring in the vicinity of Darwin, Australia during the active monsoon have been observed with embedded convective cells and even convective line-type structures (Houze 1989; Keenan and Carbone 1992; Keenan and Rutledge 1993; Mapes and Houze 1993a). In precipitating events near the coast of northern Australia, Keenan and Carbone (1992) showed that these embedded convective features can be initiated from interactions of local land breeze and the large scale monsoon circulations. In these situations, stratiform regions often develop in places where convection is dissipating, so that the distinction between convection and stratiform features is not necessarily unambiguous. Because of the lack of clearly defined substructures, the partitioning of non-squall type MCSs into convective and stratiform components can be a rather subjective procedure.

In addition to convective and stratiform partitioning, many previous observational studies of propagating middle latitude and tropical squall lines have observed a low-middle level reflectivity trough and associated surface precipitation minimum in the region located between the rear of the convective line and the characteristic bright band associated with stratiform precipitation (Ligda 1956; Houze 1977; Sommeria and Testud 1984; Smull and Houze 1987a; Chalon et al. 1988; Rutledge et al. 1988; Biggerstaff and Houze, 1993; and others). This region, commonly referred to as the transition zone, is characterized by deep subsidence (e.g., Chalon et al. 1988). Moreover, detailed dual Doppler analysis has shown that the transition zone consists of two separate downdrafts: a mechanically forced downdraft in the upper troposphere resulting from convergence of air near storm top in the vicinity of the tropopause and a microphysically forced downdraft in the lower troposphere induced by melting and evaporation of hydrometeors (Biggerstaff and Houze 1993).

### 1.3 Overview of observational research on MCS vertical air motion

A number of studies have documented vertical air motion patterns within tropical and middle latitude MCSs using rawinsonde networks, aircraft penetration data, and Doppler radar analysis techniques (Houze 1989). These studies have focused on vertical air motion profiles of tropical MCSs from various parts of the equatorial region, including the eastern Atlantic Ocean region [GATE (GARP Atlantic Tropical Experiment)] continental west Africa [COPT 81 (Convection Profonde Tropicale)], the South China Sea [Winter MONEX (Monsoon Experiment)], the central Pacific Ocean region near Christmas, Fanning, and Palmyra Islands (Line Islands Experiment),the vicinity of Taiwan [TAMEX (Taiwan Area Mesoscale Experiment)], the northern tip of continental Australia (DUNDEE), and the oceanic regions off northern Australia [AMEX (Australian Monsoon Experiment), EMEX (Equatorial Mesoscale Experiment)]. In the middle

latitudes, results from several observational programs [NSSL (National Severe Storms Laboratory) Spring Programs; SESAME (Severe Environmental Storms and Mesoscale Experiment); PRE-STORM (Preliminary Regional Experiment for STORM-Central)] have documented vertical air motions in several squall line-type MCSs occurring in the U.S. central plains region.

VHF wind profilers have also been used to diagnose vertical motions in a variety of mesoscale precipitating systems occurring in the tropics and middle latitudes. Balsley et al. (1988) diagnosed air motions in clear air and precipitation conditions at Pohnpei Island (7° N, 157° E) in the tropical western Pacific using a vertically-pointing wind profiler. Based on rainfall rates from a nearby rain gauge, Balsley et al. obtained composite profiles for both the convective and stratiform portions of the precipitating systems. Cifelli and Rutledge (1994b) performed a similar analysis for MCSs occurring over the Maritime Continent region near Darwin, N.T., Australia. In that study, Cifelli and Rutledge were able to extract the vertical air motions for different portions of precipitating systems that passed over a VHF wind profiler site in both the monsoon and monsoon break convective regimes.

Augustine and Zipser (1987) described the use of a 3-beam VHF wind profiler to diagnose the horizontal wind structure within several middle latitude MCSs observed during PRE-STORM. The profiler-derived horizontal wind fields were found to be qualitatively consistent with wind fields derived from nearby rawinsondes. Moreover, Yoe et al. (1992) presented a more detailed analysis of the horizontal and vertical wind fields for one of the MCSs discussed in Augustine and Zipser (1987). Using data from a VHF profiler in conjunction with two 5-cm Doppler radars, Yoe et al. (1992) showed that the wind profiler was able to identify many of the storm mesoscale features (e.g. mid-level rear inflow jet; upper-level front-to-rear flow), similar to the scanning radars. A comparison of the vertical air motions diagnosed by profiler and scanning radars using

a single-Doppler retrieval technique showed that the vertical velocity profiles were in reasonable agreement for most heights above the melting level (for the one analysis time presented in the study).

VHF profiler data have also been used to diagnose vertical air motions in precipitating systems over Japan (Wakasugi et al. 1986; Wakasugi et al. 1987; Sato et al. 1990; Larsen et al. 1991). In particular, Larsen et al. (1991) used VHF wind profiler data to diagnose vertical motions using the VAD (Velocity Azimuth Display) technique as well as direct measurements of the clear air during a cold frontal passage. Their study concluded that the methods agreed well in regions of isotropic scatter. However, poorer correlations were found in regions of strong stratification or anisotropic scattering (aspect sensitivity). Chilson et al. (1993) diagnosed the vertical air motion and precipitation fall speeds in a thunderstorm which passed over a VHF profiler site in Puerto Rico. In that study, collinear beams from UHF and VHF profilers were used to analyze the precipitation and wind structure of the thunderstorm.

Ralph et al. (1993) described the use of 50 MHz wind profiler data in conjunction with automated surface meteorological and rawinsonde data to resolve a ducted mesoscale gravity wave during a period of extensive convective activity in southwestern France in the LANDES-FRONTS 84 experiment. The array of instrumentation provided a mutually consistent picture of the detailed vertical structure of the wave from the ground level to just above a critical level. However, the data did not permit the role of the wave in initiating or modulating the convective activity to be deduced. Crotchet et al. (1990) describe the application of 50 MHz wind profiler data to delineate the 3-dimensional wind field and frontal features prior to and during the passage of an extratropical cyclone in western Europe. The wind profiler was able to resolve many features of the disturbance including the warm frontal zone and upper level jet streaks.

### 1.3.1 MCS vertical air motion structure

In this section, a brief overview of observational research results on the vertical draft structure tropical and middle latitude MCSs is presented. It should be noted that the observational results cited in the literature represent a wide range of sample sizes and temporal and spatial averaging. Many of the salient features of these studies are summarized in Houze (1989) and include:

1) A predominant profile of upward motion in the convective region. However, the location of maximum ascent in the convective portions of tropical MCSs has considerable variability. For example, profiles from Pohnpei Island in the western pacific (Balsley et al. 1988) and west Africa (Chong et al. 1983) indicate regions of maximum ascent in the mid - to - upper troposphere. In contrast, heating profiles derived by Johnson (1984) from winter MONEX suggest a lower troposphere peak of maximum ascent in the western Pacific region. Moreover, profiles from the eastern tropical Atlantic (GATE) indicate a double peak ascent structure in the lower and mid-troposphere (Houze and Rappaport 1984; Gamache and Houze 1985). Because of the different sampling techniques employed in these studies, it is difficult to determine the extent to which the contrasts in the vertical air velocity profiles between different geographical regions can be attributed to meteorological phenomena (e.g., differences in the wind and moisture structure in the environment of the MCS), or differences inherent in the various techniques used to diagnose vertical air motion. Results from COPT 81 (Chong et al. 1983) suggest that the upward motion peak for continental tropical convection may be located higher in the troposphere compared to oceanic convection (i.e., the eastern Atlantic region sampled in GATE). In the middle latitudes, results from an Oklahoma squall line diagnosed by rawinsonde data (Ogura and Liou 1980) and dual-Doppler

analysis (Smull and Houze 1987a) indicate a primary peak of upward motion in the convective region centered in the lower troposphere. It should be noted that Biggerstaff and Houze (1993) diagnosed the maximum vertical air velocity in the middle troposphere during the passage of the convective region of a Kansas squall line using area-averaged dual-Doppler results.

2) Profiles from stratiform regions indicate significantly smaller vertical air motions than in convective regions with descent in the lower troposphere below the melting level (due primarily to melting and evaporation) and ascent in the upper troposphere, supporting the growth of ice particles by vapor deposition (Rutledge and Houze 1987). Results from previous studies on tropical oceanic cases suggest maximum upward/downward motion on the order of 0.20 m $s^{-1}$; while for continental tropical MCSs, peak vertical motions are on the order of 0.30-0.45 m $s^{-1}$.

In addition to the studies discussed in Houze (1989), Frank and McBride (1989) described the evolution and vertical structure of vertical air motion in oceanic MCSs in the Gulf of Carpenteria region of AMEX, based on composited rawinsonde data. They showed that MCSs in the developing stage had a double peak ascent structure, one peak in the lower troposphere (near 650 mb) and another peak of lesser magnitude in the upper troposphere (near 250 mb). During the period when MCSs were producing maximum rainfall, a single peak of ascending motion was found in the middle troposphere near 550 mb (5 km). Near the end of the system's lifecycle, the position of maximum ascent moved upward to roughly 400 mb (7.5 km). Frank and McBride (1989) also compared vertical air velocity profiles from AMEX to corresponding GATE results. Their results showed that GATE profiles consistently had larger vertical velocities below 700 mb compared to AMEX while upward motions in AMEX MCSs extended to higher levels compared

to the GATE region. Thompson et al. (1979) and Frank and McBride (1989) attributed the lower level peak in the GATE vertical air velocity profiles to a shallower layer of low-level convergence and weaker instability in the east Atlantic, as compared to the west Pacific.

Johnson and Bresch (1991) analyzed vertical air motion and diabatic heating fields for selected cases during the 1987 TAMEX. They used 6 hour sounding data in order to construct profiles of vertical air velocity and heating. Moreover, radar reflectivity data was available in order to deduce the precipitation features associated with the vertical air motion field. Analysis of the deep convective portion of one particular case (Johnson and Bresch 1991; their Fig. 8) showed a double peak structure of upward motion with maximum ascent centered near 600 mb (4.5 km) and 300 mb (9.5 km). This double peak vertical air velocity structure is remarkably similar to the systems analyzed in the initial stages of the AMEX and GATE MCSs (Frank and McBride 1989). Profiles constructed 24 hours later in the TAMEX case were more representative of stratiform conditions with peak ascent centered near 650 mb (4 km). Descending motion was found above 500 mb (5.5 km) and below about 800 mb (2 km).

Results from flight-level aircraft data in several tropical oceanic environments including GATE (Zipser and LeMone 1980), TAMEX (Jorgensen and LeMone 1989), and EMEX (Lucas et al. 1994) have shown that the vertical draft sizes in precipitating oceanic convection are much weaker than in continental thunderstorms. The results are consistent with the overwhelming concentration of global lightning to continental and island locations as opposed to open ocean regions (Orville and Henderson 1986). In addition, these studies point to the importance of warm rain collision coalescence processes to precipitation production in the tropics, with the majority of precipitation falling out below the 0°C isotherm and a rapid conversion to ice above this level (consistent with the observed steep reduction in radar reflectivity above the 0°C isotherm).

Jorgensen and LeMone (1989) showed using a one-dimensional steady state model that water loading and entrainment played a significant role in reducing both the convective core virtual temperature excess with respect to the environment and the updraft velocity from what would be expected based on parcel theory. Moreover, Lucas et al. (1994) suggest that, although the amount of water loading in land-based and oceanic convection may be similar, the effect of water loading is greater in the case of oceanic convection since these systems tend to have a narrower positive area region on a thermodynamic diagram compared to continental convection [i.e., oceanic soundings usually have "skinny" positive areas compared to "fat" positive area regions and land-based convection, even though the overall values of Convective Available Potential Energy (CAPE) may be similar].

Gallus and Johnson (1991) used a rawinsonde network deployed during the PRESTORM to diagnose vertical air motion and diabatic heating and moistening profiles for a continental squall line in its mature to dissipating stages. The study documented the existence of three mesoscale jets within the MCS, consistent with previous investigations using radar and wind profiler data. The diagnosed vertical air motion profiles showed deep ascent in the convective region with a peak near 400 mb that subsequently weakened and tilted rearward over time. The stratiform region was characterized by upper level ascent and lower level descent. However, Gallus and Johnson (1991) noted that the sounding network was barely adequate to resolve the convective line and that some merging of convective and stratiform features occurred.

Lin and Johnson (1994) also performed a rawinsonde budget analysis for a different PRESTORM MCS. Their study showed that the development of the stratiform region played an important role in the evolution of several mesoscale circulation features, including the strengthening of the RTF (Rear-To-Front) relative flow and the appearance of a midlevel mesolow

and mesohigh couplet. During the early stages, upward vertical air motion in the convective line peaked near 550-600 mb; however, similar to Gallus and Johnson (1991), the sounding resolution allowed aliasing between the convective and stratiform regions. In the stratiform region, the profile of vertical air motion showed a peak ascent near 450 mb with weak descent in the lower troposphere. Similar to many previous studies, the results of Lin and Johnson (1994) show a close correspondence in the vertical structure of the apparent diabatic heat source ($Q_1$) and the profile of vertical air motion.

In addition to vertical motion fields deduced within the cloud boundaries, recent attention has focused on the vertical motion field in the vicinity of the tropopause in regions of deep convection. In the tropics, Gray (1972) and Gray and Jacobson (1977) suggested that enhanced subsidence occurred in the environment of upper-level cirrus clouds in response to radiative cloud top cooling. Johnson and Young (1983) documented downward motion in the vicinity of the tropopause during Winter MONEX using 6 hour composited sounding data. More recently, Balsley et al. (1988) used wind profiler data from Pohnpei Island to show a secondary peak of upward motion occurring near cloud top and a shallow layer of downward motion (10-15 cm $s^{-1}$) extending into the lower stratosphere. Houze (1989) suggested that the descent may be due to strong divergent outflow from the tops of MCSs. Carter et al. (1991) also found a similar region of downward motion in the vicinity of the tropopause near Darwin. No information relating vertical motion to specific cloud features could be analyzed in either the Balsley et al. (1988) or Carter et al. (1991) studies.

Downward motion in the vicinity of the tropopause has also been documented in middle latitude cases as discussed by Johnson et al. (1990) who used composited sounding data to show the existence of downward motion centered in a 2-3 km layer near the tropopause, above the

stratiform region of an MCS. The magnitude of this motion was on the order of 5 cm $s^{-1}$. Similar regions of downward motion was diagnosed by Gallus and Johnson (1991) and Lin and Johnson (1994) above the anvil tops of middle latitude MCSs using rawinsonde data. Moreover, Johnson et al. (1990) showed that the descent was largely independent of radiative effects and was associated with adiabatic cooling in the vicinity of the top of the MCS with downward sloping isentropes to the rear of the convective line. As Johnson et al. (1990) argued, the localized cooling at upper levels in response to overshooting tops from convection within MCSs may at least partially explain the global occurrence of low water vapor mixing ratios which are known to occur in the lower stratosphere.

## Chapter II

## METHODOLOGY

The majority of data for this research were collected near Darwin, N.T., Australia during the wet seasons (defined in Ch. 3) of 1989-1990 and 1990-1991. The 1989-1990 season coincided with the second phase of the DUNDEE while the 1990-1991 wet season did not correspond with a formal experiment field project, other than the ongoing TRMM (Tropical Rainfall Measuring Mission; Simpson et al. 1988) ground truth program. During DUNDEE, two C-band 5-cm Doppler radars (MIT and TOGA) were utilized in conjunction with the 50 MHz NOAA/BMRC (Bureau of Meteorology Research Centre) Darwin wind profiler to sample tropical convection. The location of the radars and the wind profiler are shown in Fig. 2.1. The wind profiler was positioned about 4 km from the TOGA radar, approximately along the baseline between MIT and TOGA. For the 1990-1991 wet season, the TOGA radar and the 50 MHz wind profiler remained in place and continued to collect data. Characteristics of the MIT and TOGA radars, as well as the Darwin wind profiler are shown in Table 2.1.

Data were also collected in the western Pacific warm pool region during the COARE IOP (Intensive Observing Period; November 1992-February 1993). During COARE, the MIT and TOGA radars were deployed aboard the R.V. Vickers and Xiangyanghong #5 (hereafter referred

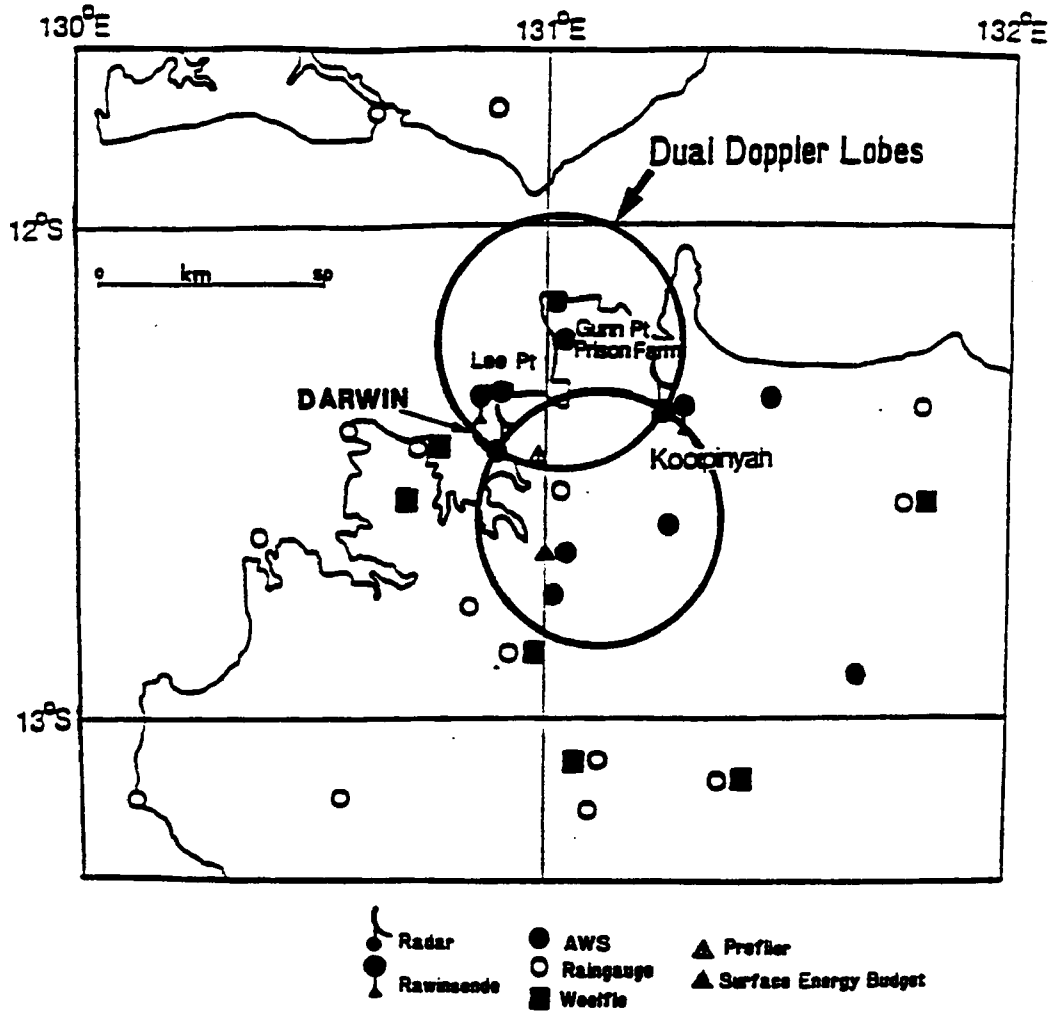


Fig. 2.1. Location of the observational network used during the DUNDEE field program (adapted from Rutledge et al. 1992). The TOGA radar, wind profiler, and rain gauge network remained operational during the 1990-1991 wet season (other instrumentation ceased operation after DUNDEE). Note that only a portion of the rain gauge network is shown in the figure.

Table 2.1. Characteristics of the MIT-TOGA microwave radars and the Darwin VHF wind profiler used during the DUNDEE and the 1990-1991 wet seasons.

| Characteristic | MIT[1] | TOGA[2] | Wind Profiler[2] |
|---|---|---|---|
| Wavelength (cm) | 5.4 | 5.3 | 600 |
| Peak power (kw) | 250 | 250 | 30 |
| Pulse length ($\mu$sec) | 1.0 | 0.50, 1.9 | 6.7 |
| Beamwidth (°) | 1.4 | 1.65 | 3.4 |
| Minimum detectable signal (dBm) | -106 | -113 | -165* |
| Pulse repetition frequency ($s^{-1}$) | 921 | 921 | 1000 |
| Antenna gain (dB) | 42.2 | 40.8 | 29.7 |
| Number of gates | 226 | 224 | 50 |
| Polarization | Horizontal | Horizontal | Horizontal |

[1] Instrument platform available for DUNDEE only
[2] Instrument platform available for DUNDEE and 1990-1991 wet seasons
* The minimum detectable signal of the VHF wind profiler has an estimated uncertainty of $\pm$ 20 dB.

to as the PRC 5) research vessels, respectively. The ships were typically separated by 125-225 km in the vicinity of 2°S, 156°E in order to sample atmospheric convection and diagnose rainfall over a portion of the COARE IFA (Intensive Flux Array). The nominal location of the ship radar platforms are shown in Fig. 2.2. The ships remained on-station collecting data in the COARE IFA almost continuously for four months, providing an un-precedented record of the life-cycle characteristics of a wide range of convective features occurring in the IFA. An additional ship-based radar platform, the Keifu-Maru with a non-coherent C-band radar, also participated in TOGA COARE for a brief period near the beginning of the IOP (Fig. 2.2) but was not used in this study.

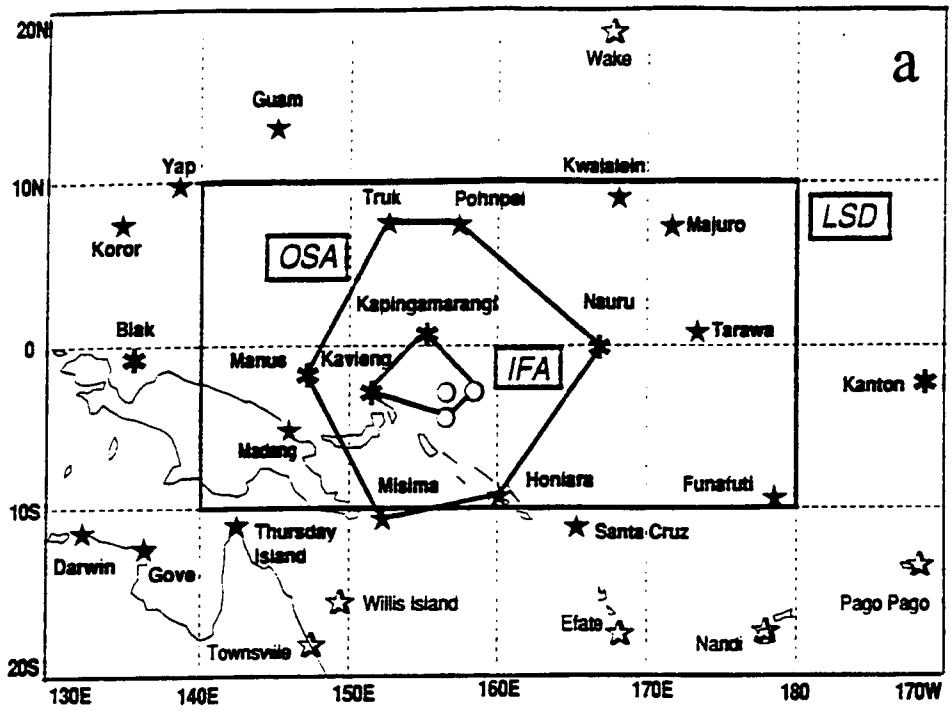


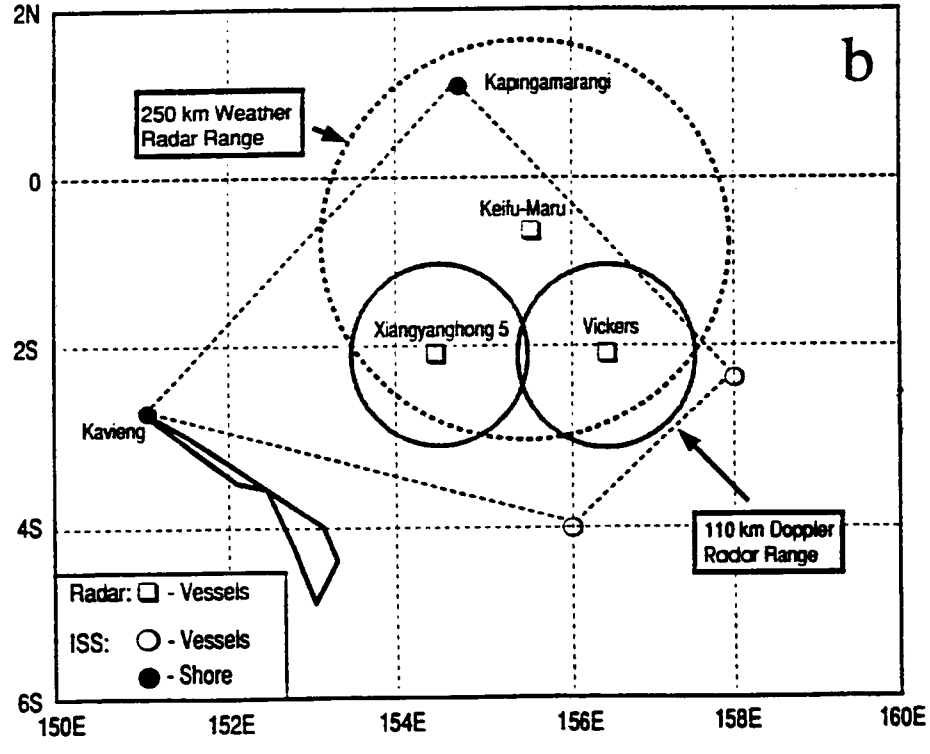


Fig. 2.2. Location of the observational network deployed during the TOGA COARE IOP. (a) The entire COARE domain with the Large-Scale Domain (LSD), Outer Sounding Array (OSA), and Intensive Flux Array (IFA) outlined (from Webster and Lukas 1992). (b) The location of the radar ships deployed in the IFA with approximate limits of radar coverage indicated.

In addition to the C-band radars on ship platforms, X-band (3-cm) radars were also deployed on several research aircraft during COARE. These platforms included the two NOAA P-3 aircraft (Jorgensen et al. 1996) and the NCAR Electra (Hildebrand et al. 1994). The aircraft were stationed in Honiara, Solomon Islands, ferrying several hours to the COARE domain in order to make detailed measurements of convective system structures and transports in the Pacific warm pool region. For this study, only the NOAA P-3 data were used and the Electra-ELDORA radar platform will not be reviewed here. Characteristics of the C-band MIT and TOGA radars and the NOAA P-3 X-band radars deployed during TOGA COARE are shown in Table 2.2.

Table 2.2. Characteristics of the MIT, TOGA, and NOAA P-3 tail-mounted radars during TOGA COARE (adapted from Rutledge et al. 1993 and Jorgensen et al. 1996).

| Characteristic | MIT | TOGA | NOAA P-3 |
|---|---|---|---|
| Wavelength (cm) | 5.37 | 5.35 | 3.22 |
| Peak power (kw) | 155 | 250 | 60 |
| Pulse length ($\mu$sec) | 1.0 | 0.48, 1.82 | 0.5 |
| Beamwidth (°) | 1.6 | 1.55 | 1.35,1.90* |
| Minimum detectable signal (dBm) | -115 | -105 | -111 |
| Pulse repetition frequency ($s^{-1}$) | 250-1500 | 250-1500 | 1600 |
| Antenna gain (dB) | 40.5 | 40.0 | 40.0* |
| Number of gates | 581 | 581 | 512 |
| Polarization | Horizontal | Horizontal | Horizontal |

* Steerable antenna

## 2.1 Darwin wind profiler

### 2.1.1 Signal processing characteristics

The Darwin VHF wind profiler operates at a frequency of 50 MHz[1], allowing both clear air and precipitation echoes to be measured directly (Carter et al. 1991; see Appendix A for a discussion of echoing mechanisms). During the DUNDEE field program, the profiler was operated with a single beam pointed at vertical incidence, providing a nearly continuous record of the vertical air and precipitation motions. Each profiler observation had a temporal resolution of 100 seconds and a gate spacing of 495 m. The range to the first gate was 1.354 km during the DUNDEE and 1.504 km during the 1990-1991 field season. The unambiguous velocity was designed to automatically switch from $\pm$ 6 m $s^{-1}$ to $\pm$20 m $s^{-1}$ whenever the Doppler spectral width exceeded the 6 m $s^{-1}$ range (Carter et al. 1991). The unambiguous velocity of 20 m $s^{-1}$ usually coincided with the occurrence of precipitation at the surface. During the 1990-1991 field season, a 3-beam configuration was used on the wind profiler and the update time on the vertical beam was increased from 100 seconds to approximately 4.5 minutes. This procedure reduced the spatial resolution capability of the wind profiler as described below in Sec. 2.1.2.

### 2.1.2 Effects of averaging

Prior to extracting the vertical air velocity, the raw spectra were averaged in time in order to reduce random noise fluctuations and improve the statistical significance of the results. In the stratiform regions, the individual spectra were averaged over an approximate 10 minute period

---

[1] A second wind profiler operating at 915 MHz was deployed in 1992 and was co-located with the 50 MHz platform.

(depending on the number of spectra used), the approximate length of time required to perform a single-Doppler radar volume scan. Sensitivity analysis of the averaging period showed that the vertical velocity estimates in the stratiform region did not vary appreciably over intervals of 5-15 minutes (Fig. 2.3). In the convective portion of each MCS, the averaging time of the profiler data was reduced to approximately 4-5 minutes, due to large turbulence and resulting wide spectra. Longer averaging intervals in the convective region usually "smeared out" the precipitation and clear air components of the spectra so that estimates of vertical air velocity could not be accurately determined (see below). Because of the different averaging length intervals used in the convective and stratiform regions, the spatial scale sampled by the profiler in each region also varied, since this scale is dependent on the speed of the MCS relative to the profiler, the profiler beam width, and the length of the averaging interval. For the events described herein, this spatial scale ranged from approximately 3-5 km in convective features to 5-9 km in the stratiform regions.

Due to the increase in the update time on the profiler vertical beam in the 1990-1991 season compared to the 1989-1990 season, the resolution capability of the wind profiler was reduced. The resolution reduction can be understood by considering a periodic feature (e.g., an updraft-downdraft couplet) that is advecting over the wind profiler at a constant rate (assume 10 m $s^{-1}$) and is not evolving appreciably. In order to properly resolve this feature, assume further that five observations are needed during its passage over the profiler. Thus, the feature must have a wavelength of at least $5\Delta T$ (where $\Delta T$ is the period) for the profiler to resolve it. For the 1989-1990 season, the wind profiler vertical beam was updating every 100 s, allowing a feature wavelength of $\sim$ 5 km to be resolved in any particular observation. If the feature is smaller than the 5 km threshold wavelength, it will be smeared (aliased) to a degree depending on its actual horizontal dimension. The effect of the smearing will appear as an increase in spectral width.

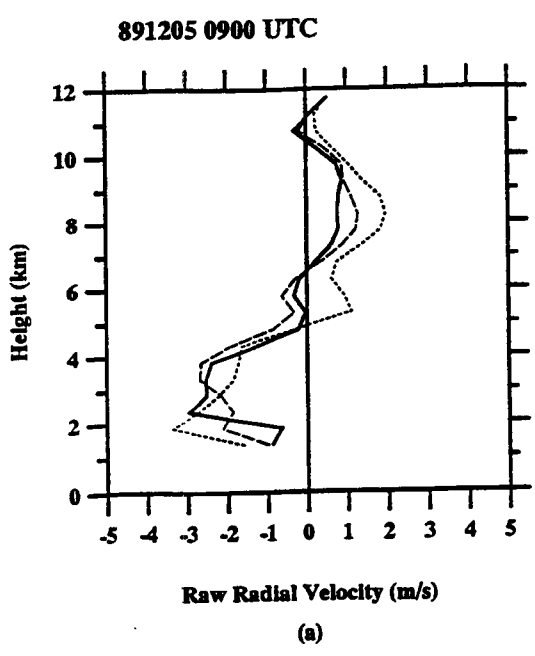
891205 0900 UTC
Height (km)
0
2
4
6
8
10
12
-5 -4 -3 -2 -1 0 1 2 3 4 5
Raw Radial Velocity (m/s)

(a)

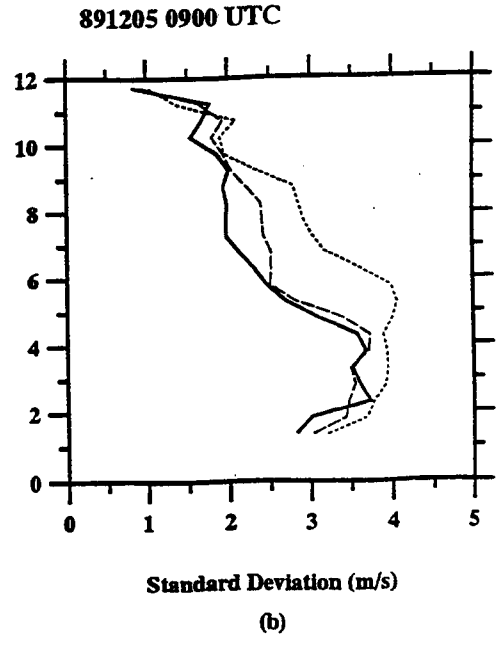
891205 0900 UTC
0
2
4
6
8
10
12
0 1 2 3 4 5
Standard Deviation (m/s)

(b)

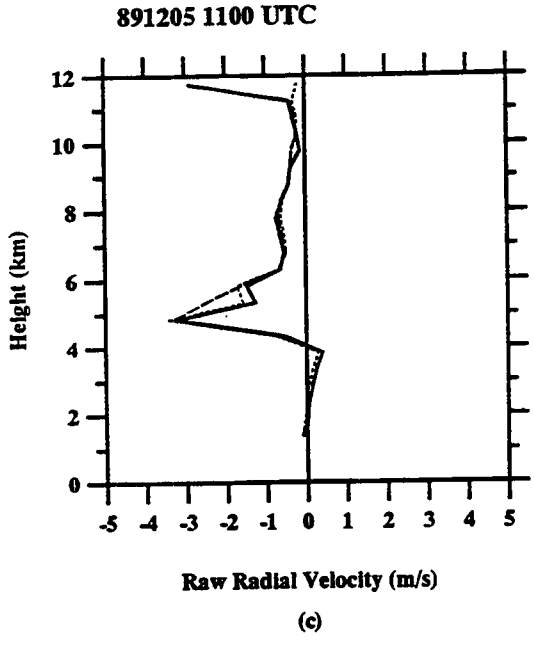
891205 1100 UTC
Height (km)
0
2
4
6
8
10
12
-5 -4 -3 -2 -1 0 1 2 3 4 5
Raw Radial Velocity (m/s)

(c)

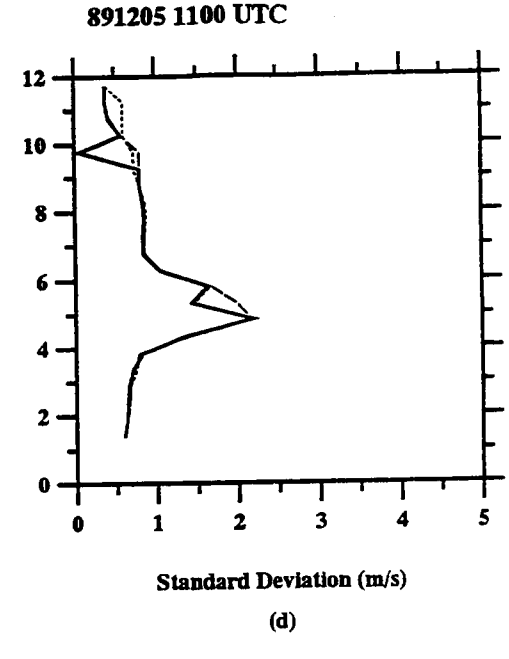
891205 1100 UTC
0
2
4
6
8
10
12
0 1 2 3 4 5
Standard Deviation (m/s)

(d)

Fig. 2.3. Representative profiles of mean clear air vertical motion and standard deviation for the 5 December 1989 MCS using the results of the curve-fit algorithm. In (a) and (b), spectra were collected during the passage of the convective line (0900 UTC), while profiles in (c) and (d) represent spectra collected under stratiform conditions (1100 UTC). The solid, long-dashed, and short-dashed lines represent the profiles obtained after averaging the spectra over 5, 10, and 15 minutes, respectively, and running the curve-fit algorithm. In (a) and (c), positive (negative) radial velocity indicates upward (downward) motion. Note the relatively large changes in radial velocity and standard deviation between the different profiles in the convective region compared to similar profiles in the stratiform region. Also note that the radial velocities have not been adjusted to account for particle fall speed biases (see text for details).

Now consider the 1990-1991 data with the wind profiler update time of 4.5 minutes (270 s). In this case, the updraft-downdraft couplet must have a wavelength of at least 13.5 km for the wind profiler to accurately resolve it. Thus, for measurements which include features with small horizontal scales (e.g., updraft-downdraft cores in the convective portion of an MCS), there is likely to be larger variance (i.e., wider spectral width) in the data when the wind profiler is operating in the 1990-1991 configuration compared to the 1989-1990 configuration.

During the sampling period of each MCS, the Nyquist interval occasionally alternated between $\pm 6$ and $\pm 20$ m $s^{-1}$. Because the average profiles were generated using only data with the same unambiguous velocity, they did not always contain the same number of raw spectra profiles and the averaging time occasionally varied by a few minutes. Within a given averaging interval, the magnitude of vertical air velocity in the averaged profile was not particularly sensitive to the number of individual spectra used in the time-averaging. Individual spectra were scrutinized in order to avoid contaminating the averaged results with spurious spectral power signals (i.e. radio interference, electrical discharges, etc.).

A comparison of the wind profiler and scanning radar sampling volumes is provided in Appendix A. Here, it is simply noted that the atmospheric volume measured by the wind profiler is a small fraction of the volume sampled by a scanning radar, even when the wind profiler spectra are averaged over a long time period.

### 2.1.3 Retrieval of the profiler Doppler spectra components

A number of different techniques have been used to separate the clear air vertical motion from the hydrometeor fall speed in VHF wind profiler spectral data. Some of the procedures

include: first moment analysis of the Doppler spectra (Clark and Carter 1980); least squares fit of the Doppler spectra with one or two Gaussian approximations (Yoe et al. 1992); and least squares fit of the Doppler spectrum with a drop size distribution approximation for the hydrometeor component of the spectra and a Gaussian distribution to the turbulent component (Wakasugi et al. 1986; Wakasugi et al. 1987; Sato et al. 1990).

#### 2.1.3.1 Objective algorithm description

In this study, a combination of methods was developed to separate the clear air and precipitation components in the averaged spectra. First, an objective algorithm to derive both atmospheric turbulence and precipitation parameters was developed based on the method described by Sato et al. (1990). The Sato et al. technique utilizes a Marshall-Palmer distribution to approximate the precipitation component of the spectra and a Gaussian distribution to fit the turbulence component to the observed Doppler spectrum $S(\upsilon)$ according to:

$$S(\upsilon) = S_t(\upsilon) + S_p(\upsilon) * S_0(\upsilon) + P_n \,, \tag{2.1}$$

where $S_t(\upsilon)$ represents the Doppler power at frequency $\upsilon$ associated with backscatter from irregularities in the refractive index due to turbulence, $S_p(\upsilon)$ represents the Doppler spectrum due to liquid precipitation, $S_0(\upsilon)$ is a normalized form of $S_t(\upsilon)$, $P_n$ represents the noise level in the Doppler spectrum and the symbol * denotes the convolution operation (Sato et al. 1990). $S_t(\upsilon)$ is approximated by the Gaussian function

$$S_t(\upsilon) = P_0 \exp\left[\frac{-(V-w)^2}{2\sigma^2}\right], \tag{2.2}$$

where $w$ is the mean radial (vertical) wind velocity, $V$ is the hydrometeor terminal fall speed, and $\sigma$ is the spectral broadening. It is noted that the effects of beam broadening and wind shear can distort the shape of the vertical air component from a Gaussian distribution (Hocking 1983). $S_p(\upsilon)$ is expressed as

$$S_p(\upsilon) = C \cdot N(D) \cdot D^6 \left| \frac{d[V(D)]}{dD} \right|^{-1} , \qquad (2.3)$$

where $N(D)dD$ is the number of raindrops per unit volume with diameters between $D$ and $D + dD$, and $C$ is a constant related to the backscattered power. The relation between drop diameter $D$ (mm) and drop fall speed $V$ (m s$^{-1}$) is taken from Gunn and Kinzer (1949) as

$$V(D) = -[9.65 - 10.3\exp(-0.6D)] \cdot \left[ \frac{\rho_0}{\rho} \right]^{0.4} , \qquad (2.4)$$

where $\rho_0$ and $\rho$ are the air densities at the surface and aloft, respectively. As noted by Sato et al. (1990), (2.4) is only valid for $D$ larger than $D_{min}$, the diameter required to make $V(D)$ in (2.4) zero. That is

$$D_{min} = -\ln \left[ \frac{(9.65/10.3)}{0.6} \right] = 0.11 , \qquad (2.5)$$

and it is assumed that there are no rain drops with diameters less than $D_{min}$. It is also assumed that the drop diameter cannot exceed 6mm ($D_{max}$) without breaking into smaller particles. The maximum drop fall speed ($V_{max}$) corresponding to $D_{max}$ is determined from (2.4). The Marshall and Palmer (1948) drop size distribution in (2.3) is expressed as

$$N(D) = N_0 \exp(-\Lambda \cdot D) , \qquad (2.6)$$

where $\Lambda$ is the distribution slope (m$^{-1}$) and $N_0$ is the slope intercept (m$^{-4}$). The term $S_o(\upsilon)$ in (2.1) is a normalized form of $S_t(\upsilon)$ and is expressed as

$$S_0(\upsilon) = \frac{1}{(2\pi)^{1/2}\sigma} \exp\left[\frac{-(V-w)^2}{2\sigma^2}\right]. \qquad (2.7)$$

The convolution operation in (2.1) implies that the raindrops instantaneously respond to atmospheric turbulence (Wakasugi et al. 1987). In practice, a window function is usually applied to the Doppler spectrum S(υ) in order to account for data truncation effects and to improve the curve-fit along the edges of the Doppler spectrum (Wakasugi et al. 1986). Because the objective of this analysis was only to determine the mean vertical air velocity and due to computational time constraints, no windowing function was utilized in the curve-fit procedure.

The objective algorithm was applied to each gate in the averaged wind profiler spectra. The curve-fit solution is the set of parameters obtained through a nonlinear least squares minimization of the error ϵ defined as

$$\epsilon = \sum_{i=ifs}^{ife} |\log [S_{obs}(\upsilon_i)] - \log [S(\upsilon_i)]|^2 . \qquad (2.8)$$

In (2.8), $S_{obs}(\upsilon_i)$ is the observed Doppler spectra and *ifs* and *ife* are the range of frequency points in the spectra as follows

$$\begin{aligned} ifs &= j_{pp} - 20 \\ ife &= j_{pt} + 20 \end{aligned}, \qquad (2.9)$$

where $j_{pt}$ and $j_{pp}$ are the frequency points where the turbulence and precipitation echoes are maximized, respectively (Sato et al. 1990). Note that the data point corresponding to zero Doppler shift is removed from the analysis in order to reduce clutter contamination.

In practice, the algorithm was applied to the power spectra at each gate by first assuming that the spectra only had a contribution from the clear air. That is, (2.1) is modified to

$$S(\upsilon) = S_t(\upsilon) + P_n \ . \qquad (2.10)$$

This procedure greatly reduced the computational time required for the analysis since the error minimization in (2.8) only had to be performed on four parameters ($P_0$, $w$, $\sigma$, and $P_n$). However, if the resulting chi-square statistic from the curve-fitting procedure exceeded an empirical threshold, it was assumed that both components, precipitation and turbulence, were present and the algorithm re-analyzed the power spectra according to (2.1). In this case, the error minimization (2.8) had to be performed on seven parameters ($P_0$, $w$, $\sigma$, $P_n$, $N_0$, $\Lambda$, and $V_{max}$). As described in Sato et al. (1990), a range of initial values was selected for $N_0$, $\Lambda$, and $V_{max}$, and the error minimization $\epsilon$ was calculated to find the minimum among all combinations of these parameters.

### 2.1.3.2 Manual editing procedure

Sensitivity analysis with the curve-matching program showed that the algorithm fit the spectra reasonably well below the melting level ($\sim$ 4.7 km) and above about 9 km; however, in the region between about 4.5 - 9.0 km, the algorithm was often unable to distinguish between the vertical air velocity and precipitation components (Fig. 2.4). This was probably due to the existence of water drops, snow, and other types of ice particles in the mixed phase region of the cloud with fall speeds comparable to the vertical air motions (Carter et al. 1991). Because of the wide range of hydrometeor fall speeds (i.e., a broad precipitation spectra), the precipitation and vertical air velocity components of the spectra "merged together" to the point that the curve-fit program attempted to fit both parts of the spectra with a single Gaussian distribution (i.e., the fit was underdetermined; Fig. 2.4b). Merging of the precipitation and turbulence components caused the center of the Gaussian curve fit (i.e., mean vertical air velocity) to be shifted to the left (i.e.,

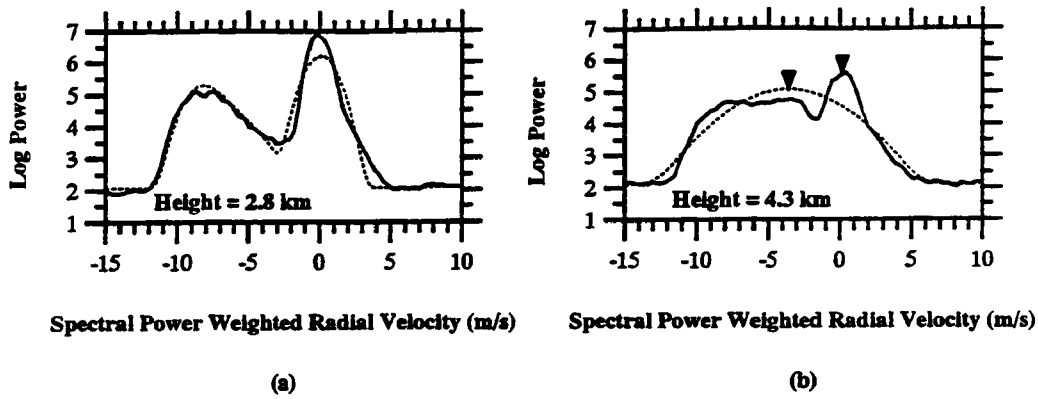


Fig. 2.4. Ten-minute averaged spectra collected at 1100 UTC 5 December 1989 at (a) 2.8 km and (b) 4.3 km. The solid line shows the observed spectra with the left peak indicating hydrometeor fall velocity and the right peak indicating vertical air velocity. Positive (negative) radial velocities represent upward (downward) motion. The dashed line represents the results of the curve-fit algorithm. In (b), the left (right) triangle indicates the vertical air velocity estimate selected by the curve-fit algorithm (manual editing). Note the change in shape of the precipitation component of the spectra in (b) compared to (a).

toward negative radial velocities) relative to the center of the turbulence peak power. Similar difficulties in separating the vertical air motion from the particle fall speeds using a VHF profiler were reported by Chilson et al. (1993) while sampling a thunderstorm in Puerto Rico; however, in that study, data from a collocated UHF profiler were used to help extract the vertical air component. In situations where the components of the spectra could not be objectively separated, a second analysis technique was used to extract the vertical air velocity information from the spectra. In these cases, the center of the Gaussian was manually edited so that the mean vertical air motion coincided with the approximate location of the turbulence peak power (Cifelli and Rutledge 1994b). This procedure greatly increased the time required to retrieve profiles of the vertical air motions in each MCS.

Figure 2.5 shows composite profiles of several statistical parameters associated with the curve-fit algorithm to quantify potential errors in the vertical air motion estimates. These statistics were generated for the convective, transition, and stratiform regions using all of the averaged spectra from the break MCSs sampled during DUNDEE[2]. Figure 2.5a shows the mean composite vertical air standard deviation of the averaged spectra as determined by the curve-fit procedure. Since this statistic was generated by the curve-fit algorithm, it provides a measure of vertical air velocity variance in regions where the algorithm generated a reasonable match to the spectra (i.e., no merging of the turbulence and precipitation components).

The degree of spectra merging is indicated in Fig. 2.5b, which shows profiles of the average difference (absolute value) of the curve-fit and manually edited vertical air velocity estimates

---

[2] Because the update time on the profiler vertical beam increased substantially in the 1990-1991 season compared to DUNDEE, the spectra were not included in this statistical analysis (see discussion in Sec.2.1.2)

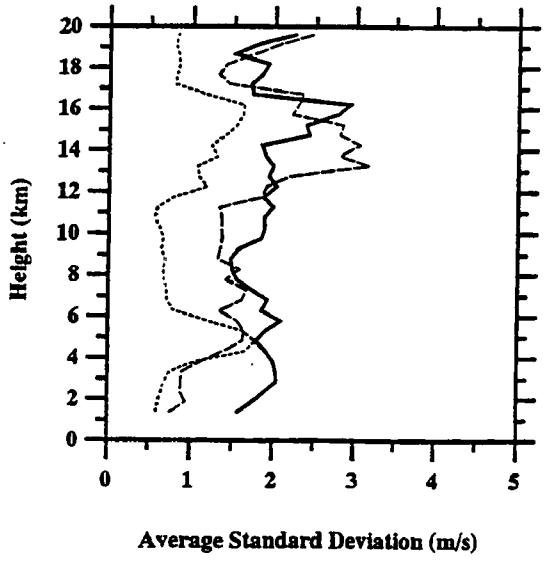
Height (km)
Average Standard Deviation (m/s)

(a)

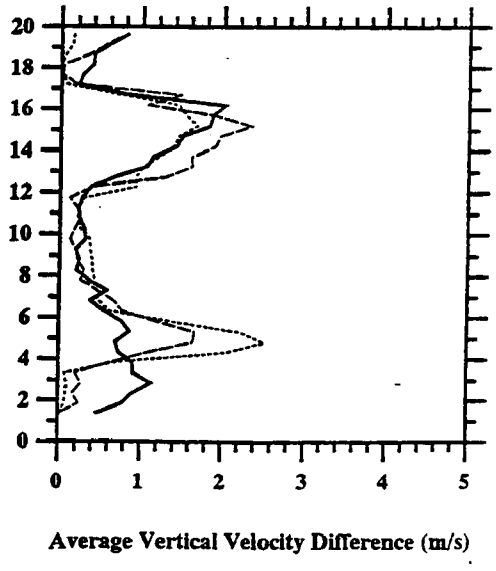
Average Vertical Velocity Difference (m/s)

(b)

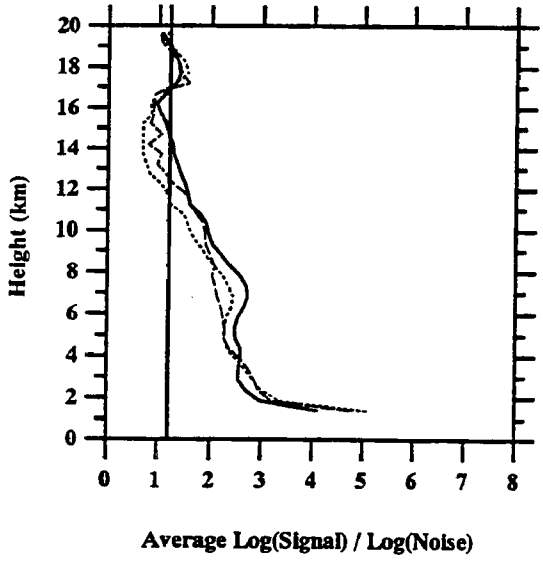
Height (km)
Average Log(Signal) / Log(Noise)

(c)

Fig. 2.5. Composite profiles for the convective line (solid line), transition (long-dashed line), and stratiform (short-dashed line) regions of four break MCSs sampled during the 1989-1990 wet season, based on results from the curve-fit algorithm. (a) Standard deviation. (b) Vertical velocity difference calculated as the absolute value difference of the vertical air velocity estimate generated by the curve-fit algorithm and the manually edited value. This statistic indirectly measures the degree of spectra merging in the data (see text for details). (c) Signal-to-noise ratio, log (signal power)/log (noise power).

(hereafter referred to as velocity difference) for each region of the MCS. This parameter indicates the magnitude of the bias in the program-retrieved vertical air velocity estimate due to particle fall speed contamination. In regions where the algorithm identified separate spectra components for precipitation and turbulence, the magnitude of the velocity difference is relatively small, indicating that the corresponding standard deviation values are reasonable estimates of the variability of vertical air velocity around the mean value. However, in places where the vertical air and precipitation components merged, the difference in vertical velocity estimates is large due to the particle fall speed bias (compare Figs. 2.4a and 2.4b). In these situations, the algorithm usually generated a single Gaussian curve-match and assigned a standard deviation value based on the combined width of the vertical air and precipitation components. Therefore the standard deviation values in the region of merged spectra shown in Fig. 2.5a provide conservative (maximum) estimates of the vertical air velocity variability. More accurate estimates of the vertical air velocity standard deviation alone would require a very subjective estimate of the shape of the turbulence spectra component and resulting Gaussian curve-fit inflection point.

In the convective region, the profile of composite standard deviation is relatively large (1.5-2.0 m $s^{-1}$) with a peak in the lower troposphere, due to the existence of broad spectra (Fig. 2.5a). The large variability in the lower troposphere is coincident with large magnitudes of the velocity difference profile (Fig. 2.5b), indicating that the convective region spectra are most affected by merging in the lower troposphere. In the stratiform region, the shape of the standard deviation profile is significantly different from the convective region. The magnitudes of the composite stratiform standard deviation profile are on the order of 0.65-0.7 m $s^{-1}$ below about 3.5 km and above 6.5 km, significantly less than the corresponding convective region profile (Fig. 2.5a). In the vicinity of the melting level ($\sim$ 5 km), the stratiform standard deviations are of similar magnitude to the convective region ($>$ 1 m $s^{-1}$) due to the large hydrometeor component of the

spectra relative to the clear air and the resulting spectra merging (Fig. 2.5b). Vertical air velocities were shifted over 2 m $s^{-1}$ on average (to more positive values) to correct for the particle fall speed contamination in this region. Moreover, as can be seen from Fig. 2.5b, the magnitude of the particle fall speed bias gradually tapers off with increasing height above 6.5 km (similar to the convective region profile), as the intensity of the hydrometeor component is reduced. As expected, the magnitude and shape of the composite transition zone profile has similar characteristics to both the convective and stratiform regions.

Additional errors in the deriving vertical velocity measurements from 50 MHz wind profiler data can occur due to aspect sensitivity (Larsen et al. 1991). This error occurs when the refractive layers (providing turbulence backscatter) are inclined with respect to the horizontal plane. Because the strongest scatter is produced in a direction perpendicular to the refractive layer, tilted layers will allow a component of the horizontal wind to be resolved along with the projection of the vertical component along the effective beam direction (Larsen et al. 1991).

#### 2.1.3.3 Signal to noise criteria

An arbitrary threshold of signal to noise was developed in order to determine if the power return at a particular level represented meteorologically significant data or was part of the noise spectrum. If the ratio of log(signal peak) / log(noise), determined by the curve fitting algorithm was below 1.2, it was assumed that the power return was insignificant and no vertical air velocity value was recorded for that particular gate. Since the signal power decreased gradually with height, there were many borderline cases where the ratio was approximately 1.2. In these situations, continuity of the velocity and width of the turbulence Doppler spectra with spectra at lower levels (where the threshold was exceeded) was used to determine if the power return at the

gate in question was meteorologically significant. The value of 1.2 was often found to be approximately coincident with the location of cloud top height, based on available GMS satellite imagery.

A comparison of the signal to noise threshold was performed with a similar empirical formula used by the NOAA AL. The NOAA AL algorithm is an empirical threshold based on the number of points in the spectra, the number of spectra averaged in the data processing, and an empirically derived constant (Dr. Anthony Riddle, personal communication). The results showed that the two methods of determining meteorologically significant data were in close agreement for the spectra profiles that were evaluated.

### 2.1.4 Partitioning profiler data into convective and stratiform components

In this study, MCS vertical air motions were partitioned into convective and stratiform components using two techniques. While recognizing the subjectivity involved in any applying any partitioning method, the procedure was done in order to facilitate comparisons of the wind profiler results with previous studies of MCS vertical air motion.

In the first method, an objective algorithm was developed to partition a volume of scanning radar data into convective and stratiform components, based on gradients of reflectivity. The method closely follows the algorithm of Steiner and Houze (1993) in which convective features in the volume of gridded radar data are identified based on the horizontal gradient of reflectivity at a height near the surface (i.e., 2 km). After identification at low levels, the features are extrapolated upward to the top of the radar volume. From this extrapolation, mean profiles of convective and stratiform reflectivity are calculated in order to obtain information on the vertical

structure of convective and stratiform areas. Although this procedure can sometimes produce misleading feature geometries in situations of large wind shear, it was found to produce reasonable results, in a volume average sense, in most sensitivity tests of tropical MCSs and to be the most computationally time efficient technique out of several that were attempted (Demott et al. 1995). This method was applied to as many available scanning radar volumes as possible in order to achieve a similar time-resolution to the wind profiler data (i.e., 10 minutes). Radar CAPPI's (Constant Altitude Plan Position Indicator) plots at a height of 2 km were then constructed and visually inspected to determine if a given feature over the location of the profiler was convective or stratiform. The CAPPI's were also used to partition the rain trace from each of the available rain gauges in the Darwin rain gauge network into convective and stratiform components (as described below in Sec. 2.3).

In situations where scanning radar data were not available at 10 minute intervals during the wind profiler observation period, a second technique was used to partition the wind profiler vertical air motion profiles. In this case, the variance of the wind profiler vertical air motion data were used to stratify the profiles into convective and stratiform components, similar to Willis et al. (1995). Specifically, the standard deviation statistic generated by the curve-fit algorithm were evaluated for each averaged spectra and assigned as convective or stratiform based on the following empirically derived criteria. If the standard deviation of the vertical air motion exceeded 1.25 m $s^{-1}$ for a continuous range of at least 3 km, then the entire spectra was partitioned as convective. It was found through sensitivity analysis that the continuous range of 3 km helped to eliminate stratiform spectra from consideration as convective, since spectra merging (as described above in Sec. 2.1.3.2) rarely occurred continuously for a range of more than 2.5 km. Sensitivity tests also revealed that the results of the wind profiler partitioning method were in close agreement with the scanning radar partitioning method described above.

In addition to convective and stratiform partitioning, several of the MCSs occurring during the monsoon-break had well-defined transition zone features observable in the radar reflectivity data as the system propagated over the wind profiler. In these situations, the vertical air motion data were partitioned into a transition zone category. The monsoon MCSs did not have clearly identifiable reflectivity trough features during their passage over the wind profiler and transition zone partitioning was not performed for these MCSs.

For each of the MCSs studied, approximately 3.5-10 hours of wind profiler data were obtained as the systems passed over the profiler site. A total of 498 vertical air motion profiles were constructed for all 13 of the MCSs. A summary of the number of convective, stratiform, and transition zone spectra used for each MCS is provided in Table 2.3.

## 2.2 Scanning radar

### 2.2.1 Darwin

Scanning Doppler radar data for the Darwin portion of this study were collected from both the MIT and TOGA radars during DUNDEE and from the TOGA radar, which continued to collect data, during the 1990-1991 field season. The scanning radar data was used to partition the wind profiler vertical air motion and surface rain gauge network data into convective and stratiform components, correlate the vertical draft structure with inferred cloud microphysical processes, and retrieve the kinematic flow patterns in the stratiform portion of several MCSs for comparison with similar wind profiler data.

Table 2.3. Summary of the number of wind profiler averaged spectra (convective, stratiform, and transition zone) analyzed for each of the 13 MCSs.

| Event Date (YYMMDD) | Type Regime | # Convective Spectra | # Stratiform Spectra | # Transition Spectra | Hours of Coverage |
|---|---|---|---|---|---|
| 891205 | Break | 7 | 27 | 3 | 6.2 |
| 900110 | Monsoon | 6 | 23 | | 4.8 |
| 900112 | Monsoon | 6 | 18 | | 4.0 |
| 900118 | Break | 13 | 4 | 1 | 3.0 |
| 900122 | Break | 9 | 12 | 4 | 4.2 |
| 900128 | Break | 8 | 14 | 6 | 4.7 |
| 901121 | Break | 7 | 29 | | 6.0 |
| 901210 | Monsoon | 14 | 28 | | 7.0 |
| 901212 | Monsoon | 17 | 43 | | 10.0 |
| 901215 | Break | 14 | 32 | | 7.7 |
| 910109 | Monsoon | 31 | 20 | | 8.5 |
| 910129 | Monsoon | 19 | 42 | | 10.2 |
| 910130 | Monsoon | 9 | 32 | | 6.8 |
| Totals | | 160 | 324 | 14 | 83.0 |

A description of the radar partitioning procedure is provided in Sec. 2.1.4. Details of the single-Doppler radar and wind profiler kinematic retrieval comparison is provided in Appendix B. A discussion of procedures to correlate the radar reflectivity and profiler vertical motion data is provided below.

#### 2.2.1.1 Correlation of radar reflectivity and profiler vertical motion

In order to infer cloud microphysical and precipitation production processes occurring within an MCS, it is useful to compare the vertical air motion pattern with the corresponding profile of

radar reflectivity. Ideally, the reflectivity data would be retrieved from the same platform as the vertical motion (i.e., wind profiler), since using data from a remotely-located instrument (i.e., the scanning radars) introduces problems of comparing different sampling volumes as well as requiring assumptions about beam attenuation and beam filling. Because the Darwin 50 MHz wind profiler had no absolute calibration, it was not possible to convert the measured backscattered power from precipitation targets at each range gate to a radar reflectivity factor value. Moreover, in the region where the two components of the spectra are merged, it would be difficult to accurately estimate the total power contribution from the precipitation component alone (see Fig. 2.5).

Another way to back-out the radar reflectivity factor from the wind profiler data would be to use the drop size distribution data $N(D)\,dD$ (see Eq 2.6) retrieved by the curve-fit algorithm to calculate the radar reflectivity factor $Z$ according to:

$$Z = \sum_i N_i D_i^6 \,, \tag{2.11}$$

where $N_i$ is the number concentration of drops with diameters between $D_i$ and $D_i + \Delta D_i$ ($D$ is the diameter of the melted equivalent particle). This procedure would work well below the melting level where the components of the Doppler spectra are clearly separated; however, the method will fail in regions above the melting level where the spectra merge or the precipitation component is too weak, since in these cases, the algorithm attempts to fit the spectra with a single Gaussian curve distribution and no drop size distribution parameters are retrieved. Even when no spectra merging has occurred, it is expected that the retrieved drop size parameters above the melting level would produce an inaccurate estimate of $Z$ since the algorithm assumes a Marshall-Palmer distribution which is only valid for liquid precipitation (i.e., below the melting level).

During the 1989-1990 DUNDEE season when MIT scanning radar data were available, time-height cross sections of radar reflectivity could be constructed over the wind profiler site and correlated with the profiler vertical air motion data. The reflectivity cross sections were generated with MIT data since the location of this radar relative to the wind profiler allowed for reflectivity data to be examined over the profiler up to a vertical distance of about 12 km. Radar volumes were analyzed approximately every 10 minutes in order to achieve the same temporal resolution as the wind profiler data. In cases where radar data were unavailable, linear interpolation was used to fill gaps in the reflectivity cross sections. The TOGA radar data were not used for the cross section analysis due to the close proximity of the TOGA radar to the wind profiler site, which precluded data retrieval above the melting level (see Fig. 2.1). No scanning radar reflectivity cross sections were constructed over the profiler location during events occurring in the 1990-1991 season as well as the 28 January 1990 MCS since MIT data was not available.

Since it was determined that an accurate retrieval of the vertical profile of reflectivity factor could not be computed from the wind profiler spectra and because it was not always possible to construct reflectivity cross sections over the profiler, a different approach was used to contrast the vertical reflectivity structure in monsoon and break MCSs. Available radar volume data for each event were analyzed using the radar partitioning algorithm described above in Sec. 2.1.4. In this way, the vertical reflectivity structure for each event could be analyzed in a *volume average* sense.

In the break MCSs, the period of radar analysis was defined by the first and last recorded rainfall in the rain gauge network. This time period varied from about 5-10 hours and bracketed the observation period at the profiler. For the monsoon events, it was more difficult to define the beginning and end of a particular event and a 12 hour period, which bracketed the time of profiler coverage, was selected for radar analysis. Although somewhat arbitrary, 12 hours was chosen

since it is the approximate time required for a radar observed feature to cross the rain gauge network (assuming that it moves at 8-10 m $s^{-1}$). Subsequent to the partitioning analysis, time-height cross sections of convective and stratiform reflectivity as well as composite profiles were constructed for each MCS.

### 2.2.2 COARE Domain

For the COARE data set, both single and multiple Doppler analysis methods were applied to recover the kinematic flow patterns in several MCSs that were sampled with the ship (MIT and TOGA) C-band and aircraft (NOAA P-3s) X-band radars. The MIT and TOGA radar antennas were stabilized to account for ship roll, pitch, and heading motions via an INU (Inertial Navigation Unit) mounted on the antenna pedestal (Rutledge et al. 1993). A GPS (Global Positioning System) receiver provided latitude, longitude, and time information. The stabilization was accomplished by providing rapid updates (200 Hz) of the antenna position from the INU to the antenna controller in order to maintain the desired azimuth and elevation angles.

Position errors in the ship radar data occurred due to a Schuler oscillation in the INU with a period of about 84.4 minutes (Leary et al. 1993). This low frequency oscillation is present in the $u$ and $v$ components of the ship's velocity data. The amplitude of the oscillation ranged from $\pm$0.25-2 m $s^{-1}$ for the MIT radar to 1-7 m $s^{-1}$ for the TOGA radar. The magnitude is larger for the TOGA radar, since the INU on this platform was manually updated from the GPS at intervals of about one hour (the procedure as done automatically and at a much higher frequency for the MIT radar). In order to eliminate bias in the radial velocity estimates, the Schuler oscillation must be removed from the ship motion data as described by Leary et al. (1993). In this study, no correction was made for Schuler oscillations in either the MIT or TOGA radar data since the

magnitude of the bias during sampling of the MCSs reported herein were within the uncertainty of the radial velocity measurements ($\sim < 1$ m s$^{-1}$).

The NOAA P-3 X-band radars are mounted in the tail section of the aircraft and scan in a vertical plane (Jorgensen et al. 1996) These radar antennas were also stabilized in COARE by an INU and GPS system to account for aircraft motion (Jorgensen et al. 1996). Similar to the ship-based radars, an INU Schuler oscillation was present in the aircraft motion data. A variational scheme was developed at NOAA NSSL to account for the Schuler oscillation drift and remove the bias prior to multiple Doppler synthesis (Dr. Sharon Lewis, NOAA/NSSL).

Characteristics of all the radars deployed during TOGA COARE are shown in Table 2.2. Similar to the Darwin radar data, the COARE radar data was partitioned into convective and stratiform components using the partitioning algorithm described in Sec. 2.1.4.

#### 2.2.2.1 Single-Doppler radar analysis

The single-Doppler analyses include the EVAD and CEVAD retrieval techniques, which are described in detail in Appendix B. Briefly, these techniques make assumptions about variations in the horizontal wind across the analysis domain in order to transform the measured radial wind field into a two-dimensional horizontal wind vector, calculate horizontal divergence through a least squares solution of the model, and then use the mass continuity equation to calculate a profile of vertical air velocity. The methods are most reliable in situations where the wind field is relatively homogeneous (i.e., stratiform as opposed to convective regions of MCSs) so that the wind field assumptions are not significantly violated. In the vertical air velocity calculation, EVAD makes

assumptions about the magnitude of vertical air motion at the top of the column whereas CEVAD imposes a constraint on particle terminal fall speed.

The single-Doppler retrievals were performed in the stratiform portion of two convective systems which passed over the MIT radar during the latter part of the COARE IOP and produced extensive areas of stratiform cloud lasting for several hours. As recommended by Matejka and Srivastava (1991), the volume scans were optimized to perform the EVAD and CEVAD analyses: the scan tilts in each volume ranged from 0.8°-52.6° or 55.1° in elevation angle (total of 17 to 20 scan tilts in each volume). A total of 27 volumes were analyzed in the two MCSs to retrieve the kinematic flow field. The radar volumes were collected at approximately 10 minute intervals, allowing for detailed time-height cross sections to be generated for the retrieved parameters in each MCS.

#### 2.2.2.2 Multiple Doppler analysis

Multiple Doppler syntheses, performed in a total of four TOGA COARE MCSs, were used in this study to examine profiles of vertical air motion and reflectivity and compare these with the Darwin results. One convective system was sampled by the ship-based radars which provided several hours of wind field information using the dual-Doppler synthesis procedure (described in Appendix C). An additional set of multiple Doppler analyses were performed on data collected by the NOAA P-3 Doppler radars from three MCSs that were sampled using the quad Doppler methodology (described in Appendix C).

A summary of multiple Doppler methodology is provided in Appendix C. Briefly, in the analysis of multiple Doppler data, two or more radars each provide an estimate of the radial wind

at a given location in the sampling domain which allows the horizontal wind field to be determined with minimal error (when beam crossing angles exceed 25° or so). Thus, the technique is applicable to all regions of the precipitating cloud, including the convective region. If two radars are used in the analysis (i.e., dual-Doppler), then the full three dimensional wind field can be recovered, provided that the terminal fall speed of the precipitation particles is known, or assumed. This is normally done by application of a radar reflectivity ($Z$) vs. hydrometeor fall speed ($V_T$) relationship. The vertical air velocity is then diagnosed using the assumption of mass continuity and applying a constraint on the vertical air velocity at one or both boundaries of the integration column, similar to the EVAD and CEVAD single-Doppler methods. When three or more radars are used in the analysis, the vertical component of particle motion $W_p$ can be directly measured, allowing for a more reliable upper boundary condition in the integration procedure to diagnose vertical air velocity $w$ since $W_p = V_T + w$.

## 2.3 Darwin rain gauge network

Surface rainfall data were available from the Darwin area rain gauge network (Fig. 2.1) and were used to compute rainfall statistics for each of the convective events. The Darwin rain gauge network covers an area exceeding 45,000 km$^2$ centered on the TOGA radar. Most of the gauges are located within 75 km of Darwin in order to correlate radar and rain gauge rainfall estimation for TRMM objectives. A summary of the rain gauge locations relative to the TOGA radar are provided in Appendix D. A total of 30 rain gauges were available for analysis during the 1989-1990 season and 24 were available during the 1990-1991 season. However, due to malfunctions, several of the rain gauges did not record data for particular convective events studied herein so that the actual number of gauges available for each event varied.

Rainfall was recorded digitally using a tipping-bucket gauge. The tipping bucket recorded data whenever rainfall accumulation exceeded 0.2 mm (T. Keenan, personal communication). Whenever available, data from the Berrimah rain gauge (TOGA radar site) was utilized for comparing rainfall with vertical air velocity measured with the wind profiler. This particular gauge was the closest gauge to the wind profiler ($\sim$ 4 km separation distance).

For each convective event, the rain gauge trace was partitioned into convective and stratiform components, based on the scanning radar algorithm described above in Sec. 2.1.4. This procedure allowed for the relative rainfall contribution of convective and stratiform components of each MCS to be determined. Rainfall statistics for each event are presented in Ch. 5 and the rainfall traces for all gauges for are presented in Appendix D.

## 2.4 Atmospheric sounding data

Radiosondes launched by the Bureau of Meteorology in Darwin were used to construct heat and moisture budget profiles and to calculate various thermodynamic parameters. The soundings were launched twice daily (00 and 12 UTC) from the Darwin airport, located approximately 8 km from the TOGA radar site.

### 2.4.1 Budget calculations

Profiles of the apparent heat source $Q_1$ and moisture sink $Q_2$ (Yanai et al. 1973) were derived by assuming that the vertical advection of dry static energy $s$ and specific humidity $q$ were the dominant terms in the equations [see Eqs. (1.1) and (1.2)]. In order to facilitate comparison with

other studies, the $Q_1$ and $Q_2$ budgets were partitioned into convective and stratiform components and normalized by the distribution of rainfall within the MCS (Johnson 1984). That is

$$\frac{Q_1}{P_0} \equiv Q'_1 = \frac{f}{P_m} Q_{1m} + \frac{(1-f)}{P_c} Q_{1c} , \tag{2.12}$$

$$\frac{Q_2}{P_0} \equiv Q'_2 = \frac{f}{P_m} Q_{2m} + \frac{(1-f)}{P_c} Q_{2c} , \tag{2.13}$$

where $Q'_1$ and $Q'_2$ are the normalized budgets, $f$ is the fraction of precipitation associated with mesoscale (stratiform) features, $P_m$ is the stratiform rain rate (cm $d^{-1}$), $P_c$ is the convective region rain rate (cm $d^{-1}$) and $P_0$ is the area averaged rain rate (cm $d^{-1}$). The values of $P_m$ and $P_c$ for each MCS were derived from the rain gauge network data and are presented in Ch. 5.

### 2.4.2 Thermodynamic variables

An algorithm was used to calculate CAPE (Convective Available Potential Energy) and construct profiles of available thermal buoyancy from the sounding data. The program closely follows the equations for moist thermodynamic analysis in Emanuel (1994). In order to calculate CAPE and thermal buoyancy, a 50 mb mixed layer depth was specified for all soundings and pseudo adiabatic parcel ascent (with no contribution from ice processes) was assumed. In addition, CAPE values were taken to be the positive area on the sounding. That is

$$CAPE_i = \int_i^{LNB} B\,dz = \int_{P_n}^{P_f} R_d (T_{vp} - T_{va})\, d\ln p , \tag{2.14}$$

$$B = g \cdot \left( \frac{T_{vp} - T_{va}}{T_{va}} \right) , \qquad (2.15)$$

where $B$ is buoyancy, $g$ is the acceleration of gravity, $R_d$ is the gas constant for dry air, $T_{vp}$ is the virtual temperature of the parcel, $T_{va}$ is the virtual temperature of the environment, $P_n$ is the pressure at the *LNB* (Level of Neutral Buoyancy - the equilibrium level), and $P_f$ is the pressure at the LFC (Level of Free Convection). In practice, the virtual temperature difference at each pressure level was calculated by solving the expression for moist entropy (Emanuel 1994). It should be remembered that the profiles of thermal buoyancy represent a theoretical maximum virtual temperature excess that a parcel rising from low levels could achieve, since the effects of entrainment and water loading are not included in the analysis.

# Chapter III

# CONVECTIVE REGIMES

## 3.1. Convective Regimes in Northern Australia

Darwin is located at the southern tip of the Maritime Continent and experiences a monsoon type climate (Holland 1986; Rutledge et al. 1992). The onset of the active (wet) period usually occurs in early November and typically lasts through early March. Previous investigations of active season cloudiness patterns in the vicinity of northern Australia have shown that the cloudiness is a maximum in the morning hours over the ocean and in the late afternoon over the land region of northern Australia, based on satellite and radar data (Keenan et al. 1989). The observed diurnal variations were found to be associated with interactions of solar-forced local circulations (e.g., sea breeze fronts) and the large scale flow.

During the wet season, there are two convective regimes that occur over tropical northern Australia: monsoon and break (Rutledge et al. 1992). Monsoon convection occurs when the axis of the ITCZ (Inter Tropical Convergence Zone) moves south of the Darwin area, providing deep northwesterly flow from over the ocean and placing the continental northern Australia region in a maritime air mass. Break period convection occurs when the axis of the ITCZ is north of Darwin. This juxtaposition of the monsoon trough results in low level southeasterly flow over the "Top End" of northern Australia and allows strong surface heating and intense continental convection to

develop. Although a number of cloud, rainfall, and wind based definitions have been used to describe the onset and cessation of the Australian summer monsoon, Holland (1986) found the most objectively-based classification to be the first and last occurrence of westerly flow at 850 mb. Similar to Keenan and Carbone (1992), monsoon conditions were identified whenever the daily mean surface to 3 km flow was westerly. Break conditions occurred when the daily mean flow was easterly.

On average, break period conditions occur during approximately 20% of the summer monsoon season with a mean period of 40 days (Holland 1986). Numerous studies (e.g. Madden and Julian 1972; Krishnamurti and Subrahmanyam 1982; Hendon and Liebmann 1990a) have shown that the duration of the monsoon and break regimes may be sensitive to the 30-50 day oscillation in the Indian and west Pacific oceans. Moreover, Hendon and Liebmann (1990b) have shown that the onset of the Australian monsoon season is associated with the passage of the 30-50 day oscillation over Darwin.

As pointed out by Keenan and Carbone (1992), the primary trigger for both monsoon and break regime MCSs are land and sea breeze circulations. Typically, monsoon MCSs originate over the ocean north and west of Darwin and spread over the continental region of northern Australia. Characteristic monsoon MCSs consist of wide spread stratiform precipitation with embedded convective bands aligned (at least initially) parallel to the coastline. Keenan and Carbone showed that these embedded convective features can be initiated from convergence of the local land breeze circulation and the large scale monsoon flow. Wind shear is typically concentrated in the lowest 1.5 km during the monsoon and over a 3 km depth in the monsoon break.

During break conditions, continental MCSs often originate over the Oenpelli escarpment region approximately 300 km east of Darwin, on modest mountain ranges 100-200 km southeast of Darwin, or on sea breeze convergence zones (Keenan and Carbone 1992). The continental systems often evolve into propagating squall lines with a distinct leading line of convection and a trailing stratiform region, similar to the conceptual model developed from previous observations of tropical and middle latitude squall line systems (e.g., Houze et al. 1989). Keenan and Carbone (1992) observed that the squall lines they studied during the 1987-1988 wet season moved at a speed similar to the 700 mb flow and that both monsoon and break MCSs tend to initially align parallel to the lower tropospheric shear but later evolve in a orientation perpendicular to the low-level shear vector. Similar results were demonstrated by Alexander and Young (1992) for EMEX convective lines.

Typically, the squall systems achieve maximum intensity before they reach the coastline at Darwin. All of the break MCSs in this study were sampled in their mature to dissipating stages of convective activity [stages defined by Leary and Houze (1979a)]. The 13 MCSs used in the analysis include six from the break regime and seven from the monsoon regime.

### 3.2 Convective Regimes in the Pacific warm pool

The Pacific warm pool region contains the largest area of warm water on Earth, with long term December-February SSTs (Sea Surface Temperatures) in excess of 28° C (Webster and Lukas 1992). The warm water results in a strong coupling between the ocean and atmosphere through exchanges of heat, moisture, and momentum. The fluxes of heat and moisture from the ocean surface to the atmosphere give rise to atmospheric convection occurring over a wide range of time and space scales, establishing global-scale gradients of diabatic heating, and emphasizing

the importance of the warm pool to the general circulation of the atmosphere (Webster and Lukas 1992). Indeed, the ascending branch of both the zonal Walker and meridional Hadley circulations occur over the warm pool region. Moreover, the effect of the warm ocean water is also directed downward since the resulting atmospheric convection can influence ocean circulation patterns by producing a fresh water flux at the ocean surface, thereby establishing temperature and salinity gradients that may, in turn, influence future convective activity.

COARE was designed to increase understanding of the dynamical processes operating in the Pacific warm pool coupled atmospheric-oceanic system (Webster and Lukas 1992). Among the objectives for the atmospheric component was to determine the kinematic structure, including the heat, moisture, and momentum transports within regions of convective activity over the warm pool region.

A recent satellite climatology study by Mapes and Houze (1993b) of the Indian and Pacific warm pool region showed that the cloud clusters they sampled were approximately lognormally distributed in size, with no separate meso scale sized peak in the distribution. In particular, over the COARE IFA 25% of the cold cloud area (i.e., blackbody temperature $T_{BB} < -65°$ C) was associated with CEs (Cloud Elements: spatially connected areas of cold cloudiness at 10 km resolution) with areas less than $\sim$ 6,000 km$^2$, 50% by CEs less than 20,000 km$^2$, and 75% by CEs smaller than 65,000 km$^2$. The diurnal cycle of cold cloudiness was found to be sun-synchronous within the largest CEs, reflecting the lifecycle of associated MCSs; however, the incidence of small CEs was nearly independent of time of day. The deep convection in the largest CEs peaked before dawn and decreased through the morning (Mapes and Houze 1993b).

Subsequent to the completion of the COARE, a convective climatology has been developed based on the horizontal morphology of precipitating convective systems observed with the shipboard radar data (Rickenbach 1995). The classification scheme is based on the spatial scale of contiguous convective echo as well as the presence or absence of linear arrangement in the convective echo pattern. Using the MIT radar data during the entire four month COARE IOP, Rickenbach found that nearly 75% of the total rainfall was associated with precipitating systems greater than 100 km in horizontal extent, even though they were present only 37% of the time. The results suggest that the majority of rainfall is produced by large MCSs which occur relatively infrequently. Scattered, isolated convection was present about half the time (the most common mode of convective activity) and produced about 16% of the total rainfall. The majority of stratiform precipitation (75%) was found to occur in association with convection organized into lines at least 100 km long. Also, the vast majority (78%) of the total COARE IOP rainfall was found to be associated with convective (as opposed to stratiform) features (T. Rickenbach, personal communication). There was a nocturnal (i.e., midnight to dawn) maximum in the total (and convective fraction) rainfall followed by a mid to late morning minimum and a weaker secondary maximum in the late afternoon hours. Research is continuing to explain the diurnal rainfall patterns as well as to correlate the observed convective morphology with changes in the large scale environment.

# Chapter IV

# INDIVIDUAL ANALYSIS OF DARWIN MCS EVENTS

This chapter provides an analysis of each MCS as it crossed over the observational network. The MCSs are categorized into monsoon and break and the results summarized in terms of environmental sounding and scanning radar characteristics, as well as wind profiler measurements in conjunction with nearby surface rain gauge information. The individual MCSs are named according to their date of observation in UTC (= L - 9.5 hr) with the format YYMMDD. For example, 5 December 1989 is referred to as 891205.

## 4.1 Break events

### 4.1.1 Environmental characteristics

Environmental soundings and corresponding profiles of thermal buoyancy for each of the six break MCSs are shown in Figs. 4.1 and 4.2, respectively. It should be noted that some of the soundings were launched several hours prior to the arrival of the MCS over Darwin and therefore may not be entirely representative of the environment supporting the MCS. However, as will be shown below, the vertical draft structure in the MCSs sampled by the wind profiler is at least partially consistent with the thermodynamic properties of the environment sampled by these soundings.

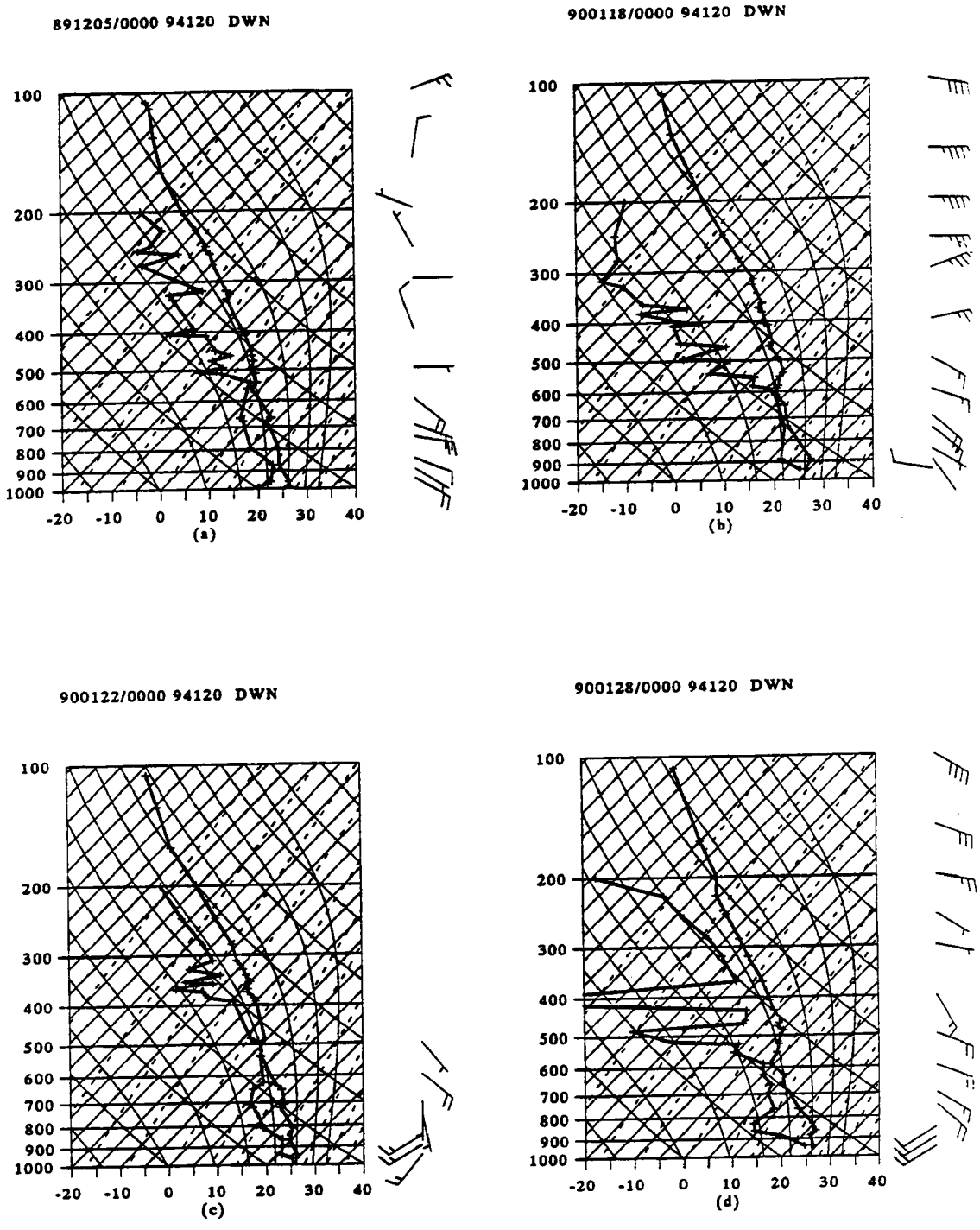


Fig. 4.1. Skew-T plots of upper-air soundings from Darwin for each of the six break period MCSs. Temperature and dewpoint traces (°C) are indicated by the bold solid lines. Wind data are shown in the right portion of each plot with wind speed (knots) represented by the length of the barb (long barb: 10 kt; short barb: 5 kt). The date and time of each sounding is indicated at the top of each plot.

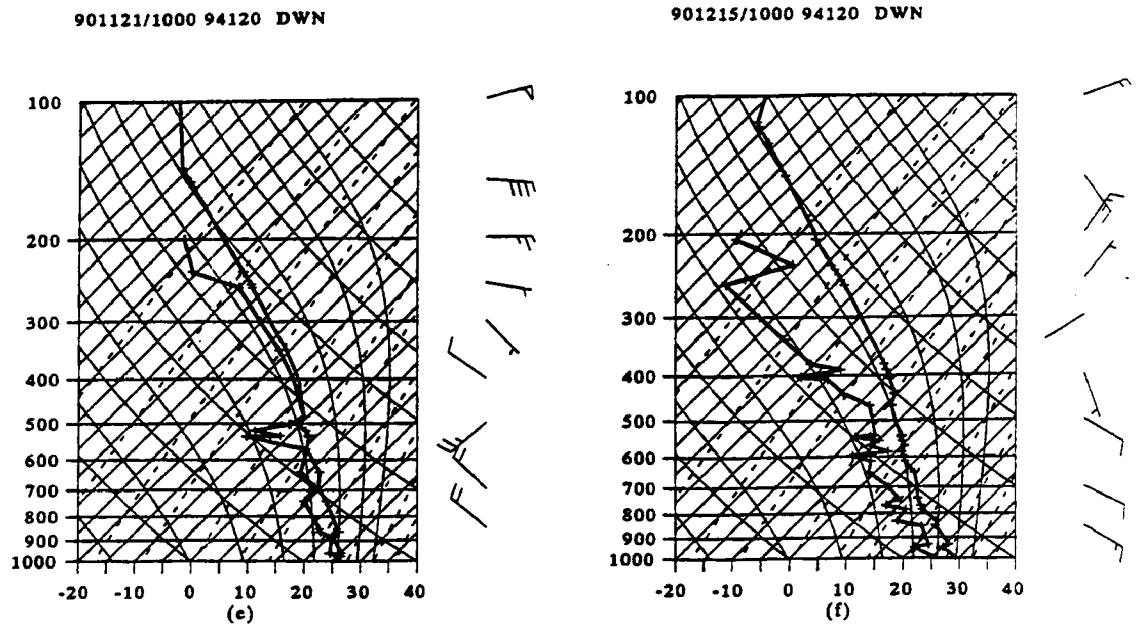


Fig. 4.1. (*continued*).

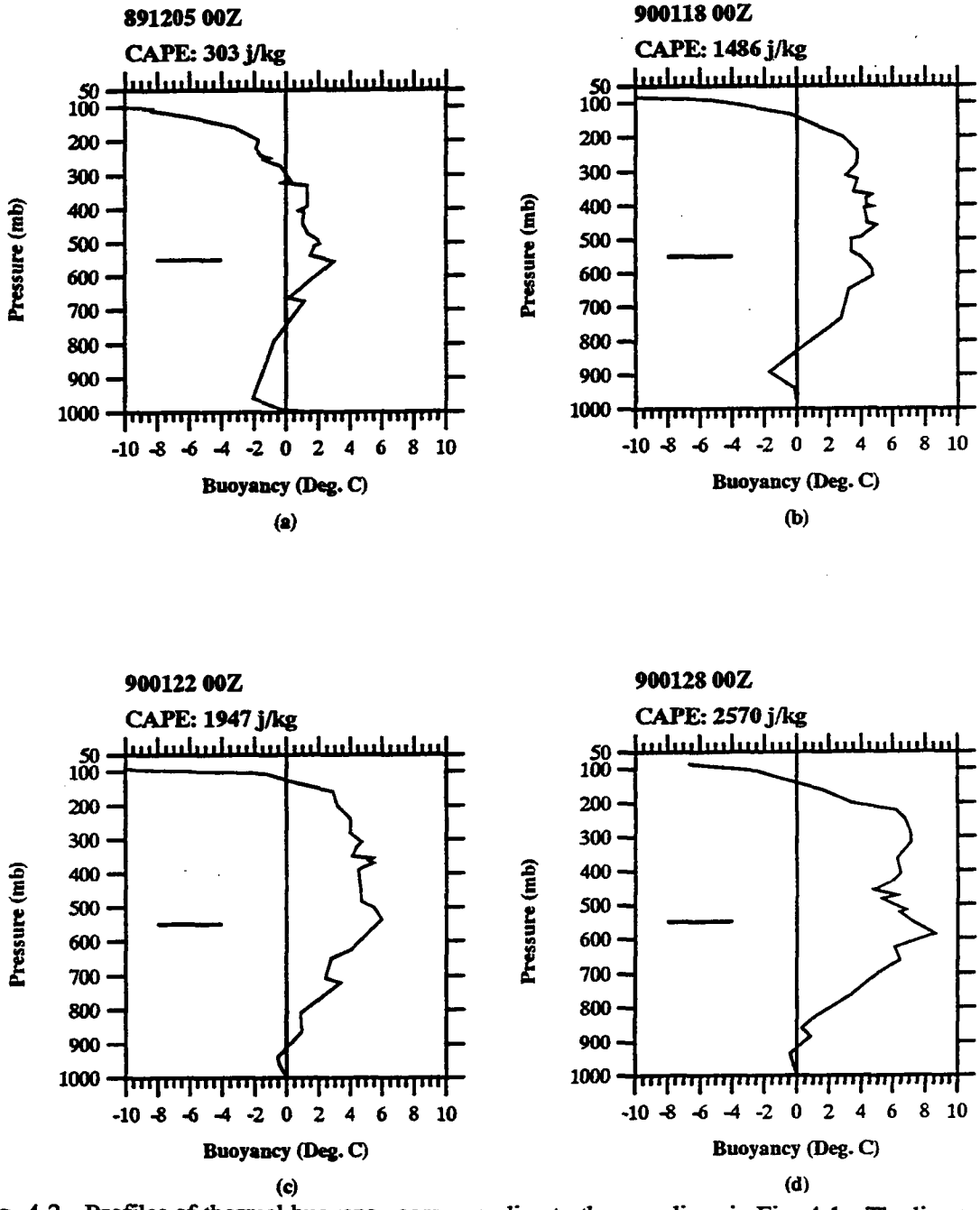


Fig. 4.2. Profiles of thermal buoyancy corresponding to the soundings in Fig. 4.1. The line trace in each plot indicates the magnitude of virtual temperature excess (°C) between a parcel rising from low levels and the environment. The 0°C isotherm is shown by the horizontal line in the left portion of each plot. The date and time of each profile, as well as the CAPE in the sounding, is indicated at the top of each plot.

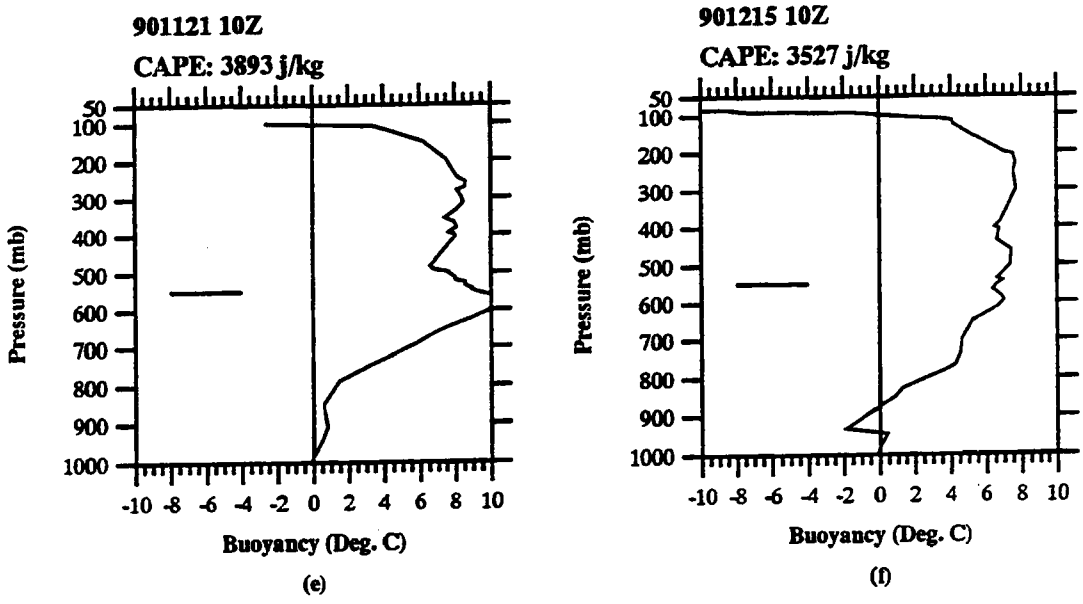


Fig. 4.2. (*continued*).

The soundings all show approximately moist adiabatic ascent above 500 mb; however, there is considerable variability in the temperature and moisture profiles below 500 mb. In general, the soundings all show at least one dry layer in the lower troposphere below about 600 mb. With the exception of 901121 and 901215, the break soundings show a relatively stable sub-cloud layer. The low-level wind typically has a southeast component, consistent with flow off the continent in the break regime. Figure 4.2 shows that the corresponding CAPE values are large (with the exception of 891205), ranging from ~ 1500-3900 J $kg^{-1}$. Moreover, the profiles in Fig. 4.2 indicate a rapid increase in buoyancy between about 800-600 mb with positive buoyancy extending to above 150 mb in most cases. The maximum virtual temperature excess between a rising low-level parcel and the environment was usually greater than 5°C above 600 mb (note the virtual temperature excess is above 10°C for the 901121 sounding). Several soundings in Fig. 4.2 also indicate a secondary, minor thermal buoyancy peak in the upper troposphere (i.e., 900128, 901121, and 901215). The low-level negative thermal buoyancy varied from essentially 0°C for 901121 (Fig. 4.2e) to greater than 2°C for 891205 (Fig. 4.2a).

### 4.1.2 Partitioned radar reflectivity characteristics

Time-height cross sections of partitioned volume average reflectivity for the six break MCSs are shown in Fig. 4.3. With the exception of 900118, all of the convective region cross sections indicate maximum reflectivities occurring in the late afternoon to evening (local time), consistent with the sun-synchronous cloudiness maximum over the northern tip of Australia identified by Keenan et al. (1989). Moreover, all the cross sections show at least one period in which the 30 *dBZ* contour extends near or above the melting region (*in a volume average sense*), suggesting the presence of relatively large vertical drafts in the convective cells required to loft significant amounts of liquid water into the mixed phase region of the cloud and marking an intense phase of

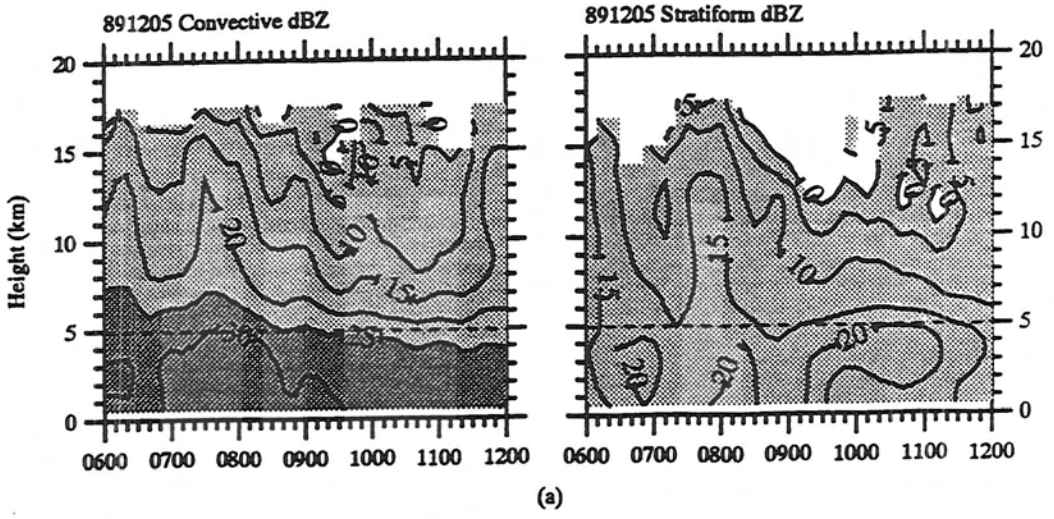
891205 Convective dBZ
891205 Stratiform dBZ
Height (km)
0600 0700 0800 0900 1000 1100 1200

(a)

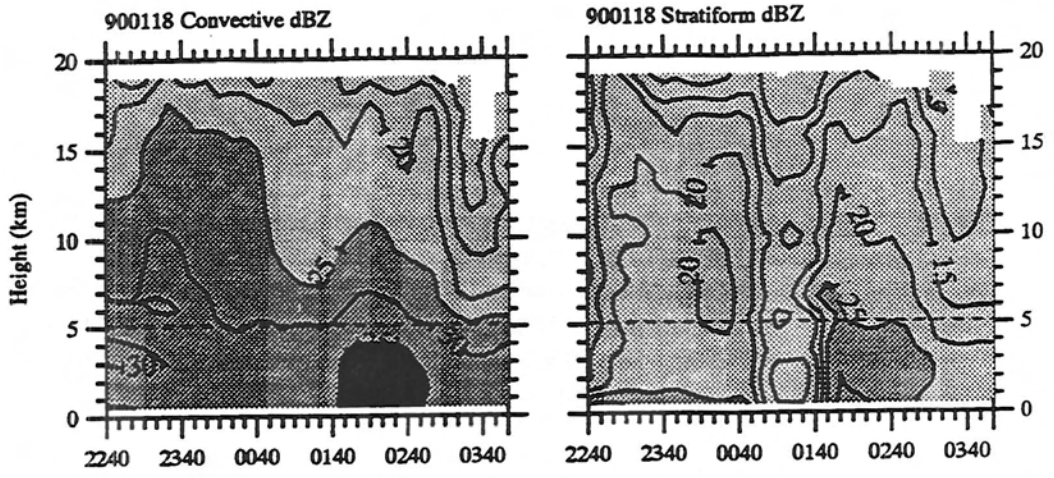
900118 Convective dBZ
900118 Stratiform dBZ
Height (km)
2240 2340 0040 0140 0240 0340

(b)

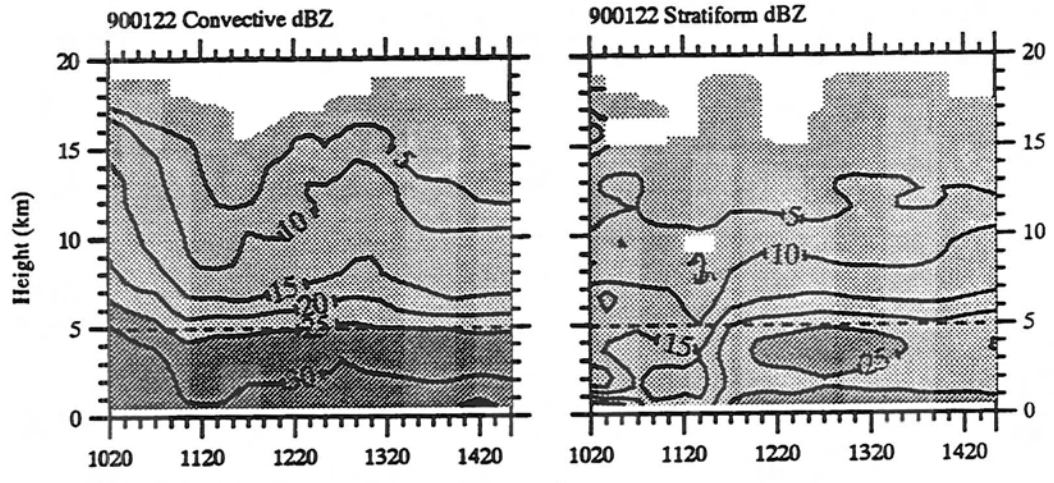
900122 Convective dBZ
900122 Stratiform dBZ
Height (km)
1020 1120 1220 1320 1420

(c)

Fig. 4.3. Partitioned time-height cross section of volume average radar reflectivity within 120 km of the radar location for each of the six break period MCSs. Left hand column represents the convective region and the right hand column is the stratiform region. The MCS corresponding to each row in the figure is indicated at the top of each plot. Units are reflectivity (*dBZ*) contoured in 5 dB increments with shading for *dBZ*s 0-25 (light), 25-35 (medium), and > 35 (dark). The dashed horizontal line in each plot indicates the approximate location of the 0°C isotherm.

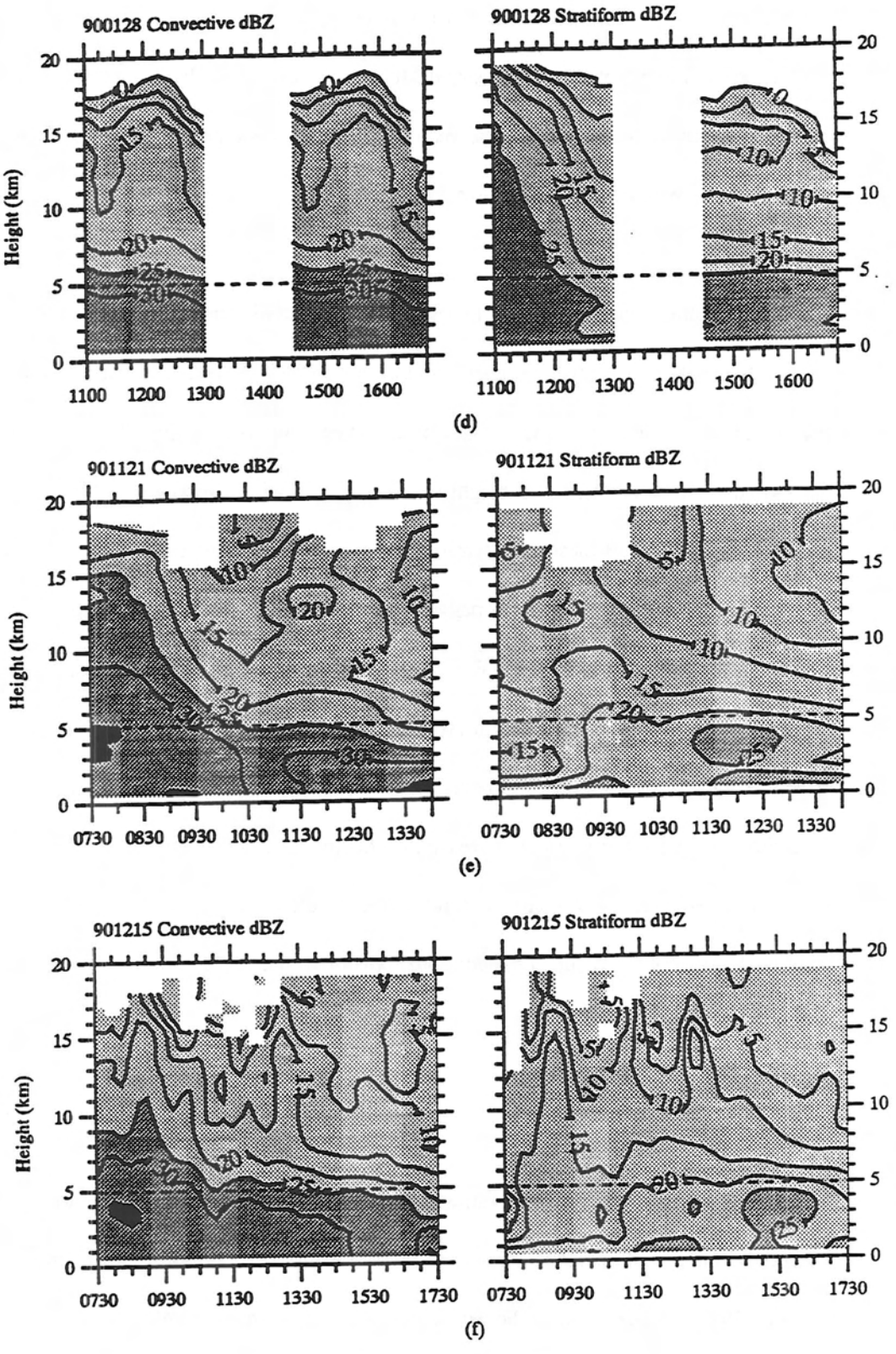


Fig. 4.3. (*continued*).

convective activity. This profile is consistent with observations of high lightning flash rates associated with many of the break period MCSs studied herein (Petersen 1992). In general, the convective activity waned toward the end of each observation period as the MCS moved over open water north or west of Darwin and dissipated.

The volume average stratiform cross sections generally show the development of enhanced radar reflectivities in the trailing region to the rear of the convective line just below the melting region during the middle to latter stages of the observation period (Fig. 4.3). This feature, marking the existence of a radar bright band, coincides with a decrease in convective reflectivity and the development of mesoscale (stratiform) precipitation features over the observational network to the rear as the MCS propagated toward Darwin. The exception to this trend in stratiform development is 900118 (Fig. 4.3b) which does not show a clear bright band feature in the partitioned stratiform time height cross section. As described below, this MCS remained more or less as a line of convection and never developed a significant region of trailing stratiform precipitation. Also, the marked decrease in reflectivity evident from 0100-0140 UTC in the stratiform cross section indicates the time period during which a sector scanning strategy was employed to sample only the convective line portion of the MCS.

### 4.1.3 MCS general description

In this section, general observational characteristics of the break MCSs are presented and interpreted in light of previous investigations of break period convection (e.g., Keenan and Carbone 1992). Since most of the MCSs developed in a similar fashion, this discussion summarizes the salient features in the evolution of the MCSs as they moved over the network as well as any anomalous characteristics.

All of the break MCSs studied herein were squall lines, characterized by a leading line of convection, where new cell growth was concentrated along with deeper, mature cells, and a trailing region of stratiform precipitation, similar to previous studies of tropical and middle latitude squall line systems (Houze et al. 1989). Often, a reflectivity trough (i.e., transition zone) was observed between the convective line and the stratiform region. An example of an MCS with the characteristic squall line structure is shown in Fig. 4.4.

With the exception of 891205 and 900118, all of the break MCSs developed over higher terrain southeast of Darwin. The 891205 event formed south of Darwin near the coastline, perhaps along a sea breeze front, while the 900118 MCS developed over the Van Dieman Gulf region and moved across the northern tip of Australia. This system was tracked for approximately 24 hours by the MIT radar crew prior to its passage over Darwin (S.A. Rutledge, personal communication).

Radar observations indicated that the MCSs evolved through a distinct diurnal lifecycle pattern, similar to that described by Leary and Houze (1979a) for a GATE tropical cloud cluster. The squall systems tended to initiate during the late morning to afternoon hours over the higher terrain regions and propagate toward the coastline, reaching Darwin in the evening hours. Figure 4.5 shows selected CAPPIs of the lifecycle stages observed in two of the break period MCSs. In the formative stage (Fig. 4.5a and b), the radar echo pattern is characterized by a group of isolated convective cells. Later in the afternoon, the cells merge into a single broader echo in which newer cells appear as intense convective cores (Fig. 4.5 c and d). This marks the intensifying stage. In the mature stage (Fig. 4.5 e and f), an areally extensive region of widespread precipitation develops to the rear of the line of convective cells. Typically, the widespread precipitation region contains a radar bright band signature. Finally, in the dissipating stage (usually in the late evening

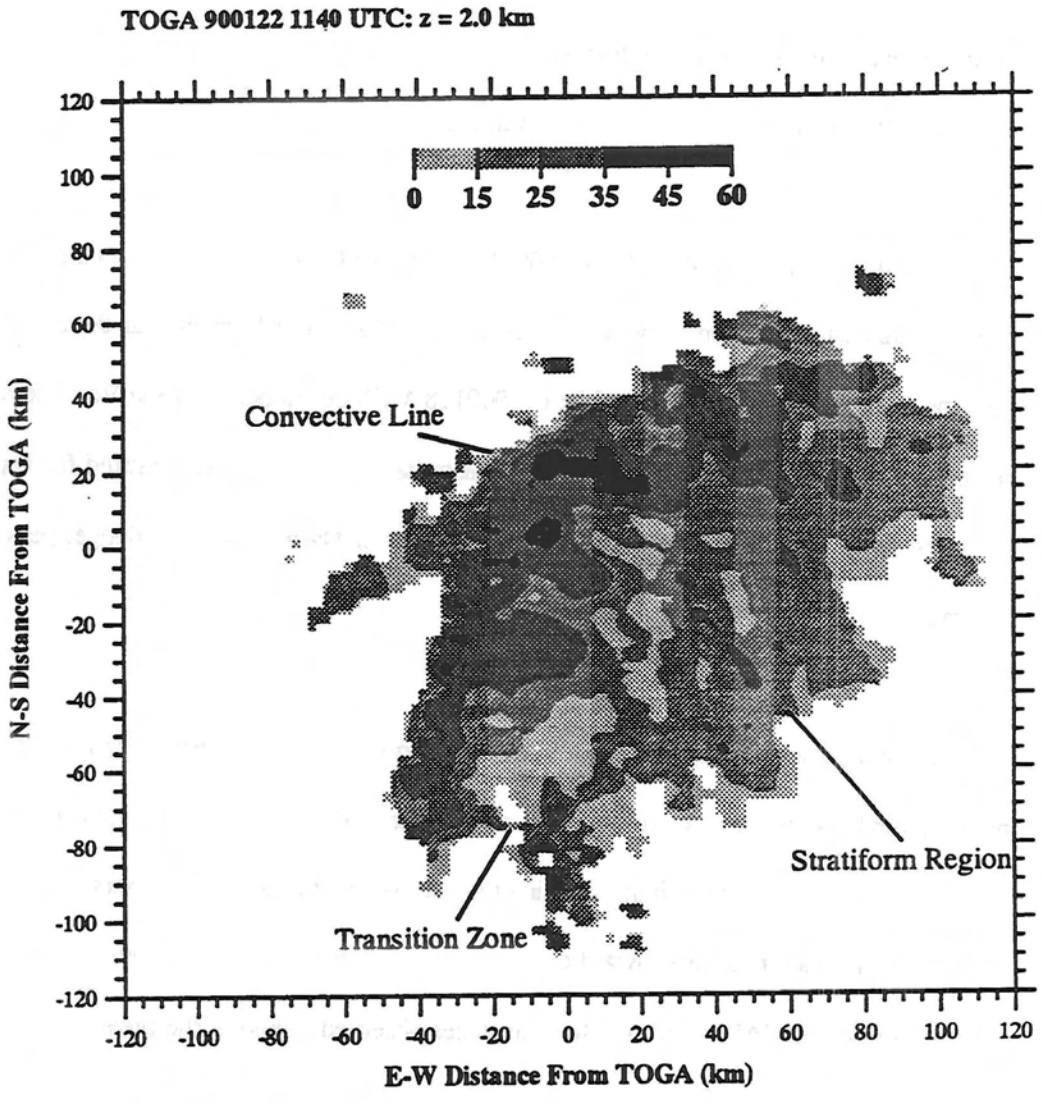


Fig. 4.4. Representative low level radar reflectivity CAPPI of a break period squall line MCS showing the convective line, transition zone, and stratiform regions (indicated on the plot). Units are *dBZ* with scale indicated near the top of the plot.

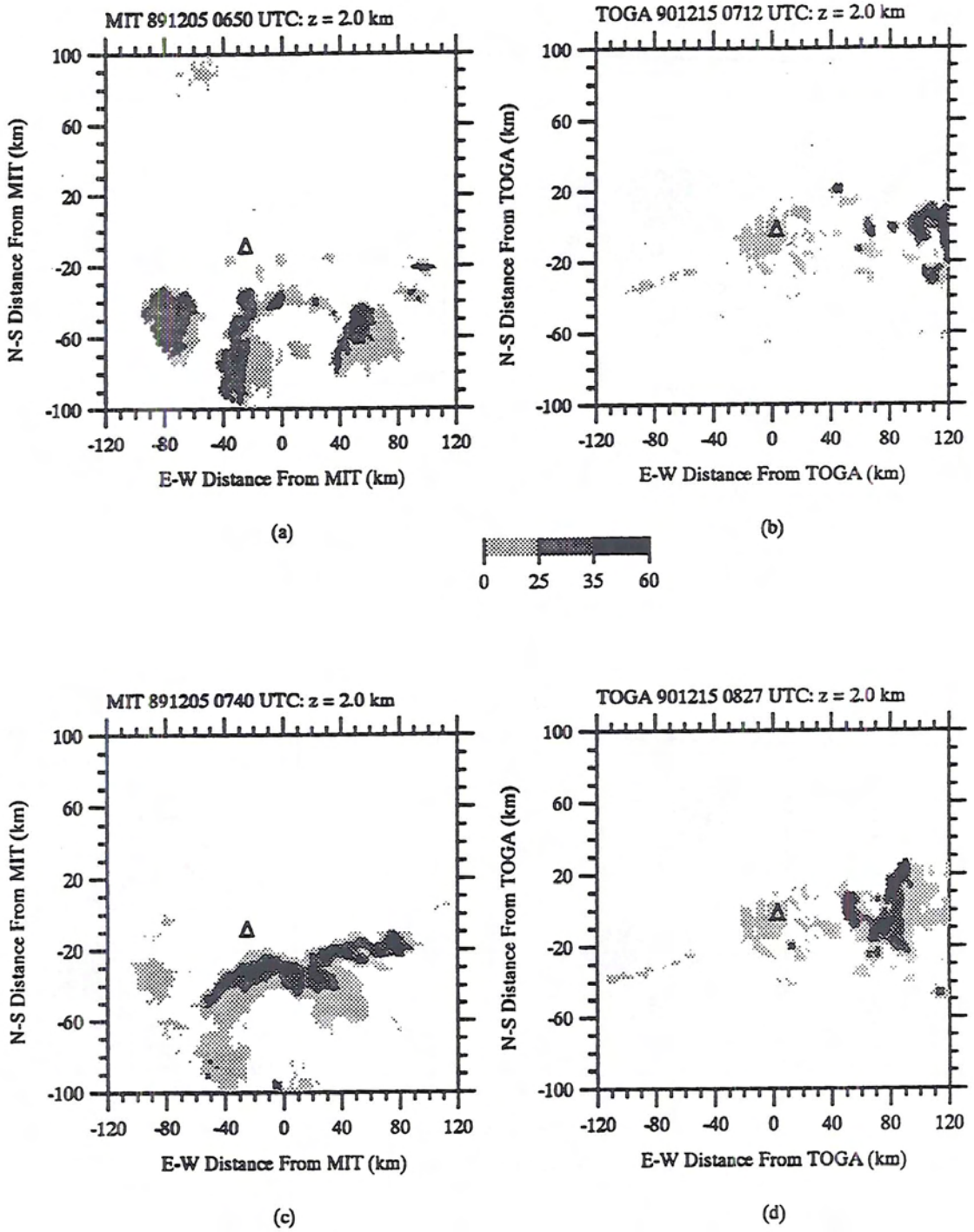


Fig. 4.5. Low level radar reflectivity CAPPIs for two selected monsoon break MCSs (891205 and 901215) showing characteristic lifecycle evolution. (a) and (b) formative stage, (c) and (d) intensifying stage, (e) and (f) mature stage, (g) and (h) dissipating stage (after Leary and Houze 1979). The location of the wind profiler in this and subsequent plots is indicated by the triangle in each plot. Scale (*dBZ*) is shown in the middle of the figure.

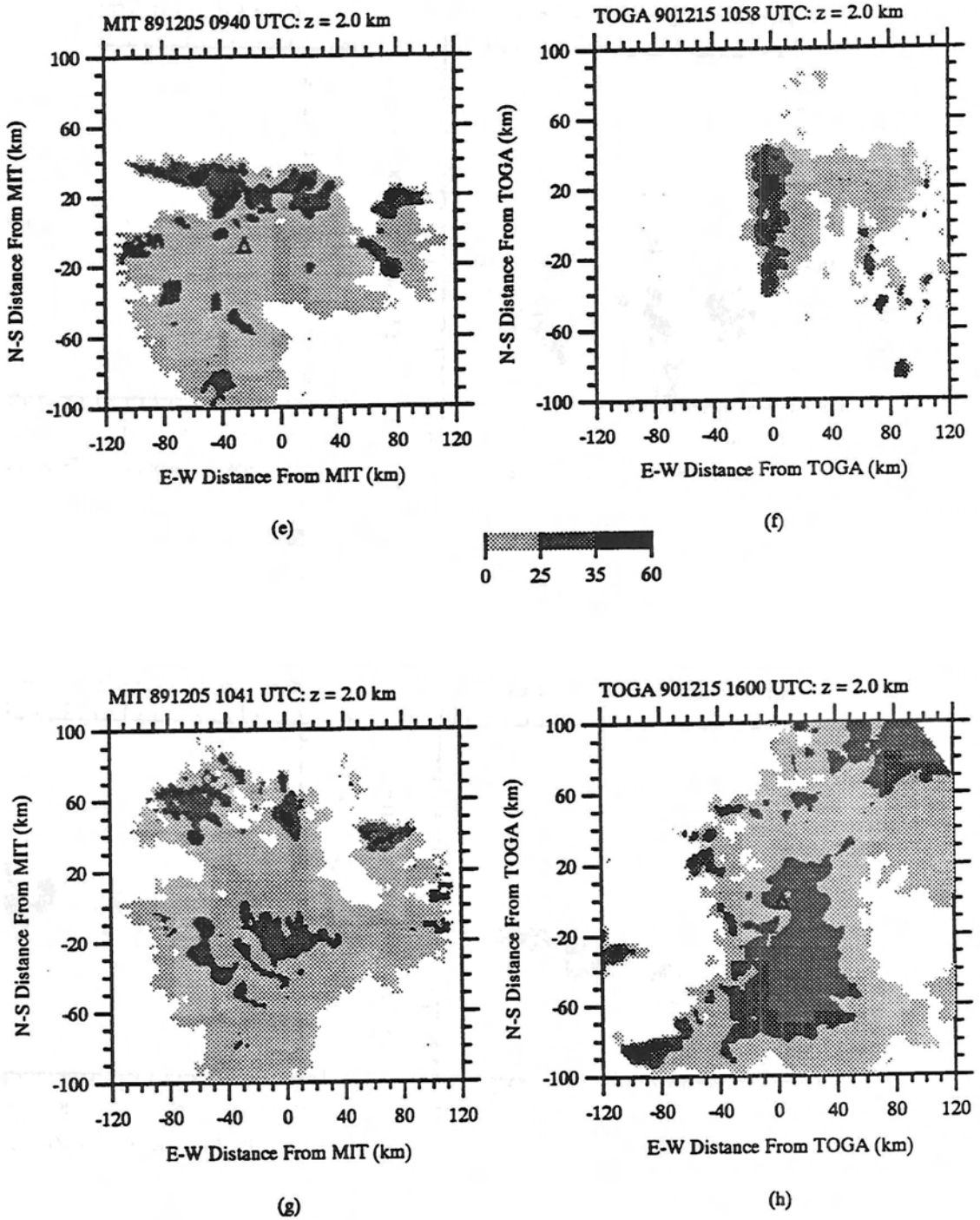


Fig. 4.5. (*continued*).

to early morning hours), the convective cells become progressively shallower and weaker (in terms of radar echo intensity) and the entire echo pattern begins to dissipate (Fig. 4.5 g and h). Unlike the first three stages which generally last 1-5 hours, the dissipating stage may last more than 8 hours (Leary and Houze 1979a).

Most of the break period MCSs were oriented with convective lines approximately perpendicular to the low-level shear, consistent the observations of Keenan and Carbone (1992) for Darwin area squall systems. The systems moved at roughly 8-14 m $s^{-1}$; however, discrete propagation of cells often made it difficult to accurately determine the convective line speed. Radar echo tops of the break MCSs typically ranged up to 16-18 km, although several of the squall lines (900118 and 900128) were particularly intense in terms of reflectivity structure, with echo tops exceeding 20 km and reflectivity cores in excess of 50 *dBZ* in selected cross sections (not shown).

Radar observations indicated that the squall lines sometimes interacted with local circulation patterns (i.e., sea breeze circulations) as they propagated toward the coast line. An example of this interaction is provided in Fig. 4.6 for the 900118 MCS. As the 900118 MCS approached the MIT radar site near 0050 UTC, an east-west oriented convective feature formed about 30 km ahead (i.e., west) of the MCS, probably in response to a local sea breeze convergence circulation (Fig. 4.6a). It was not clear to what extent the east-west band formed as a result of diurnal heating along the coastline or was forced as a result of outflow from the approaching squall line. The band later merged with the squall line as it propagated toward the southwest. Approximately one hour later, the squall line developed a distinct bow shape after crossing over the profiler location (Fig. 4.6b), suggesting the presence of a relatively strong storm relative rear inflow

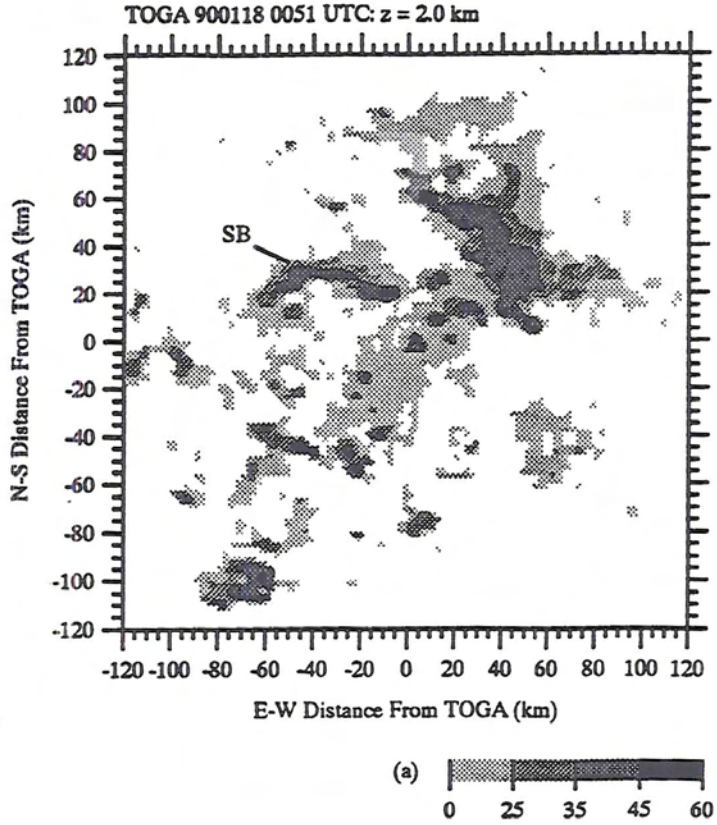
TOGA 900118 0051 UTC: z = 2.0 km
SB
N-S Distance From TOGA (km)
E-W Distance From TOGA (km)
120
100
80
60
40
20
0
-20
-40
-60
-80
-100
-120
-120 -100 -80 -60 -40 -20 0 20 40 60 80 100 120
(a)
0 25 35 45 60

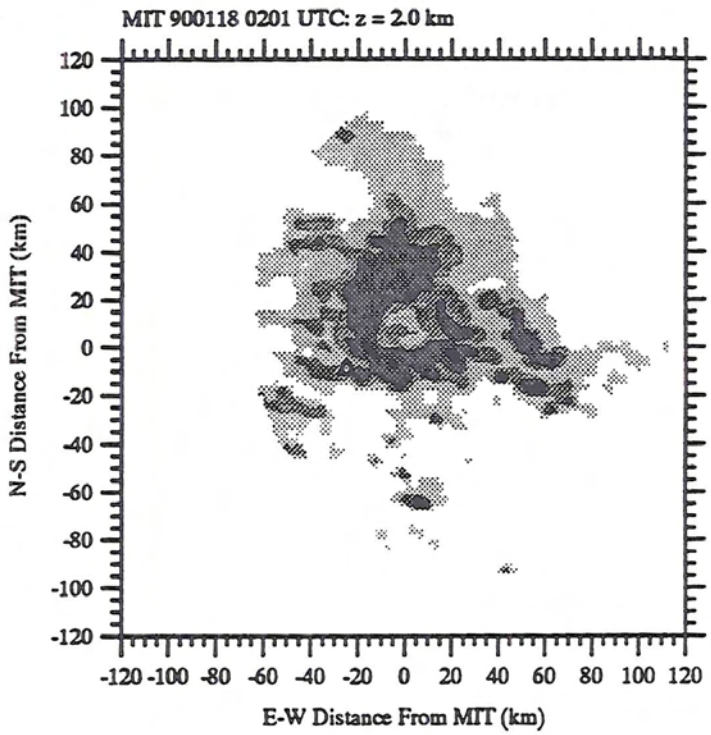
MIT 900118 0201 UTC: z = 2.0 km
N-S Distance From MIT (km)
E-W Distance From MIT (km)
120
100
80
60
40
20
0
-20
-40
-60
-80
-100
-120
-120 -100 -80 -60 -40 -20 0 20 40 60 80 100 120

(b)

Fig. 4.6. Low level radar reflectivity CAPPIs for the 900118 MCS. (a) Approaching squall line in the northeast sector of the plot and the sea breeze front (labeled SB in the plot) at 0051 UTC. (b) Development of bow echo structure at 0201 UTC. Note that the plot is centered on TOGA in (a) and on MIT in (b). Scale (*dBZ*) is indicated in the figure.

circulation. Similar features have been observed in middle latitude squall line type MCSs (Smull and Houze 1987b; Rutledge et al. 1988).

Convective activity would often re-intensify over the open water region straddling the mainland and the Tiwi Islands off the north coast after the initial squall line had passed over the coastline and begun to dissipate, probably as a result of interaction between storm outflow and the local land breeze circulation. An example of this re-intensification process is shown in Fig. 4.7 for the 901121 system. In Fig. 4.7a, the squall line in its mature phase approaches Darwin, eventually passing out to sea and dissipating (Fig. 4.7b), and finally producing additional convective activity along the southern coast of the Tiwi Islands (top portion of Fig 4.7c).

### 4.1.4 Wind profiler results

#### 4.1.4.1 Analysis of time-height cross sections results

This section provides an analysis of the vertical air motions sampled by the wind profiler as each break period MCS crossed over the observational network. Salient features in the vertical motion patterns analyzed in all the squall lines were most clearly observed in the 891205 event. Therefore, a detailed description is provided for this event and the other squall line MCS analyses are compared to 891205.

1) 891205

Time-height cross sections of radar reflectivity, vertical air velocity and surface rainfall for the 891205 MCS are shown in Fig. 4.8. Comparing the cross sections of reflectivity, surface

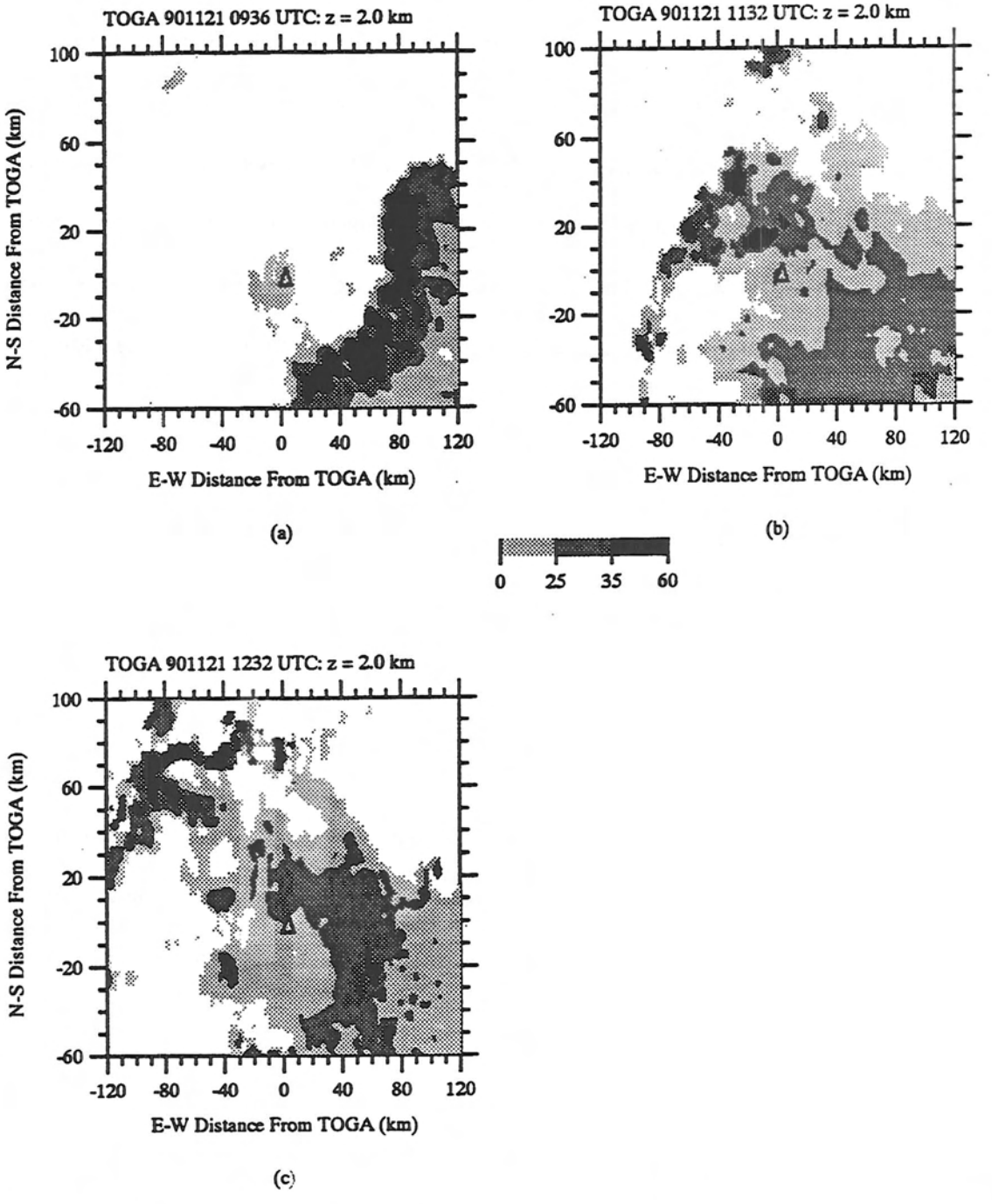


Fig. 4.7. Selected low level radar reflectivity CAPPIs for the 901121 break period MCS showing the approach of the squall line (a), the passage of the convective line over the ocean during dissipation (b), and the re-intensification of convection along the south coastline of Bathurst and Melville Islands (c). Scale (*dBZ*) is indicated in the figure.

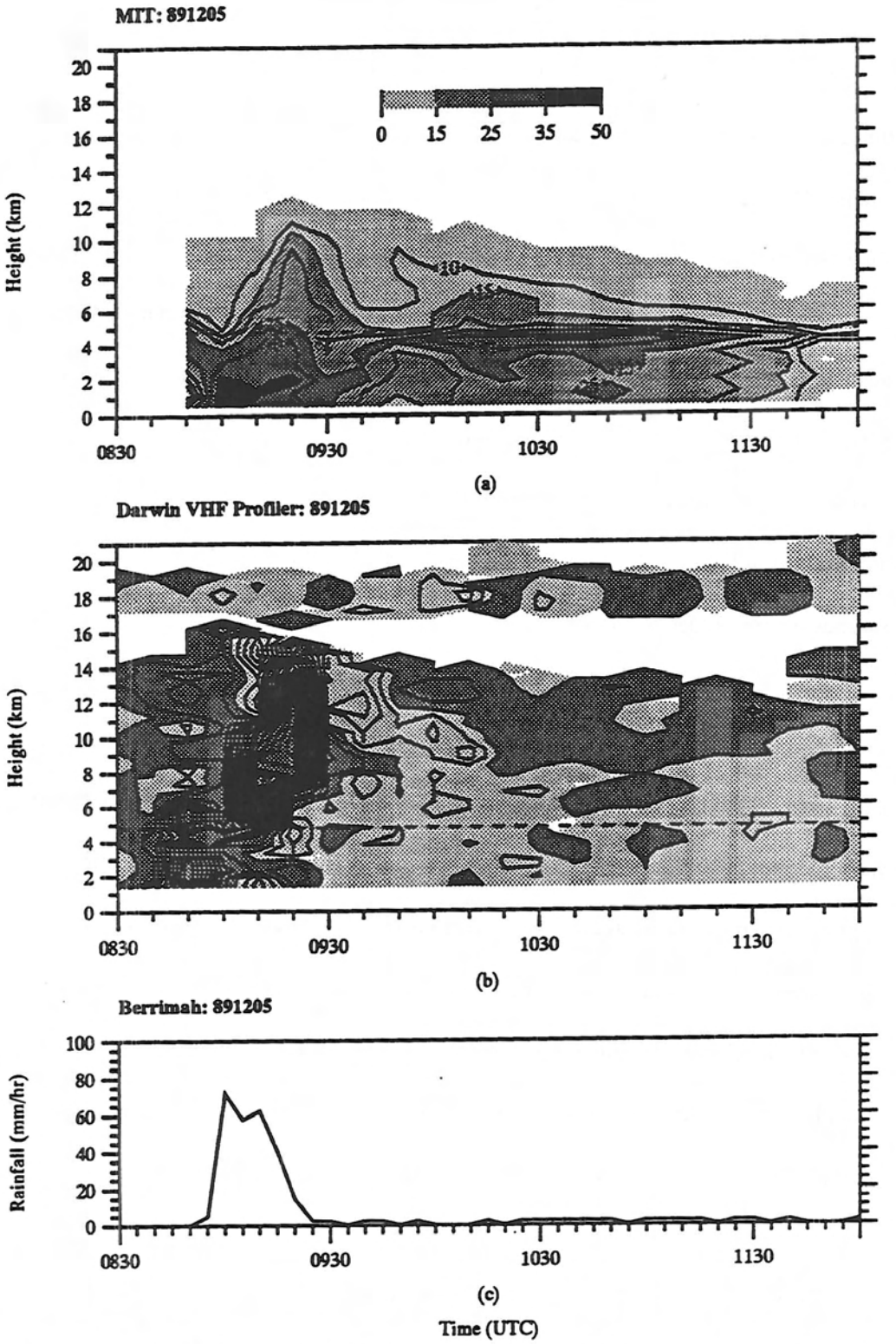


Fig. 4.8. Time-height cross sections for the 891205 MCS. (a) Radar reflectivity (*dBZ*) from the MIT radar contoured every 5 dB stating at 10 *dBZ* with shading indicated by gray scale at top of plot. (b) Vertical air velocity, from the wind profiler (m $s^{-1}$). Regions of upward (dark) and downward (light) motion contoured every 0.5 m $s^{-1}$. (c) Surface rainfall measured at the Berrimah rain gauge site in mm $h^{-1}$. In (a), (b), and (c), horizontal axis is time (UTC). In (a) and (b), the dashed horizontal lines indicate the melting level.

rainfall, and vertical velocity, it can be seen that the squall line's leading edge passed over the profiler near 0840 UTC. At this time, an updraft with magnitudes up to 4.5 m $s^{-1}$ was centered in the lower troposphere, at the leading edge of the MCS. Above about 7 km, weaker ascent extended through the troposphere. Vertical cross-sections generated with MIT radar data (not shown) suggest that this leading region of low-level ascent was associated with the development of new convection along the leading edge of the MCS. This leading low-level updraft developed as the system tilted rearward (i.e., the opposite direction toward which the line was moving) and persisted for several hours after the convective region passed over the observational network. The characteristic tilting of convective cells along the leading edge of MCSs has been previously documented in both middle latitude and tropical MCSs (Houze 1977; Smull and Houze 1987a; Rasmussen and Rutledge 1993).

The cross section in Fig. 4.8a indicates a rapid decrease in reflectivity above the melting level (near 0900 UTC) associated with the low-level updrafts. Szoke et al. (1986) and Jorgensen and LeMone (1989) also documented sharp decreases in reflectivity above the melting level in tropical convection and suggested the reflectivity gradient was due to the inability of the updraft to carry large drops a significant distance above the 0°C level. The profile in Fig. 4.8a is consistent with a low-level precipitation generation by a collision-coalescence process. Inspection of the rainfall intensity trace (Fig. 4.8c) shows that a sharp peak in rainfall intensity (72 mm $hr^{-1}$) occurred near 0900 UTC, in association with the low-level updraft peak.

Between about 0910-0920 UTC, a deep updraft core with magnitudes exceeding 9 m $s^{-1}$ passed over the profiler site (Fig. 4.8b), with maximum ascent centered between 9-10 km. Based on extrapolation of data compiled in Jorgensen and LeMone (1989; their Fig. 4) the magnitude of this updraft is greater than the strongest 10% average updraft reported for tropical oceanic

systems, but is less than the value reported for continental systems studied in the Thunderstorm Project (i.e., the regions of central Florida and Ohio).

The deep updraft was flanked by subsidence at upper levels. This subsidence (approximately 1-2 m $s^{-1}$) was probably a dynamical response of ascending air impinging on the stable region above cloud top (in the vicinity of the tropopause) and being forced to descend by mass balance constraints. The position of these downdrafts are remarkably similar to downdrafts in other squall line studies diagnosed from dual-Doppler analyses (Heymsfield and Schotz 1985; Smull and Houze 1987a Biggerstaff and Houze 1993). Coincident with the strengthening of the maximum ascent region in the middle troposphere, the cross section in (Fig. 4.8a) shows a sharp increase in reflectivity above the melting level with the 20-30 *dBZ* contour extending up to about 10 km. The relatively large reflectivities (up to 30 *dBZ*) co-located with the strong upward motion are likely associated with the presence of graupel. The shift of the maximum updraft to the middle troposphere and the increase in reflectivity above the 0°C level reflects the passage of mature, deep convective cells across the profiler site at this time. A secondary peak in rainfall intensity occurred at 0910 UTC in conjunction with the passage of the deep updraft core in the middle troposphere. To the extent that the single rain gauge trace (Fig. 4.8c) represented the rainfall rates associated with the passage of the leading edge of the MCS, it is important to note that the peak rainfall rates associated with the low-level updraft and the deeper, mid-to-upper troposphere updraft are similar in magnitude (72 and 62 mm $h^{-1}$ respectively). It will be shown that a similar bimodal structure was evident in most of the Berrimah rain gauge traces for all six of the break regime MCSs.

Deep subsidence (on the order of 1.5 m $s^{-1}$) was present over the profiler from 0940-1010 UTC (Fig. 4.8b). This downward motion coincided with a reflectivity trough (transition zone) in

both the reflectivity cross section (Fig. 4.8a) and the low-level horizontal reflectivity pattern (not shown). The reflectivity trough was most pronounced in the upper and lower troposphere and was separated by a region of higher reflectivity at middle levels (4-6.5 km). Although the precise relationship between the upper and lower reflectivity minima is not clear, the trough below the melting level could be related to melting and evaporation of hydrometeors in the presence of a downdraft. As discussed previously, the upper level subsidence was probably associated with divergent outflow from the convective region. Biggerstaff and Houze (1993) have argued that this subsidence would cause sublimation and reduced aggregation of ice phase hydrometeors advected rearward of the convective line thus explaining the lower reflectivity minimum. The Berrimah rain gauge time series shows that this period was characterized by very light rain (Fig. 4.8c).

After about 1010 UTC, upward motion was present in the middle to upper troposphere, with mesoscale downward motion at lower levels. This upward motion coincided with the development of a distinct maximum in radar reflectivity (bright band) near the melting level, consistent with the development of more widespread stratiform precipitation over most of the observational network at this time. The magnitudes of vertical air motion in the stratiform region were generally weak, ranging up to about 0.5 m $s^{-1}$ with the updraft generally restricted to the upper troposphere. Inspection of radar-derived relative flow structure (not shown) indicated the presence of weak rear inflow, restricted to heights below the 0°C level. Thus, the depth of the mesoscale downdraft in this case does not appear to be linked to the location of the rear inflow jet, in contrast to the results of Rutledge et al. (1988) and others for middle latitude squall lines.

The reflectivity cross section in Fig. 4.8a indicates a cessation of the bright band after about 1110 UTC. The reduction in the bright band appears to be related to enhanced subsidence occurring at this time. The precipitation intensity remained very light throughout the duration of

the stratiform region in the vicinity of the profiler. During the observational period, a total of 25 mm of rain was recorded at the Berrimah rain gauge, with 89% occurring in association with the passage of the convective region (see Appendix D).

2) 900118

The time-height cross section of reflectivity, vertical air motion, and surface rain for the 900118 MCS is shown in Fig. 4.9. The wind profiler results in Fig. 4.9b reveal a more complicated vertical air motion pattern associated with the evolution of the MCS as it crossed over the profiler site compared to 891205. A low-level updraft peak of about 3 m $s^{-1}$ was sampled at 0100 UTC in association with convective cells forming ahead of the 900118 MCS (Fig. 4.6a). Near 0150 UTC, the leading edge of the main portion of the 900118 MCS passed over the profiler with a low-level updraft of about 4 m $s^{-1}$. Similar to the 891205 MCS, this updraft was associated with a relatively intense, brief rainfall spike( $\sim$ 60 mm $hr^{-1}$) at the Berrimah rain gauge (Fig. 4.9c). Approximately 10 minutes later (0200 UTC), a reflectivity trough passed over the profiler associated with deep subsidence and absence of surface precipitation (Figs. 4.9a); however, by 0210 UTC the profiler was again sampling a portion of the convective line due to the bowing of the MCS and resulting concave shape of the convective line (Fig. 4.6b). The convection sampled at this time was deeper compared to the vertical draft core at 0150 UTC, with the 30 *dBZ* contour extending well above the freezing level (Fig. 4.9a) and the peak vertical air motions occurring above 9 km (Fig. 4.9b), also similar to the mature convective cell sampled in the 891205 event. The wind profiler continued to sample elements along the convective line through about 0250 UTC, which became weaker with time and apparently were separated by regions of overturning (subsidence). During this time period, the Berrimah rain gauge recorded rainfall rates up to $\sim$ 20 mm $hr^{-1}$, much weaker than the rainfall associated with the low-level draft along the leading edge.

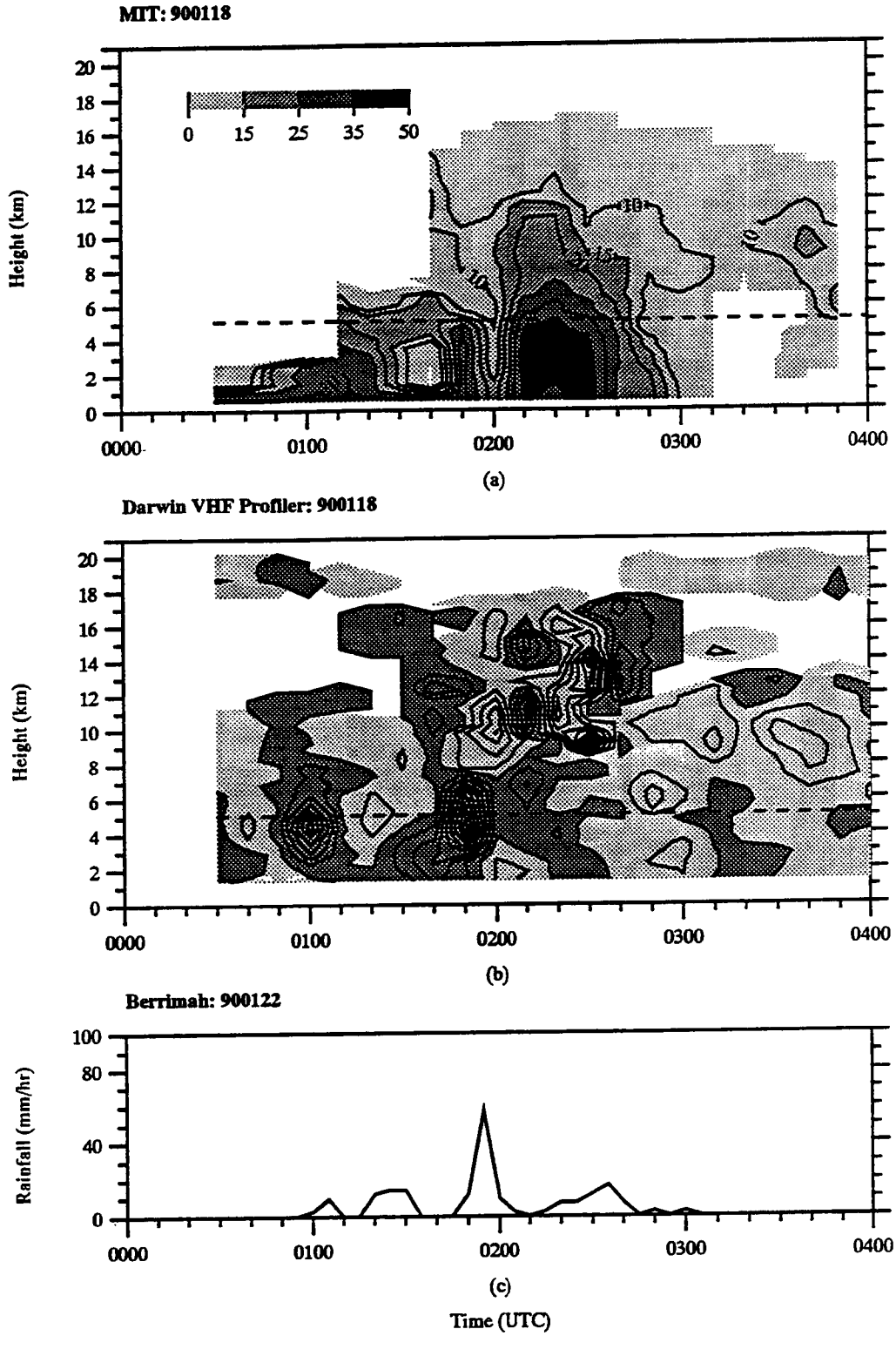


Fig. 4.9. Same as Fig. 4.8 except for the 900118 MCS.

Stratiform conditions persisted over the profiler for a short period subsequent to the passage of the convective line; however, there was no characteristic bright band during this time period. The results are consistent with the Berrimah rain gauge trace which indicated that 99% of the rainfall was associated with the convective region (Appendix D).

3) 900122

Cross sections of reflectivity, vertical motion and rain rates for the 900122 case are shown in Fig. 4.10. The convective line passed over the profiler around 1100 UTC as indicated by the low-level reflectivity patterns (Fig. 4.10a) and the development of a lower troposphere updraft core (Fig. 4.10b). At the Berrimah rain gauge, the onset of precipitation occurred at 1105 UTC (Fig. 4.10c). Similar to the previous MCSs, the pattern is due to low-level convective cells on the leading edge of the squall line. However, the reflectivity and vertical air motions cross sections in Fig. 4.10 indicate that the 900122 MCS was weaker than the 900118 and 891205 events. Figure 4.3c shows that the most active convective phase of 900122 occurred prior to its passage over the wind profiler. Also, selected reflectivity cross sections (not shown) indicate that the most intense convection passed to the northeast of the profiler site. At the Berrimah rain gauge, the maximum rainfall intensity (about 24 mm $h^{-1}$) occurred around 1120 UTC in association with the passage of the low-level updraft. In contrast to the 891205 and 900118, the 30 *dBZ* contour was confined to heights below the 0°C level during the passage of the convective line.

Additional updraft cores, centered in the middle to upper troposphere, passed over the profiler site at between 1140-1200 UTC (Fig. 4.10b); however, the radar reflectivity cross section does not indicate any intensification of the MCS during this time interval (Fig. 4.10a). Upper level subsidence occurring ahead and behind the peak updraft at 1150 UTC was weak ($< 0.5$ m

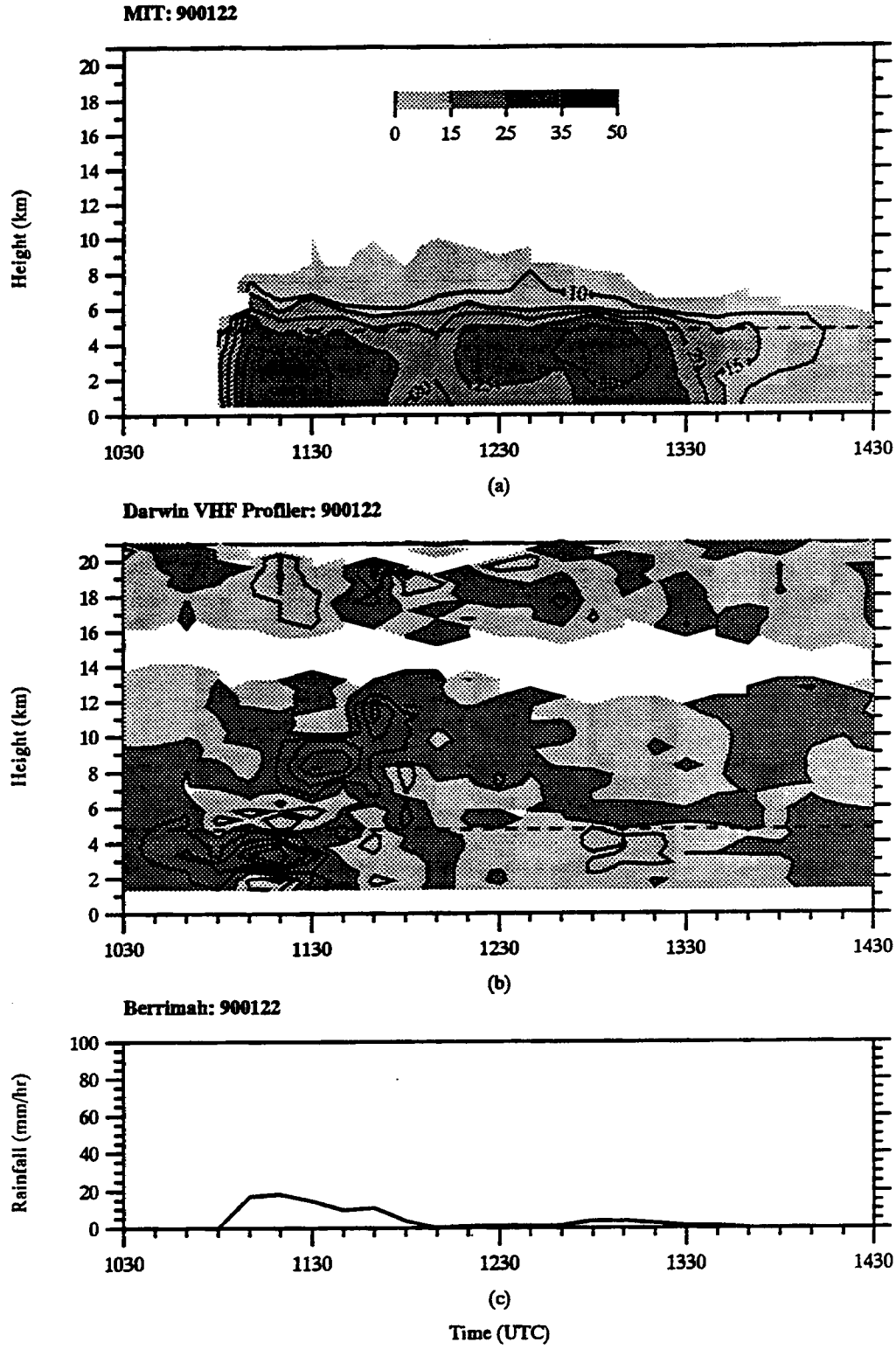


Fig. 4.10. Same as Fig. 4.8 except for the 900122 MCS.

$s^{-1}$) and shallow compared to 891205 and 900118. The surface rainfall at Berrimah shows a small increase in rainfall intensity which is roughly coincident with the passage of the middle and upper troposphere updrafts.

A radar bright band formed over the wind profiler beginning near 1300 UTC, accompanied by a slight increase in surface rainfall intensity (Fig. 4.10a and c), suggesting the development of stratiform conditions. The stratiform region of the 900122 MCS was characterized by alternating regions of downward and upward motion at upper levels (Fig. 4.10b). Upper level subsidence was present over the profiler from about 1250-1340 UTC. During this time, ascent was confined to a thin region above the bright band. Approximately 88% of the total precipitation recorded at the Berrimah site was associated with the passage of the convective region for the 900122 case (Appendix D).

4) 900128

Cross sections of vertical air velocity and surface rainfall, for the 900128 case are shown in Fig. 4.11. Since MIT radar data were not available on this day, a time-height cross section of reflectivity over the location of the wind profiler was not possible.

Inspection of low-level radar reflectivity data (not shown) indicate that the wind profiler began to sample convection out ahead (i.e., west) of the main portion of the convective line around 1225 UTC (Fig. 4.11a), although no surface rainfall at the Berrimah rain gauge was associated with the convective activity at this time. It is interesting to note that a GMS IR image collected at 1133 UTC showed that the area encompassed by the rain gauge network was almost entirely covered by a region of cloud top temperatures $< 200°$ K; however, only four of the rain gauge

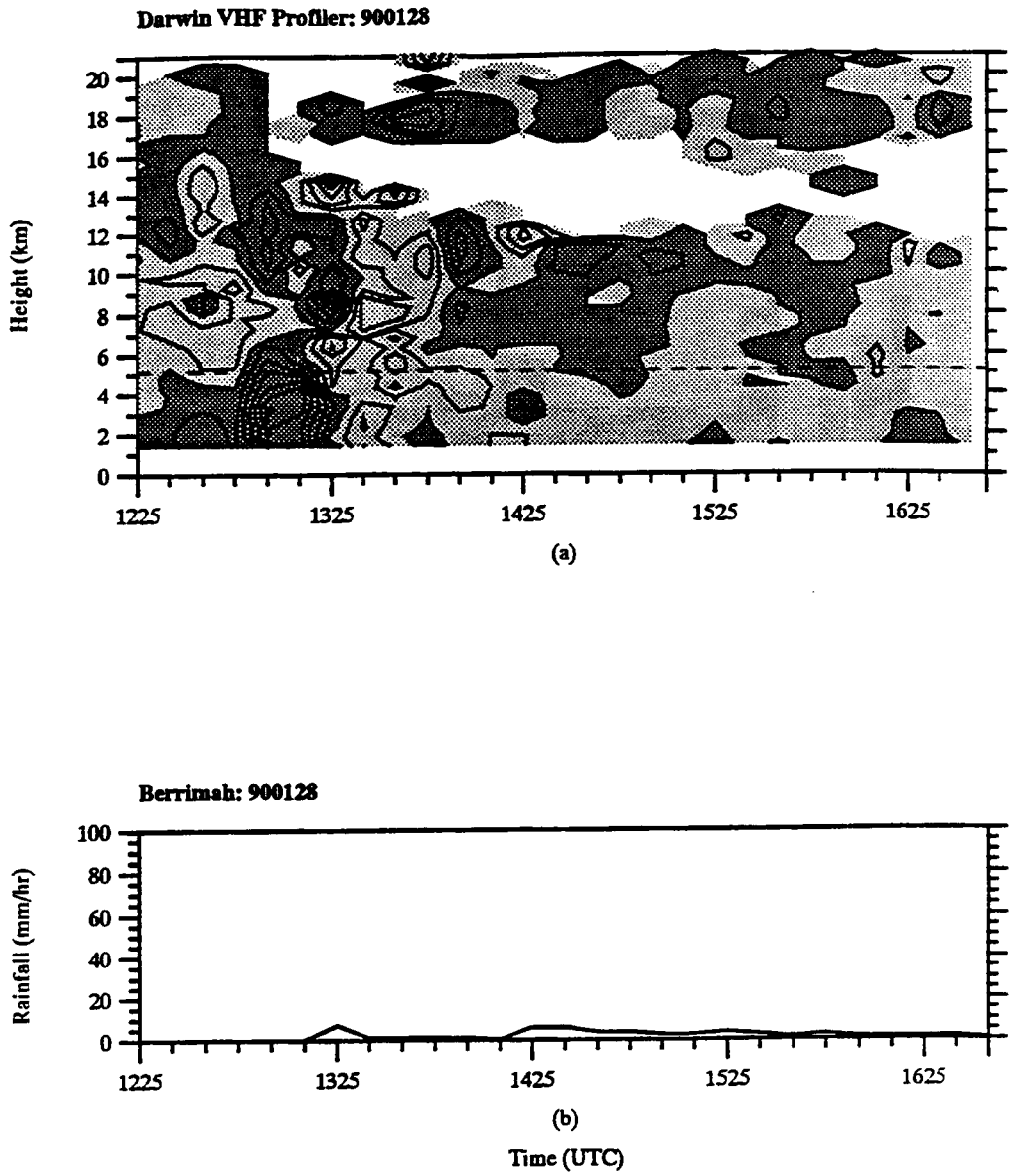


Fig. 4.11. Same as Fig. 4.8 except for the 900128 MCS [note that (a) is vertical air velocity and (b) is rain intensity]. Also, since the MIT radar was not operational for this event no time-height cross section of radar reflectivity was constructed over the location of the wind profiler.

sites, located in the eastern part of the network, reported rainfall between 1100-1200 UTC (Appendix D).

The leading edge of the 900128 convective line passed over the profiler site about 1305 UTC (Fig. 4.11a). Similar to the previously described squall lines, the profiler sampled a bimodal updraft structure associated with the convective region. A low-level updraft crossed the profiler around 1310 UTC and was centered near 3 km with a magnitude of about 3 m $s^{-1}$ (Fig. 4.11a). Weaker ascent (1 m $s^{-1}$) was also occurring in the mid-to-upper troposphere at this time. The two updraft regions were nearly split by downward motion in the 7-9 km level. At 1325 UTC, another updraft core centered near the 9 km passed over the wind profiler which was flanked by subsidence near the tropopause. The passage of this middle troposphere updraft core coincided with the onset of rain at the Berrimah rain gauge site.

There was considerable spatial variability in the intensity and amount of rainfall recorded in the rain gauge network during the passage of the 900128 system. At the Berrimah site, only a total of 6.2 mm of rain were recorded and the rainfall rate never exceeded about 8 mm $h^{-1}$ during the observation period. In contrast, the Humpty Doo rain gauge located approximately 43 km southeast of the wind profiler site recorded 30 mm of rain in a 30 minute period, with a 10 minute average maximum intensity of 64 mm $h^{-1}$ (Appendix D). The significant variability of surface rainfall suggests corresponding large variability in the magnitude of vertical air velocity along the convective line portion of the squall line.

Subsidence occurred throughout the troposphere from 1330-1355 UTC, suggesting the existence of a transition zone rearward of the convective line (Fig. 4.11a). The pattern is consistent with low-level reflectivity plots (not shown) which indicated the existence of a 20-30 km

wide reflectivity trough about 40 km east of the MIT radar site at 1305 UTC. Using the translation speed of the MCS ($\sim 10$ m s$^{-1}$)and assuming steady state conditions, this feature could have been advected over the profiler around 1400 UTC. Minimal rainfall accumulations occurred at the Berrimah site from 1335-1425 UTC, probably as a result of the enhanced subsidence and subsequent evaporation.

By about 1430 UTC, a broad stratiform region developed over the profiler. In the vertical motion cross section (Fig. 4.11a), subsidence in the mid-to-upper troposphere was replaced by a mesoscale updraft with magnitudes ranging up to 1 m s$^{-1}$. Data from the Berrimah site showed an increase in surface rainfall corresponding to the development of the stratiform region (Fig. 4.11b). The depth of the mesoscale updraft was variable, ranging from less than 1 km to about 8 km. In general, the deepest regions of updraft corresponded with the largest magnitudes. After about 1515 UTC, the magnitude and depth of the updraft generally decreased, indicating that the stratiform region was dissipating at this time. In contrast to the previously discussed break MCSs, a large portion of the total rainfall (77%) recorded at the Berrimah site for the 900128 was associated with the passage of the stratiform region (Appendix D). The larger stratiform contribution may be associated with the stronger updrafts sampled by the wind profiler in the stratiform portion of the 900128 MCS compared to 891205, 900118, or 900122. However, as discussed in Ch. 5, the majority of rainfall measured from all the rain gauges for 900128 was associated with the passage of the convective line.

5) 901121

The time-height cross section of vertical air motion over the wind profiler and the Berrimah rain gauge trace for 901121 are shown in Fig. 4.12. The convective line portion of the MCS

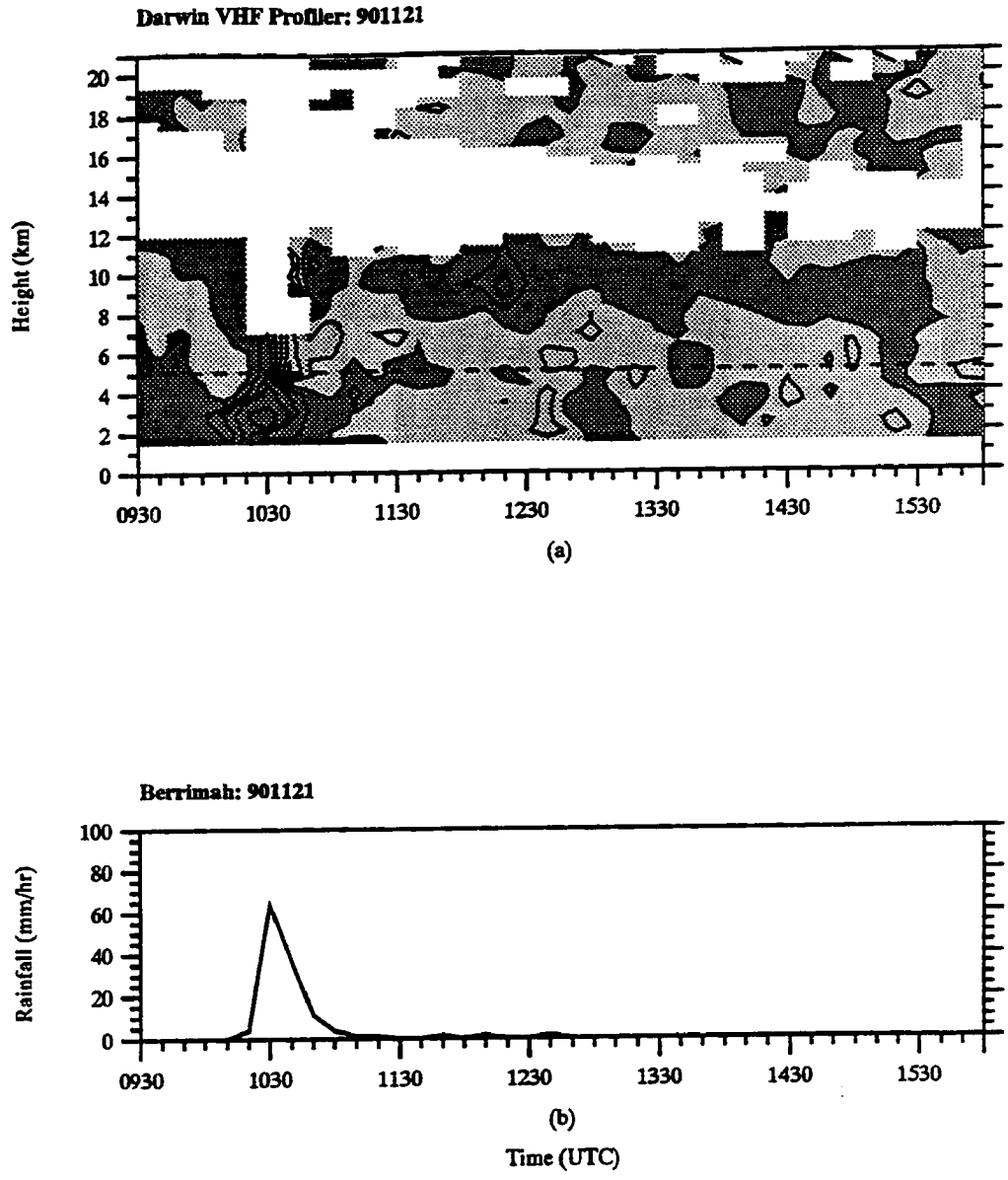


Fig. 4.12. Same as Fig. 4.11 except for the 901121 MCS.

crossed over the profiler near 1030 UTC, associated with a relatively weak updraft core ( ~ 2 m $s^{-1}$) and brief, heavy rain ( ~ 65 mm $hr^{-1}$), similar to the 8901205, 900118, and 900122 squall lines. A secondary weak updraft centered in the upper troposphere passed over the profiler near 1050 UTC, flanked by subsidence. This pattern is consistent with all of the previously described squall systems. The Berrimah rain gauge recorded minimal rainfall associated with the upper level updraft core. Deep subsidence was sampled rearward of the upper level draft near 1110 UTC, similar to the previous squall line cases; however, a clearly defined reflectivity trough was not apparent in the radar data in the vicinity of the wind profiler.

Stratiform conditions developed over the profiler by about 1130 UTC (Fig. 4.7b) coincident with a relatively consistent pattern of ascending motion generally occurring above about 8 km and descending motion below this level. The stratiform region was sampled until 1600 UTC. Minimal rainfall was recorded at the Berrimah rain gauge during this time interval. For the entire MCS, 97% of the rainfall recorded at the Berrimah rain gauge was associated with the passage of the convective line (Appendix D).

6) 901215

The time-height cross section of vertical motion over the wind profiler and the resulting rain trace from the Berrimah rain gauge are shown in Fig. 4.13. The 901215 MCS actually consisted of two separate squall convective lines which passed over the observational network on this day. The first line passed over the profiler around 1030 UTC, shortly before it began to decay over open water west of Darwin. A trailing region of stratiform precipitation persisted over the profiler for several hours before the next convective line, weaker and less organized than the first, crossed over the profiler around 1430 UTC.

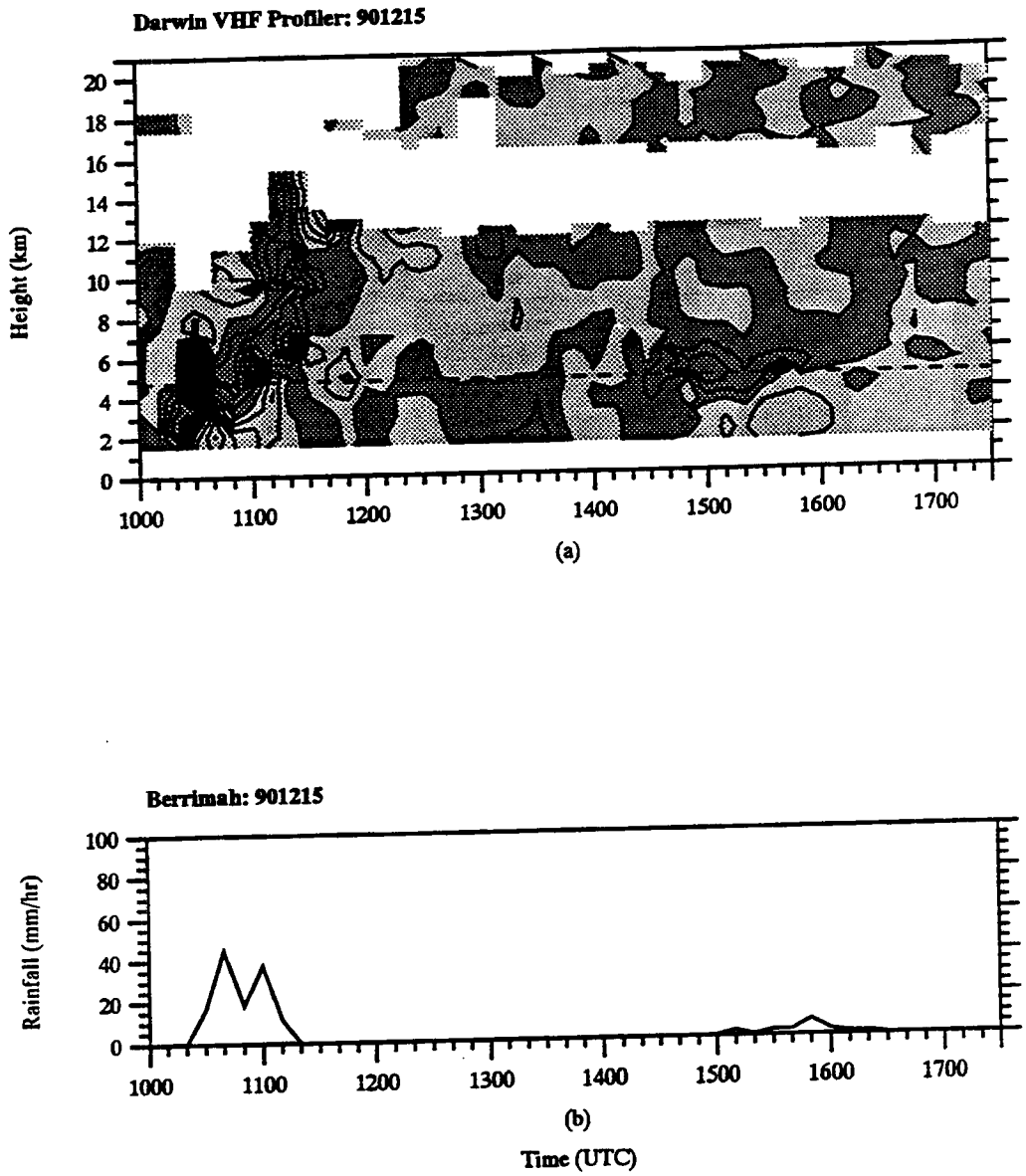


Fig. 4.13. Same as Fig. 4.11 except for the 901215 MCS.

The vertical air motion time-height cross section shows the passage of a rather intense ($\sim$7 $ms^{-1}$) low-level updraft centered below the melting level trailed by several deeper, but less intense updrafts in the middle to upper troposphere associated with the passage of the first line (similar to the observations of the previous squall line MCSs). The rain trace shows a sharp peak ($\sim$ 40 mm $hr^{-1}$) associated with the low-level updraft; however, it's not clear which of the deeper updrafts the second, slightly weaker, rainfall peak is associated with. Subsidence flanks the upper level updrafts near the tropopause. The vertical air motion pattern sampled in the stratiform region between the passage of the first and second convective lines is rather complicated (i.e., Fig. 4.13 at $\sim$ 1200-1400 UTC). Arbitrary cross sections through the radar data as well as the partitioned stratiform time-height cross sections (Fig. 4.3f) do not indicate the presence of a well defined radar bright band feature and the Berrimah rain gauge did not record any precipitation during this time interval. It is only after the passage of the second convective line (i.e., after 1430 UTC) that the mesoscale updraft-downdraft couplet is present in association with the bright band signature and measurable surface precipitation (Figs. 4.3f and 4.13c). Results from the Berrimah rain gauge trace indicate that 87% of the recorded rainfall in the vicinity of the wind profiler was associated with the passage of the convective lines (Appendix D).

#### 4.1.4.2 Partitioned vertical air motion results

Composite profiles of partitioned vertical air motions for the six break period MCSs are shown in Fig. 4.14. Each plot includes a composite profile of convective updrafts, convective downdrafts, total convective drafts (updraft and downdraft), total stratiform, and total transition (not observed in all cases). In the convective region, each composite updraft shows a bimodal pattern with peak vertical air motions centered in the vicinity of the melting level and in the middle to upper troposphere. As discussed in Sec. 4.1.4.1, the low-level updrafts occurred on the leading

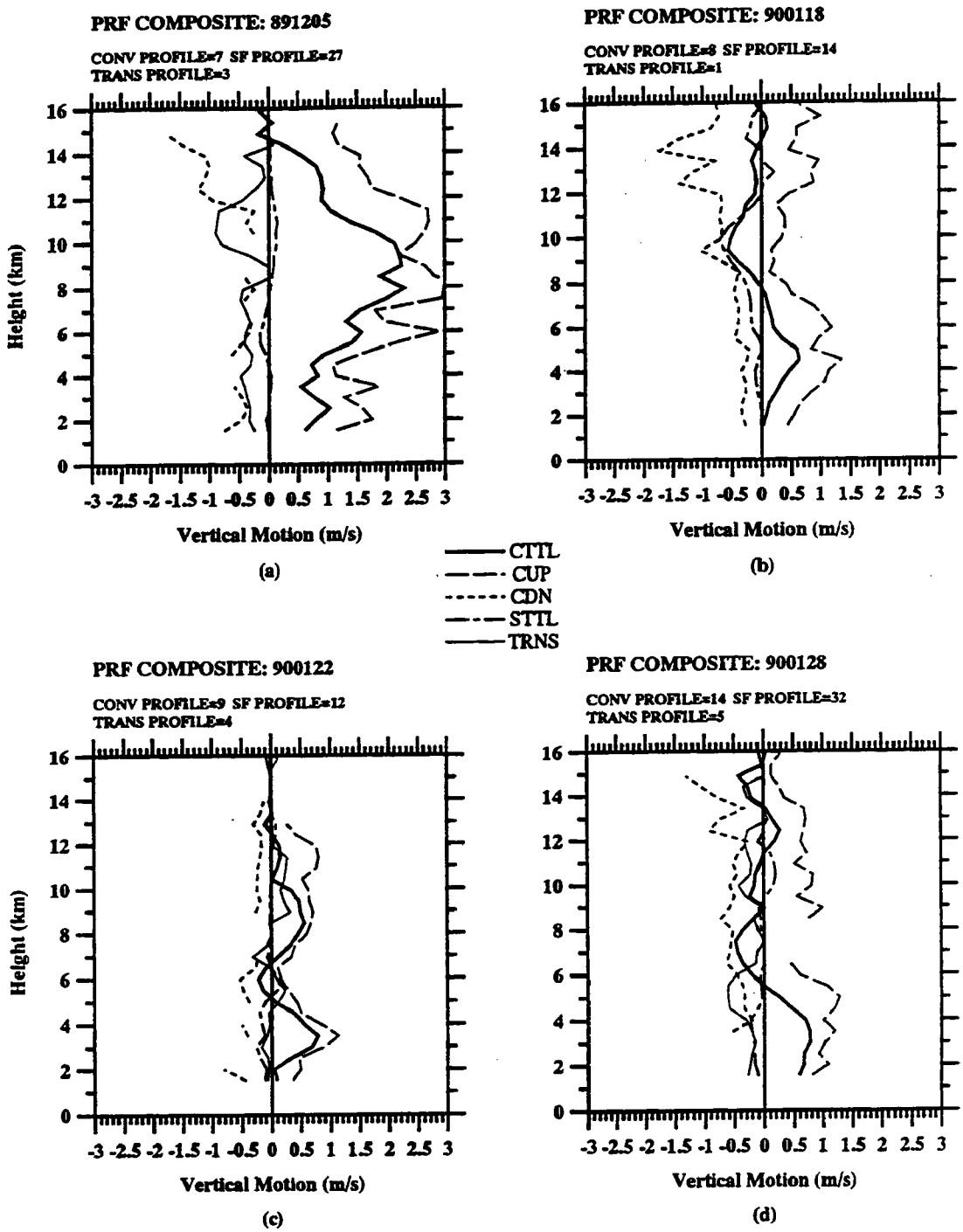


Fig. 4.14. Composite profiles of partitioned vertical air motion (m $s^{-1}$) for the six break period MCSs. Legend with corresponding line type is shown in the middle of the figure. Net (up and down drafts) convective region profile (CTTL; bold solid line), convective updrafts (CUP; long dashed line), convective downdrafts (CDN; short dashed line), total stratiform profile (STTL; long-short dashed line) and total transition profile (TRNS; thin solid line). The MCS corresponding to each set of composites is shown at the top of each plot as well as the number of individual profiles used in each composite.

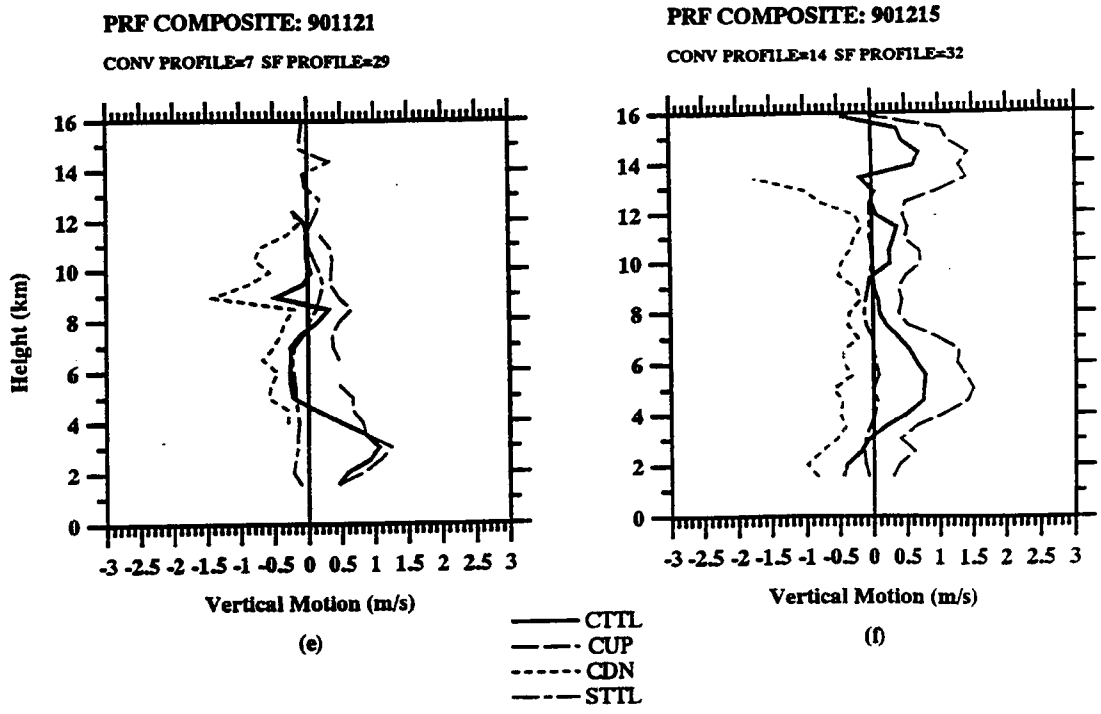


Fig. 4.14. (*continued*).

edge of each squall line and were probably associated with a collision-coalescence precipitation mechanism in each case. The upper level updraft was associated with deeper convective cells which trailed the leading low-level updraft. The location of the peak updraft in the middle to upper troposphere is quite variable compared to the lower level peak (i.e., the centroid ranges from ~8.5 km in 901121 to ~15 km in 900118), suggesting that the upper level peak may be more influenced by lifecycle effects of the MCS as it crossed the observational network and/or variability in the relative intensity of the MCS in the along-line direction (i.e., the low-level updraft may have a more two-dimensional structure compared to the upper level peak). It should be noted that for the one break period MCS in which dual-Doppler analyses were available (900122), the resulting pattern of vertical air motions averaged over the length of the convective line were in excellent agreement with the wind profiler composite (Fig. 4.14c), suggesting that, at least for this one MCS, the profiler obtained a representative sample of the convective region structure.

The composite updraft profiles in the lower troposphere are at least consistent with the corresponding profiles of thermal buoyancy (Fig. 4.2), which all show large positive virtual temperature excesses (suggesting large positive acceleration of the vertical wind) in the vicinity of 550 mb. The correlation is somewhat surprising considering that the effects of entrainment and water loading are neglected in this analysis, as well as the fact that the sounding data was sometimes collected many hours in advance of the MCS passage over the profiler. Several of the profiles in Fig. 4.2 also indicate a secondary virtual temperature increase above 500 mb (~ 6 km); however, the correlation with the corresponding peak vertical wind in the upper troposphere is not nearly as evident as the correlation in the lower troposphere. The results suggest that the soundings may not have been entirely representative of the environment supporting the MCS (as indicated in Sec. 4.1.1) or that additional forcing mechanisms are required to explain the location

of the peak drafts in the upper troposphere (note that the 891205 had the largest magnitude upper level updraft despite the narrowest positive thermal buoyancy region).

Figure 4.14 indicates that the largest convective downdrafts generally occurred in the upper troposphere, consistent with a dynamically forced subsidence response of convective drafts converging on the tropopause, followed by descent. The effect of the large upper level subsidence is to produce net downward motion in many of the total convective draft profile composites (900118, 900128, 901121, and 901215). Downward motion is also indicated in the transition zone composite (with the exception of 900122), consistent with the observed reflectivity trough and near absence of measurable precipitation. The stratiform composite of vertical drafts are much weaker than the corresponding convective composites with downward motion generally occuring below the melting level. However, in the middle to upper troposphere the stratiform composites can be of similar in magnitude to the net convective profiles (with the exception of 891205), due to the near cancellation of convective updrafts and downdrafts. Also, the depth of upper level ascent in the stratiform profiles is highly variable in the break MCSs, ranging from non-existent in 901215 to more than 6 km in 891205.

## 4.2 Monsoon events

### 4.2.1 Environmental characteristics

Atmospheric soundings and the corresponding profiles of thermal buoyancy for the seven monsoon MCSs are shown in Figs. 4.15 and 4.16, respectively. All of the soundings show nearly saturated conditions and approximately moist adiabatic lapse rates through a significant fraction of the troposphere, consistent with the active monsoon environment (Keenan and Rutledge 1993).

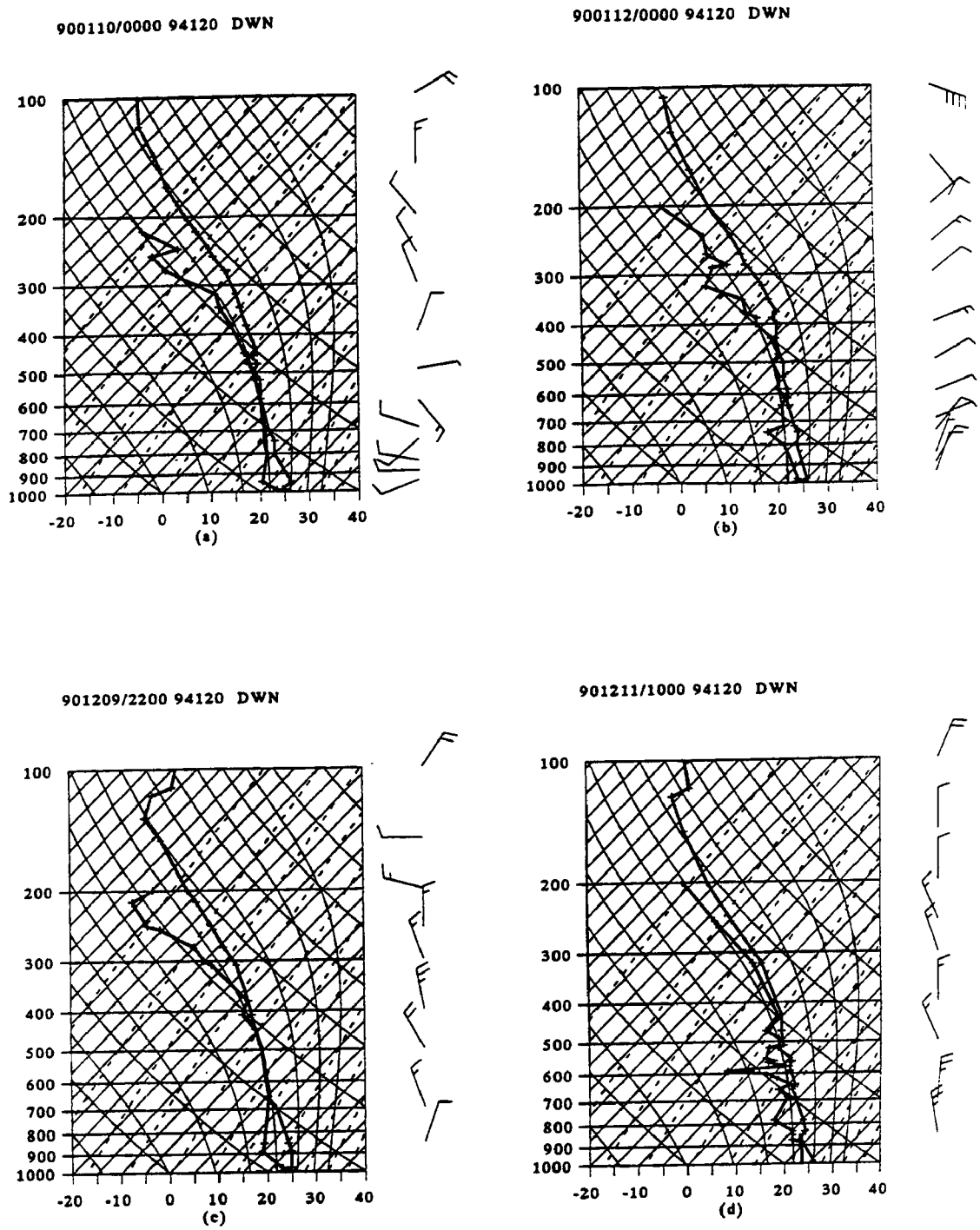


Fig. 4.15. Same as Fig. 4.1 except for the seven monsoon MCSs.

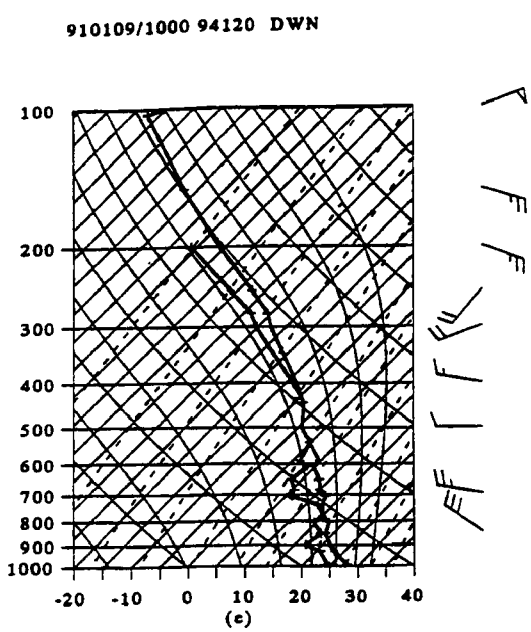


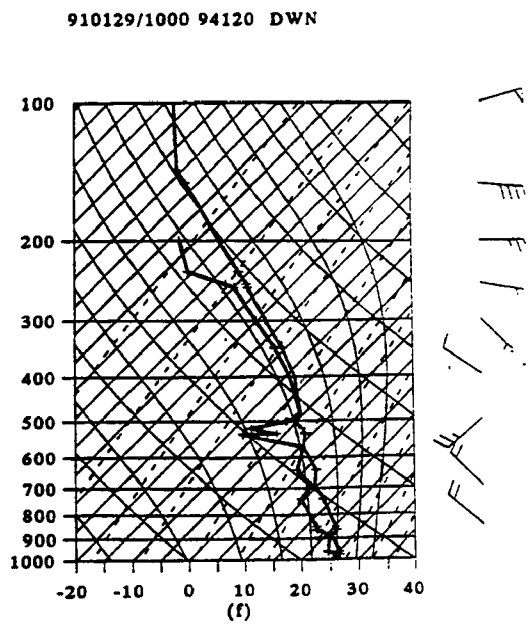


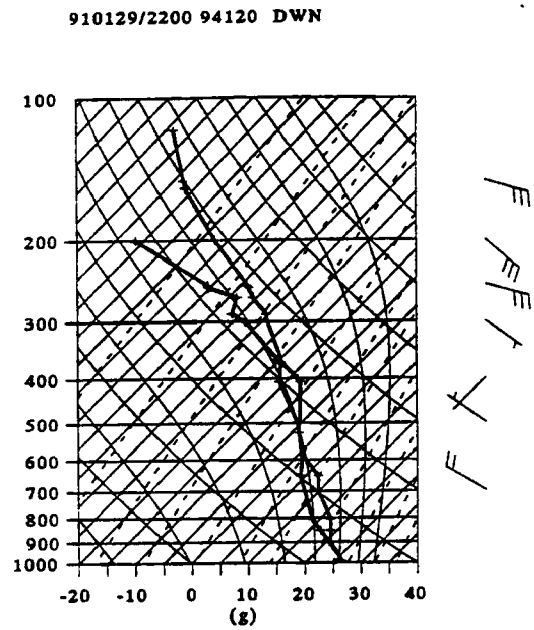


Fig. 4.15. (*continued*).

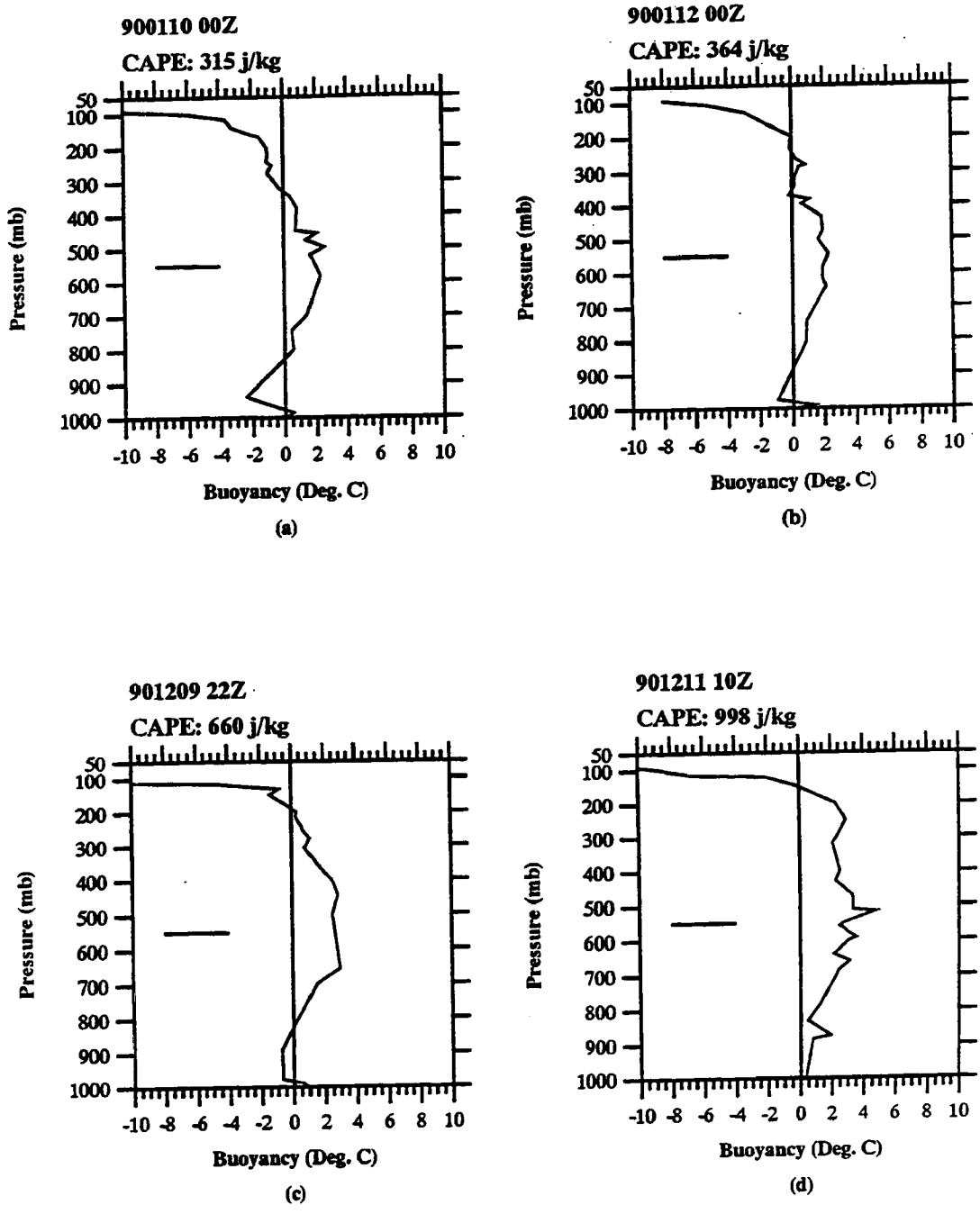


Fig. 4.16. Same as Fig. 4.2 except for the seven monsoon MCSs.

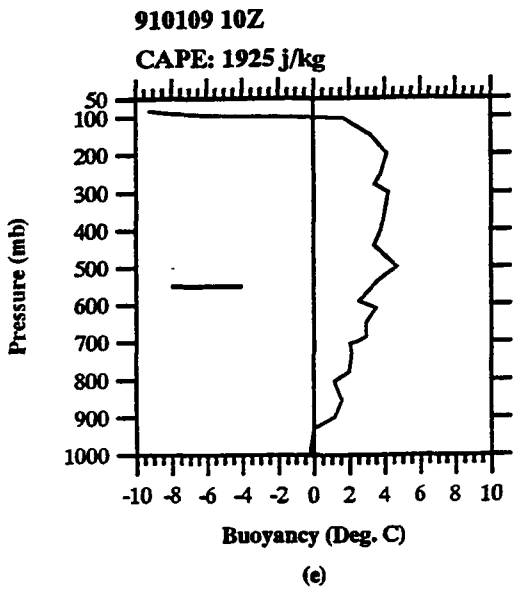


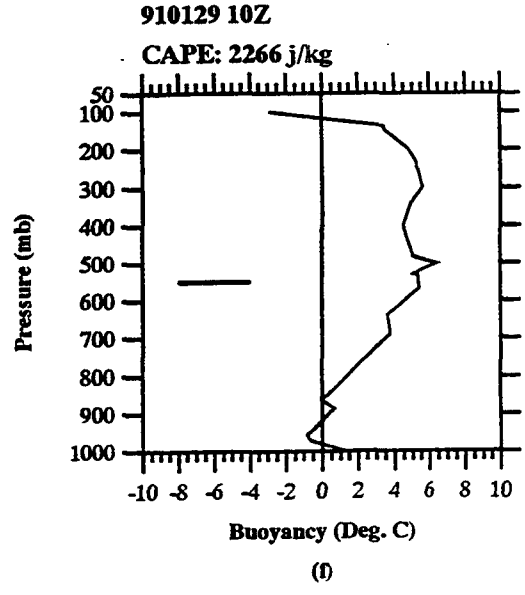


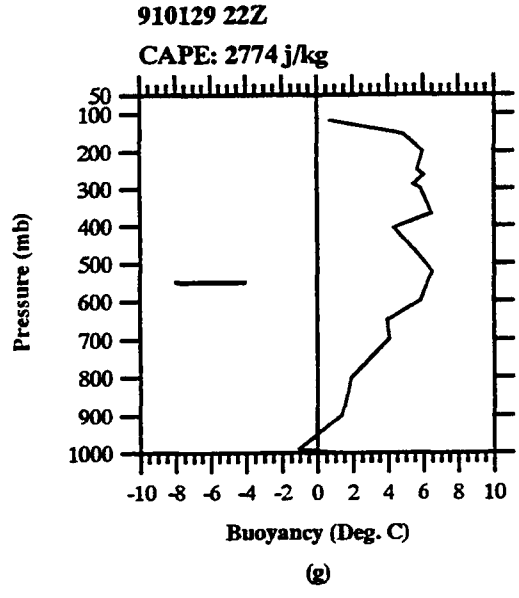


Fig. 4.16. (*continued*).

The corresponding CAPE values (Fig. 4.16) are generally small to moderate for the first four events (a-d in Figs. 4.15 and 4.16) but are moderate to high in the remaining three events (e-g in Figs. 4.15 and 4.16), due to the higher surface moisture and mid level regions where temperatures are slightly cooler than moist adiabatic values (Fig. 4.15).

The maximum virtual temperature excess corresponding to each sounding (Fig. 4.16) generally occurs in the vicinity of 500 mb with several soundings showing a secondary peak in the upper troposphere, similar to the break events described previously; however, the virtual temperature excess rarely exceeded 4°C in the monsoon profiles (the highest values never more than 6.5°C). Also, the vertical gradient of buoyancy in the lower troposphere is typically less than in the corresponding break profiles (Fig. 4.2).

### 4.2.2 Partitioned radar reflectivity characteristics

Time-height cross sections of partitioned volume average reflectivity for the seven monsoon events are shown in Fig. 4.17. The convective region cross sections all show a relatively sharp gradient of reflectivity in the vicinity of the melting level with the 30 *dBZ* contour either absent or usually confined to the lowest levels, indicating that the monsoon MCSs were less intense than their break period counterparts. These profiles are consistent with previous investigations of tropical oceanic convection (e.g., Szoke et al. 1986; Jorgensen and LeMone 1989; Rutledge et al. 1992; Williams et al. 1992; Keenan and Rutledge 1993; Zipser and Lutz 1994) suggesting the presence of relatively weak low-level vertical drafts which are unable to loft substantial quantities of supercooled liquid water into the mixed phase region of the cloud. It is expected that mostly glaciated conditions with small particle sizes occur above the 0°C level. The profile is also

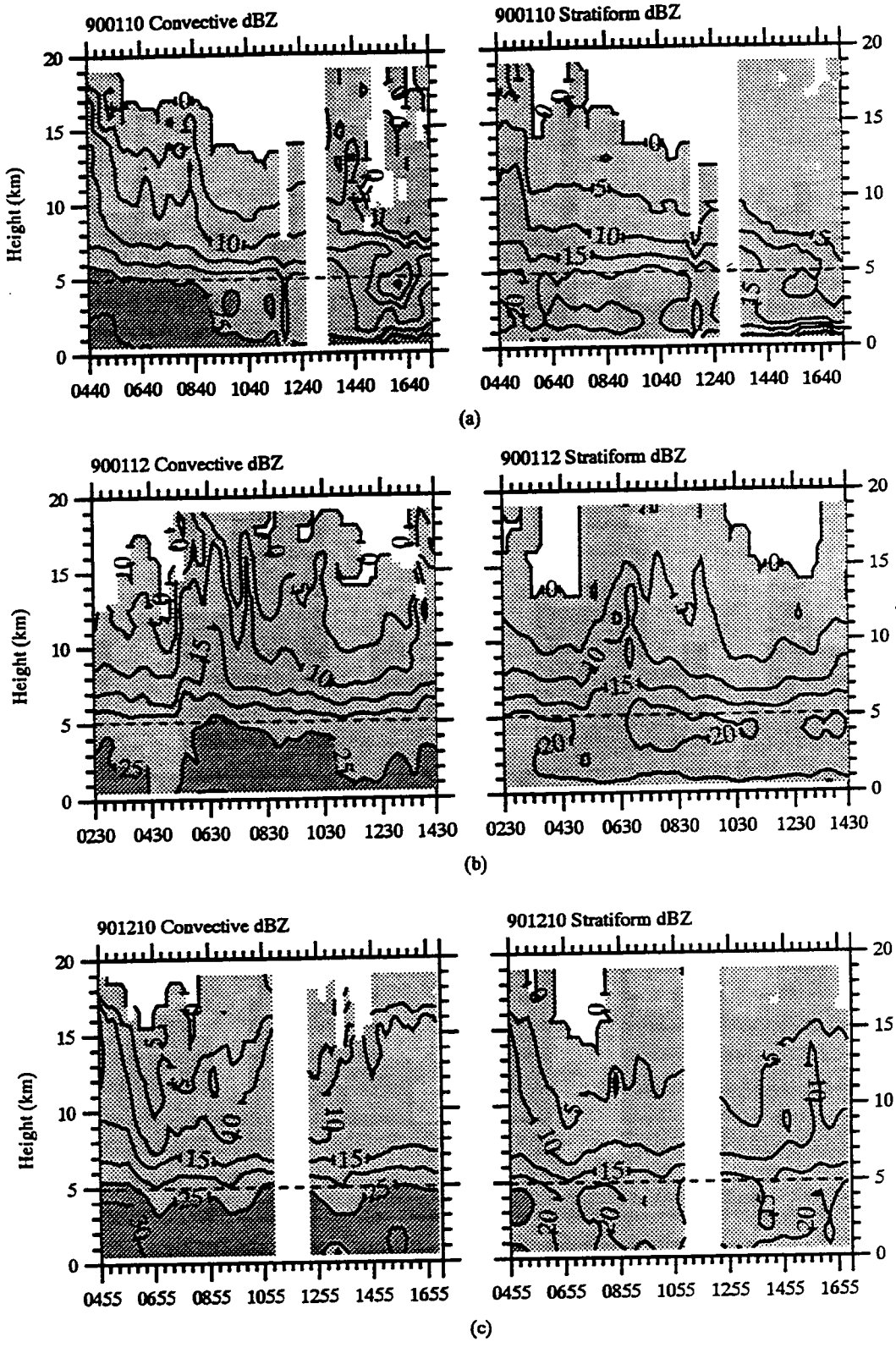


Fig. 4.17. Same as Fig. 4.3 except for the seven monsoon MCSs.

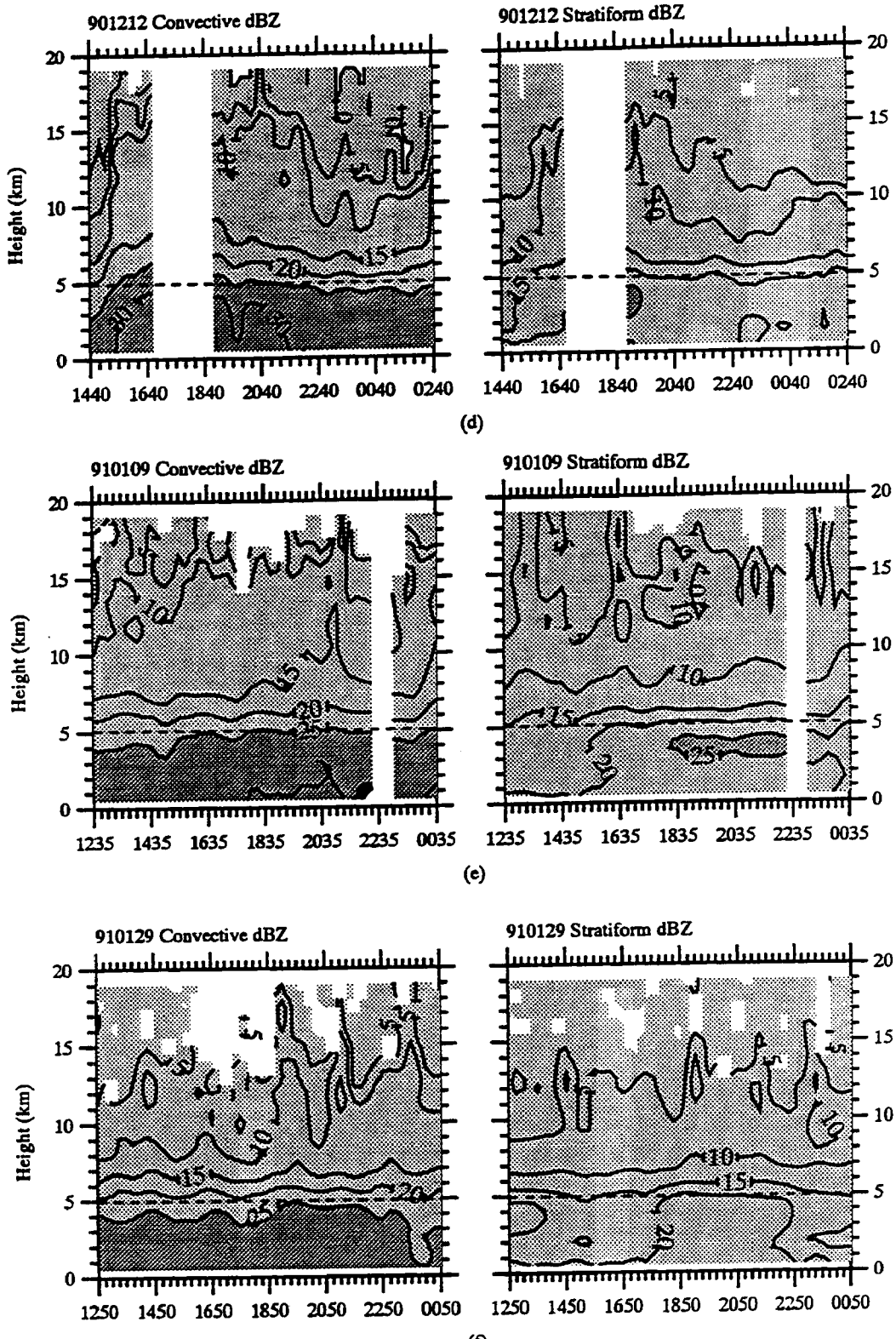


Fig. 4.17. (*continued*).

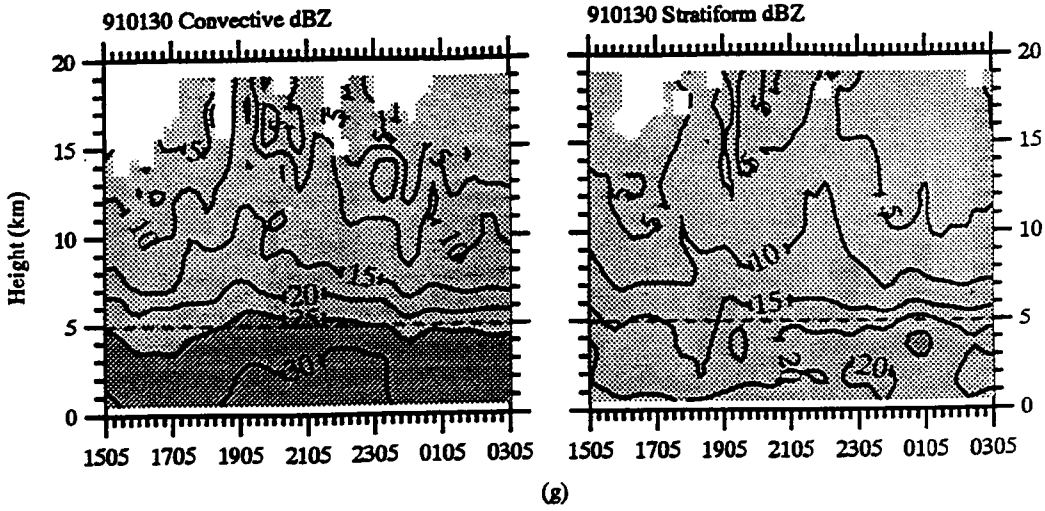


Fig. 4.17. (*continued*).

consistent with Petersen (1992), Rutledge et al. (1992), and Randell et al. (1994) who showed relatively low lightning flash rates in monsoon convection, suggesting weaker convection.

There is also a tendency for the convective reflectivity patterns in Fig. 4.17 to remain relatively constant during the observation period of each MCS with less pronounced variability in the height of selected contours compared to the break profiles in Fig. 4.3. This result is consistent with Keenan et al. (1989) who showed that oceanic convection off northern Australia displayed much less pronounced diurnal variability compared to land-based convective activity over the continent. All of the monsoon MCSs showed evidence of a radar bright band signature in the partitioned stratiform composite cross section for at least part of the observation period.

### 4.2.3 MCS general description

In this section, a brief description of the evolution characteristics of the seven monsoon MCSs from a radar perspective is provided. Because of the disorganized nature of the monsoon convection, it is difficult to make many generalizations about the evolution of convective activity. Herein, an attempt is made to discuss only the most salient features common to the events analyzed.

During the monsoon, convective activity (as determined by the occurrence of radar echo) tended to pulsate over a period of several days with individual events usually lasting less than 12 hours. Typically, the convective activity of each event initiated as scattered cells (Fig. 4.18a) and became loosely organized into linear bands of enhanced precipitation (hereafter referred to as convective bands) embedded in areally extensive stratiform cloud (Fig. 4.18b). With time, the

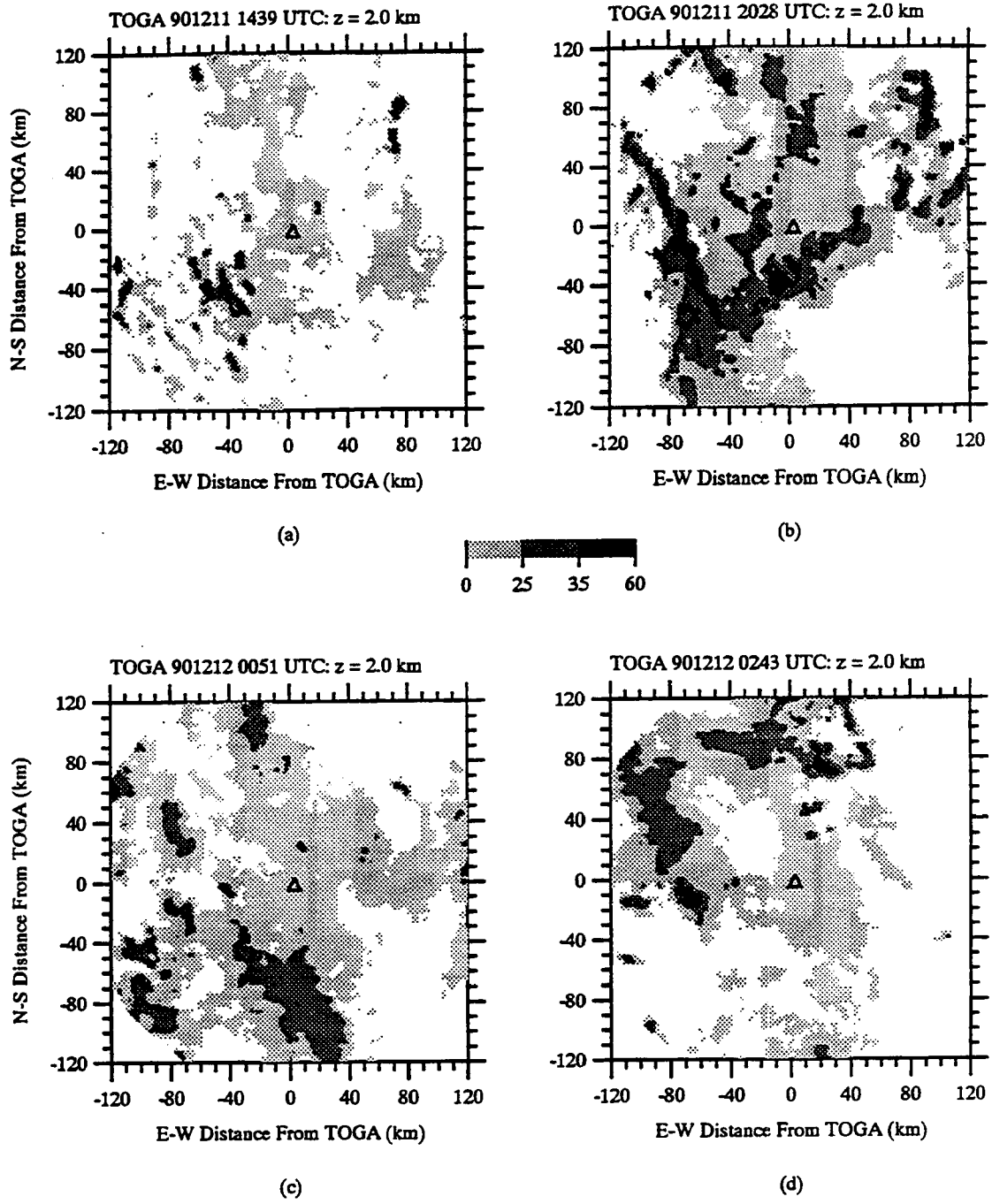


Fig. 4.18. Selected low-level radar CAPPIs for the 901212 monsoon MCS showing a typical progression of convective activity. Date and time of each CAPPI is shown at the top of the plot. Units are *dBZ* with the scale shown in the middle of the figure.

intensity of the bands decreased, leaving a region of widespread stratiform precipitation which gradually decreased (Fig. 4.18c and d).

All of the monsoon MCSs formed over the ocean north or west of Darwin and moved onshore in the westerly monsoon flow. The embedded convective bands would often form parallel to the coastline (approximately parallel to the 850 mb wind), suggesting that local sea breeze circulations may have played a role in initiating convection, consistent with the radar observations of Keenan and Carbone (1992) in the Australian summer monsoon. Radar data indicated that the convective bands could range from less than 50 km in length (Fig. 4.19a) to more than 150 km (Fig. 4.19c and d), sometimes with more than one preferred direction of orientation (Fig. 4.18b). Moreover, the convective bands would often interact with local sea breeze circulation features as they propagated on shore (Fig. 4.20). It was also commonly observed that convective elements formed, intensified, merged with other cells, and decayed into a region of stratiform precipitation within a span of about one hour, sometimes without appreciable movement with respect to the ground, making it difficult to generalize the overall organizational structure of these MCSs.

Several of the monsoon MCSs have been studied previously (i.e., 900112 and 901210) and provide a base of comparison for this study. Keenan and Rutledge (1993) used dual-Doppler radar data to diagnose the kinematic flow patterns of the 900112 MCS. This event had some characteristics of a squall line: a leading line of convection and trailing stratiform region with a mesoscale vortex circulation. However, the vertical circulations in the stratiform region were highly variable, characterized by decaying convective cells with regions of overturning (subsidence) alternating with regions of ascent.

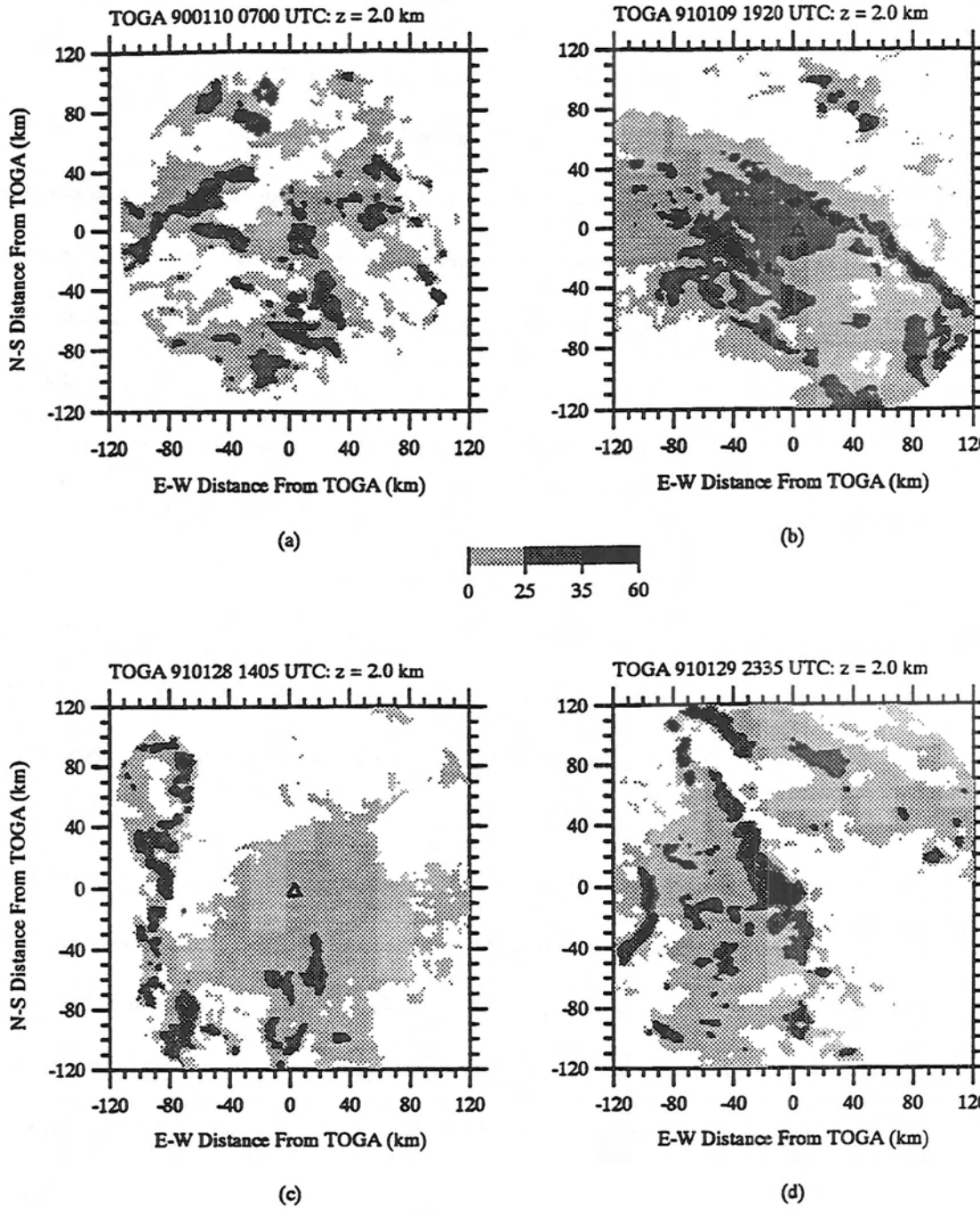


Fig. 4.19. Selected low-level radar CAPPIs for the 900110 (a), 910109 (b), 910129 (c), and 910130 (d) MCSs showing different orientations of lines observed in the monsoon events. Date and time of each CAPPI is shown at the top of the plot. Units are *dBZ* with the scale shown in the middle of the figure.

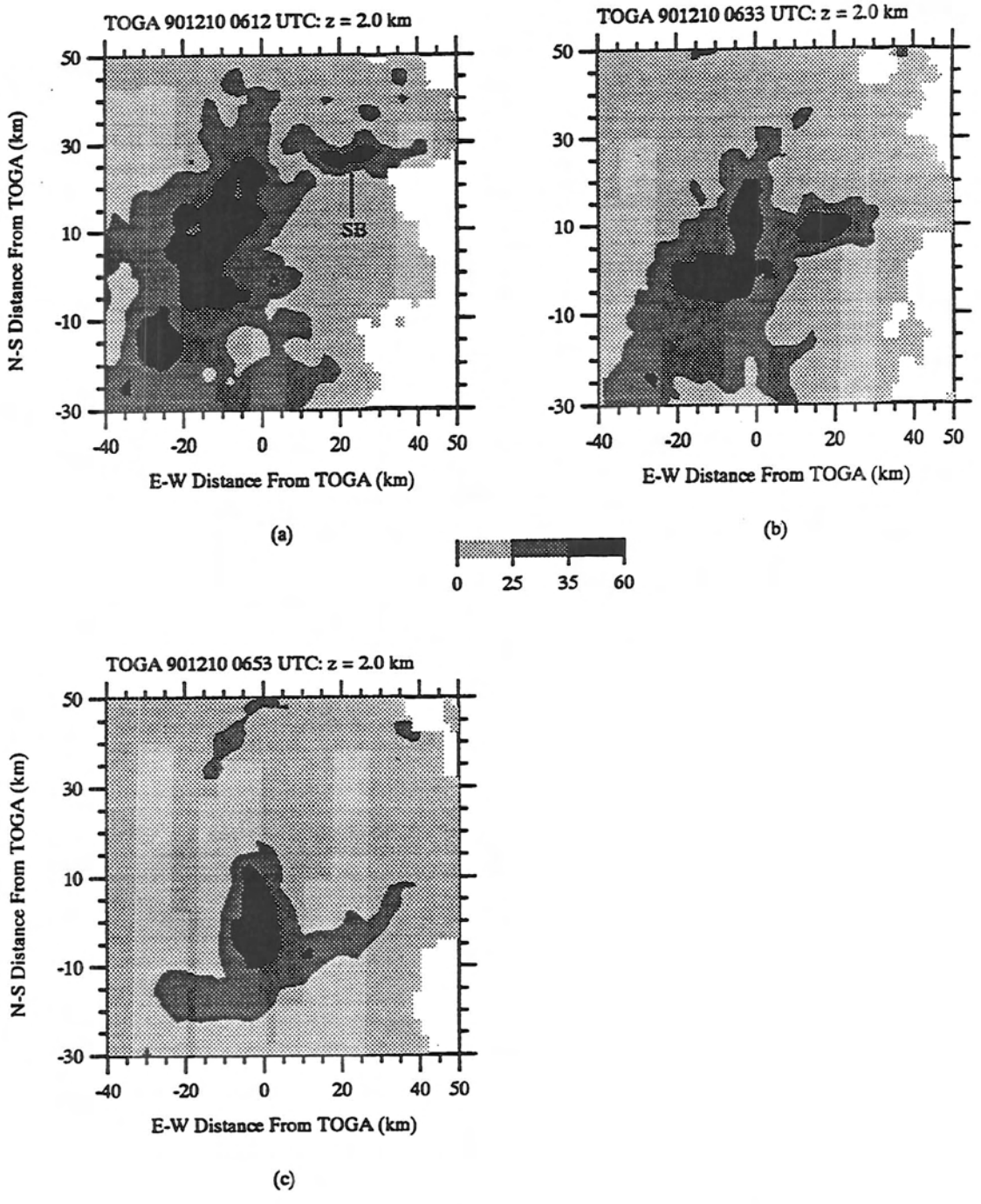


Fig. 4.20. Selected low-level radar CAPPIs for the 901210 MCS showing the interaction of a monsoon convective band with a local sea breeze circulation feature [identified in (a) as "SB"]. Date and time of each CAPPI is shown at the top of the plot. Units are *dBZ* with the scale shown in the middle of the figure.

May (1995) used radar and wind profiler data to study the 901210 MCS which was part of a weak tropical cyclone disturbance (Laurance). May described the existence of cyclonically rotating spiral rainbands in Laurance which moved radially outward from the eyewall at 6-8 m $s^{-1}$. The bands were organized at two different scales; the rainbands themselves formed about 100 km from the storm center and were characterized as regions of mostly stratiform precipitation about 60 km wide. Within the bands, convective lines developed at regular intervals oriented $\sim 45°$ to the rainband and propagated outward with respect to the flow at all levels, acting as a partial barrier to radial inflow (May 1995). May hypothesized that the convection was initiated by inertia-gravity waves propagating from near the storm eye.

### 4.2.4 Wind profiler results

#### 4.2.4.1 Analysis of time-height cross sections results

1) 900110

The time-height cross section of wind profiler vertical air motion, MIT radar reflectivity over the wind profiler, and the Berrimah surface rain gauge trace for 900110 are shown in Fig. 4.21. The vertical air motion and reflectivity cross sections indicates that several relatively weak convective bands, separated by about one hour, passed over the profiler during the observation period. The small magnitude drafts are consistent with the reflectivity pattern over the profiler (Fig. 4.21a), which shows that the higher reflectivity regions are restricted to heights below the melting level with a relatively sharp reflectivity gradient in the vicinity of 5 km. Selected radar cross sections (not shown) indicated that the 30 *dBZ* contour did not extend above 6 km in any part of the MCS during the observation period, suggesting the predominance of ice phase precipitation

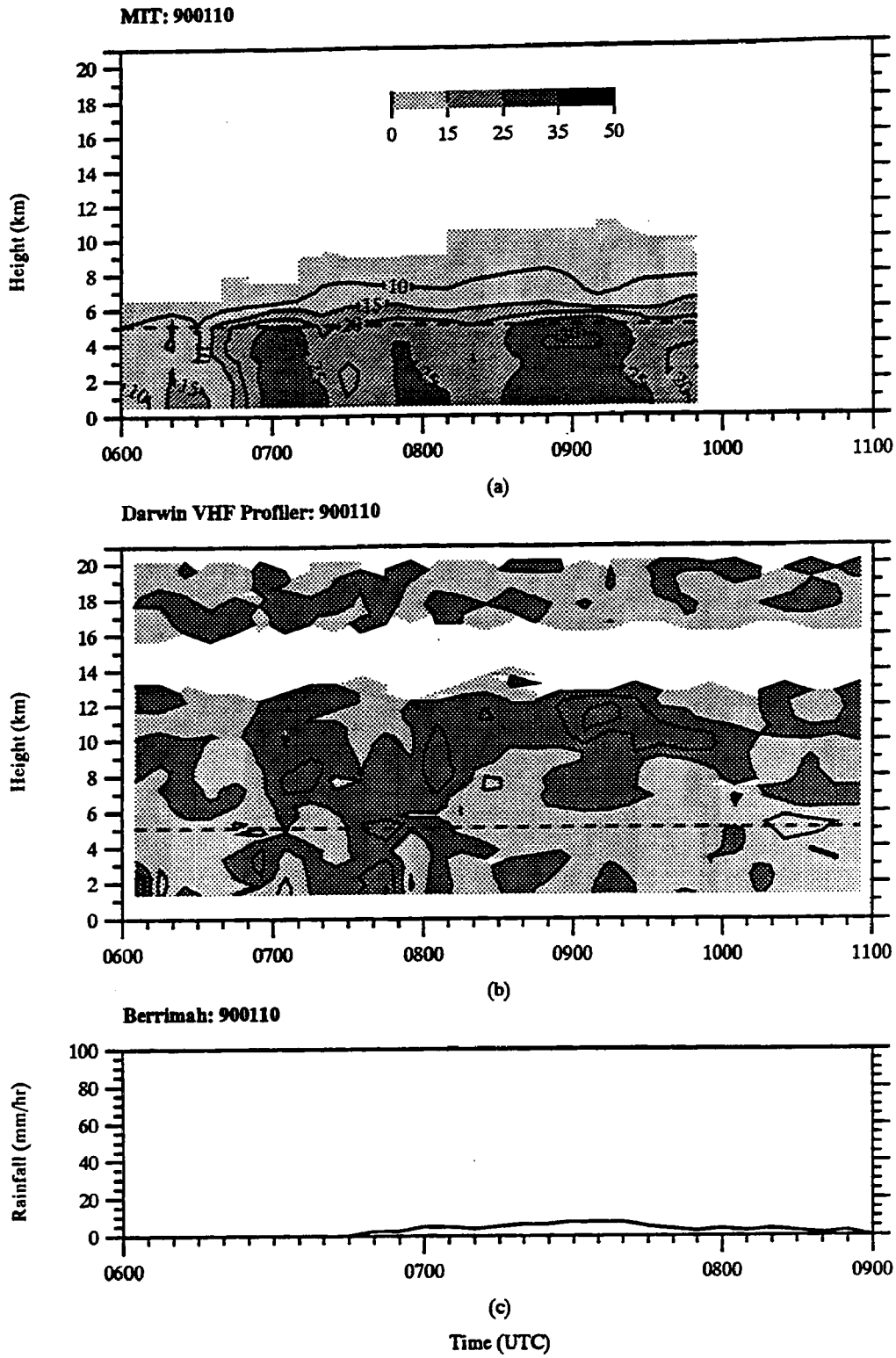


Fig. 4.21. Same as Fig. 4.8 except for the 900110 MCS.

above the melting level, consistent with previous observations of tropical oceanic convection (Houze and Churchill 1984; Jorgensen and LeMone 1989; Gamache 1990; Rutledge et al. 1992; Keenan and Carbone 1992; Williams et al. 1992).

The first band at 0700 UTC produced no rain at the nearby Berrimah rain gauge site. A similar band passed over near 0750 UTC, coincident with the onset of rain at Berrimah. After 0830 UTC, the vertical motion cross section indicates enhanced upper level ascent, corresponding with the development of a small radar bright band and slightly enhanced surface rainfall in the vicinity of the profiler (Fig. 4.21). By 0930 UTC, convective activity associated with the 900110 MCS was dissipating as revealed in the vertical air motion pattern over the profiler and volume average reflectivity cross section (Fig. 4.17a).

2) 900112

Time height cross sections of vertical velocity and reflectivity over the profiler are shown in Fig. 4.22. Because the MIT radar was collecting only surveillance scan data prior to 1010 UTC, the reflectivity cross section (Fig. 4.22a) could only be constructed from 1010 UTC to the end of analysis period (1230 UTC). Also, instrument problems prevented rainfall data from being recorded at the Berrimah site on this date. In Fig. 4.22c, rainfall data is shown from the Darwin aerodrome rain gauge, located about 7 km northwest of the wind profiler.

Inspection of Fig. 4.22b shows a series of updraft cores which passed over the profiler during the sampling period. Low-level CAPPI's (not shown) indicated that the regions of ascent were associated with convective bands which crossed over the wind profiler location, with the first band corresponding to convection along the leading edge of the MCS as it propagated from the ocean

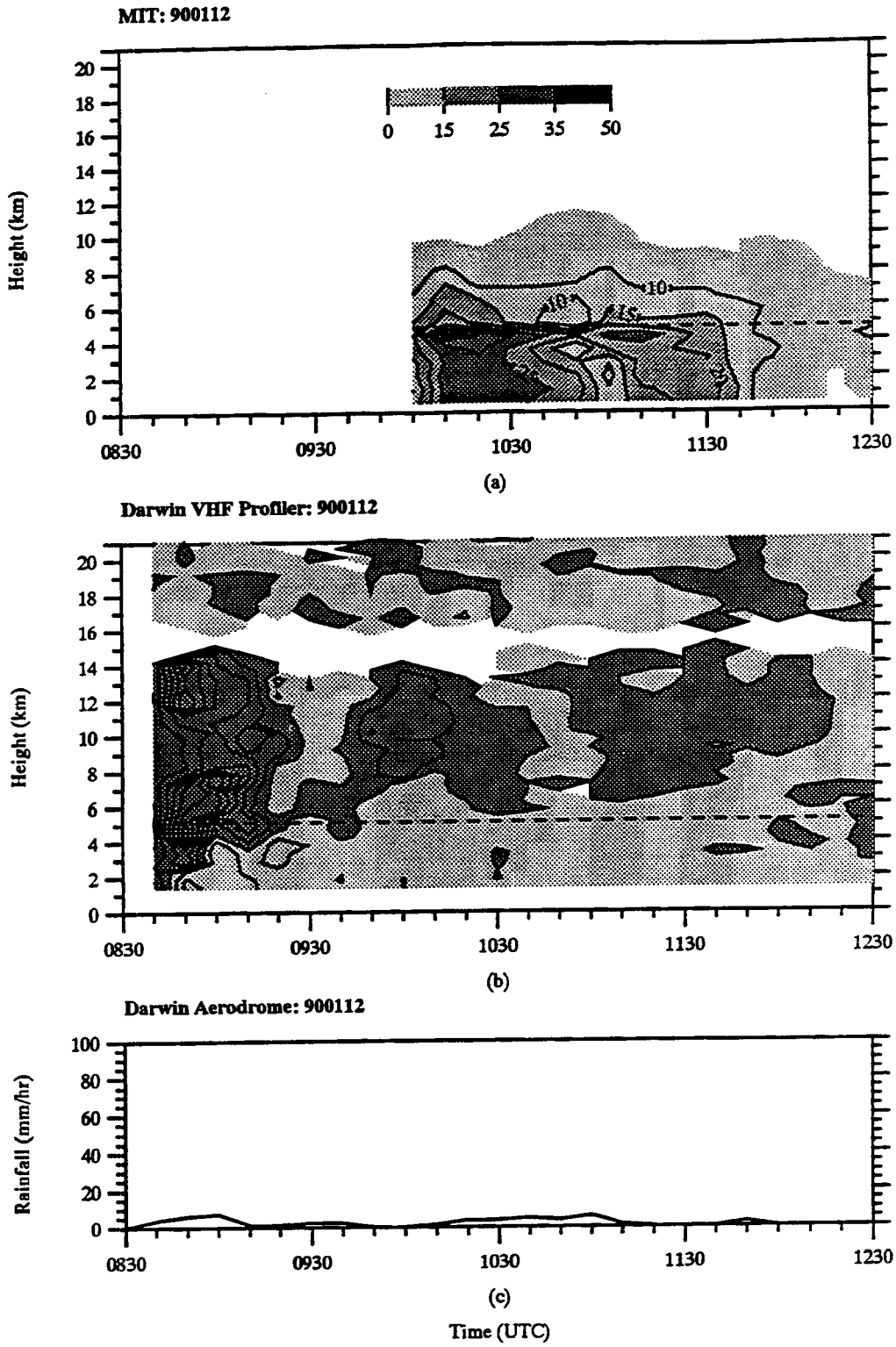


Fig. 4.22. Same as Fig. 4.8 except for the 900112 MCS. Note that the location of the rain trace in (c) is the Darwin Aerodrome.

northwest of Darwin toward the southeast (see Kennan and Rutledge 1993 for a detailed description of the evolution of the 900112 MCS). The strength of the updrafts progressively decreased from about 2-3 m $s^{-1}$ in the first band (0830-0920 UTC) to less than 0.5 m $s^{-1}$ in the last band (1100-1200 UTC). The magnitude of the peak updraft is in reasonable agreement with previous studies of oceanic convection (LeMone and Zipser 1980; Zipser and LeMone 1980; Jorgensen and LeMone 1989). Each of these ascent regions were separated by relatively narrow regions of subsidence. Moreover, with the exception of the earliest observational time (0830 UTC), subsidence occurred at low-levels throughout the passage of the system and became progressively deeper with time. The wind profiler analysis is consistent with the results of Keenan and Rutledge (1993) who documented a series of convective bands in the 900112 MCS oriented parallel to the direction of storm motion which they attributed to convective scale overturning.

The reflectivity cross section (Fig. 4.22a) shows several higher reflectivity regions with small bright band signatures separated by region of lower reflectivities, in agreement with the overall vertical velocity structure. This pattern is also consistent with the interpretation of Keenan and Rutledge (1993) that convective elements were being advected rearward from the leading line convection in a front to rear storm relative flow and decaying into the stratiform region. In this view, the stratiform region developed from decaying convection. Selected radar cross sections (not shown), as well as the cross section over the location of the profiler (Fig. 4.22a), showed that the largest reflectivities in the 900112 MCS were confined to heights at or below the melting level (similar to the 900110 MCS), suggesting that glaciated conditions occurred throughout the middle-to-upper troposphere and that the precipitation from this system may have had significant contributions from a low-level warm rain (coalescence) process (Keenan and Rutledge 1993).

The rain trace at the Darwin aerodrome site for the wind profiler observation period is shown in Fig. 4.22c. The rain trace shows a relatively small amount of rainfall occurred (8.4 mm total). The first onset of rainfall appears to be associated with the passage of the first band over the profiler site (e.g., the time period 0830-0910 UTC); however there is somewhat of a phase lag at later times. Also, there is no evidence in the rain trace that the first band was more intense than later bands. Similar to 900110, the accumulation of rainfall was relatively evenly distributed throughout the observational period.

3) 901210

The time-height cross section of vertical air motion sampled by the wind profiler for 901210 and the corresponding rain trace from the nearby Berrimah rain gauge are shown in Fig. 4.23. The profiler data shows the simultaneous passage of updraft cores in the lower and upper troposphere near 0650 UTC marking the arrival of a rather intense convective band (Fig. 4.20). Selected radar cross sections (not shown) indicated that this convective band was more intense as it approached the coastline west of the profiler, with the 30 *dBZ* contour extending to near 9 km and echo top heights approaching 15 km, but weakened considerably as it propagated onshore toward the profiler. The passage of the drafts at roughly the same time is consistent with selected cross sections of reflectivity (not shown) which indicate that most of the convective cells within the bands had little vertical tilt as they propagated to the southeast. Overall, the pattern of vertical air motion in this band was very similar to the pattern observed in the first band of the 900112 event. The rain trace from Berrimah shows a sharp peak ($\sim$ 60 mm $hr^{-1}$) associated with the passage of the updrafts, though it is not possible to tell if the peak is due primarily to the low or upper level draft.

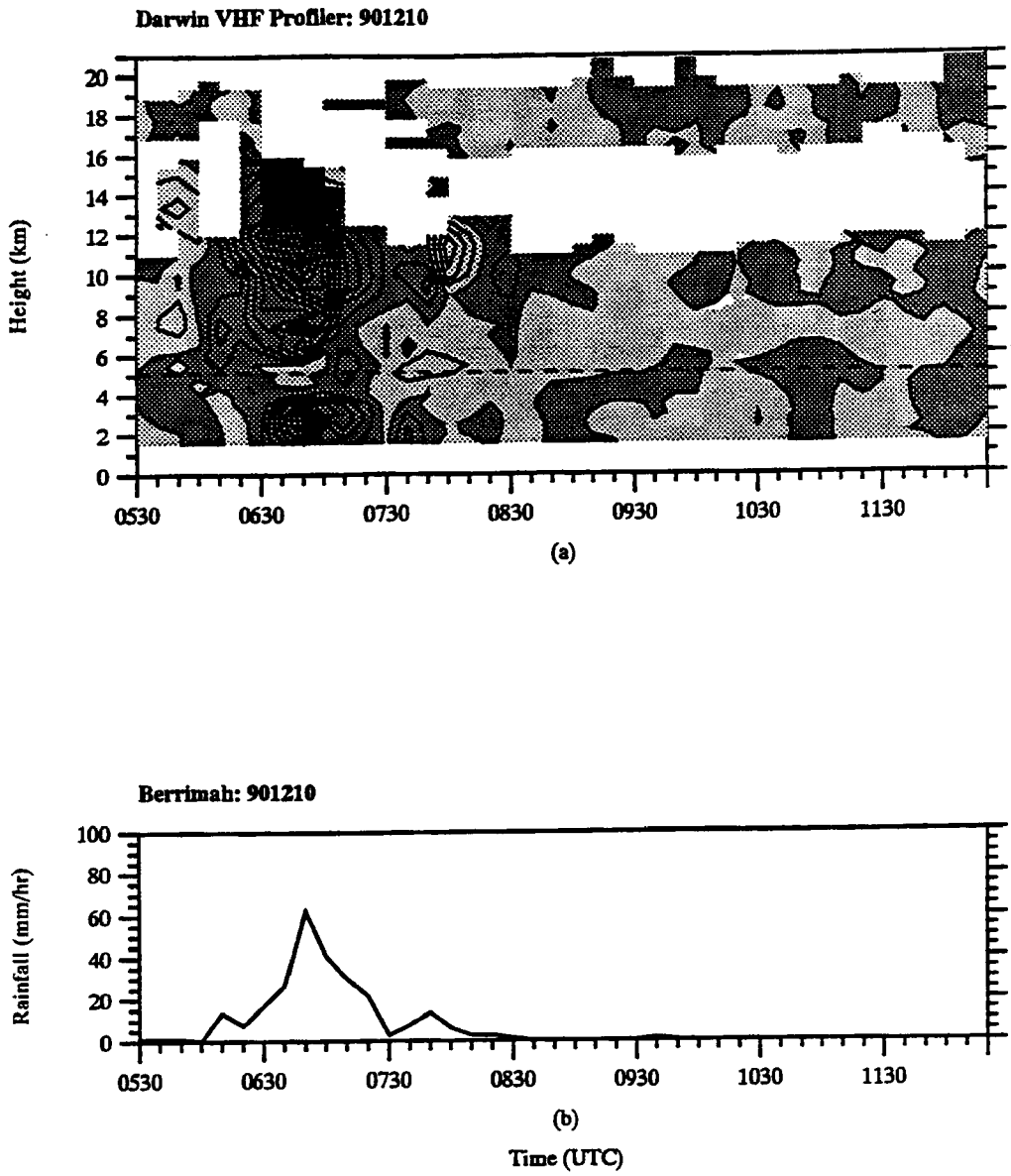


Fig. 4.23. Same as Fig. 4.11 except for the 901210 MCS.

Near 0750 UTC, a second embedded convective band passed over the profiler; however, the vertical air motion and rain gauge plots suggest that this band was weaker than the first. Again, the pattern is consistent with 900112, though the 901210 event, as sampled by the wind profiler, was more intense. The vertical air velocity data after 0750 UTC is difficult to interpret without adequate reflectivity coverage over the profiler. Based on selected radar cross sections (Fig. 4.24), it appears that the pattern may reflect the decay of convective elements rearward of the main convective band.

4) 901212

The time-height cross section of vertical air motion over the wind profiler and the surface rainfall pattern from the Berrimah rain gauge for 901212 are shown in Fig. 4.25. Overall, the vertical air motion pattern is noisy and weak with drafts never exceeding about 1 m $s^{-1}$ through the observation period. Similar to the previous monsoon MCSs, low-level CAPPIs showed that the regions of enhanced vertical air motion corresponded to the passage of several weak convective bands embedded in more uniform stratiform region. The passage of the bands over the profiler occurred near 1830, 1930, and 2230 UTC and are approximately delineated by the occurrence of rain at the Berrimah rain gauge site; however, consistent with the weak vertical air motions, the rainfall intensity at Berrimah never exceeded about 10 mm $hr^{-1}$.

The radar data indicated that the convective bands weakened considerably as they propagated on shore and over the mainland. This fact was also revealed in the rainfall statistics for 901212 which showed a sharp west to east gradient of rainfall intensity with maximum values exceeding 90 mm $hr^{-1}$ along the west coast and Island stations and less than 20 mm $hr^{-1}$ in the eastern portion

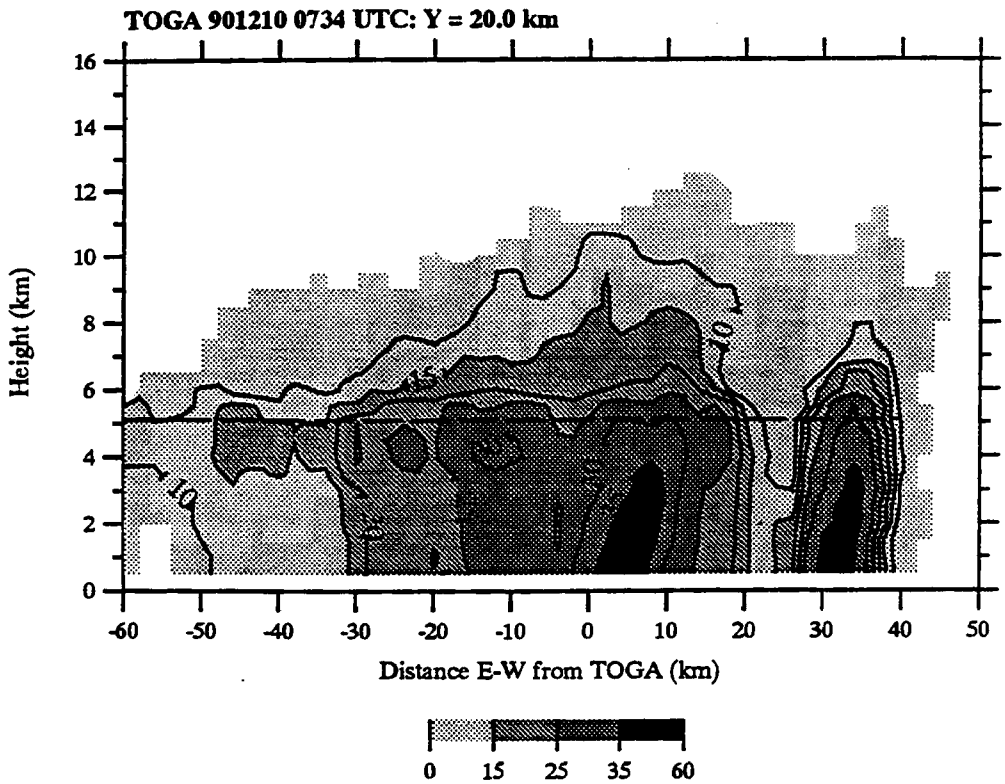


Fig. 4.24. East-west cross section of TOGA radar reflectivity for the 901210 MCS showing observed reflectivity characteristics. Date and time is shown at the top of the plot. Units are *dBZ* with the scale shown at the bottom of the figure. The dashed horizontal line indicates the approximate level of the 0°C isotherm.

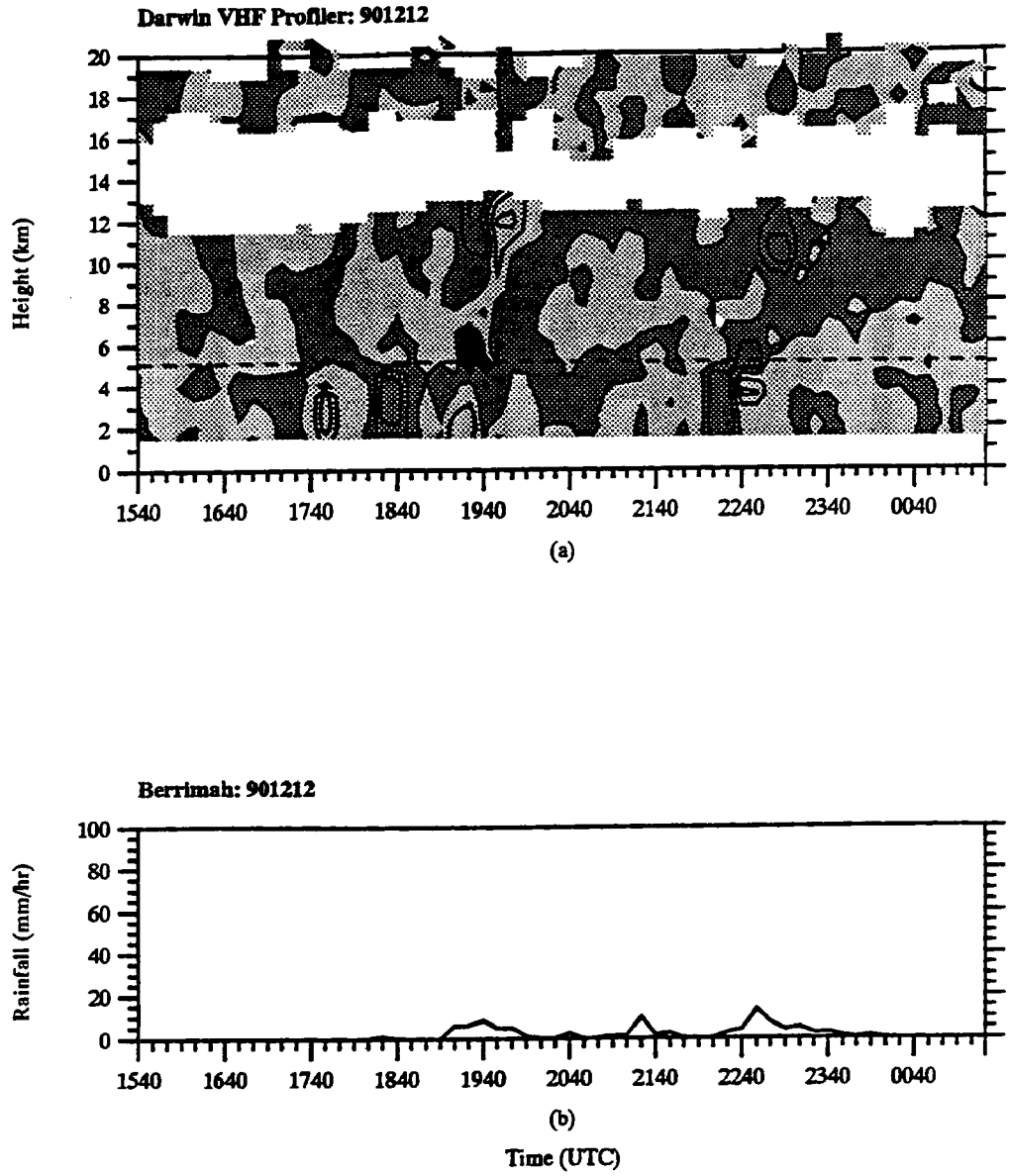


Fig. 4.25. Same as Fig. 4.11 except for the 901212 MCS.

of the network. During the observation period, 15.6 mm of rain was recorded at Berrimah with the vast majority (83%) associated with the convective bands (Appendix D).

5) 910109

The time-height cross section of vertical air motion and the Berrimah rain gauge trace for 910109 are shown in Fig. 4.26. The vertical motion plot shows generally weak vertical drafts with a characteristic stratiform structure of upper level ascent and lower level descent. This pattern was interrupted by several episodes of relatively large vertical drafts associated with the passage of intense convective bands over the profiler. The vertical air motion pattern between about 1830-2200 UTC is consistent with the volume average stratiform reflectivity pattern which shows an enhanced bright band over the observational network at this time (Fig. 4.17e).

The passage of the first convective band occurred between about 1730-1800 UTC and is revealed by vertical drafts exceeding 4-5 m $s^{-1}$ in the lower and upper troposphere and a small increase in surface rainfall at the Berrimah gauge. Two other bands crossed over near 2230 and 0000 UTC with peak vertical air motions centered in the middle to upper troposphere. The band feature near 0000 UTC had a peak updraft exceeding 9 m $s^{-1}$ and was accompanied by a rainfall rate exceeding 40 mm $hr^{-1}$ for 30 minutes (Fig. 4.26b). Eighty one percent of the total rainfall recorded at the Berrimah rain gauge during the 910109 observation period was associated with the convective band features, the remainder from stratiform rain (Appendix D).

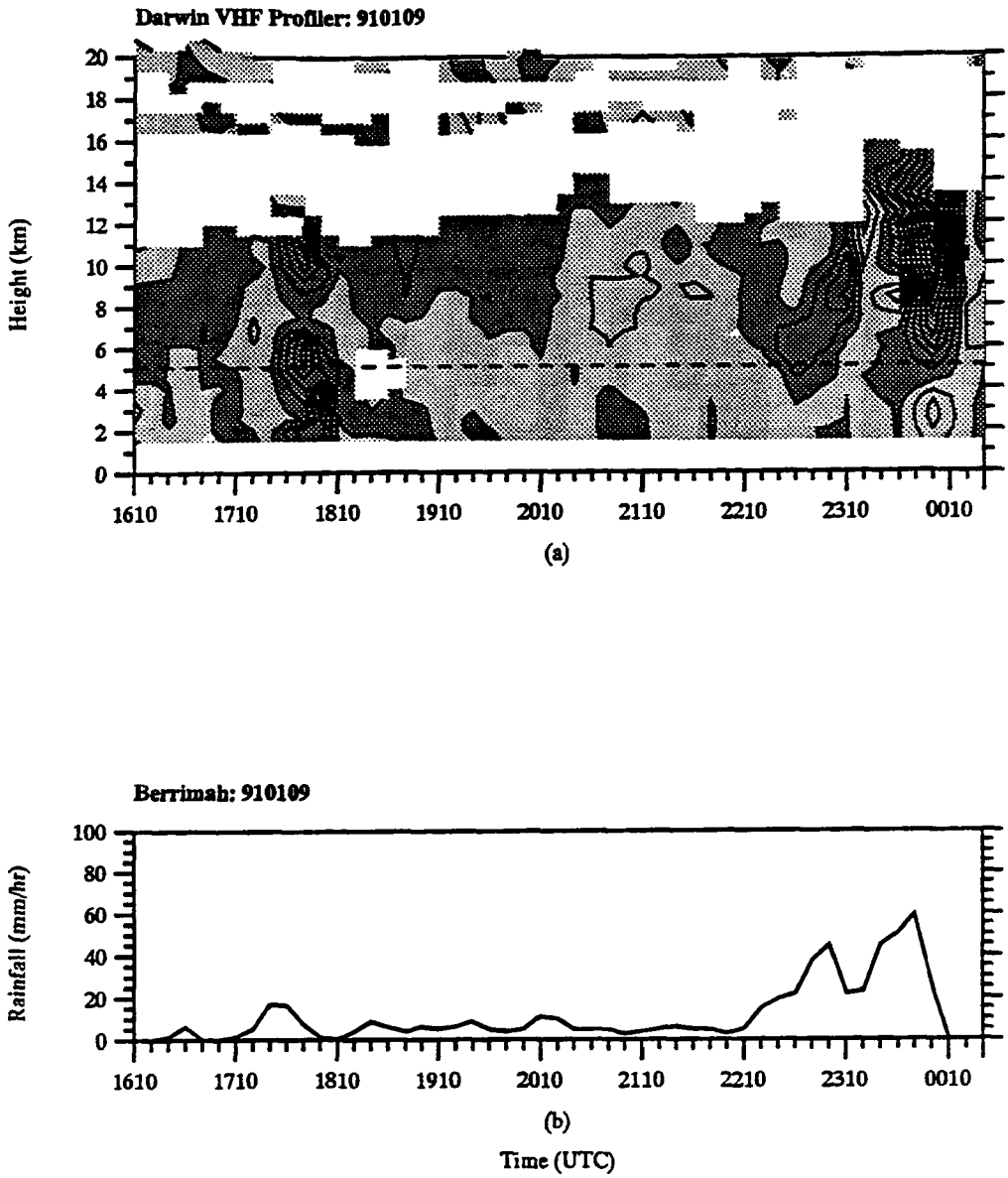


Fig. 4.26. Same as Fig. 4.11 except for the 910109 MCS. Note that the vertical air motion plot is contoured at 1 m $s^{-1}$ intervals.

6) 910129

The time-height cross section of vertical air motion and nearby surface rain gauge trace for the 910129 event are shown in Fig. 4.27. Similar to 901212, the vertical air motion pattern is relatively noisy throughout the observation period. Vertical air motions are generally weak ($< 1$ m $s^{-1}$) with the exception of the time period near 1800 UTC and 0230 UTC where updrafts were on the order of 2 m $s^{-1}$. Similar to the previous monsoon MCSs, the regions of higher vertical air velocities coincided with the passage of the convective bands over the profiler location. The rainfall observed at the Berrimah rain gauge was relatively light (i.e., less than 15 mm $hr^{-1}$) throughout the majority of the observation period and was restricted to the passage of the convective bands; however the last band at 0230 UTC produced a brief heavy rain rate ($\sim$ 65 mm $hr^{-1}$). In this case, 83% of the precipitation was associated with the convective bands (Appendix D).

7) 910130

The time-height cross section of vertical air motion for the 910130 event are shown in Fig. 4.28. Unfortunately, surface rain gauge data in the vicinity of the profiler was not available for this event. The vertical air motion cross section indicates relatively weak drafts throughout the majority of the analysis period, consistent with low-level radar CAPPIs which generally indicated the absence of intense convection in the vicinity of the profiler. An exception to this trend occurred between about 2340-0030 UTC in which radar data showed the passage of a convective band over the profiler site. Selected radar cross sections (not shown) indicated that this band was relatively intense as it approached the mainland coastline from the west-southwest with echo tops approaching 16 km and the 30 *dBZ* contour extending to near 7 km. Similar to several of the

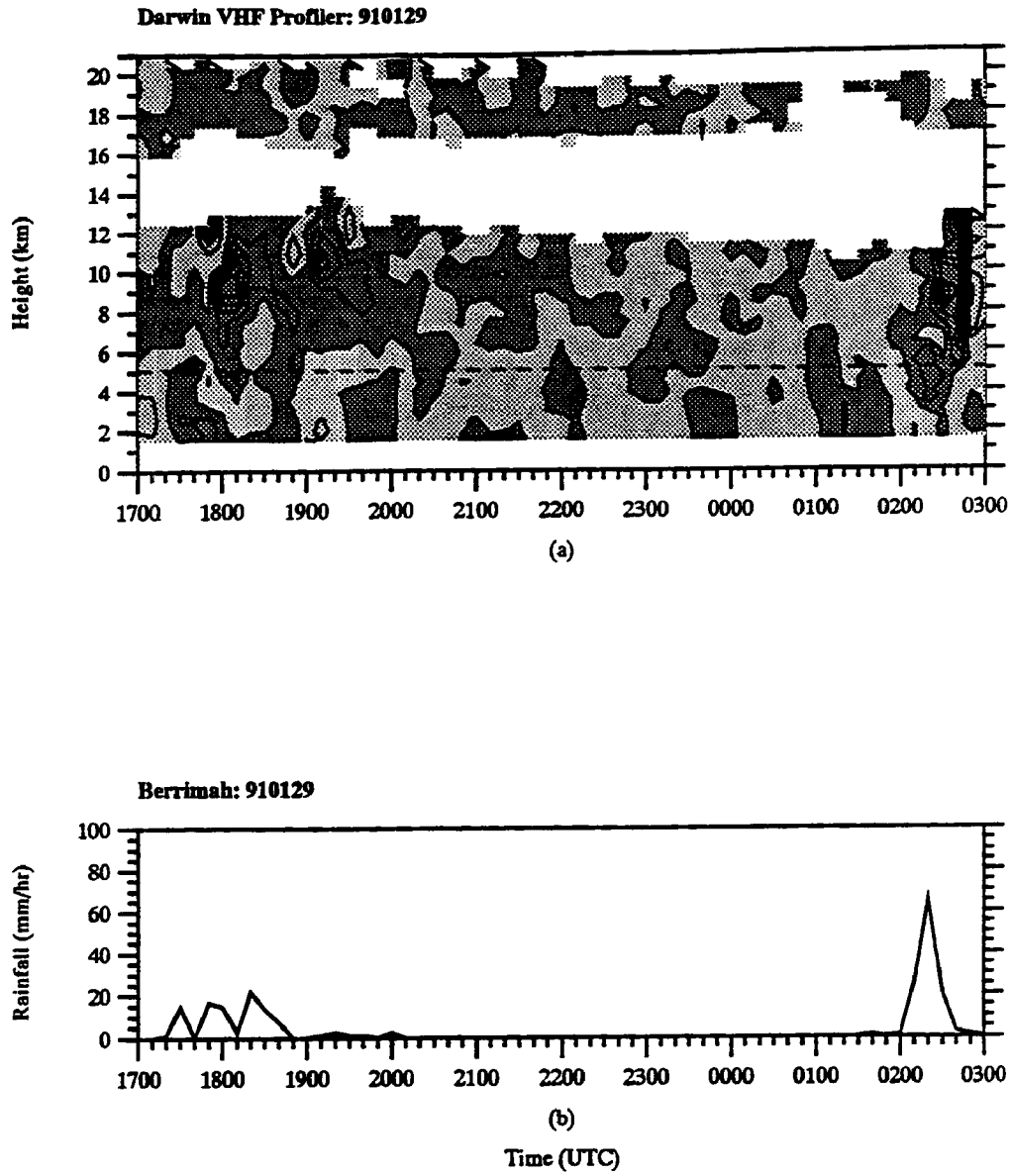


Fig. 4.27. Same as Fig. 4.11 except for the 910129 MCS.

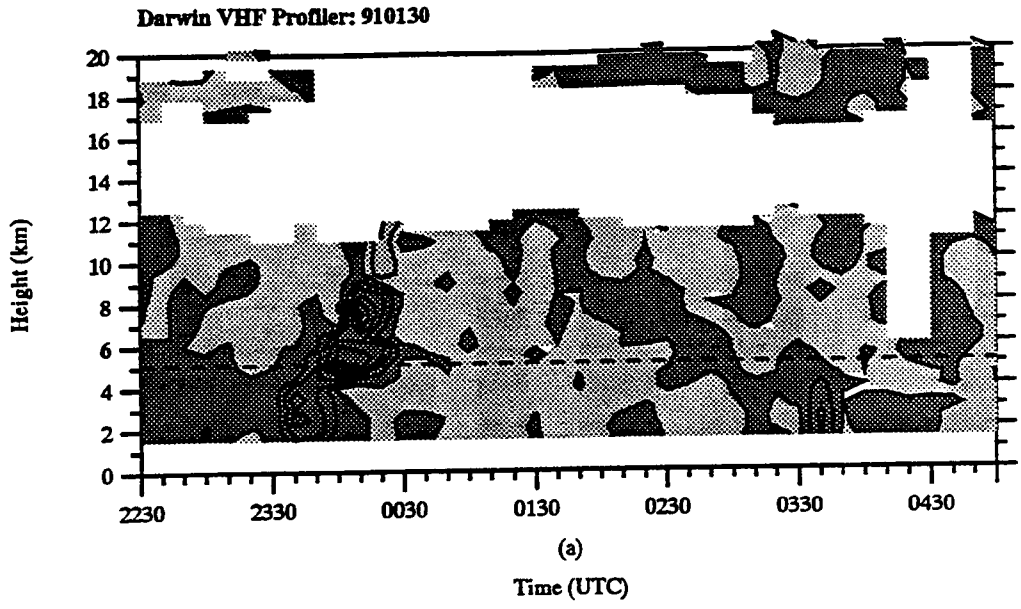


Fig. 4.28. Same as Fig. 4.11 except for the 910130 MCS.

previously described monsoon MCSs, this band weakened considerably as it propagated onshore. The vertical air motion sampled by the wind profiler shows peak vertical drafts $< 2$ m s$^{-1}$ centered below about 8 km, consistent with the band weakening as it crossed over the coastline.

#### 4.2.4.2 Partitioned vertical air motion results

Partitioned composite vertical air motion profiles for each of the monsoon MCSs are shown in Fig. 4.29. The convective region composite profiles show large variability in the magnitude of the drafts that were sampled in each MCS. The largest monsoon updrafts occurred in the middle to upper troposphere (901210 and 910109). Many of the composites (900110, 900112, 901210, 901212) show a bimodal updraft structure similar to the break period MCSs described earlier; however, the lower troposphere updrafts were often weak (900110, 901212, 910129, 910130) compared to the break composites consistent with the smaller virtual temperature excess in the thermal buoyancy profiles (Fig. 4.16). All other factors being equal, the reduced virtual temperature excess available to air parcels rising in monsoon convective cells means that water loading plays a proportionally larger role in reducing the total bouyancy forcing of the vertical wind compared to break period convective cells.

As stated in Sec.4.2.1, many of the thermal buoyancy profiles in Fig. 4.16 show small increases in the virtual temperature excess in the upper troposphere consistent with the renewed vertical acceleration observed in this region; however, it is not clear to what extent the additional thermal buoyancy is due to the release of latent heat of fusion as suggested by previous investigators (e.g., Williams and Renno 1993). Similar to the break period MCSs, the correlation between the thermal buoyancy and the vertical wind peaks in the upper troposphere is not always clear (e.g., 900110, 900112, 901210, and 910130).

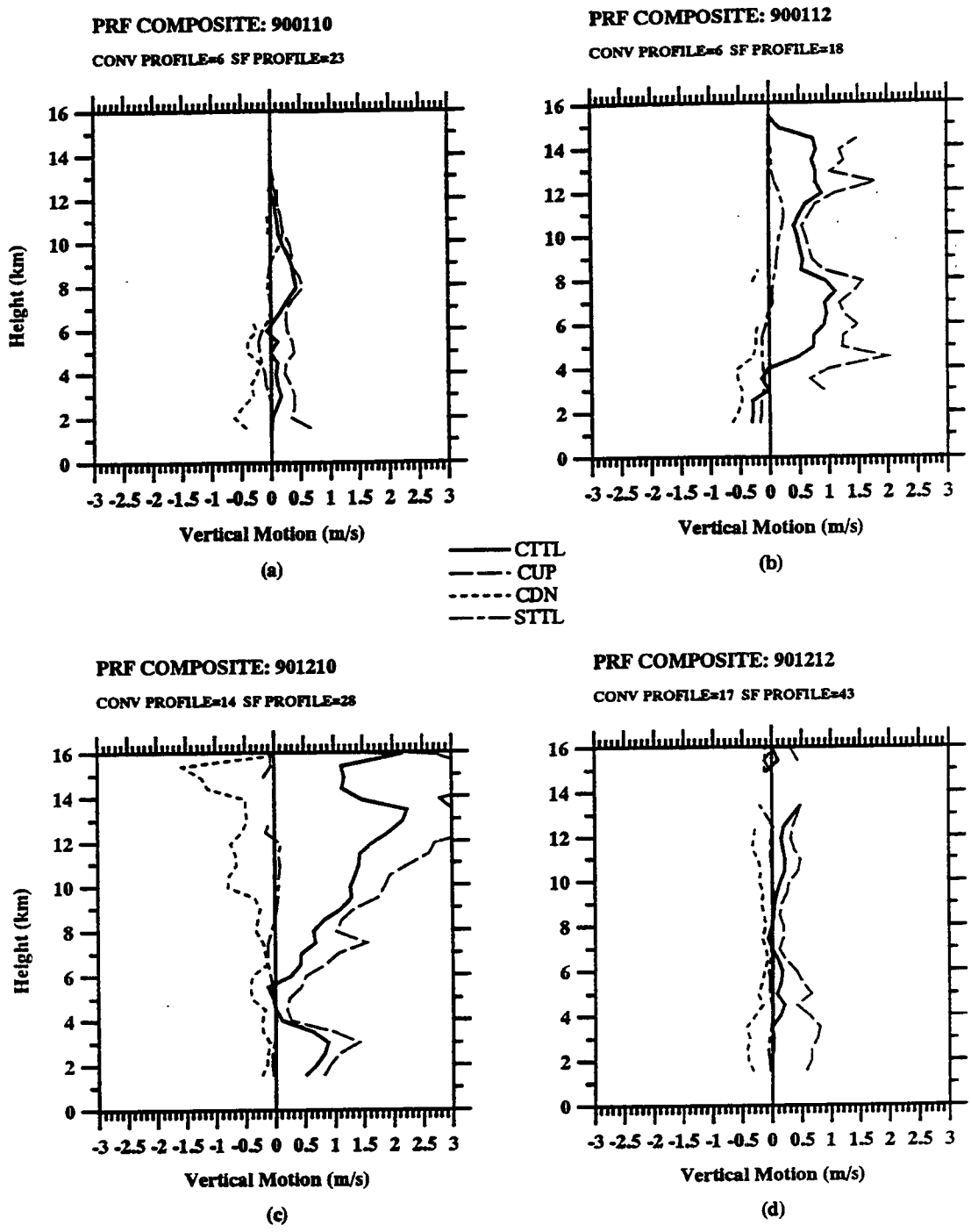


Fig. 4.29. Same as Fig. 4.14 except for the seven monsoon MCSs.

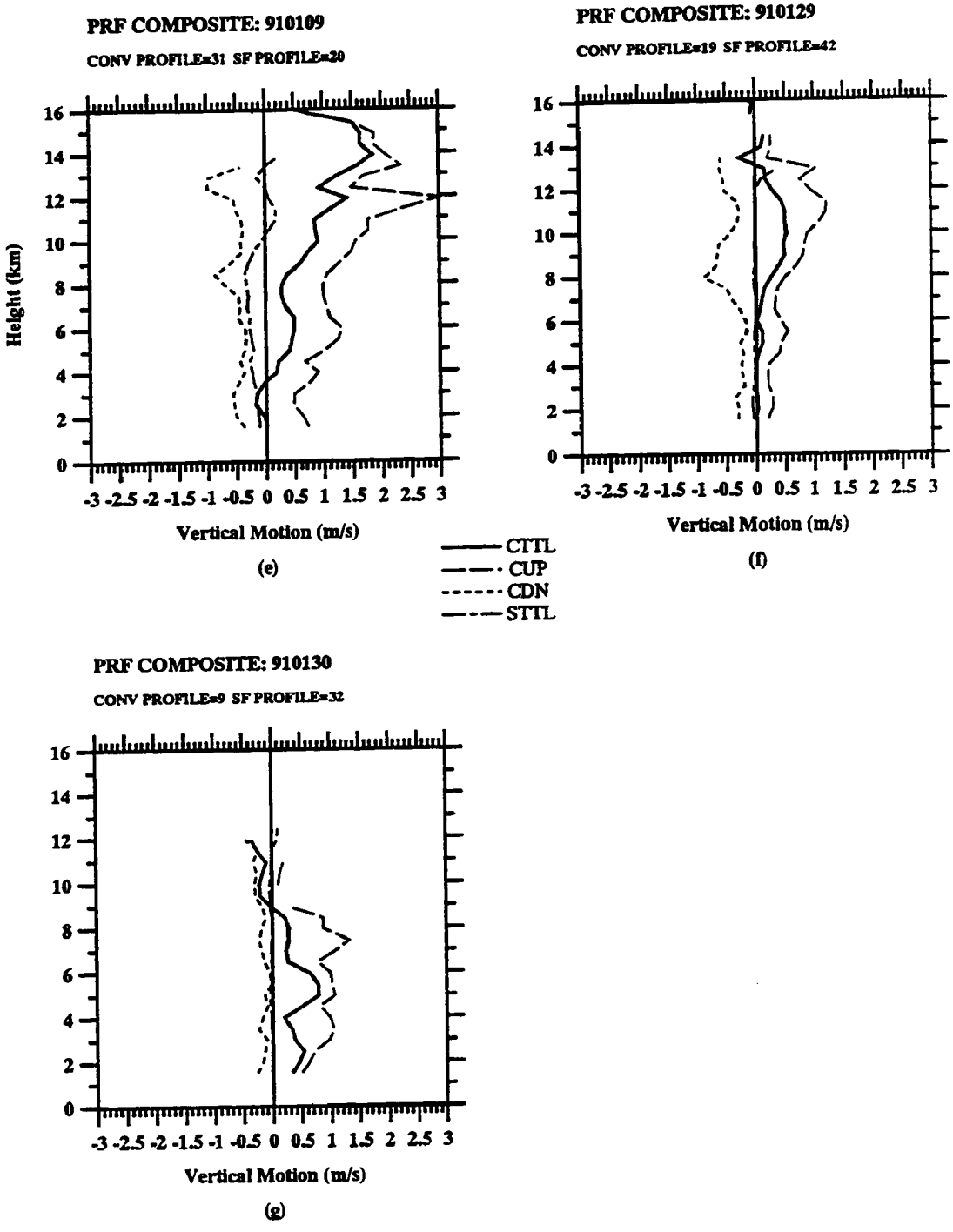


Fig. 4.29. (*continued*).

The location of the peak convective downdraft was variable in the monsoon events, sometimes occurring at upper levels (901210, 910109, 910129) similar to the break period MCSs and sometimes in the lower troposphere (900110, 900112, 901212). Similar to the break events, the stratiform vertical drafts were weak compared to the convective region (with the exception of 900110) and the depth of the upper level ascent region was variable, ranging from essentially zero (901212) to ~ 7 km (900112).

# Chapter V

## COMPOSITE ANALYSIS OF DARWIN EVENTS

This chapter presents a comparison of the monsoon and break period MCSs in terms of environmental, scanning radar, and wind profiler composite characteristics. In Ch. 6, further comparisons of the Darwin composites are made with similar results from other geographical regions including COARE.

### 5.1 Thermal Buoyancy

The monsoon and break period composite profiles of thermal buoyancy are shown in Fig. 5.1. Each profile was constructed by averaging all of the individual profiles shown in Figs. 4.2 and 4.16 for the break period and monsoon regimes, respectively. The composites are similar just above the surface with less than about 1 °C of negative buoyancy below 900 mb and positive buoyancy extending to near 150 mb. The major difference in the profiles occurs above 800 mb (~2 km), where the break period composite shows a large increase in the positive gradient of thermal buoyancy (~ 2°C $km^{-1}$) up to about 600 mb (4.5 km); whereas the monsoon profile shows a much smaller buoyancy increase (~ 0.8°C $km^{-1}$) in this region. The virtual temperature excess of the monsoon composite is almost 4°C less than the corresponding break period profile at 4.5 km.

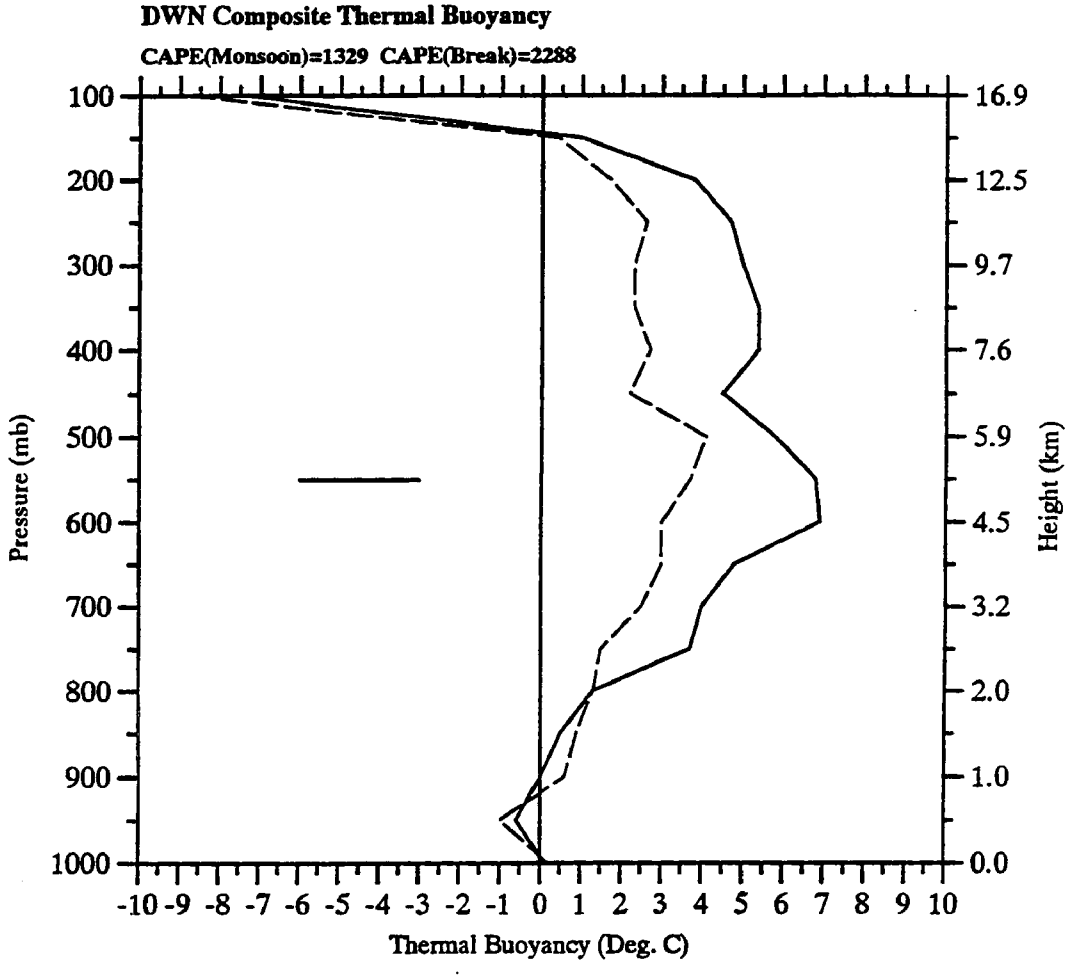


Fig. 5.1. Composite thermal buoyancy profiles (°C) for the 6 break (solid line) and 7 monsoon (dashed line) regime MCSs. The horizontal line in the left portion of the plot represents the approximate 0°C isotherm. The corresponding composite CAPE values are indicated at the top of the plot.

Both profiles show similar patterns in the middle to upper troposphere, marked by a decrease of several degrees in buoyancy to 450 mb (6.7 km), a small increase to 350 mb (8.6 km) and a general falloff to the top of the profiles. The virtual temperature excess of the monsoon composite remains several degrees less than the corresponding break period profile in the middle to upper troposphere. The profiles are consistent with the hypothesis of Lucas et al. (1994) that oceanic environments have a narrow (i.e., skinny) positive area region on a sounding compared to continental soundings. Similarly, the composite CAPE value of the break period is nearly double the corresponding monsoon value (Fig. 5.1). The difference in CAPE between the monsoon and break contrasts with the results of Keenan and Carbone (1992) who found that the two regimes had very similar CAPE on average. However, in that study, Keenan and Carbone utilized a much larger sample (an entire season of data) to compare the potential buoyant energy characteristics of the two regimes.

## 5.2 Partitioned radar reflectivity results

Composite profiles of partitioned volume average reflectivity for the monsoon and break period MCSs are shown in Fig. 5.2. The monsoon convective and stratiform composites were generated by averaging individual profiles from 406 radar volumes while the break period composites were generated from 166 radar volumes. The large difference in the number of volumes used is due to the fact that there were seven monsoon systems analyzed compared to six break period systems in this study. Also, the monsoon systems were generally observed for longer periods over the observational network compared to the break period MCSs.

In the convective region, both the monsoon and break period profiles show relatively high reflectivities below the melting level with only a small vertical gradient ($\sim$ -1 dB km$^{-1}$). The

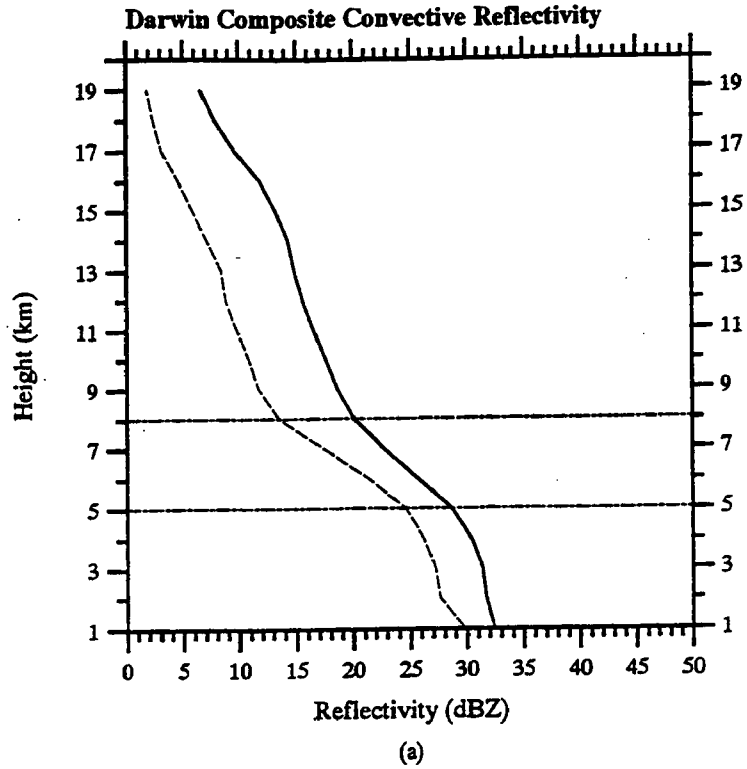


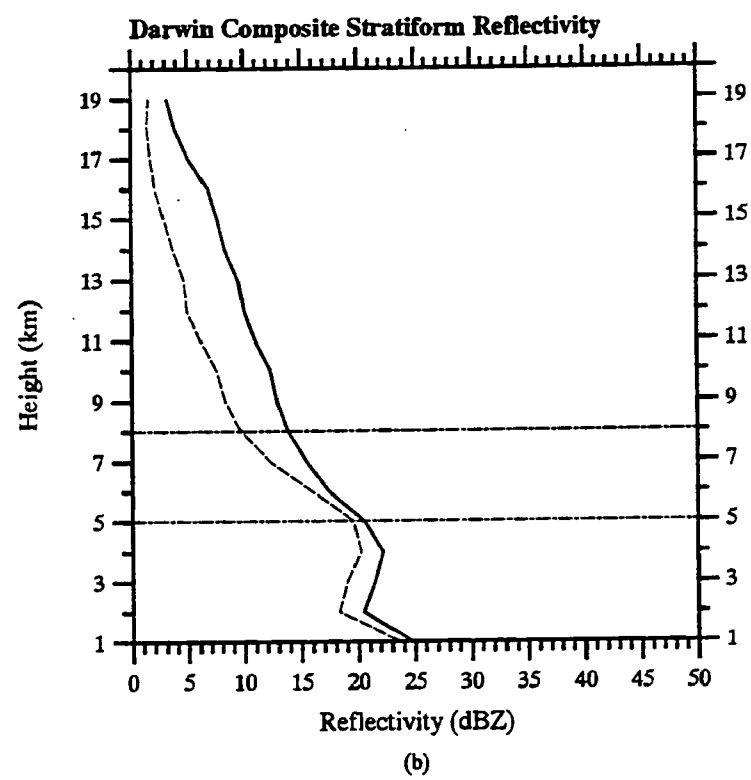


Fig. 5.2. Composite radar reflectivity profiles (*dBZ*) for the convective (a) and stratiform (b) regions of the break period (solid) and monsoon (dashed line) MCSs. The dashed horizontal lines indicate the approximate location of the mixed phase (-20° - 0°C) region. 166 (406) individual profiles were used to generate the break (monsoon) composite profile.

break composite is 3-4 dB higher than the monsoon reflectivity in this region, on average; however, it is not clear to what extent the difference may reflect the much larger sample of monsoon radar volumes compared to the break. Meteorologically, the monsoon (maritime) environment might be expected to produce higher low-level reflectivities compared to the break (continental) due to the larger and fewer CCN (Cloud Condensation Nuclei) in the maritime regime and resulting higher rates of collision-coalescence growth. However, the larger low-level updrafts in the break MCSs (presented in Ch. 4 and also discussed below in Sec. 5.3) are expected to more than off-set the effect of smaller initial particle sizes, based on numerical simulation results (Young 1993).

In the mixed phase region (approximately the region with temperatures of 0° to -20°C), extending from the melting level to ~ 3 km above the 0° C isotherm, the monsoon and break period convective composites show different gradients with the monsoon reflectivity decreasing approximately 4 dB $km^{-1}$ and the break period decreasing at about 3 dB $km^{-1}$ (Fig. 5.2). The higher reflectivity gradient in the monsoon convective profile is consistent with previous results from Rutledge et al. (1992), Williams et al. (1992), and Zipser and Lutz (1994) for selected convective cells in Darwin area convection. In the Zipser and Lutz study, the monsoon vertical reflectivity gradient between 0° and -20°C was approximately double the corresponding break period reflectivity gradient. The difference is easily explained due to the relatively small number of convective cells used in the Zipser and Lutz study (i.e., 41-44 individual cells) compared to this analysis (166-406 radar *volumes*, each with numerous convective cells used in the compositing) as well as differences in the partitioning of stratiform and convective features in volumes of radar data.

Independent of the actual vertical reflectivity gradients, the monsoon profile indicates a relatively rapid reflectivity decrease above the melting layer compared to the break period composite. The results are consistent with previous interpretations for nearly complete glaciation and a paucity of large particles above the melting level in the majority oceanic convective cells (Zipser et al. 1981; Szoke et al. 1986; Jorgensen and LeMone 1989; Rutledge et al. 1992; Williams et al. 1992; Zipser and Lutz 1994). Moreover, in-situ microphysical observations in hurricane convective clouds have documented high concentrations of small ice particles and the near absence of large graupel or supercooled raindrops at temperatures as warm as -2° to -5°C (Black and Hallett 1986).

These results are not surprising, given the relatively narrow region of virtual temperature excess documented in the monsoon systems compared to the break period (Fig. 5.1) and the corresponding weak (on average) vertical air motions sampled by the wind profiler in monsoon convection (Fig. 4.29) in this study. The weak vertical air motions in the lower to middle troposphere of tropical oceanic convection has been documented previously by LeMone and Zipser (1980), Jorgensen and LeMone (1989), and Lucas and Zipser (1994) using aircraft penetration data.

The monsoon and break period stratiform composites (Fig. 5.2) are similar, with maximum reflectivity occurring in the region below the 0°C isotherm and the profiles decreasing above and below this region. Above the freezing level, the stratiform composite profiles are similar to their convective counterparts (Fig. 5.2) and are consistent with ice particle growth by deposition and aggregation occurring just above the melting layer (Leary and Houze 1979b; Rutledge and Houze 1987). Similar results were documented by Szoke et al. (1986) for GATE MCSs and selected hurricanes. Direct measurements in tropical MCSs from aircraft during MONEX at the 7-8 km

level indicated ice particle growth by vapor deposition and minimal amounts of liquid water (Churchill and Houze 1984; Houze and Churchill 1984). These results suggest that ice predominates above the melting level in both the monsoon and break period stratiform regions.

### 5.3 Vertical air motion

Composite profiles of vertical air motion for the monsoon and break regimes are shown in Fig. 5.3. Each profile was constructed by averaging all of the vertical air motion data from each regime for the convective and stratiform regions. All of the composite profiles exhibit large variance, with variability on the order of the mean values. The large variability reflects the small scale variations that were sampled by the profiler in each of the MCSs.

In the convective region, large differences in the updraft profiles occur in the lower troposphere near the melting level, where the break period composite shows about twice the ascent compared to the monsoon, and in the upper troposphere where the monsoon composite is much larger than the corresponding break period profile. The differences in the lower troposphere reflect the presence of the low level updraft peak evident in the break regime squall lines (Fig. 4.14). The low-level peak was associated with convective elements forming along the leading edge of the convective line in each case. This low-level upward motion evidently drove a warm rain coalescence process which was responsible for brief, but yet heavy rain rates (e.g., Fig. 4.8).

In contrast, this low-level vertical motion peak was usually absent in the monsoon systems sampled by the profiler (Fig. 4.29). The difference is consistent with the composite thermal buoyancy profiles (Fig. 5.1) which indicate that the break period MCSs had a greater positive lapse rate and larger magnitude of virtual temperature excess over their environment in the region

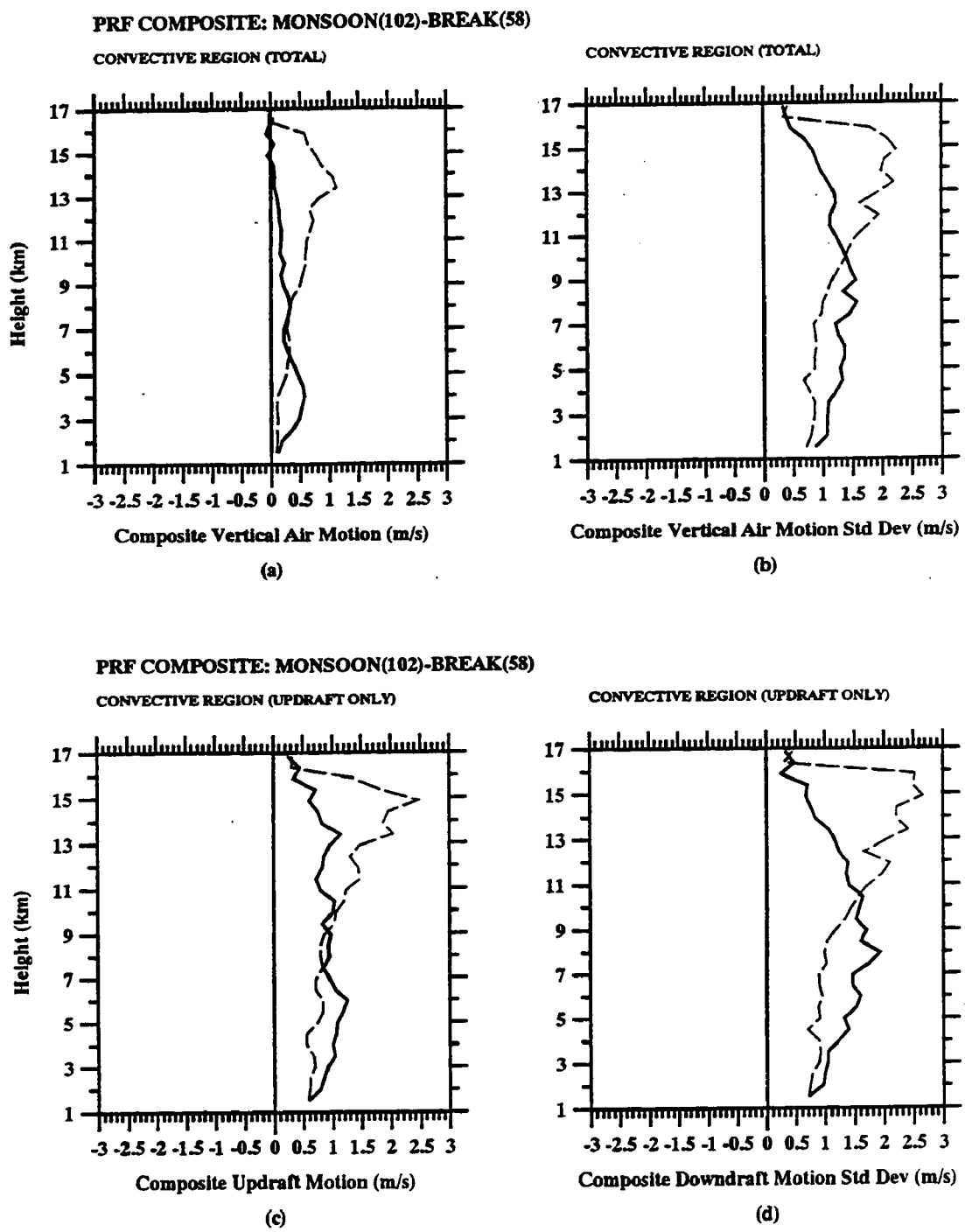


Fig. 5.3. Composite vertical air motion and standard deviation profiles (m $s^{-1}$) for the break (solid line) and monsoon (dashed line) partitioned into convective region net [(updraft and downdraft); a and b], convective region updraft (c and d), convective region downdraft (e and f), and stratiform region total (g and h). The number of profiles composited in the convective and stratiform regions is indicated at the top of the left column plots.

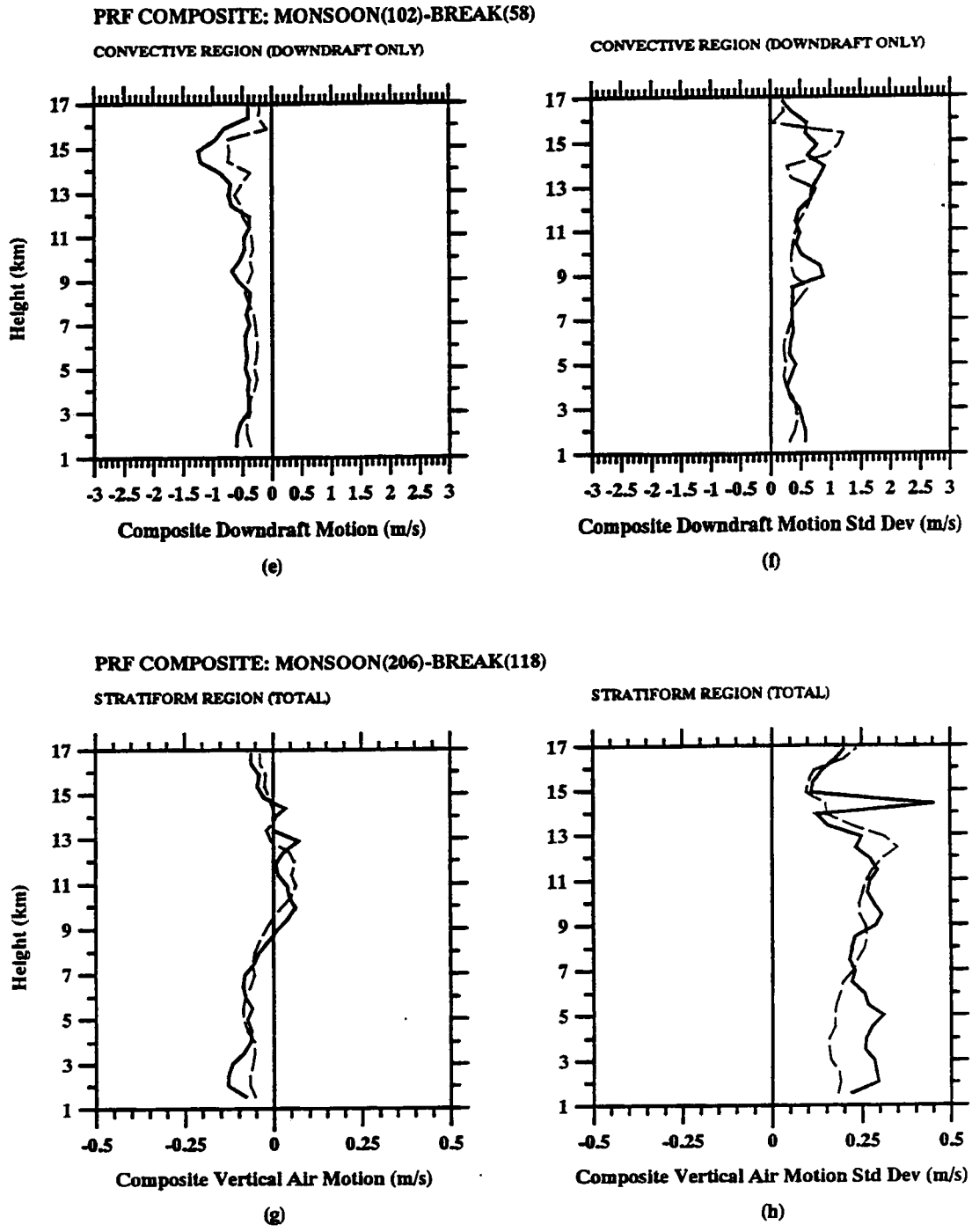


Fig. 5.3. (*continued*).

extending from 2 km to above the 0°C isotherm, compared to the monsoon MCSs. As noted in Ch.4, the reduced thermal buoyancy suggests that water loading would have a proportionally greater impact on the total buoyancy of monsoon convective cells. Since total buoyancy is related to the vertical acceleration of the wind, it is expected that parcels rising in the break period environment would achieve larger vertical air motions in this region, all other factors being equal.

The differences between the monsoon and break period updraft composites are also consistent with the radar reflectivity profiles presented in Fig. 5.2 which show smaller convective region vertical reflectivity gradients in the mixed phase region of the break period MCSs compared to the monsoon MCSs. The electrification results of Rutledge et al. (1992), Williams et al. (1992), and Petersen (1992) documented increased electrical activity (i.e., substantially greater lightning flash rates) in the break period compared to the monsoon. The increase in electrical activity is thought to be a consequence of a precipitation-based non-indicative charging mechanism, whereby small ice particles and graupel separate charge in the presence of supercooled liquid water. In order to facilitate the charge separation, relatively large vertical drafts are necessary to carry supercooled drops above the melting level into the mixed phase region of the cloud, aiding the onset of the ice phase via drop freezing, and providing for supercooled cloud droplets via condensation .

In the middle to upper troposphere, the break period composite shows relatively constant ascent, due to the variability in the vertical structure of trailing deep updraft cores sampled by the wind profiler. The upper level ascent was associated with deep, mature convective elements behind the leading edge of each squall line. Precipitation processes in these deep updrafts evidently were associated with mixed phase processes, based on vertical radar reflectivity profiles.

The composite monsoon convective updraft profile shows vertical air motion increasing from the middle troposphere to the vicinity of the tropopause. The large magnitude of upper level ascent in the monsoon composite is biased by the large drafts sampled in the 910109 and 901210 events; however, as noted in Ch. 4, many of the monsoon MCSs exhibited peak vertical motions in the upper troposphere (Fig. 4.29). Similar profiles showing large vertical air motion well above the freezing level have been observed in other tropical MCSs and will be discussed in Ch. 6.

The differences in the convective region updraft composites in the upper troposphere are not evident in the thermal buoyancy profiles (Figs. 5.1 and 5.3). As noted in Ch. 4, the results suggest that the soundings may not have been entirely representative of the environment supporting the sampled MCS convective activity, the sampling of the upper level peak updraft in the break regime cases may have been biased by lifecycle effects, and/or that the resulting vertical air motion structure is not a consequence of thermal buoyancy forcing alone.

In contrast to the convective updraft profiles, the monsoon and break period convective downdraft composites (Fig. 5.3) are similar with the largest downdrafts occurring near the tropopause and relatively constant subsidence through the troposphere. As argued by Heymsfield and Schotz (1985) and others and discussed in Ch. 4, the peak downward motion is consistent with deep updrafts converging on the tropopause stable region and being forced to ascend through mass balance constraints. Because of the similarities in the convective downdraft composites, the differences in the total convective profiles is, to a large extent, determined by the differences in the updraft profiles (Fig. 5.3).

In Fig. 5.4a and b, the composite vertical air motion results are presented in histogram [CFAD(Contoured Frequency by Altitude Diagram; Yuter and Houze 1995)] format for the

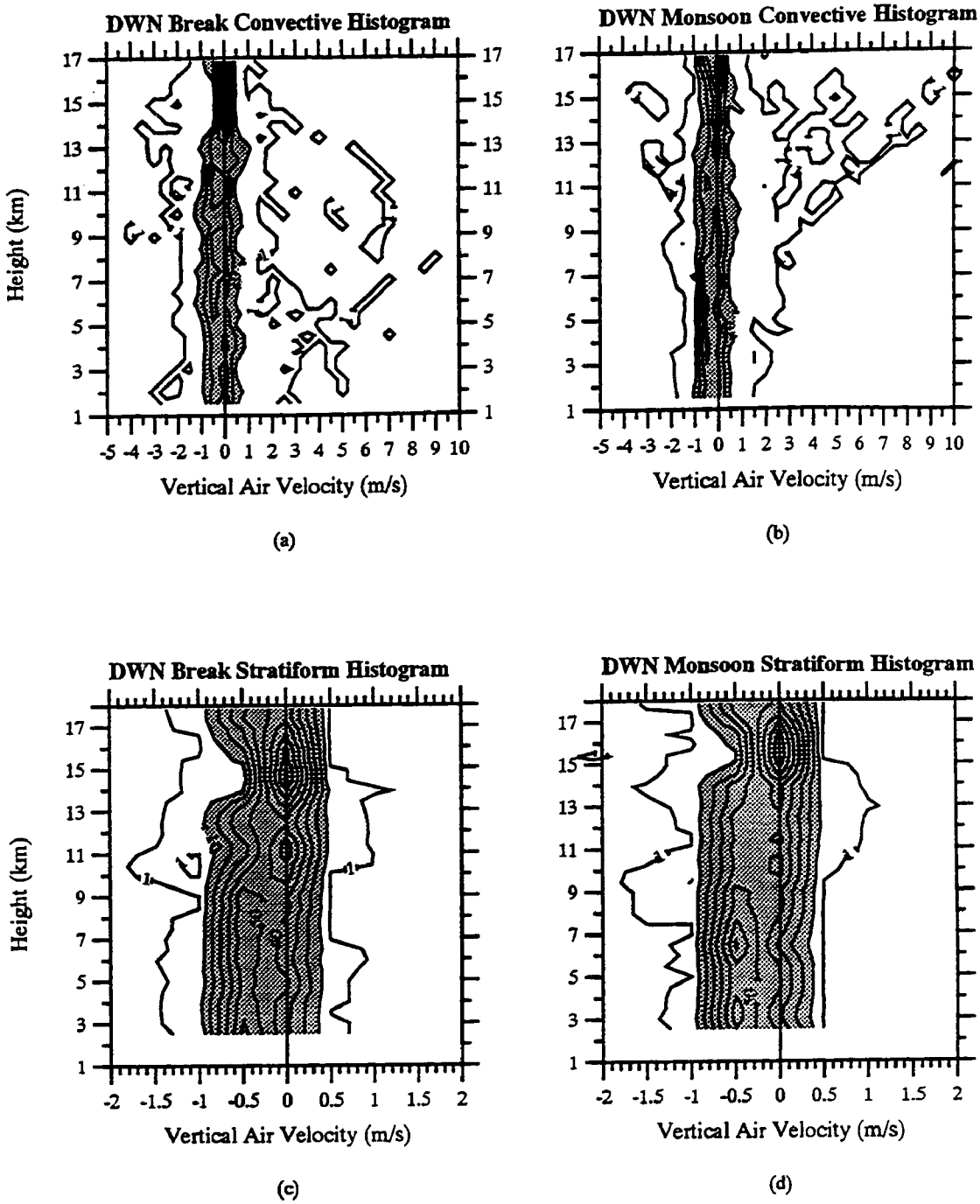


Fig. 5.4. Histogram (CFAD) of composite vertical air motion for the convective (a and b) and stratiform (c and d) regions. These plots show the vertical air motion relative frequency of occurrence (%) as a function of height. The left (right) column represents the break (monsoon). Relative frequency of occurrence is contoured at intervals of 1,10,20,30,40, etc. with shading for values ≥ 10%.

convective region of the break and monsoon MCSs. The contours in these plots represent the relative frequency of occurrence of the vertical air motion estimates as a function of height. As Fig. 5.4a and b show, the bulk of the vertical air motion distributions sampled by the profiler in each regime are similar with most of the estimates centered at small negative values. The major difference in the monsoon and break convective histograms is the vertical distribution of the largest updrafts (i.e., $\leq$ 1% frequency of occurrence). In the monsoon (Fig. 5.4b), updrafts exceeding 3 m $s^{-1}$ occur only above 8 km whereas these drafts show a distinct low-level, as well as a middle to upper troposphere peak, in the break regime

The monsoon and break period stratiform composite profiles are similar, with generally weak motion through the troposphere (Fig. 5.3). The profiles show the characteristic superposition of low-level downward motion and upper level ascent; however the crossover height is displaced several kilometers above the melting level. The frequent occurrence of relatively deep downward motion in the monsoon and break stratiform regions is revealed in the corresponding histogram plots (Fig. 5.4c and d). As discussed in Ch. 6, the elevated crossover level is somewhat anomalous compared to the results from many previous studies. Both profiles also show downward motion above about 14.5 km. This subsidence in the vicinity of the tropopause has also been documented in many previous studies of tropical and middle latitude events (Johnson and Young 1983; Balsley et al. 1988; Carter 1991; Johnson et al. 1990; Gallus and Johnson 1991; Lin and Johnson 1994). Houze (1989) suggested that the descent may be due to strong divergent outflow from the tops of MCSs.

## 5.4 Partitioned network rain trace results

Summaries of the rainfall statistics for each of the break period and monsoon MCSs are provided in Tables 5.1 and 5.2, respectively. For the squall line MCSs examined herein, the contribution of stratiform rain to the total MCS rainfall was small, ranging from 10-26% (18% on average), indicating that the vast majority of the recorded rainfall was associated with the passage of convective features over the rain gauges. These results are in agreement with Simpson et al. (1993) who examined rainfall contributions from MCSs occurring over Melville and Bathurst Islands (i.e., "Hector") using a *Z-R* relationship in conjunction with a least-bias adjustment from a network of rain gauges. The results are also similar to Rosenfeld et al. (1995a), who applied objective criteria to scanning radar data in order to classify convective and stratiform precipitation in different rain regimes over rain gauges near Darwin. In both studies, the majority of rainfall was associated with convective features (92% for island storms and 87% for continental squall lines), similar to results presented herein.

Table 5.2 indicates that the relative fraction of stratiform rainfall in the monsoon events is higher than the break period fraction and ranged from 18-37% (29% on average), in agreement with the results of Rosenfeld et al. (1995a) for monsoon convection as well as recent precipitation estimates for the COARE domain (T. Rickenbach, personal communication); however, the monsoon stratiform fraction is on the lower end of many previous estimates (30-50%) of tropical oceanic stratiform precipitation (Houze 1977; Gamache and Houze 1983; Churchill and Houze 1984; Houze and Rappaport 1984; Leary 1984). Much of the difference may be explained by the fact that these previous studies utilized a single *Z-R* relation for both the convective and stratiform components.

Table 5.1. Rainfall statistics for the six break period events using all available rain gauges from the Darwin network. The rain traces were sub-divided into convective and stratiform components using the partitioning algorithm described in Ch.2.

| Event (yymmdd) | # Gauges Available | Convective Rain (%) | Stratiform Rain (%) | Convective Rain Intensity (cm $d^{-1}$) | Stratiform Rain Intensity (cm $d^{-1}$) | Maximum Rain Intensity (mm $hr^{-1}$)* |
|---|---|---|---|---|---|---|
| 891205 | 22 | 79 | 21 | 36.0 | 6.1 | 147.6 |
| 900118 | 20 | 84 | 16 | 47.5 | 19.9 | 194.4 |
| 900122 | 20 | 87 | 13 | 27.7 | 5.9 | 70.8 |
| 900128 | 24 | 74 | 26 | 34.1 | 6.5 | 153.6 |
| 901121 | 15 | 90 | 10 | 39.3 | 4.9 | 90.0 |
| 901215 | 18 | 79 | 21 | 17.7 | 6.1 | 54.0 |
| ***Average*** | **20** | **82** | **18** | **33.7** | **8.2** | **118.4** |

* Maximum for any reporting gauge during the observation period based on rainfall accumulation over a 10 minute period

Table 5.2. Rainfall statistics for the seven monsoon events using all available rain gauges from the Darwin network. The rain traces were sub-divided into convective and stratiform components using the partitioning algorithm described in Ch.2.

| Event (yymmdd) | # Gauges Available | Convective Rain (%) | Stratiform Rain (%) | Convective Rain Intensity (cm $d^{-1}$) | Stratiform Rain Intensity (cm $d^{-1}$) | Maximum Rain Intensity (mm $hr^{-1}$)* |
|---|---|---|---|---|---|---|
| 900110 | 24 | 82 | 18 | 24.0 | 7.2 | 81.6 |
| 900112 | 26 | 77 | 23 | 17.5 | 5.5 | 88.8 |
| 901210 | 21 | 70 | 30 | 20.1 | 7.6 | 98.4 |
| 901212 | 22 | 63 | 37 | 22.1 | 14.1 | 110.4 |
| 910109 | 19 | 65 | 35 | 25.3 | 13.6 | 100.8 |
| 910129 | 18 | 68 | 32 | 15.1 | 4.9 | 46.8 |
| 910130 | 17 | 75 | 25 | 22.5 | 8.5 | 64.8 |
| ***Average*** | **21** | **71** | **29** | **20.9** | **8.8** | **84.5** |

* Maximum for any reporting gauge during the observation period based on rainfall accumulation over a 10 minute period

Recent work by Short et al. (1993) and Rosenfeld (1995b), using surface disdrometer and scanning radar data respectively, have shown that the *Z-R* relationships for convective and stratiform rain are quite different, such that a given reflectivity is matched to nearly half the rain intensity in stratiform rain as compared to convective rainfall. Rosenfeld et al. suggest that the previous studies of tropical oceanic MCSs may have overestimated the relative contribution of stratiform rainfall volume by a factor of approximately two. In any case, the important point is that, although monsoon MCSs occurring near Darwin are characterized by large areas of stratiform cloud, the vast majority of rainfall in these systems appears to be associated with convective bands embedded within those stratiform areas.

The maximum recorded rainfall intensity for the break period was quite variable, ranging from ~ 50-200 mm $hr^{-1}$ and about 40% larger than the corresponding monsoon maximum rainfall intensity on average (Tables 5.1 and 5.2). The results are consistent with the highly convective nature of the squall lines within the break regime. The difference in monsoon and break period rainfall intensities is more apparent when comparing the average convective and stratiform rain intensities for each event (Tables 5.1 and 5.2) and plotting the results (Fig. 5.5). While acknowledging the small number of samples used in this study (i.e., 13 events), Fig. 5.5 would seem to suggest that the break period and monsoon regimes are distinguishable in terms of rainfall characteristics (e.g., rainfall intensity), similar to the results of Rosenfeld et al. (1993).

The rain gauge network data were also scrutinized in order to determine if the bi (multi) modal precipitation peak sampled by the Berrimah gauge in the convective portions of the squall line (break regime) MCSs was also present at other locations along the same convective line. The

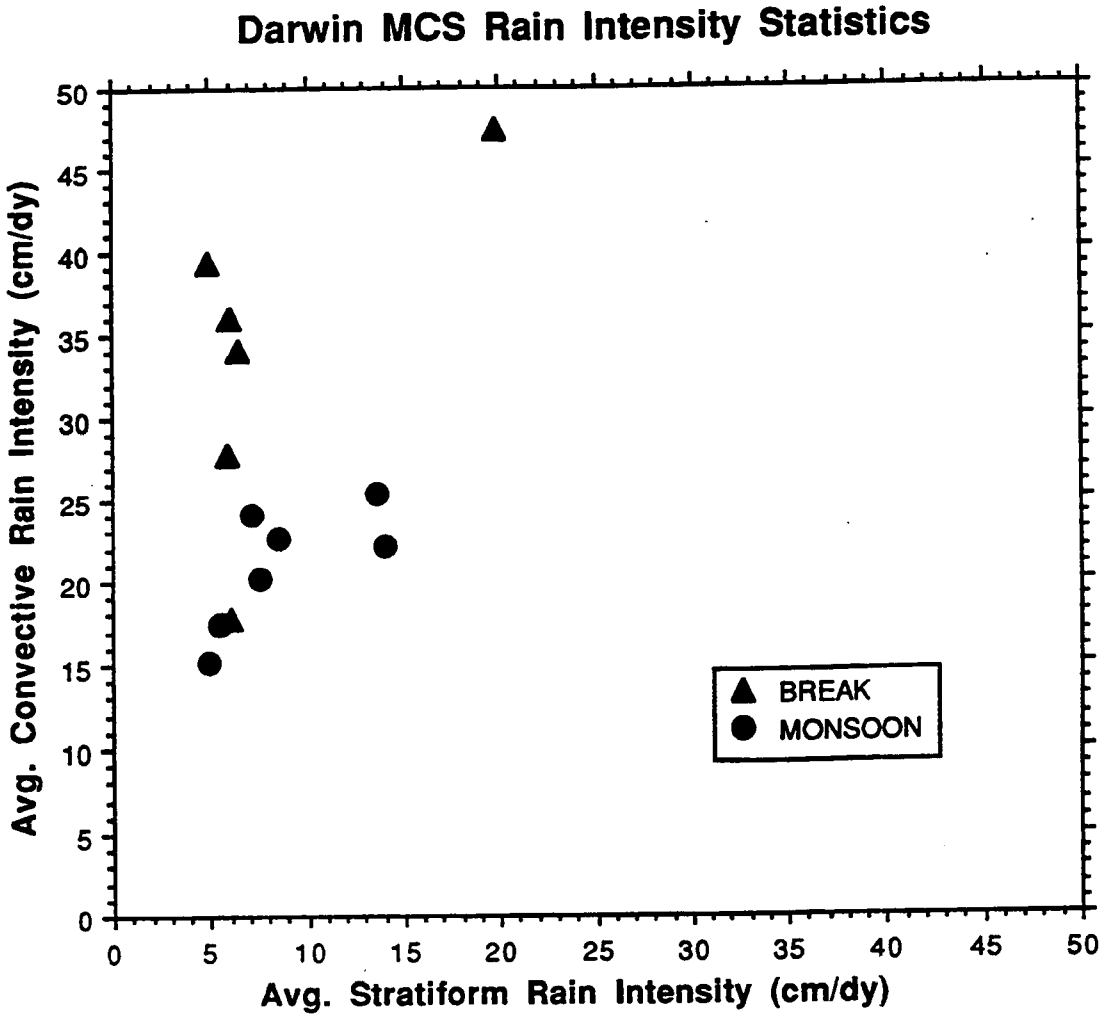


Fig. 5.5. Average convective rain intensity as a function of average stratiform rain intensity (cm $dy^{-1}$)for each of the MCS events. The rainfall statistic data were derived from the Darwin area rain gauge network and are summarized in Tables 5.1 and 5.2.

results indicated that the vast majority of the gauges showed a distinct bi or multi-modal rainfall peak(s) separated in time by 10-30 minutes (Appendix D). Moreover, in most cases the first peak (in time) had the largest magnitude of rainfall intensity. The results support the notion that these MCSs were multicellular and also suggest that warm rain coalescence processes, characteristic of the first rainfall peak, played a significant role in contributing to the total surface rainfall (and therefore latent heating) produced by the systems.

## 5.5 Apparent heat source and moisture sink

Composite profiles of the normalized apparent heat source ($Q'_1$) and moisture sink ($Q'_2$) variables for the convective and stratiform components of the monsoon and break period regimes are shown in Fig. 5.6[3]. The composites were generated by averaging the individual profiles from each event (not shown), based on the application of Eqs. 2.12 and 2.13. As discussed in Ch. 2, this methodology assumes that the vertical advection terms in the budget equations produce the dominant forcing (see Eqs. 1.1 and 1.2). Also, the results were normalized according to the average rainfall characteristics for each regime (Tables 5.1 and 5.2) in order to facilitate comparison with previous studies (discussed in Ch.6).

In the convective region, the monsoon and break period profiles are off-set from each other in the vertical due to the differences in their corresponding vertical air motion profiles (Fig. 5.3). In the break period regime, the peak diabatic heating occurs in the vicinity of 2-3 km ($\sim$4-4.5°C $dy^{-1}$ / cm $dy^{-1}$), reflecting the consistent low-level vertical air motion peak along the leading edge in the squall line MCSs and emphasizing the important role of the collision coalescence

---

[3] Transition zone $Q_1$ and $Q_2$ profiles were not constructed since this storm region category was only identified in 4 of the squall line MCSs.

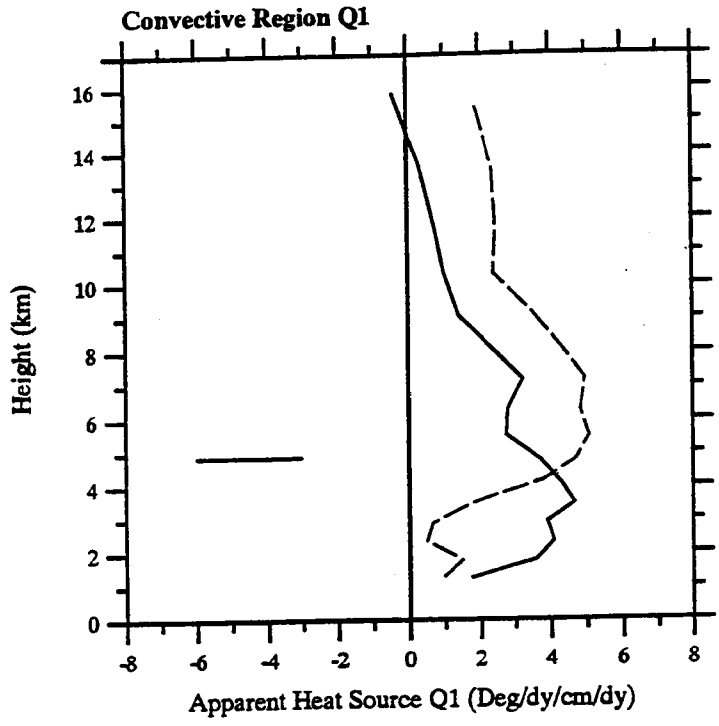


(a)

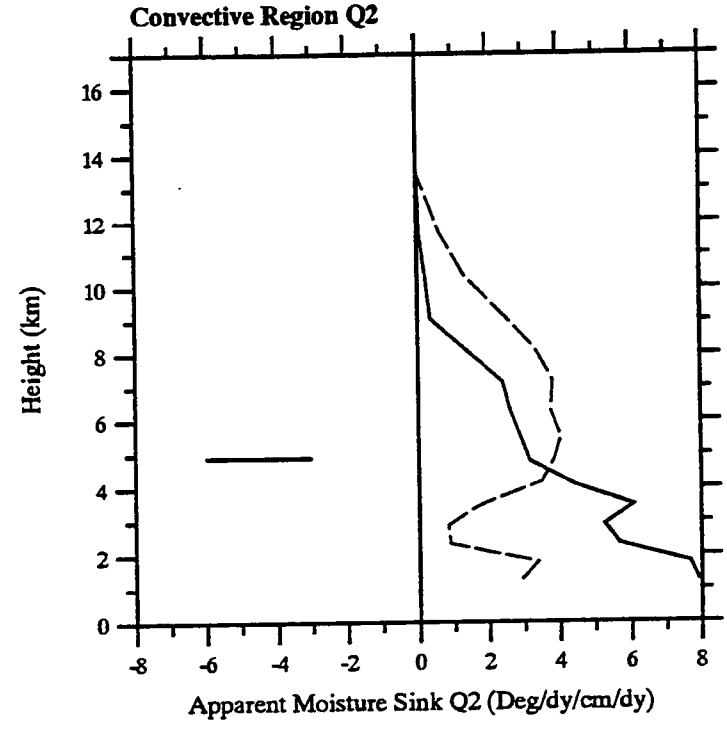


(b)

Fig. 5.6. Normalized composite profiles of (a) convective region apparent heat source ($Q'_1$), (b) convective region moisture sink ($Q'_2$), (c) stratiform region apparent heat source ($Q'_1$), and (d) stratiform region moisture sink ($Q'_2$) for the break (solid line) and monsoon (dashed line) regimes. Units are normalized to °C cm$^{-1}$ using the rainfall statistics in Tables 5.1 and 5.2.

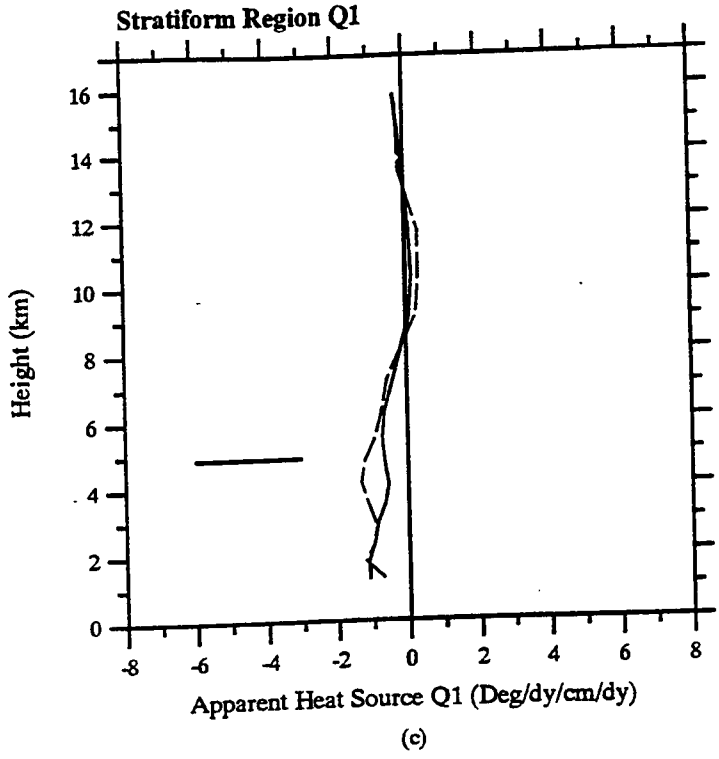


(c)

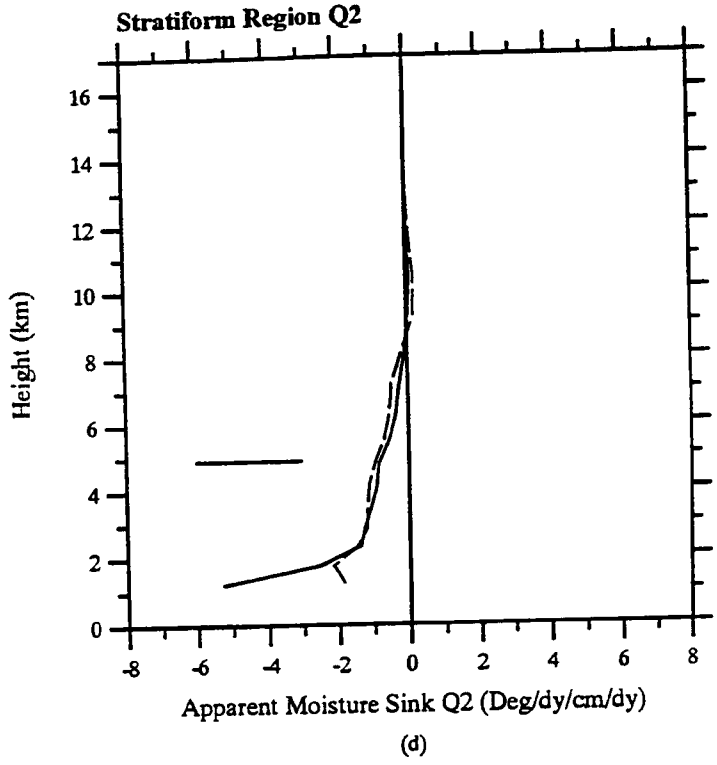


(d)

Fig. 5.6. (*continued*).

precipitation processes. A smaller heating peak is also present in the vicinity of 7 km corresponding to the occurrence of deeper trailing updrafts in the convective line. The corresponding break period $Q'_2$ profile shows peak convective drying ($\sim 8°C\ dy^{-1}$ / $cm\ dy^{-1}$) occurring below 2 km. The off-set between the break period convective heating and drying profiles is a consequence of the approximately linear decrease in dry static energy ($s$) with pressure as opposed to the exponential decrease of specific humidity ($q$). When deep convection is occurring, vertical eddy transports of $s$ and $q$ produce a separation between the $Q'_1$ and $Q'_2$ budget equations (Luo and Yanai 1984; Johnson 1984).

The monsoon convective $Q'_1$ profile (Fig. 5.6) indicates peak diabatic heating between 5-7 km ($\sim 5°C\ dy^{-1}$ / $cm\ dy^{-1}$), several kilometers higher than the corresponding break period profile. The elevated position is a consequence of the higher peak vertical air motion in the monsoon composite compared to the break period (Fig. 5.3). Also, there is no off-set between the monsoon $Q'_1$ and $Q'_2$ profiles as was observed in the break period composites. This is due to the fact that the monsoon convective vertical air motions are small in the lower troposphere where the vertical gradient of $q$ is large (see Eq. 1.2 and Fig. 5.3). The resulting lack of off-set would seem to suggest that the monsoon convective vertical air motion composite (Fig. 5.3) sampled by the wind profiler is not representative of deep convection (Luo and Yanai 1984).

As expected, the stratiform $Q'_1$ and $Q'_2$ profiles for the monsoon and break period composites are in close agreement, reflecting the similar vertical air motion structure in the stratiform region (Figs. 5.3 and 5.5). The profiles show relatively small cooling ($\leq 1°C\ dy^{-1}$ / $cm\ dy^{-1}$) in the lower troposphere, slightly off-setting the convective region heating, and in the vicinity of the tropopause. Negligible heating occurs in the upper troposphere as a consequence of the weak, shallow updrafts in the stratiform region. The corresponding stratiform $Q'_2$ profiles show

moistening below about 8 km with negligible drying in the upper troposphere. The results of Fig. 5.6 indicate that the stratiform portion of these Darwin MCSs plays a relatively minor role, except possibly at the lowest levels, in the diabatic heating and moistening of the environment.

# Chapter VI

# COMPARISON OF DARWIN RESULTS TO OTHER GEOGRAPHICAL REGIONS

This chapter provides a comparison of the Darwin wind profiler composite results described in Chapter 5 to previous analyses from other tropical and middle latitude regions. The results are described in terms of similarities and differences of the MCS vertical air motion and diabatic heating fields for the convective and stratiform regions. Because of the different observational techniques employed in the variety of previous studies, only qualitative comparisons can be made.

## 6.1 Vertical air motion

### 6.1.1 Multiple Doppler analyses in COARE

In this section, vertical air motion and radar reflectivity results are presented from a total of 4 COARE MCSs in which multiple Doppler radar data were analyzed. Three of the events were sampled by the P-3 aircraft (930209, 930221, 930222) and one was sampled by the ship-based radars (930209[4]). The P-3 and ship-based analyses on 930209 are hereafter referred to as 930209P and 930209S, respectively. The radar reflectivity and vertical air motion fields were partitioned into convective and stratiform components based on the methodology described in Ch. 2.

---

[4] The aircraft and ship-based radars sampled separate MCSs on 930209.

The COARE multiple Doppler data consists of 15 volumes of ship dual-Doppler analyses on 930209S and 4 volumes of P-3 quad Doppler data for each of the 930209P, 930221, and 930222 events. Since a relatively large number of radar volumes were collected and processed on 930209S, a time-series of partitioned horizontal divergence, vertical air motion, and radar reflectivity was constructed in order to show the evolution of this MCS during the approximately 2.5 hours it was sampled by both ship radars operating in dual-Doppler mode. The time height cross sections are shown in Fig. 6.1.

The 930209S MCS formed southwest of the MIT radar from a series of small, linear convective bands (Cifelli et al. 1994a). The bands later consolidated into a single line of convection oriented roughly parallel to the low-level shear. The system continued to grow in the along-line direction during the observation period, reaching over 400 km in length by 12 UTC. A trailing precipitation region was noted to develop in the latter stages of the dual-Doppler sampling period. In Fig. 6.1, the convective portion of the 930209S MCS shows two pulses of activity, with the first occurring near 1000 UTC and the second near 1130 UTC. Moreover, the peak vertical air motions and upper level divergence shift from near 10 km in the first pulse to near 13 km in the second pulse (Fig. 6.1a and b). Throughout the observation period, the convective region reflectivity profile showed the largest reflectivities restricted to the lower troposphere with a sharp gradient near the 0°C isotherm (Fig. 6.1c). The relatively weak vertical air motions and reflectivity structure are consistent with previous investigations of tropical oceanic convection (as discussed in Ch. 5) and with visual observations indicating a lack of lightning in this MCS (Petersen et al. 1995). The divergence and vertical air motion patterns in Fig. 6.1a, b indicate that a persistent mesoscale updraft-downdraft couplet in the stratiform region did not develop until late in the observation period.

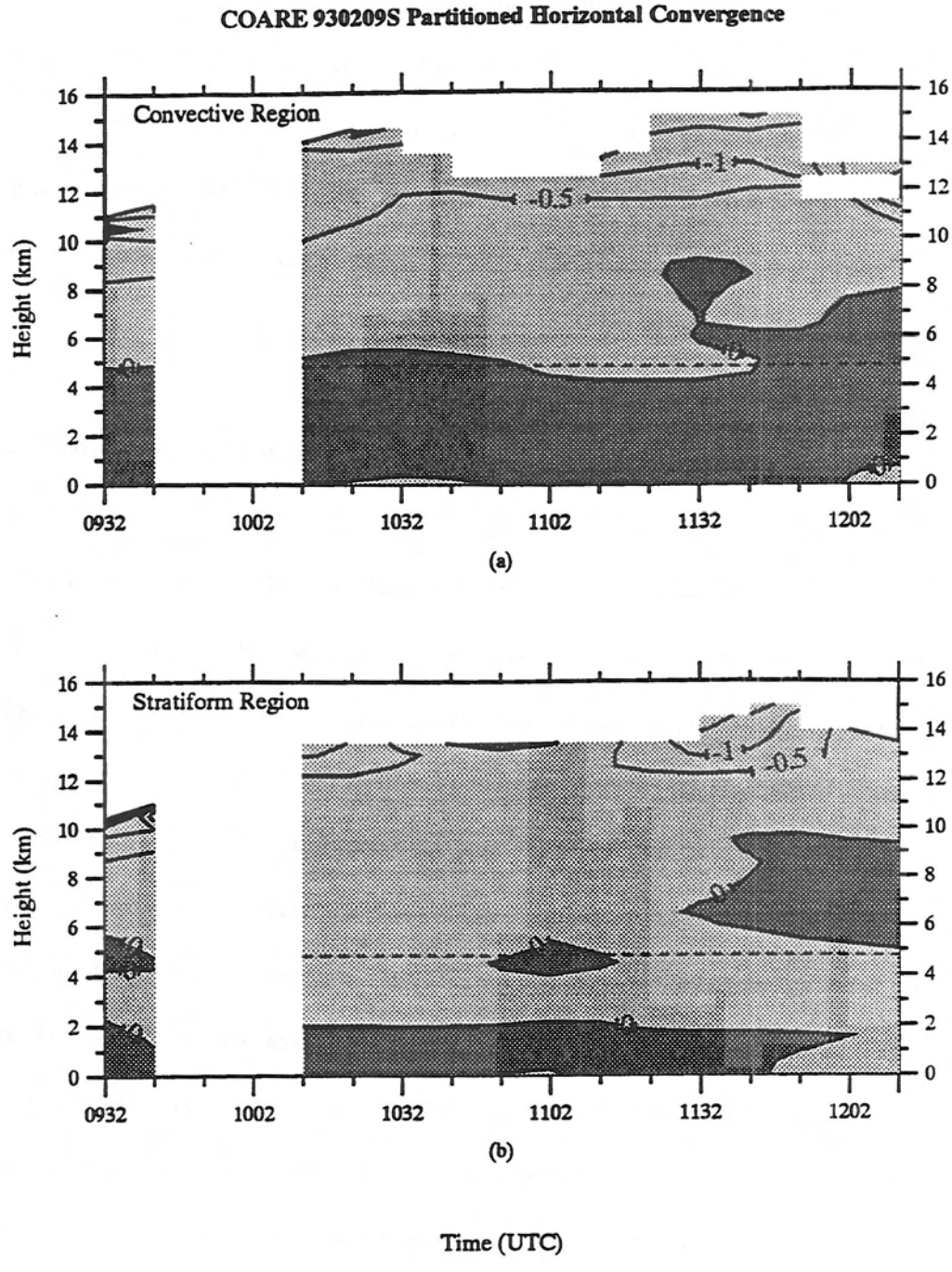


Fig. 6.1. Time-height cross section of partitioned horizontal divergence in $s^{-1}$ x $10^{-3}$ (a and b), vertical air motion in m $s^{-1}$(c and d), and radar reflectivity in *dBZ* (e and f) for the 930209S MCS. Dark (light) shading represents convergence (divergence) and upward (downward) motion . Gray shading in (c) corresponds to reflectivity scale in the middle of the plot. Plots (a), (c), and (e) are convective cross sections and (b), (d), and (f) are stratiform cross sections. The dashed horizontal line in each plot indicates the approximate height of the 0°C isotherm.

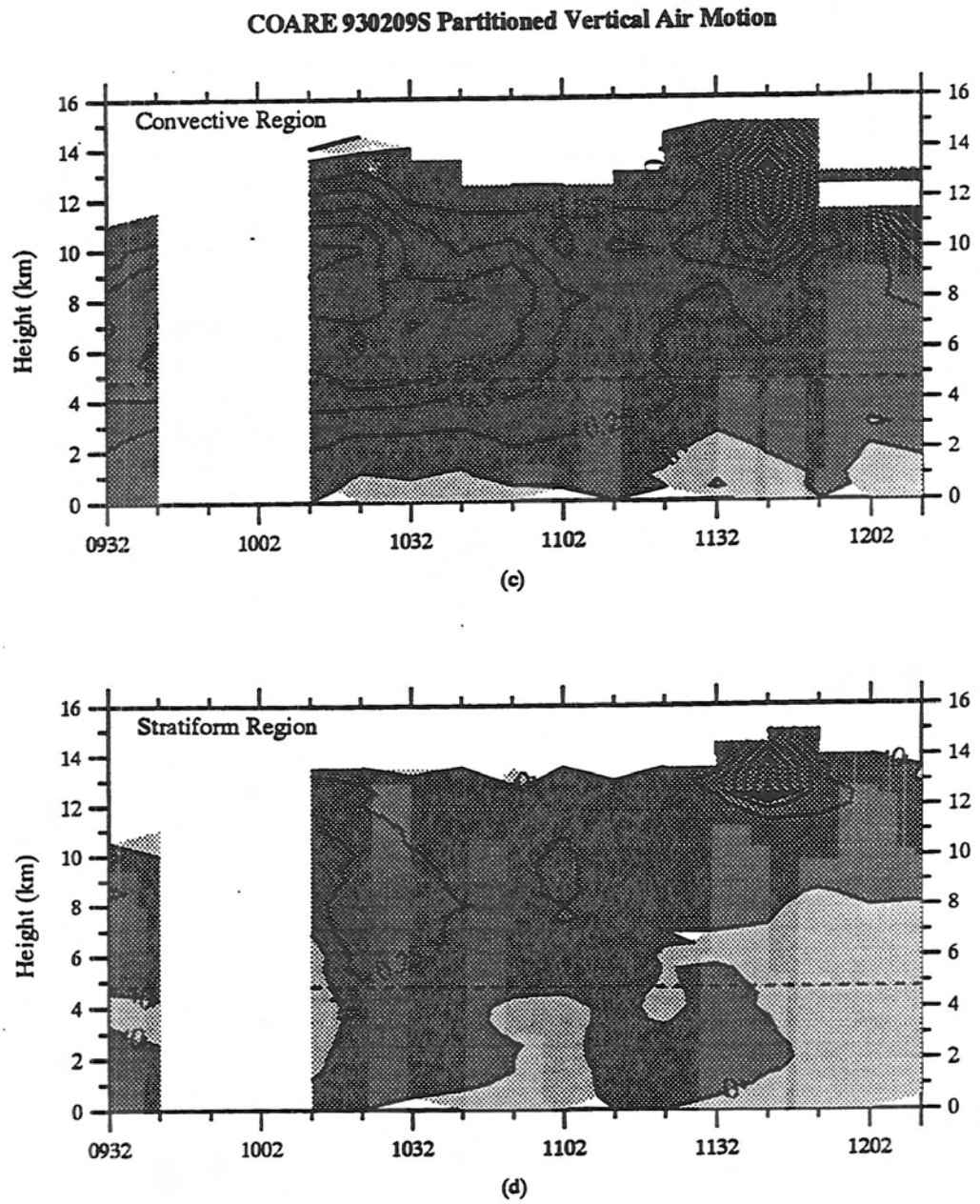


Fig. 6.1. (*continued*).

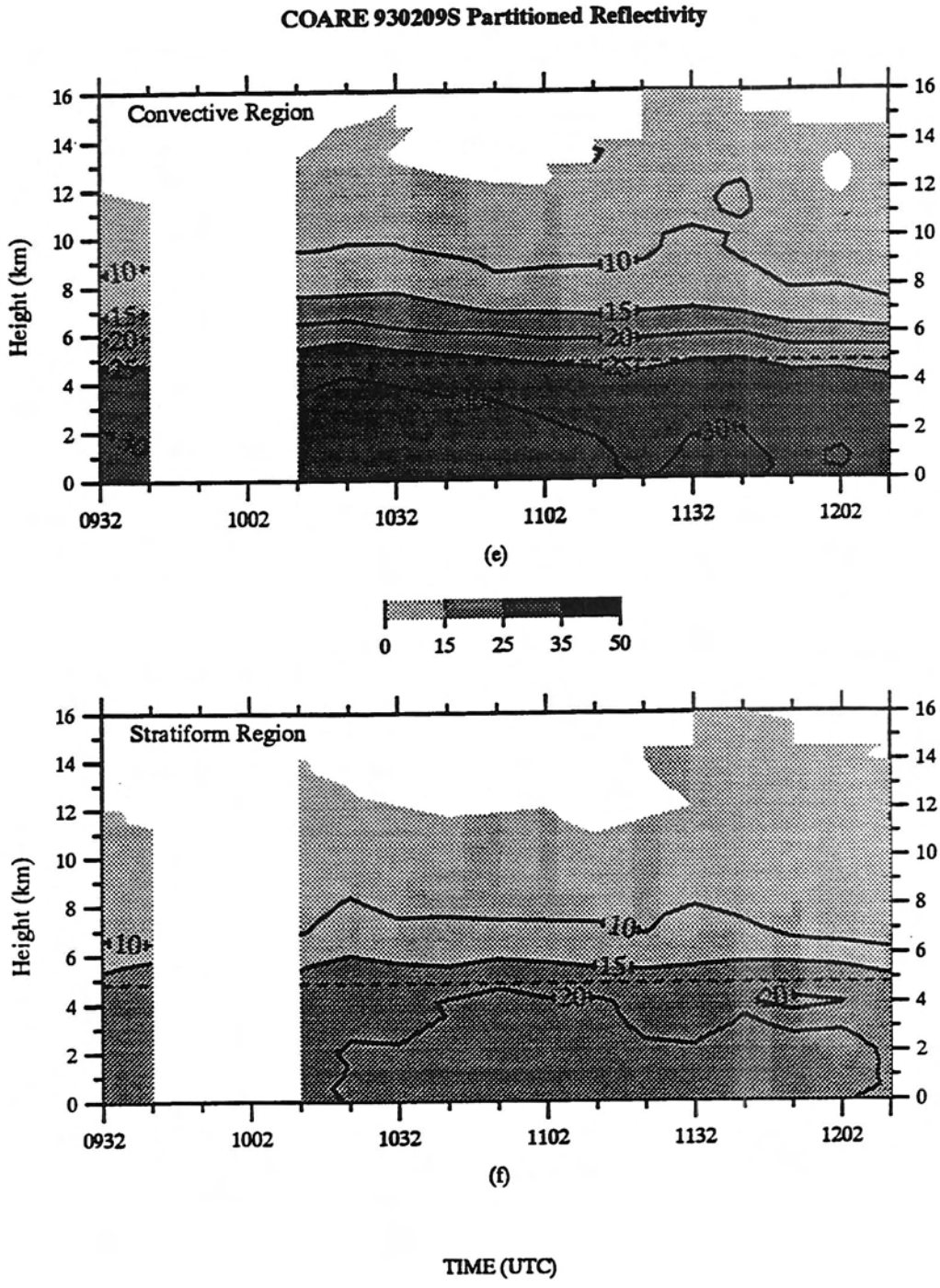


Fig. 6.1. (*continued*).

Composite vertical air motion results for each of the four COARE events analyzed with multiple Doppler techniques are shown in Fig. 6.2. For 930209S, the convective updrafts are rather weak with positive acceleration restricted to the lowest 4 km. The remaining 3 MCSs sampled by the aircraft were apparently more intense with convective updrafts attaining maximum values above 11 km, similar to many of the Darwin monsoon MCSs (Fig. 4.29), and exhibiting higher on average convective reflectivity profiles (Fig. 6.3) than 930209S. However, direct comparison of the ship and aircraft multiple Doppler results are complicated by the fact that the aircraft radar volumes were analyzed using the quad Doppler technique while the ship data employed the dual-Doppler method. As discussed in Sec. 2.2.2.2 and Appendix C, the quad Doppler technique should produce a more reliable estimate of the vertical wind since $W_p$ is measured directly at the top of the analysis domain.

The convective downdraft profiles in Fig. 6.2 show relatively good agreement among the four events with subsidence generally maximized near the top of the profiles. The pattern is consistent with dynamic induced convergence near the tropopause. Similar to the Darwin, the differences in the COARE total convective region composites is principally due to the variability in updraft structure. The stratiform region composite shows quite a bit of variability among the four events in the depth and magnitude of upper level ascent.

Composite profiles of vertical air motion and radar reflectivity for all of the COARE multiple Doppler analyses are shown, along with similar composite profiles from Darwin, in Figs. 6.4 and 6.5, respectively. Although detailed comparisons are hampered by the small number of COARE samples relative to Darwin (27 COARE vs. 58 Darwin break and 102 Darwin monsoon in the convective region and 27 COARE vs.118 Darwin break and 206 Darwin monsoon in the stratiform region), it appears that the COARE profile composites seem to have characteristics

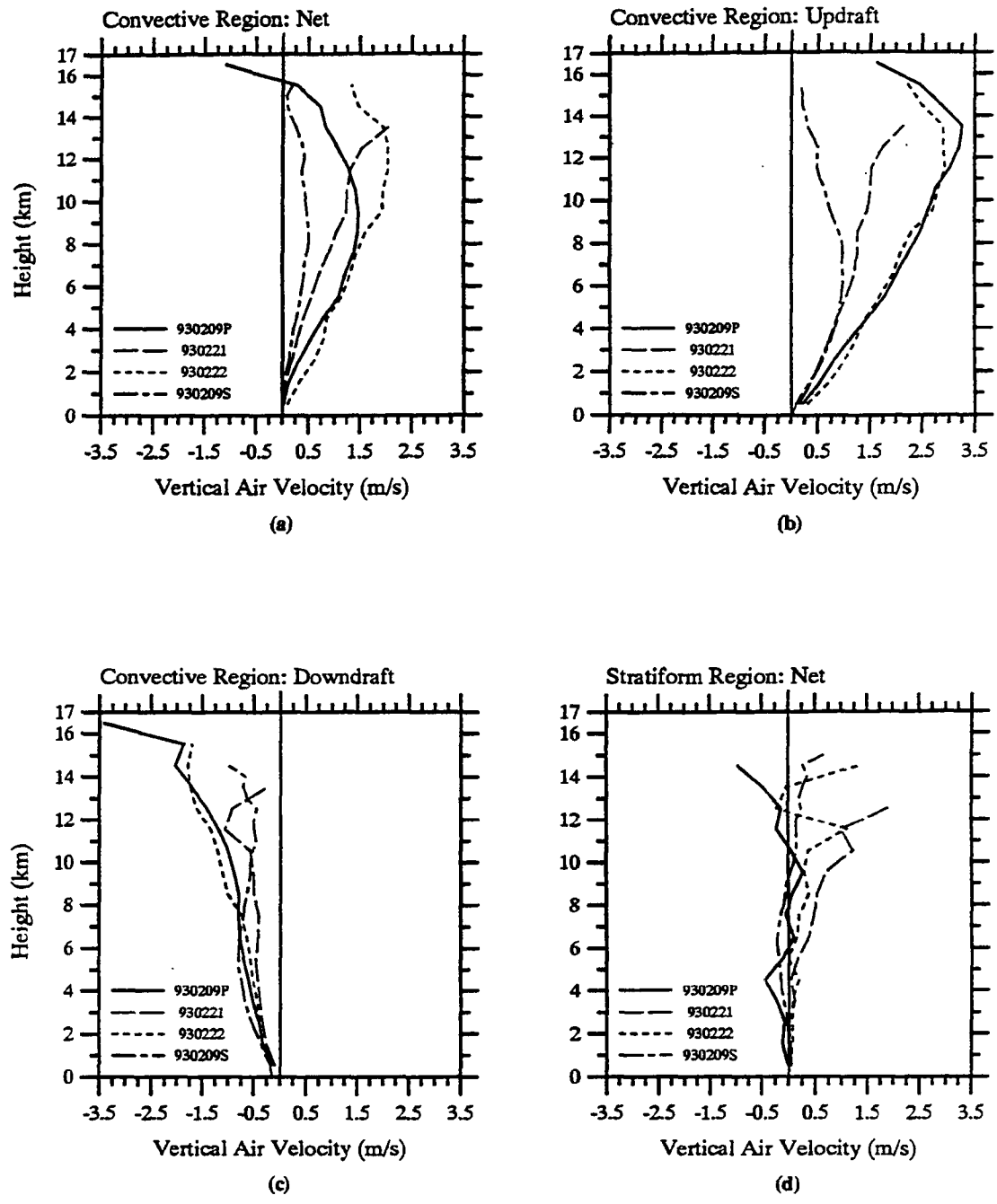


Fig. 6.2. Composite profiles of partitioned vertical air motion (m $s^{-1}$) for the four COARE MCSs analyzed with multiple radar data. Legend with line type corresponding to each MCS shown in the left corner of each plot. (a) Net (up and down drafts) convective region profiles, (b) convective updrafts, (c) convective downdrafts, and (d) net stratiform profiles.

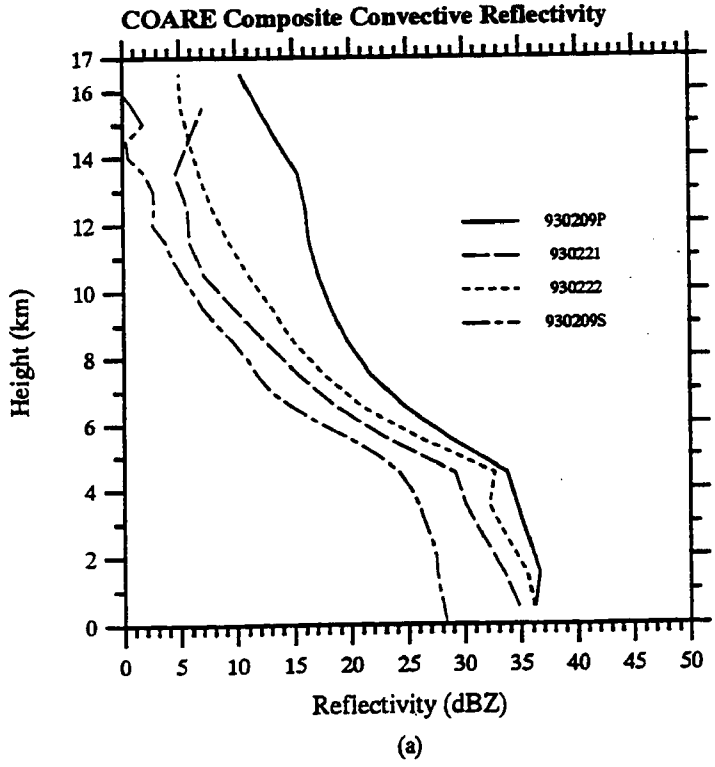


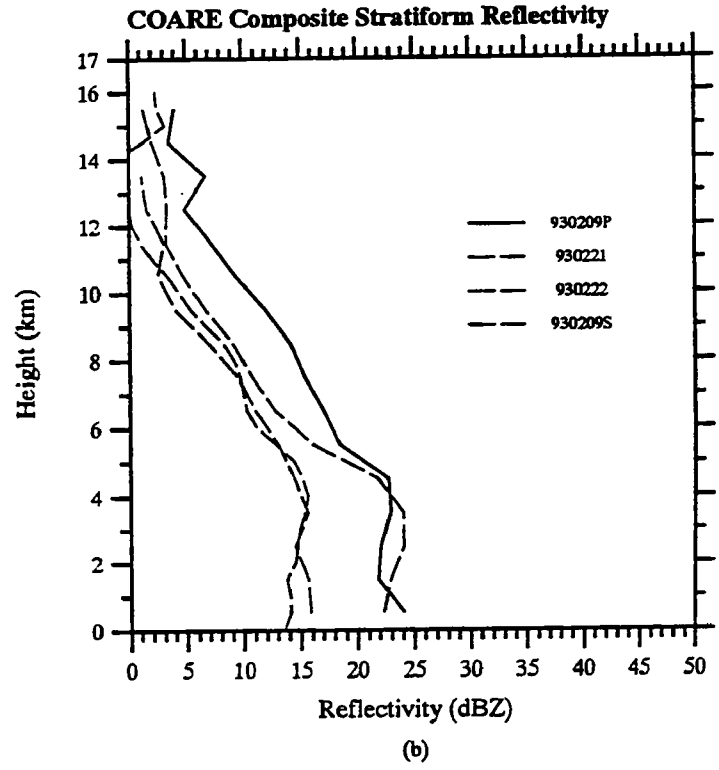


Fig. 6.3. Composite radar reflectivity profiles (*dBZ*) for the convective (a) and stratiform (b) regions of the four COARE MCS analyzed with multiple Doppler data. Legend with line type corresponding to each MCS is shown in the right portion of the plot. The profiles were constructed by averaging all of the partitioned radar volumes data for each MCS.

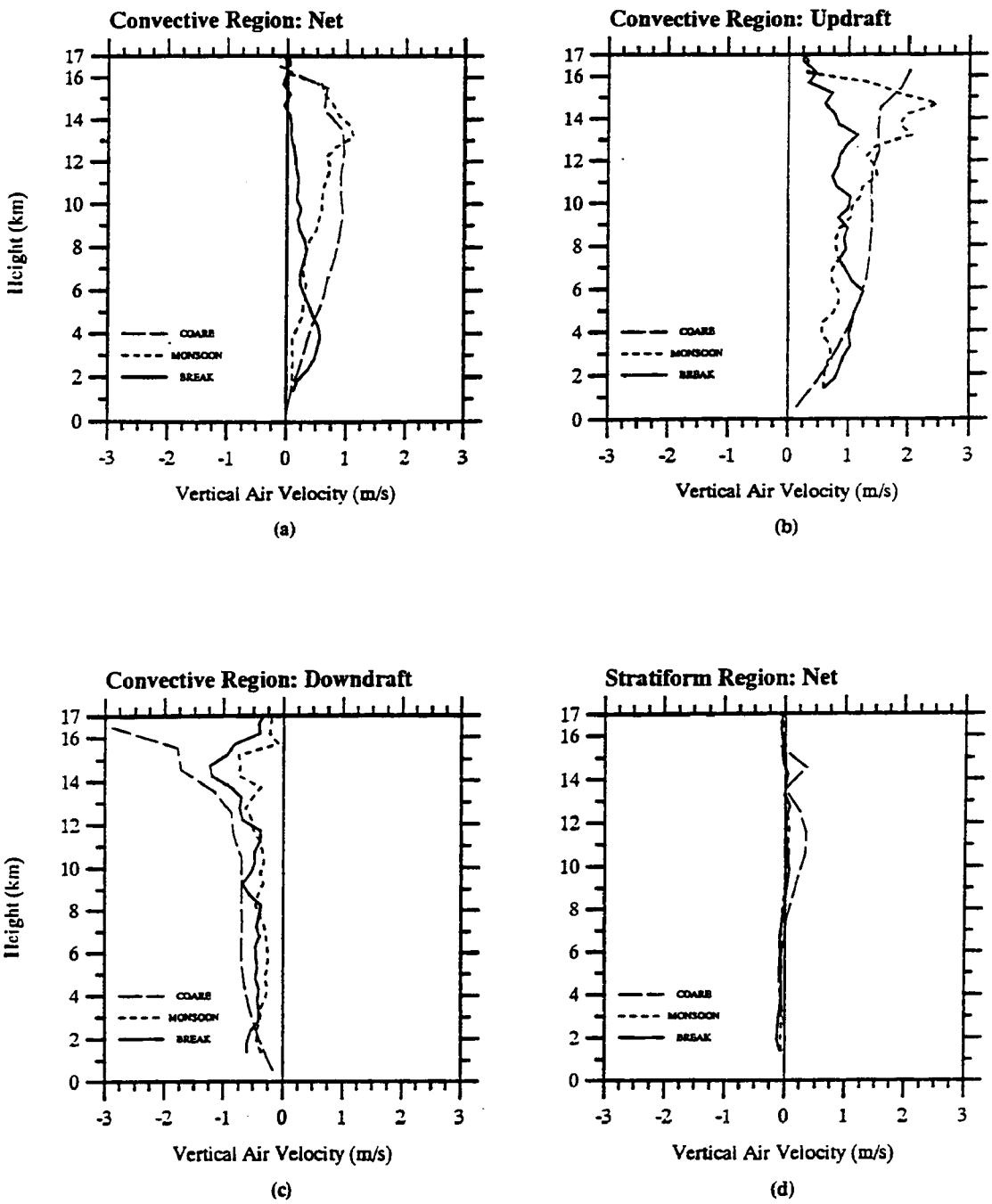


Fig. 6.4. Composite vertical air motion profiles (m $s^{-1}$) for the Darwin break (solid line), Darwin monsoon (short dashed line), and COARE (long dashed line) partitioned into net convective region [up and downdrafts; (a)], convective region updrafts (b), convective region downdrafts (c), and net stratiform region (d).

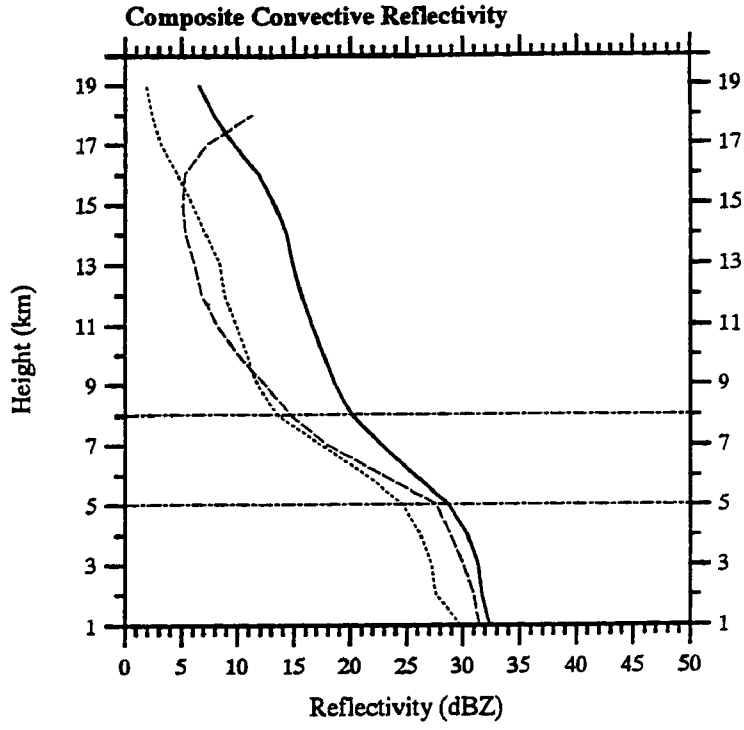


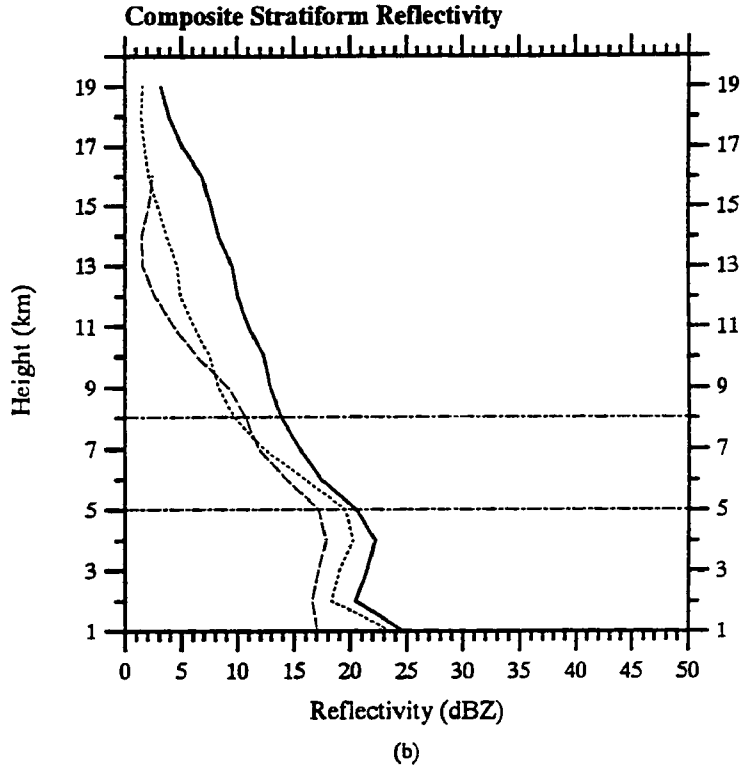


Fig. 6.5. Composite radar reflectivity profiles (*dBZ*) for the convective (a) and stratiform (b) regions of the COARE (long dashed line), Darwin monsoon (short dashed line), and Darwin break (solid line) MCSs. The dashed horizontal lines indicate the approximate location of the mixed phase (-20° - 0°C) region. The profiles were constructed by averaging the all partitioned radar volume data in each regime (i.e., 166 Darwin break, 406 Darwin monsoon, and 27 COARE).

similar to those observed in the monsoon at Darwin. For convective updrafts (Fig 6.4b), the COARE profile shows positive acceleration extending through most of the troposphere. Similar to the Darwin monsoon composite, the magnitude of the COARE vertical air motion profile is less than the Darwin break composite in the lowest few kilometers but is larger than the Darwin break in the upper troposphere[5]. The smaller vertical drafts in the lower troposphere of the COARE and Darwin monsoon composites are consistent with previous studies, indicating fundamental differences in the updraft structures and electrification processes of oceanic (i.e., COARE and Darwin monsoon) versus continental (i.e., Darwin break) MCSs (e.g., Orville and Henderson 1986; Jorgensen et al. 1989; Rutledge et al. 1992; Williams et al. 1992), as discussed in Ch. 5.

The convective downdraft composites (Fig. 6.4c) show qualitatively good agreement between COARE, the Darwin monsoon, and the Darwin break profiles with the largest vertical air velocities occurring near the tropopause. In the stratiform region, the pattern of all the profiles are similar, with low-level descent and upper level ascent, except near the tropopause. However, the COARE profile indicates much larger stratiform vertical air velocities compared to the Darwin results. This difference in magnitude is likely a consequence of the fact that each of the Darwin composites include ~100-200 samples while the COARE profile includes only 27 as well as the differences in analysis techniques used in these studies.

The COARE and Darwin radar reflectivity composites are shown in Fig. 6.5. Similar to the vertical air motion results, the large differences in sample size among the profiles in Fig. 6.5 must be considered when comparing the reflectivity structure. The low-level COARE convective

---

[5] The smaller magnitude of the COARE multiple Doppler composite compared to the Darwin break profile in the lower troposphere may be partially due to the forced constraint employed at the lower boundary in the multiple Doppler analyses (see Appendix C).

reflectivity profile brackets the Darwin monsoon and break profiles, showing relatively intense low-level structure with a small vertical gradient below the melting level. Above the melting level, the COARE convective reflectivity profile appears "monsoon-like", with a relatively steep reflectivity gradient through the mixed phase region ($\sim$4 dB km$^{-1}$). The increase in the COARE reflectivity profile above 15 km is due to the paucity of ship data above this point and the subsequent bias by the relatively intense 930209P MCS. Consistent with previous studies of tropical MCS radar reflectivity profiles (e.g., Szoke et al. 1986), the convective and stratiform COARE and Darwin reflectivity profiles are virtually indistinguishable in the upper troposphere.

### 6.1.2 Single-Doppler analyses from COARE

Single-Doppler retrievals were performed on two MCSs during COARE (930210 and 930223) using the MIT ship-based radar data. In each case, radar volume scans tailored for retrieval analyses were collected at 10 minute intervals for several hours as the MCS passed over the ship allowing detailed time-height cross sections of the kinematic fields to be constructed. Figures 6.6 and 6.7 show cross sections of retrieved fields for the 930210 and 930223 MCSs, respectively, using the EVAD and CEVAD analysis techniques (see Appendix B for a discussion of these methods). In both cases, the retrieved fields using the CEVAD and EVAD techniques are virtually identical. The only significant difference occurs in the vertical air velocity cross sections, where CEVAD generally diagnoses larger magnitudes of vertical air motion in the upper troposphere and also commonly shows subsidence in this region. The reason for the discrepancy is not obvious, especially when noting that the patterns of EVAD and CEVAD horizontal divergence are almost indistinguishable; however, the difference is probably due to the different boundary constraint as well as the solution methodology employed in the CEVAD technique compared to EVAD (see Appendix B).

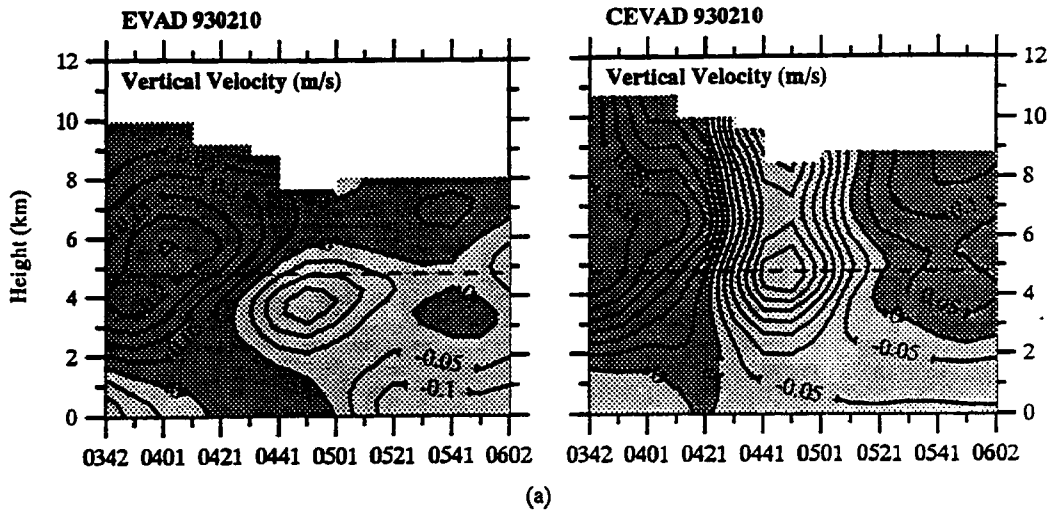
EVAD 930210
CEVAD 930210
Vertical Velocity (m/s)
Vertical Velocity (m/s)
Height (km)
-0.05
-0.1
0342 0401 0421 0441 0501 0521 0541 0602

(a)

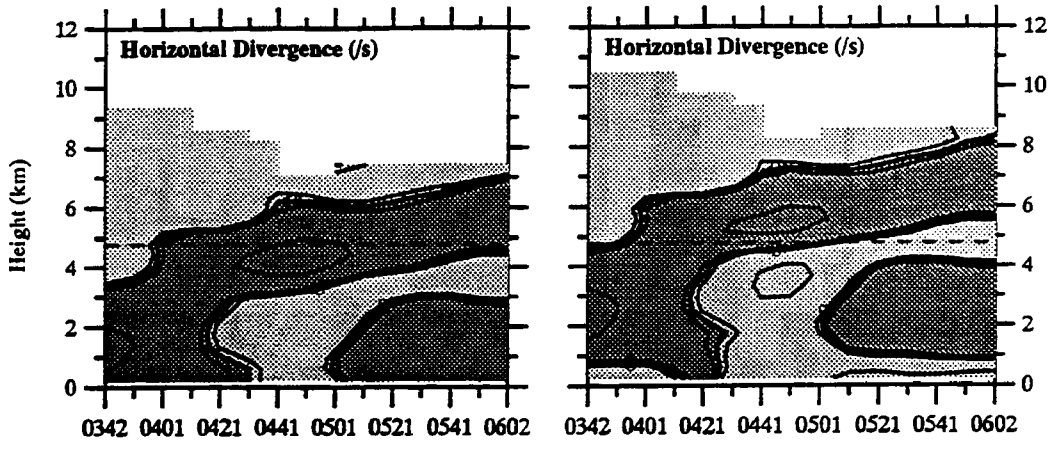
Horizontal Divergence (/s)
Horizontal Divergence (/s)
Height (km)
0342 0401 0421 0441 0501 0521 0541 0602

(b)

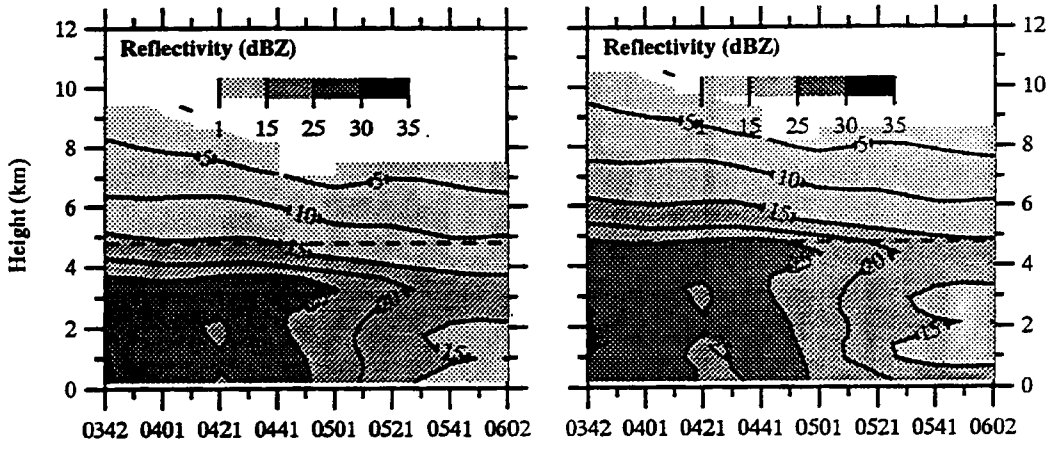
Reflectivity (dBZ)
Reflectivity (dBZ)
1 15 25 30 35
Height (km)
0342 0401 0421 0441 0501 0521 0541 0602

(c)

Fig. 6.6. Time-height cross section of (a) vertical air motion (m $s^{-1}$), (b) horizontal divergence ($s^{-1}$), (c) reflectivity (*dBZ*), and (d) particle fall speed (m $s^{-1}$) for the 930210 COARE MCS using the EVAD (left column) and CEVAD (right column) single-Doppler retrieval techniques. Dark (light) shading represents upward (downward) motion in (a), convergence (divergence) in (b) and particle fall speeds greater (less) than 3 m $s^{-1}$ in (d). Gray shading in (c) corresponds to reflectivity scale in the top portion of the plot.

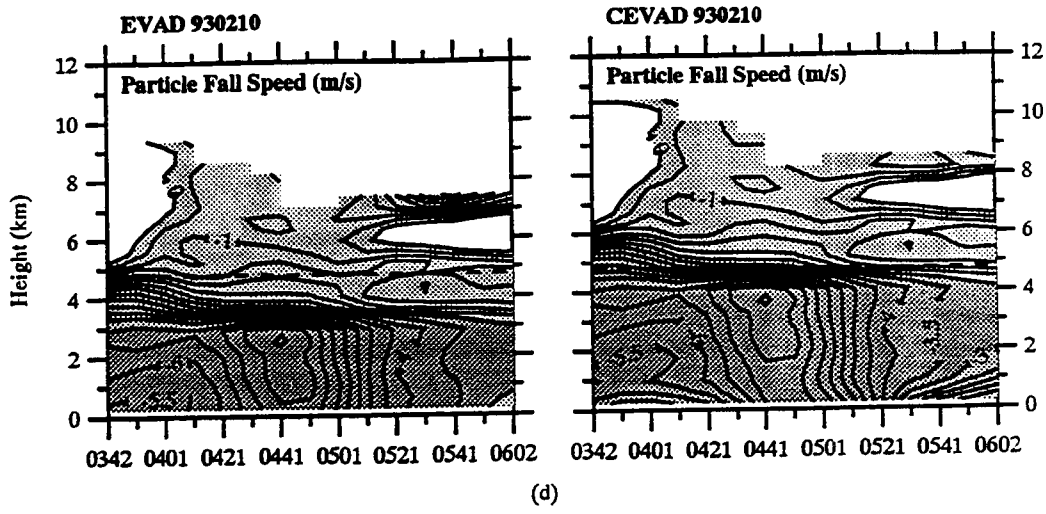


Fig. 6.6. (*continued*).

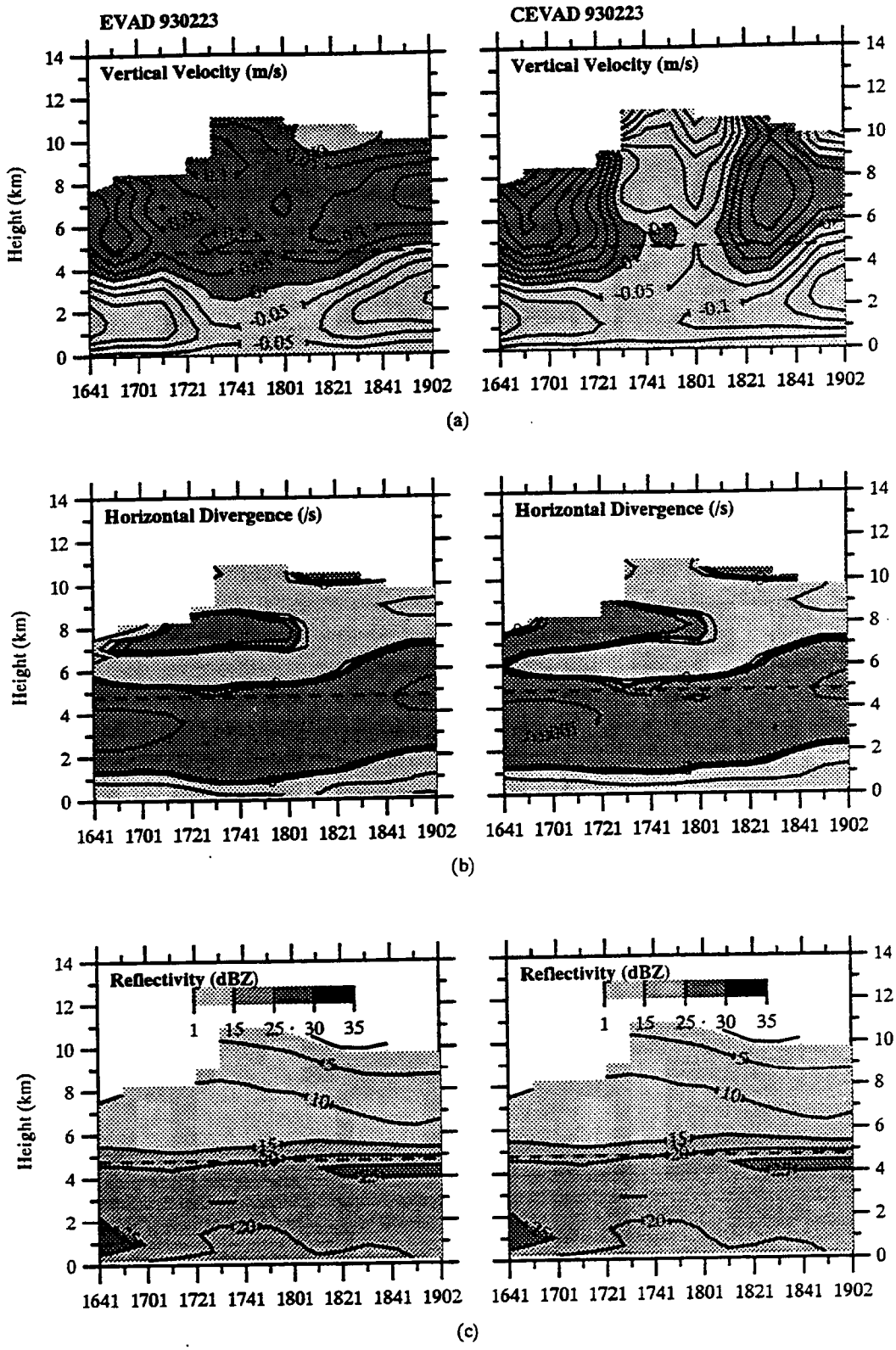


Fig. 6.7. Same as Fig. 6.6, except for the 930223 COARE MCS.

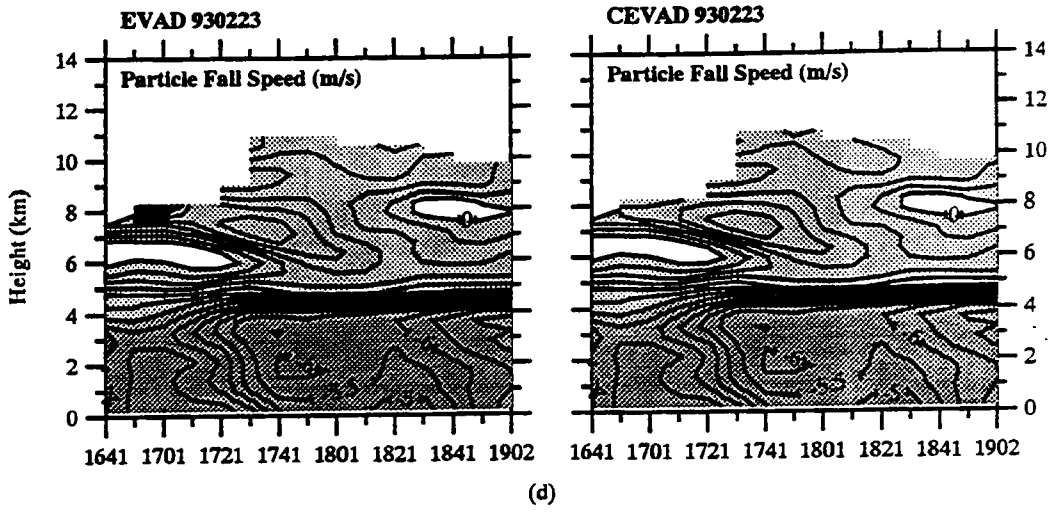


(d)

Fig. 6.7. (*continued*).

In the 930210 MCS (Fig. 6.6), the retrievals reveal the transition from convective to stratiform conditions as the MCS passed over the observational network. Early on, the retrievals indicated low-level convergence with corresponding deep upward motion and relatively intense low-level reflectivities followed by the development of a mid-level peak convergence pattern, sandwiched between upper and lower level divergence. This latter signal is consistent with the development of stratiform conditions. The occurrence of a radar bright band is rather ambiguous in this case but is weakly indicated near 0440 UTC (Fig. 6.6). The particle fall speed cross sections also indicate large hydrometeor vertical motions at this time, consistent with the melting of large aggregates. The evolution of the 930223 MCS (Fig. 6.7) is similar to 930210, although the transition from convective to stratiform conditions is not as pronounced, and 930223 shows a more clearly defined bright band compared to 930210.

Figure 6.8 shows a comparison of the partitioned multiple Doppler (930209S, 930209P, 930221, 930222: 4 events and 27 volumes of data) and single-Doppler (930210 and 930223: 2 events and 28 volumes of data) stratiform vertical air motions and horizontal divergence patterns for COARE[6]. Although the vertical air motion patterns in the single and multiple Doppler analysis are similar with upper level ascent and lower level descent, the multiple Doppler composite apparently sampled deeper, more intense systems as suggested by the offset to higher levels as well as the larger magnitude of the multiple Doppler draft composite. The difference may also reflect the fact that the multiple Doppler composite, which was derived from the partitioning of radar reflectivity in each volume, can include a wider range of features in the analysis (e.g., decaying convection or convection in the formative initial stages, as well as typical bright band features) compared to the single-Doppler retrievals.

---

[6] Horizontal divergence information was not available for all of the P-3 quad Doppler volumes and a multiple Doppler composite was therefore not constructed.

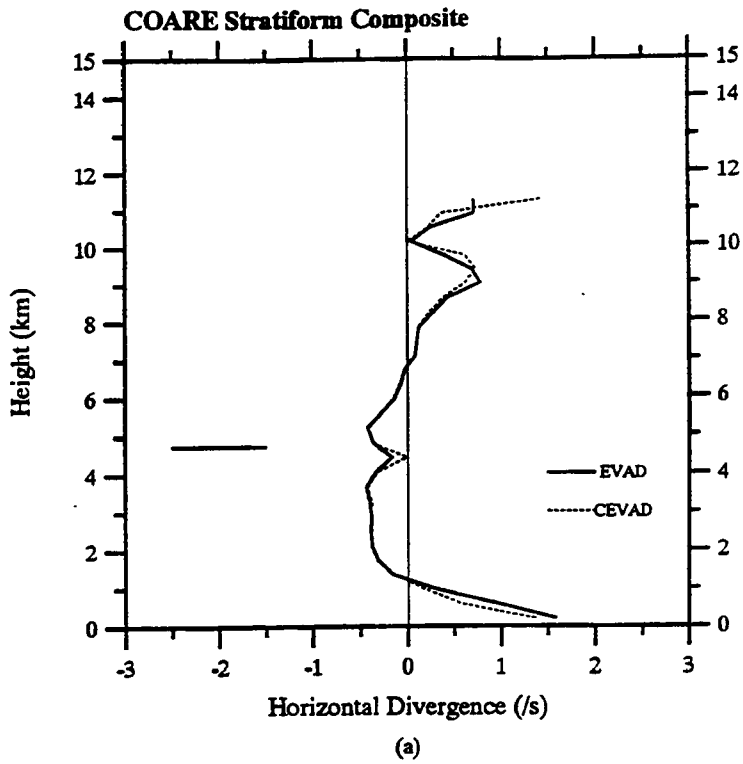


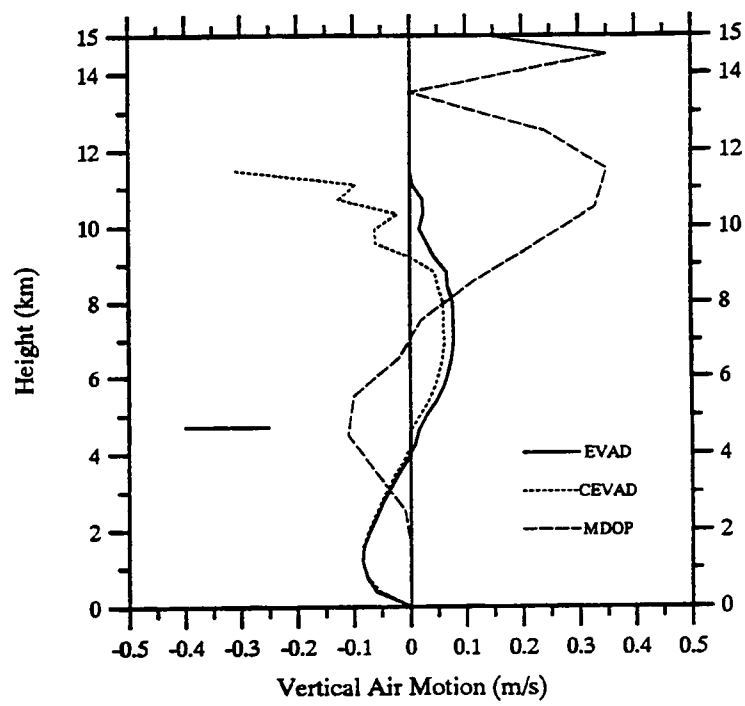


Fig. 6.8. Composite horizontal divergence (a) in $s^{-1}$ x $10^{-3}$ and vertical air motion (b) in m $s^{-1}$ for the COARE 930210 and 930223 MCSs using the EVAD and CEVAD analysis retrievals. Legend in the lower right portion of each plot indicates the profile associated with each retrieval. In (b), the partitioned stratiform profile (MDOP) from Fig. 6.4 has been added for comparison. The 0°C isotherm is indicated in the left portion of the plot.

### 6.1.3 Comparison with other geographical regions

In this section, the partitioned Darwin wind profiler and COARE multiple Doppler composites are compared to similar results from different geographic locations. The comparison is limited to radar and wind profiler studies in order to minimize differences due to analysis techniques. It should be noted that various methods are used to partition MCS substructures in these studies and that the results represent a wide range of sample sizes and spatial and temporal averaging.

Composite vertical air motion profiles from convective region MCSs, including the Darwin and COARE results from this study, are shown in Fig. 6.9. This figure includes profiles derived from a West African tropical continental MCS using dual-Doppler radar analysis (Chong et al. 1983), a composite of tropical western Pacific island MCSs using wind profiler data (Balsley et al. 1988), and a middle latitude MCS using dual-Doppler radar analysis (Biggerstaff and Houze 1993).

All of the profiles in Fig. 6.9 show upward motion extending through the depth of the troposphere. However, the location of peak ascent ranges from the lower (Darwin break) to the upper troposphere (Darwin Monsoon, COARE, and tropical West Pacific island composites). The vertical air motion profiles from both the tropical West Africa and middle latitude MCSs show an upward motion peak in the middle troposphere with magnitudes on the order of 1-2 m $s^{-1}$. The peak ascent in these profiles is roughly sandwiched between the peak ascent in the Darwin break composite (4 km) and the Darwin monsoon, COARE, and West Pacific island composites (12-13 km).

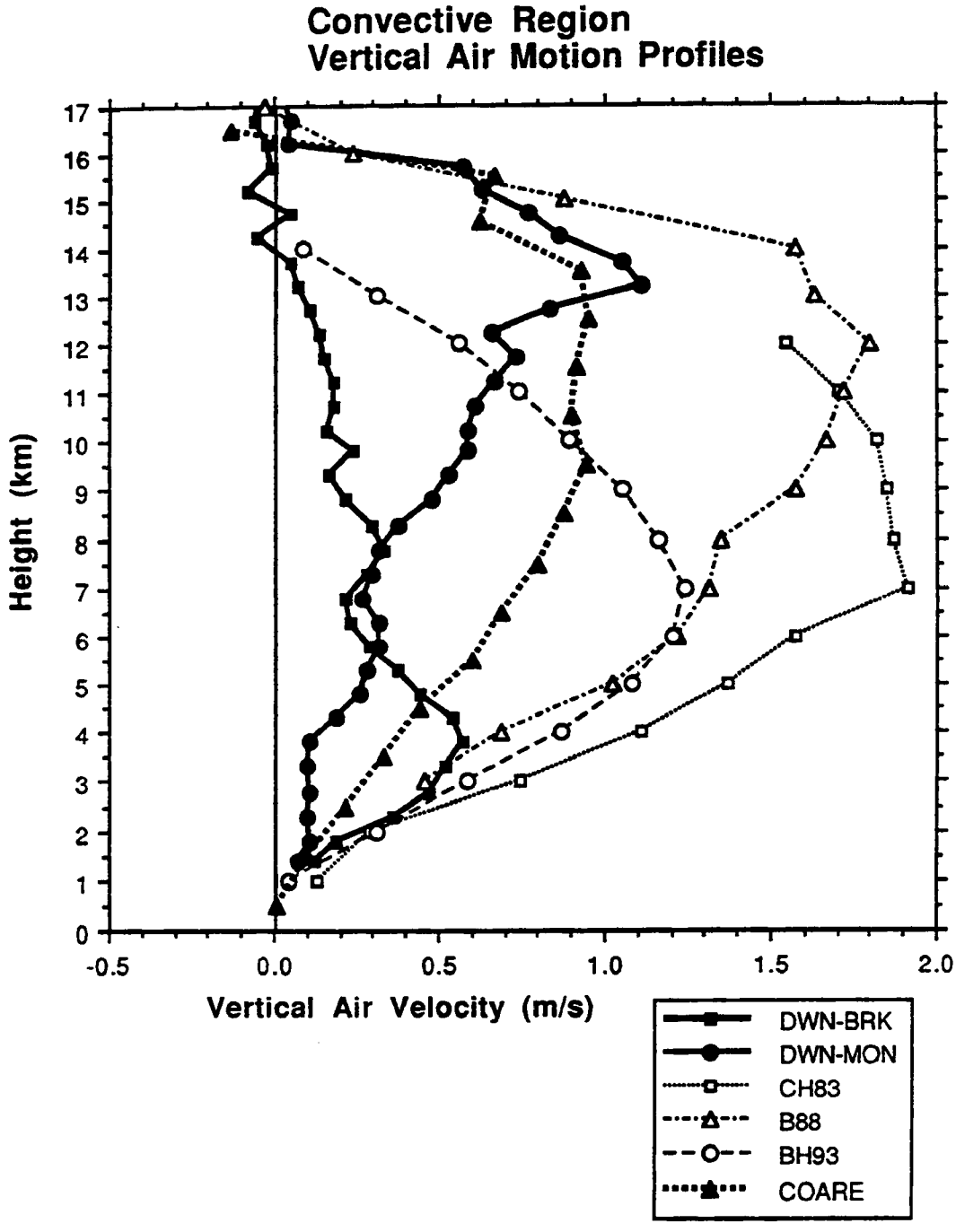


Fig. 6.9. Comparison of convective region vertical motion profiles (m $s^{-1}$). Symbols in legend refer to the following: DWN-BRK for the Darwin break composite; and DWN-MON for the Darwin monsoon composite; CH83 for Chong et al. (1983) [adapted from Houze 1989]; B88 for Balsley et al. (1988); BH93 for Biggerstaff and Houze (1993); and COARE for the COARE composite. Note that widely different sample sizes and temporal and spatial averaging go into the various curves of this figure.

The Darwin monsoon, COARE and Pohnpei Island profiles all show positive acceleration extending from low-levels into the upper troposphere. It is not possible to compare the low-level structure due to the restriction of sampling at Pohnpei Island above 3 km. The Darwin break, COARE, and West Pacific composites show a subsidence region in the vicinity of the tropopause (17 km); however, the base of the subsidence region in the Darwin break occurred about 2 km (1.5 km) below the corresponding base in the Pohnpei (COARE) profile (Fig. 6.9). The Darwin monsoon composite shows weak positive motion in this region.

In Fig. 6.10, the Darwin break transition zone composite is compared with similar results from middle latitude MCSs using dual-Doppler radar (Smull and Houze 1987a; Biggerstaff and Houze, 1993) and a West African tropical continental squall line using dual-Doppler radar (Chalon et al. 1988). The results all show subsidence below the melting level; however, one of the middle latitude profiles (Smull and Houze 1987a) shows ascending motion in the middle to upper troposphere while the others, including the Darwin break composite, indicate descending motion throughout this region. The reason for the discrepancy between the profiles above the melting level is not readily apparent but, as mentioned in the beginning of this section, may be related to the subjectivity involved in the techniques used to partition the MCSs into discrete substructures.

In Fig. 6.11, the COARE and Darwin monsoon and break stratiform composites are compared to similar profiles from the western Pacific (Pohnpei Island) using composited wind profiler data (Balsley et al. 1988), a West African tropical continental MCS using the single-Doppler radar (VAD) retrieval (Chong et al. 1987), and a middle latitude MCS using the single-Doppler radar (EVAD) retrieval technique (Rutledge et al. 1988). The profiles all indicate descent in the lower troposphere and ascent in the upper troposphere, with magnitudes ranging up to 0.5 m $s^{-1}$. The magnitude of the mesoscale downdraft is by far strongest in the middle latitude

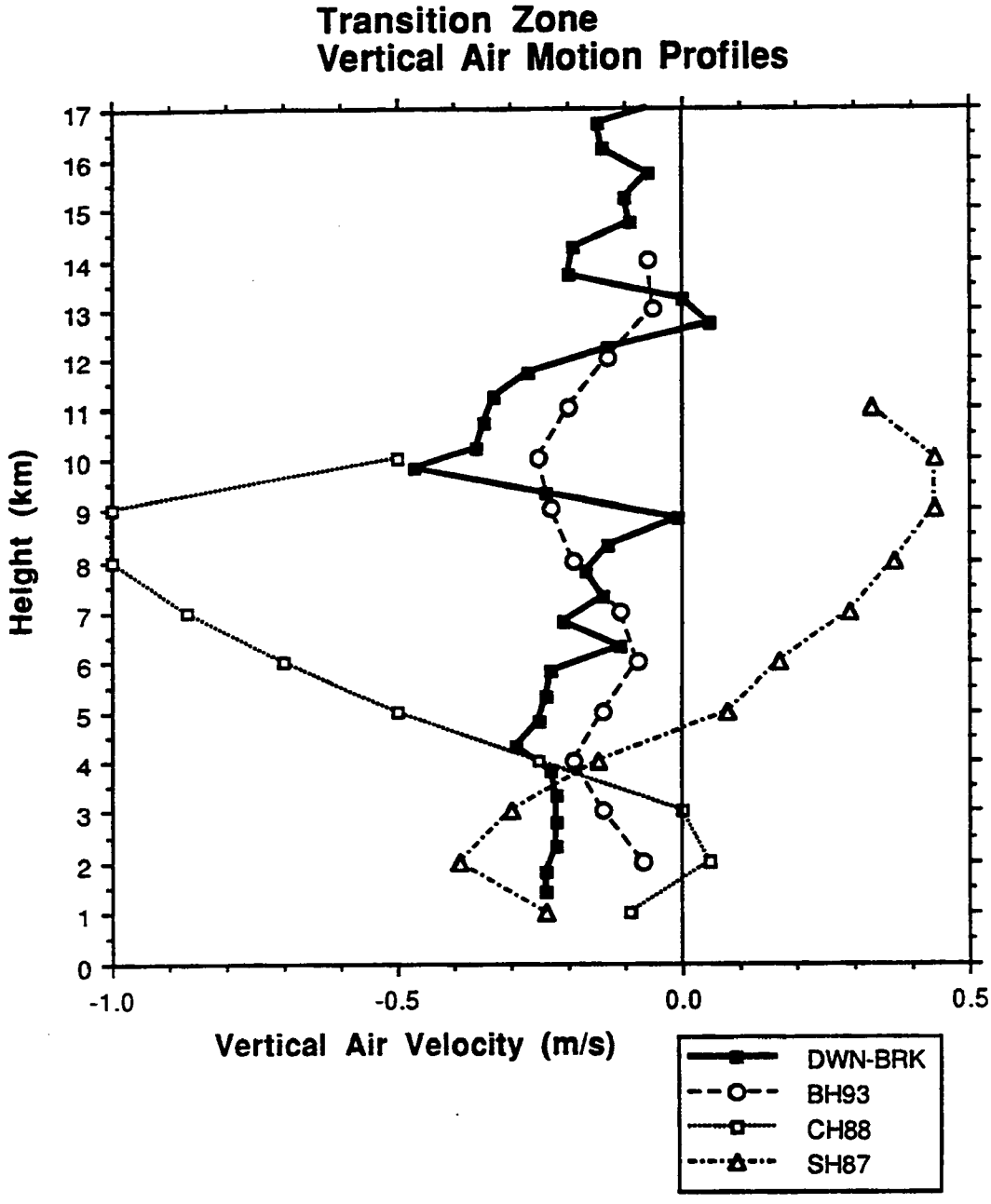


Fig. 6.10. Comparison of transition region vertical motion profiles (m $s^{-1}$). Symbols in legend refer to the following: DWN-BRK for the Darwin break composite; BH93 for Biggerstaff and Houze (1993); CH88 for Chalon et al. (1988); and SH87 for Smull and Houze (1987). Note that widely different sample sizes and temporal and spatial averaging go into the various curves of this figure.

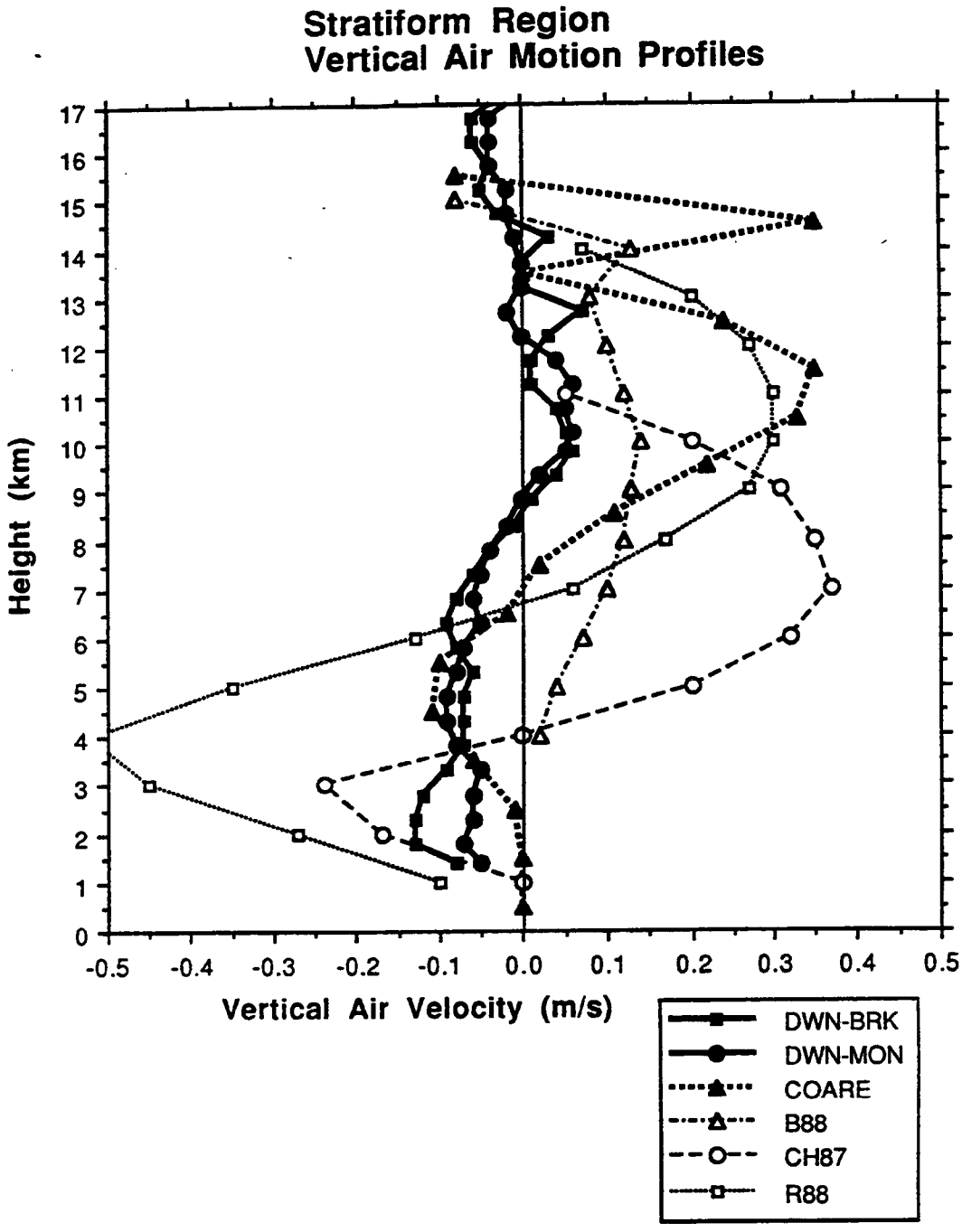


Fig. 6.11. Comparison of stratiform region vertical motion profiles (m $s^{-1}$). Symbols in legend refer to the following: DWN-BRK for the Darwin break composite; DWN-MON for the Darwin monsoon composite; COARE for the COARE composite; B88 for Balsley et al. (1988); CH87 for Chong et al. (1987); and R88 for Rutledge et al. (1988). Note that widely different sample sizes and temporal and spatial averaging go into the various curves of this figure.

case. The tropical West African profile also shows relatively strong low-level subsidence. Both the middle latitude and West African MCSs were land-based and the larger downdrafts in these cases may be a result of enhanced evaporative cooling.

The major difference between the Darwin stratiform composites and the other profiles in Fig. 6.11 is that the mean crossover to upper level ascent is displaced upward several kilometers from the melting level at Darwin. Also, the Darwin profiles have the weakest upper level ascent compared to the other studies. While acknowledging the large variability in the wind profiler vertical air estimates and the fact that the crossover level in the Darwin composites may be affected by the potential bias due to spectra merging (Ch. 2), these results are nevertheless consistent with the rain gauge network results discussed in Ch. 5 which indicated that only a small fraction ($< 30\%$ on average) of the rainfall in the Darwin monsoon and break MCSs were associated with stratiform features. The elevated crossover location would effectively reduce the region where hydrometeors could grow by vapor deposition, while at the same time increasing the depth over which hydrometeors would either sublimate or evaporate. Both processes would act to reduce the amount of stratiform precipitation reaching the surface.

There are at least two possible explanations for the displacement of the crossover in the Darwin stratiform region composite to higher elevations above the 0°C isotherm; however, as discussed below, neither of these mechanisms are entirely consistent with the observational data. One possibility is that the environmental shear profile was conducive to the development of a deep region of storm relative rear inflow with a corresponding elevated crossover to storm relative front to rear flow. However, the sounding data shown in Figs. 4.1 and 4.15 are not consistent with this hypothesis in many cases. Also, cursory examination of radar cross sections perpendicular to the

orientation of the convective line in the squall line MCSs revealed that the depth of rear inflow was generally restricted to the lower troposphere.

Another hypothesis is that, for the squall line cases, the wind profiler preferentially sampled the rearward portion of the stratiform region (with respect to the convective line) where the storm relative front to rear flow was most elevated with respect to the 0°C isotherm (as in the conceptual model of Houze et al. 1989). This situation could have occurred if the MCS propagation speed decreased after passing over the profiler. Although somewhat consistent with the pattern observed in the 900128 and 901215 MCSs (Figs. 4.11 and 4.13), there is no evidence for the height of the crossover level increasing with distance (time) in the other squall line cases. Moreover, neither of these mechanisms explain the elevated crossover in the non-squall systems which occurred during the active monsoon. Clearly, more research is needed to explain the storm relative flow patterns in these Darwin systems.

In the upper troposphere (above 14 km), the Darwin wind profiler composites, as well as the wind profiler composite from Pohnpei Island, show subsidence in the stratiform region extending upward to the vicinity of the tropopause (Fig. 6.11). A similar subsidence layer has also been diagnosed for a middle latitude MCS by Johnson et al. (1990). In their study, Johnson et al. argued that the subsidence was due primarily to downward sloping isentropes to the rear of the convective line and was independent of radiative effects. Although the Darwin profiles show near tropopause subsidence in the mean, it should be noted that the vertical air motion retrieved from the profiler was at times upward (see time-height cross sections in Ch. 4). The oscillatory nature of the vertical drafts suggests that the motion may have been associated with gravity waves forced by deep convection.

## 6.2 Diabatic heating

In this section, the Darwin partitioned $Q'_1$ composites discussed in Ch. 5 are compared to similar results from other geographical regions. A corresponding comparison is not made for $Q'_2$ since similar arguments can be made for the differences among the profiles and because the partitioned profiles for apparent moisture sink in the literature are somewhat limited compared to the apparent heat source profiles. In Fig. 6.12, vertical profiles of the convective region apparent heat source ($Q'_1$) are shown for a rawinsonde budget study using data from both the Marshall Islands as well as the South China Sea in the tropical western Pacific where the convective region profile was calculated as a residual (Johnson 1984), a rawinsonde and radar budget study from the tropical West Pacific COARE domain where the convective region profile was calculated as a residual (Carey et al. 1994), a West African continental tropical squall line (COPT 81) using dual-Doppler data and a thermodynamic retrieval (Chong and Hauser 1990), an eastern Atlantic tropical oceanic squall line (GATE) using rawinsonde and aircraft data (Gamache and Houze 1985), an idealized cloud cluster with an assumed vertical air motion profile (Houze 1982), a composite of tropical western Pacific island MCSs using wind profiler data (Balsley et al. 1988), and a middle latitude MCS using dual-Doppler radar analysis (Smull and Houze 1987a).

The convective $Q'_1$ profiles for the GATE, western Pacific Island, and middle latitude MCSs were all calculated using the corresponding vertical air motion profiles as input to a one-dimensional entraining jet model (Houze 1989). Note that neither the Houze (1982), Johnson (1984), or Carey et al. (1994) heating profiles are based on actual observations of convective region vertical air motions. Differences in the vertical position of the primary $Q'_1$ peak in these studies have been attributed to the inclusion of shallow convective clouds in the Johnson (1984) and

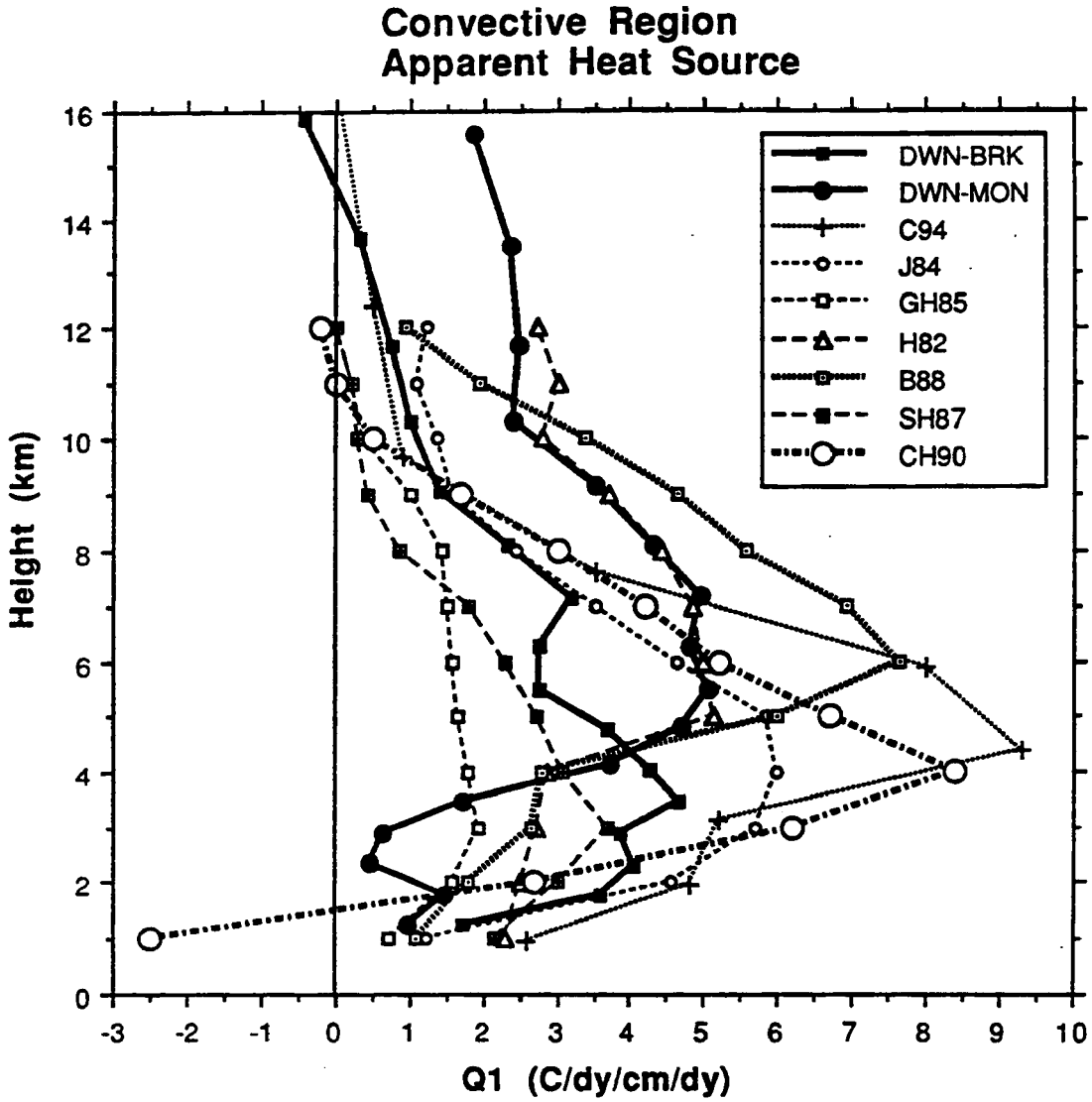


Fig. 6.12. Comparison of normalized convective region $Q'_1$ profiles (°C $dy^{-1}$ cm $dy^{-1}$). Symbols in legend refer to the following: DWN-BRK for the Darwin break composite; DWN-MON for the Darwin monsoon composite; C94 for Carey et al. (1994); J84 for Johnson (1984); GH85 for Gamache and Houze (1985); H82 for Houze (1982); B88 for Balsley et al. (1988); SH87 for Smull and Houze (1987); and CH90 for Chong and Hauser (1990);. The GH85, H82, B88, and SH87 curves have been adapted from Houze (1989).

Carey et al. (1994) heat budget analyses while only the effects of deep convective clouds were considered in the Houze (1982) study.

Almost all of the convective region $Q'_1$ profiles in Fig. 6.12 show positive heating throughout the depth of the troposphere; however, consistent with the variability in the vertical air motion profiles (Fig. 6.9), the peak diabatic heating ranges over a considerable depth (i.e., 3-6 km in elevation). The Darwin break regime convective profile (Fig. 6.12) is similar in shape and magnitude to several of the other tropical and middle latitude convective profiles including GATE (Gamache and Houze 1985), the Marshall Islands-South China Sea (Johnson 1984), COPT 81 (Chong and Hauser 1990), and the middle latitude study (Smull and Houze 1987a[7]). All of these profiles show peak heating centered in the lower troposphere (3-4 km). These results suggest that shallow convective clouds, with peak vertical air motion and collision coalescence precipitation production in the lower troposphere, can make a significant contribution to the convective region heat budget profile.

The Darwin monsoon composite, on the other hand, appears quite similar in shape and magnitude (especially above 4 km) to the idealized profile of Houze (1982) as well as the tropical West Pacific Island composite using data from Balsley et al. (1988) and Houze's one-dimensional cumulus model. The profiles reflect the shift of peak vertical air motion to greater heights in the convective region and indicate the importance of ice phase processes in determining the structure of diabatic heating in these MCSs.

---

[7] 2-D cloud model results for a different middle latitude squall line MCS also showed peak diabatic heating in the convective region centered just below 4 km (Tao et al. 1993).

A comparison of the Darwin monsoon and break composite stratiform $Q'_1$ profiles with similar results from other geographic regions is shown in Fig. 6.13. The profiles in Fig. 6.13 include a rawinsonde analysis of a mesoscale anvil during Winter MONEX in the South China Sea (Johnson 1984), radar and microphysical retrieval data for a West African squall line (Chong and Hauser 1990), an idealized model of the stratiform portion of a tropical cloud cluster with an assumed vertical air motion profile (Houze 1982), and the same idealized model using the stratiform vertical air motion profile from Houze and Rappaport (1984) for a GATE eastern Atlantic tropical squall line (Houze 1989).

All of the profiles in Fig. 6.13 indicate cooling in the lower troposphere on the order of 1-3°C $dy^{-1}$ / cm $dy^{-1}$ (at least partially off-setting the low-level convective region heating) and heating in the upper troposphere which supplements the convective heating in this region (Fig. 6.12). The major difference between the Darwin composites and the other profiles is that positive heating in the stratiform portion of the Darwin MCSs appears to be substantially smaller and restricted to a shallower layer. To the extent that the vertical advection term in the $Q'_1$ budget (i.e., Eq. 1.1) adequately represents the apparent heat source term, the results in Figs. 6.12 and 6.13 show that the stratiform region of both the Darwin monsoon and break MCSs plays a relatively minor role in the diabatic heat production compared to MCS stratiform regions from other geographical regions.

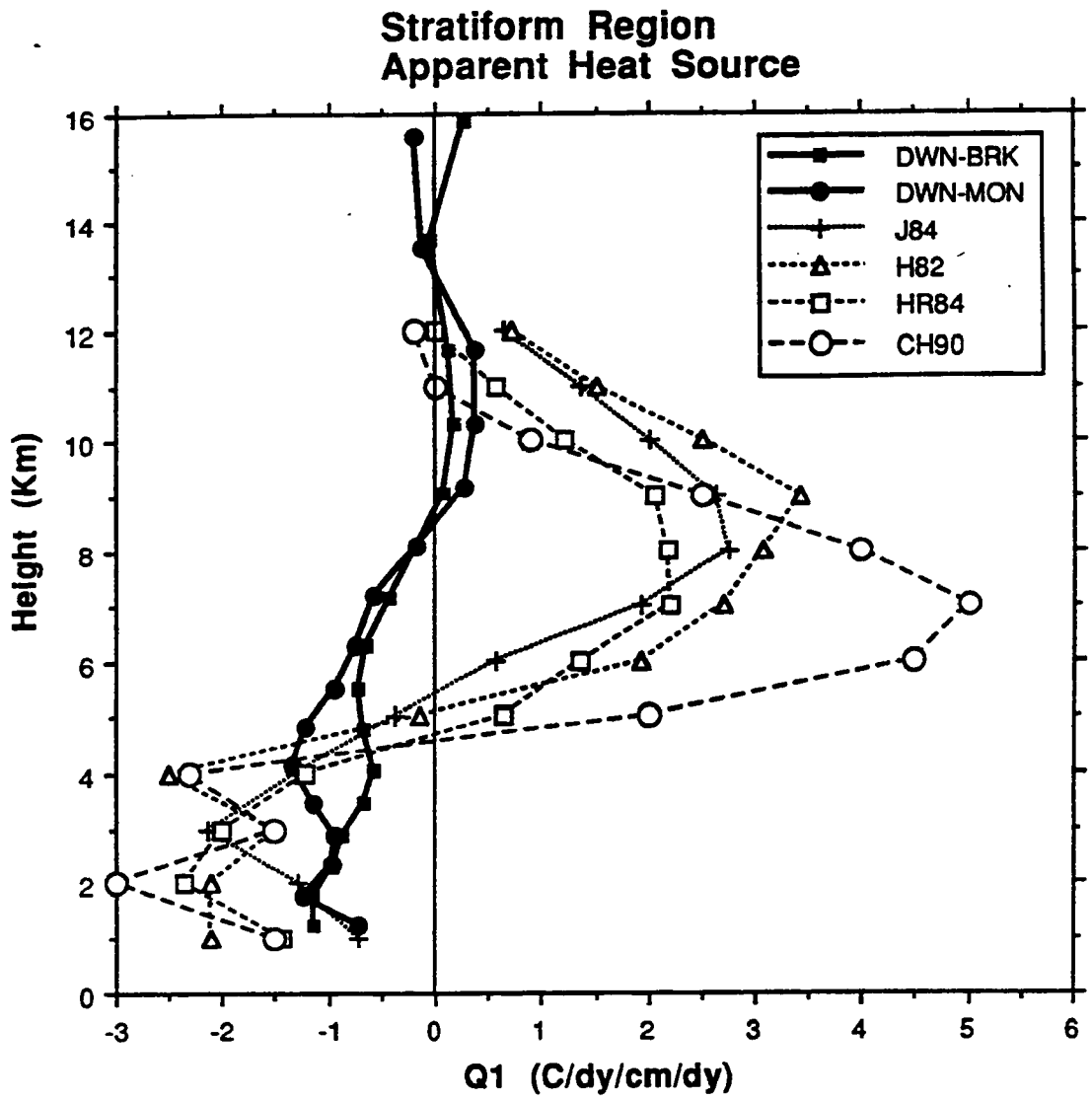


Fig. 6.13. Comparison of normalized stratiform region $Q'_1$ profiles (°C $dy^{-1}$ cm $dy^{-1}$). Symbols in legend refer to the following: DWN-BRK for the Darwin break composite; DWN-MON for the Darwin monsoon composite; J84 for Johnson (1984); H82 for Houze (1982); HR84 for Houze and Rappaport (1984); and CH90 for Chong and Hauser (1990). The H82, and HR84 curves have been adapted from Houze (1989).

## Chapter VII

# SUMMARY AND CONCLUSIONS

VHF wind profiler data were used to determine the vertical draft structure within 13 tropical Mesoscale Convective Systems (MCSs) near Darwin, Australia during the wet seasons of 1989-1990 and 1990-1991. Approximately 500 averaged spectra from the wind profiler, representing 83 hours of coverage, were examined using a combination of an objective algorithm and manual editing in order to retrieve the vertical air motions from the MCSs. Single-Doppler radar and surface rainfall data were also utilized in order to correlate the reflectivity and surface rainfall patterns with the structure of the vertical air motion sensed by the wind profiler during the passage of each system. Because of Darwin's unique location at the southern tip of the Maritime Continent, the wind profiler was able to observe vertical drafts in both the monsoon (maritime) and monsoon break (continental) convective regimes.

The break regime MCSs (6 total) were all squall lines, characterized by a leading line of convection with intense precipitation and sharp horizontal reflectivity gradients (radar echo tops ranging from 15 to > 20 km) and a trailing stratiform region with relatively small horizontal reflectivity gradients, light rainfall, and a characteristic radar bright band, similar to many previous studies of tropical and middle latitude squall systems. A reflectivity trough (transition zone) with very light precipitation was also observed between the convective line and trailing stratiform region in most cases. Most of the break MCSs formed over higher terrain east of

Darwin (Oenpelli escarpment) during the late morning to early afternoon hours and propagated toward the coast roughly perpendicular to the low level shear vector, reaching Darwin during the evening hours. All of the break MCSs studied were in their mature to dissipating stages when they were sampled by the wind profiler.

In contrast, the monsoon systems (7 total) were characterized as relatively unorganized regions of areally extensive stratiform cloud with embedded convective bands which moved on-shore in the west to northwesterly monsoon flow. There was a tendency for the bands to be oriented approximately parallel to the 850 mb wind; however, several of the monsoon events were observed with more than one band orientation. Radar cross sections and the rain gauge network indicated that the intensity of the monsoon MCSs generally decreased as the precipitation regions moved onshore. The largest reflectivities in these systems were observed below the 0°C isotherm, similar to previous studies of oceanic convection.

The wind profiler, scanning radar, and rain gauge network data were partitioned into convective and stratiform components using an objective algorithm and composited for each regime (monsoon and break). Results from the rain gauge network indicated that the vast majority of the total rainfall was associated with the convective portion of the monsoon and break MCSs (71 and 82% on average, respectively). These results are consistent with other studies of Darwin area precipitation but are on the high end of many previous studies of MCS precipitation patterns in other tropical locations.

The break regime MCSs were all characterized by relatively shallow convective cells along the leading edge of the squall line with an updraft peak near 4 km, trailed by deeper updrafts in the middle to upper troposphere. The height of the updraft peak associated with these deeper

convective clouds was quite variable, ranging from ~8.5-15 km, probably as a consequence of lifecycle effects as each system crossed over the profiler as well as the small spatial scale of convective features sampled by the profiler in each case. Thus, in a composite sense, the break MCSs showed a pronounced updraft peak in the lower troposphere, with secondary peaks at upper levels. A significant fraction of the convective rainfall was associated with the low-level updraft indicating that warm rain collision-coalescence processes were often as important to precipitation production as mixed phase processes involving both ice and supercooled liquid water (associated with the upper level peak updraft).

In the monsoon regime, the convective region vertical air motions were typically less than the break squall lines in the lower troposphere but larger in the upper troposphere. The low-level differences are consistent with the smaller virtual temperature excess observed in the monsoon soundings compared to the break soundings. All other factors being equal, the reduced virtual temperature excess available to air parcels rising in monsoon convective cells allows water loading resulting from precipitation production to play a proportionally larger role in reducing the total buoyancy forcing of upward momentum compared to break period convective cells.

In a composite sense, the monsoon convective region vertical air motion pattern showed positive acceleration extending from low-levels into the upper troposphere. The pattern is consistent with buoyancy recovery of air parcels after unloading significant amounts of liquid precipitation below the 0°C isotherm; however, the correlation between the virtual temperature excess (i.e., thermal buoyancy) and the vertical draft structure in the upper troposphere was not always clear, suggesting that the soundings were not entirely representative of the monsoon environment and/or additional forcing mechanisms are required to explain the upper level vertical air motion pattern.

The convective downdraft profiles within both the monsoon and break MCSs were similar, with the largest subsidence occurring in the vicinity of the tropopause and relatively constant downward motion below. Thus, the majority of the variability in the net monsoon and break convective profiles was a consequence of the differences in the updraft structure. The stratiform profiles of the monsoon and break were also similar with a small region of upward motion generally restricted to the upper troposphere. Although the structure is consistent with the observed small contribution of stratiform rain to the total MCS rainfall, the pattern is dissimilar to other studies of stratiform vertical air motions which indicate a deeper mesoscale updraft region with a crossover at or near the 0°C level. Several mechanisms were proposed in order to explain the apparent anomalous structure in the Darwin composites; however, neither mechanism was entirely consistent with the observations.

A relatively large number of radar volumes (572) were partitioned into convective and stratiform components in order to examine the radar reflectivity structure of the Darwin MCSs. In a composite sense, the convective regions of both the monsoon and break systems were characterized by relatively large reflectivities in the lower troposphere with only a small vertical gradient below the 0°C isotherm. The major difference in the profiles occurred in the mixed phase region where the monsoon convective composite had a larger vertical gradient compared to the break. The results are consistent with the larger, on average, vertical drafts observed by the wind profiler in the break MCSs compared to the monsoon as well as previously documented electrification differences between MCSs occurring in the continental and maritime regimes.

A relatively small number of multiple Doppler volumes (27) from four MCSs in COARE were partitioned and composited in order to compare the vertical air motion and radar reflectivity structure to the Darwin systems. Although the comparison was hampered by the small amount of

COARE vertical air motion and radar reflectivity data relative to Darwin, the results showed that the COARE convective vertical air motion profile was, on average, similar to the Darwin monsoon composite with relatively weak drafts in the lower troposphere and positive acceleration extending into the upper troposphere. The COARE convective reflectivity structure was also similar to the Darwin monsoon with a characteristic large reflectivity gradient in the mixed phase region.

Based on the Darwin composite vertical air motion results, profiles of apparent heat source ($Q_1$) and moisture sink ($Q_2$) variables were constructed for the break and monsoon regimes and normalized based on the fraction of convective and stratiform rainfall. Consistent with the vertical air motion patterns, diabatic heating and moistening profiles in the convective region showed that the break MCSs were characterized by lower level heating and drying peaks compared to the monsoon. To the extent that the normalized $Q_1$ and $Q_2$ budgets can be accurately determined by the vertical advection of dry static energy and specific humidity, respectively, the profiles emphasize the important role of shallow cumulus, with inherent liquid phase precipitation production, to the break MCS diabatic heating structure. In contrast, the higher level of peak vertical air motion in the monsoon produced corresponding elevated heating and drying profiles (relative to the break), suggesting a significant contribution from ice processes in these systems. Moreover, the magnitude of the normalized stratiform $Q_1$ and $Q_2$ profiles was relatively small so that the total diabatic heating and moistening (excluding radiative effects) was dominated by the convective region profile. The results have important implications for cumulus parameterizations in numerical models since previous studies have shown that the large scale circulation is sensitive to the vertical profile of diabatic heating in tropical MCSs.

## Chapter VIII

## REFERENCES


Alexander, G.D. and G.S. Young, 1992: The relationship between EMEX mesoscale precipitation feature properties and their environmental characteristics. *Mon. Wea. Rev.*, **120**, 554-564.

Augustine, J.A., and E.J. Zipser, 1987: The use of wind profilers in a mesoscale experiment. *Bull. Amer. Meteor. Soc.*, **68**, 4-17.

Balsley, B.B., and K.S. Gage, 1980: The MST radar technique: Potential for middle atmospheric studies. *Pure Appl. Geophys.*, **118**, 452-493.

Balsley, B.B., W.L. Ecklund, D.A. Carter, A.C. Riddle, and K.S. Gage, 1988: Average vertical motions in the tropical atmosphere observed by a radar wind profiler on Pohnpei (7° N latitude, 157° E longitude). *J. Atmos. Sci.*, **45**, 396-405.

Biggerstaff, M.I., and R.A. Houze Jr., 1993: Kinematics and microphysics of the transition zone of the 10-11 June 1985 squall line. *J. Atmos. Sci.*, **50**, 3091-3110.

Black, R.A., and J. Hallett, 1986: Observations of the distribution of ice in hurricanes. *J. Atmos. Sci.*, **43**, 802-822.

Boccippio, D.J., 1995: A diagnostic analysis of the VVP single-Doppler retrieval technique. *J. Atmos. Oceanic Technol.*, **12**, 230-248.

Browning, K.A., and R. Wexler, 1968: The determination of kinematic properties of a wind field using Doppler radar. *J. Appl. Meteor.*, **7**, 105-113.

Carter, D.A., W.L. Ecklund, J.R. McAfee, K.S. Gage, T. Keenan, and M. Manton, 1991: Results from the first year of observations using the Darwin VHF wind profiler. Preprints, *25th Int. Conf. on Radar Meteorology*, Paris, France, Amer. Meteor. Soc., 288-291.

Carey, L.D., S.A. Rutledge, and R.H. Johnson, 1994: Heat and moisture budget over the TOGA COARE IFA during the mature phase of the 24 December 1992 mesoscale convective system. Preprints, *6th Conf. On Mesoscale Processes*, Portland, Oregon, Amer. Meteor. Soc., 5-8.

Chalon, J.P., G. Jaubert, F. Roux and J.P. Lafore, 1988: The West African squall line observed on 23 June 1981 during COPT 81: Mesoscale structure and transports. *J. Atmos. Sci.*, **45**, 2744-2763.

Chilson, P.B., C.W. Ulbrich, M.F. Larsen, P. Perillat, and J.E. Keener, 1993: Observations of a tropical thunderstorm using a vertically pointing, dual-frequency, collinear beam Doppler radar. *J. Atmos. Oceanic Technol.*, **10**, 663-673.

Chong, M., and D. Hauser, 1990: A tropical squall line observed during the COPT 81 experiment in West Africa. Part III: Heat and moisture budgets. *Mon. Wea. Rev.*, **118**, 1696-1706.

Chong, M., J. Testud and F. Roux, 1983: Three-dimensional wind field analysis from dual-Doppler radar data. Part II: Minimizing the error due to temporal variation. *J. Climate Appl. Meteor.*, **22**, 1216-1226.

Chong, M., P. Amayenc, G. Scialom and J. Testud, 1987: A tropical squall line observed during the COPT 81 experiment in West Africa. Part I: Kinematic structure inferred from dual-Doppler radar data. *Mon. Wea. Rev.*, **115**, 670-694.

Churchill, D.D., and R.A. Houze, Jr., 1984: Development and structure of winter monsoon cloud clusters on 10 December 1978. *J. Atmos. Sci.*, **41**, 933-960.

Cifelli, R., S.A. Rutledge, W. Petersen, and D.J. Boccippio, 1994a: Ship-based single and dual Doppler analyses of TOGA COARE convective systems. Preprints, *Sixth Conf. on Climate Variations*, 74th Annual Meeting, Nashville, Tennessee, Amer. Meteor. Soc., J58-J62.

Cifelli, R., and S.A. Rutledge, 1994b: Vertical motion structure in Maritime Continent mesoscale convective systems: Results from a 50-MHz profiler. *J. Atmos. Sci.*, **51**, 2631-2652.

Cifelli, R., S.A. Rutledge, D.J. Boccippio, and T. Matejka, 1995: Horizontal divergence and vertical velocity retrievals from Doppler radar and wind profiler observations. *J. Atmos. Oceanic Technol.*, submitted.

Clark, W.L., and D.A. Carter, 1980: Real-time scaling of atmospheric parameters from radars using the MST technique. Preprints, *19th Conf. on Radar Meteorology*, Miami Beach, Florida., Amer. Meteor. Soc., 599-604.

Crochet, M., F. Cuq, F.M. Ralph, and S.V. Venkateswaran, 1990: Clear-air radar observations of the great October storm of 1987. *Dyn. Atmos. Oceans*, **14**, 443-461.

DeMaria, M., 1985: Linear response of a stratified tropical atmosphere to convective forcing. *J. Atmos. Sci.*, **42**, 113-121.

DeMott, C.A., R. Cifelli, and S.A. Rutledge, 1995: An improved method for partitioning radar data into convective and stratiform components. Preprints, *27th Int. Conf. on Radar Meteorology*, Vail, Colorado, Amer. Meteor. Soc., 233-236.

Emanuel, K.A., 1994: *Atmospheric Convection*. Oxford University Press, 580pp.

Frank, W.M., and J.L. McBride, 1989: The vertical distribution of heating in AMEX and GATE cloud clusters. *J. Atmos. Sci,* **46**, 3464-3478.

Gage, K.S., 1990: Radar observations of the free atmosphere: Structure and dynamics. *Radar in Meteorology*, D. Atlas, Ed., Amer. Meteor. Soc., 534-565.

Gallus, W.A., and R.H. Johnson, 1991: Heat and moisture budgets of an intense midlatitude squall line. *J. Atmos. Sci.*, **48**, 122-146.

Gamache, J.F., 1990: Microphysical observations in summer MONEX convective and stratiform clouds. *Mon. Wea. Rev.*, **118**, 1238-1249.

Gamache, J.F., and R.A. Houze Jr., 1982: Mesoscale air motions associated with a tropical squall line. *Mon. Wea. Rev.*, **110**, 118-135.

Gamache, J.F., and R.A. Houze Jr., 1983: Water budget of a mesoscale convective system in the tropics. *J. Atmos. Sci.*, **40**, 1835-1850.

Gamache, J.F., and R.A. Houze, Jr., 1985: Further analysis of the composite wind and thermodynamic structure of the 12 September GATE squall line. *Mon. Wea. Rev.*, **113**, 1241-1259.

Gossard, E.E., 1988: Measuring drop-size distributions in clouds with a clear-air sensing Doppler radar. *J. Atmos. Oceanic Technol.*, **5**, 640-649.

Gossard, E.E., W.D. Neff, R.J. Zamora, and J. Gaynor, 1984: The fine structure of elevated refractive layers: Implications for over-the-horizon propagation and radar sounding systems. *Radio Sci.*, **19**, 1523-1533.

Gray, W.M., 1972: Cumulus convection and larger-scale circulations part III: Broadscale and mesoscale considerations. Dept. of Atmos. Sci., Colorado State Univ., 80p. [Atmos. Sci. Paper No. 190]

Gray, W.M., and R.W. Jacobson, Jr., 1977: Diurnal variation of deep cumulus convection. *Mon. Wea. Rev.*, **105**, 1171-1188.

Gunn, R., and G.D. Kinzer, 1949: The terminal velocity of fall for water droplets in stagnant air. *J. Meteor.*, **6**, 243-248.

Hack, J.J., and W.H. Schubert, 1990: Some dynamical properties of idealized thermally-forced meridional circulations in the tropics. *Meteorol. Atmos. Phys.*, **44**, 101-117.

Hamilton, R.A., and J.W. Archbold, 1945: Meteorology of Nigeria and adjacent territory. *Quart. J. Roy. Meteor. Soc.*, **71**, 231-265.

Hartmann, D.L., H.H. Hendon, and R.A. Houze, Jr., 1984: Some implications of the mesoscale circulations in tropical cloud clusters for large-scale dynamics and climate. *J. Atmos. Sci.*, **41**, 113-121.

Hendon, H.H., and B. Liebmann, 1990(a): The intraseasonal (30-50 day) oscillation of the Australian summer monsoon. *J. Atmos. Sci.*, **47**, 2909-2923.

endon, H.H., and B. Liebmann, 1990(b): A composite study of onset of the Australian summer monsoon. *J. Atmos. Sci.*, **47**, 2227-2240.

eymsfield, G.M., and S. Schotz, 1985: Structure and evolution of a severe squall line over Oklahoma. *Mon. Wea. Rev.*, **113**, 1563-1589.

ildebrand, P.H., W.Lee, C.A. Walther, C. Frush, M. Randell, E. Loew, R. Neitzel, R. Parsons, J. Testud, F. Baudin, A. LeCornec, 1994,: The ELDORA airborne Doppler weather radar: Design and observations from TOGA COARE. *Bull. Amer. Meteor. Soc.*, submitted.

ocking, W.K., 1983: On the extraction of atmospheric turbulence parameters from radar backscatter Doppler spectra-I. Theory. *J. Atmos. Terrestrial Phys.*, **45**, 89-102.

olland, G.J., 1986: Interannual variability of the Australian summer monsoon at Darwin: 1952-82. *Mon. Wea. Rev.*, **114**, 594-604.

ouze, R.A., Jr., 1977: Structure and dynamics of a tropical squall-line system. *Mon. Wea. Rev.*, **105**, 1540-1567.

ouze, R.A. Jr., 1982: Cloud clusters and large-scale vertical motions in the tropics. *J. Meteor. Soc. Japan*, **60**, 396-409.

ouze, R.A. Jr., 1989: Observed structure of mesoscale convective systems and implications for large-scale heating. *Quart. J. Roy. Meteor. Soc.*, **115**, 425-461.

ouze, R.A., Jr., and D.D. Churchill, 1984: Microphysical structure of winter monsoon cloud clusters. *J. Atmos. Sci.*, **41**, 3405-3411.

ouze, R.A., Jr., and E. N. Rappaport, 1984: Air motions and precipitation structure of an early summer squall line over the eastern tropical Atlantic. *J. Atmos. Sci.*, **41**, 553-574.

ouze, R.A., Jr., B.F. Smull, and P. Dodge, 1990: Mesoscale organization of springtime rainstorms in Oklahoma. *Mon. Wea. Rev.*, **118**, 613-654.

ouze, R.A., Jr., S.A. Rutledge, M.I. Biggerstaff, and B.F. Smull, 1989: Interpretation of Doppler weather radar displays of midlatitude mesoscale convective systems. *Bull. Amer. Meteor. Soc.*, **70**, 608-619.

ohnson, R.H., 1984: Partitioning tropical heat and moisture budgets into cumulus and mesoscale components: Implications for cumulus parameterization. *Mon. Wea. Rev.*, **112**, 1590-1601.

ohnson, R.H., 1992: Heat and moisture sources and sinks of Asian monsoon precipitating systems. *J. Meteor. Soc. Japan*, **70**, 353-372.

ohnson, R.H., and G.S. Young, 1983: Heat and moisture budgets of tropical mesoscale anvil clouds. *J. Atmos. Sci.*, **40**, 2138-2147.

Johnson, R.H., and J.F. Bresch, 1991: Diagnosed characteristics of precipitation systems ov Taiwan during the May-June 1987 TAMEX. *Mon. Wea. Rev.*, **119**, 2540-2557.

Johnson, R.H., W.A. Gallus, Jr., and M.D. Vescio, 1990: Near-tropopause vertical motion within the trailing stratiform region of a midlatitude squall line. *J. Atmos. Sci.*, **47**, 220 2210.

Jorgensen, D.P., and M.A. LeMone, 1989: Vertical velocity characteristics of oceanic convection. *J. Atmos. Sci.*, **46**, 621-640.

Jorgensen, D.P., T. Matejka, and J.D. DuGranrut, 1996: Multi-beam techniques for derivir wind fields from airborne Doppler radars. *Special Issue on Radar Meteorology, Meteor Atmos. Phys.*, **58**, 83-104.

Keenan, T.D., and R.E. Carbone, 1992: A preliminary morphology of precipitation system n tropical northern Australia. *Quart. J. Roy. Meteor. Soc.*, **118**, 283-326.

Keenan, T.D., and S.A. Rutledge, 1993: Mesoscale characteristics of monsoonal convectior ınd associated stratiform precipitation. *Mon. Wea. Rev.*, **121**, 352-374.

Keenan, T.D., J. McBride, G. Holland, N. Davidson, and B. Gunn, 1989: Diurnal variatio during the Australian Monsoon Experiment (AMEX) phase II: *Mon. Wea. Rev.*, **117**, 2 35-2552.

Koscielny, A.J., R.J. Doviak, and R. Rabin, 1982: Statistical considerations in the estimatic of divergence from single-Doppler radar and application to prestorm boundary-layer observations. *J. Appl. Meteor.*, **21**, 197-210.

Krishnamurti, T.N., and D. Subrahmanyam, 1982: The 30-50 day mode at 850 mb during MONEX. *J. Atmos. Sci.*, **39**, 2088-2095.

Larsen, M.F., S. Fukao, O. Aruga, M.D. Yamanaka, T. Tsuda, and S. Kato, 1991: A comparison of VHF radar vertical-velocity measurements by a direct vertical-beam me ıod and by a VAD technique. *J. Atmos. Oceanic Technol.*, **8**, 766-776.

Lau, K.M., and L. Peng, 1987: Origin of low-frequency (Intraseasonal) oscillations in the t ıpical atmosphere. Part I: Basic theory. *J. Atmos. Sci.*, **44**, 950-972.

Leary, C.A., 1984: Precipitation structure of the cloud clusters in a tropical easterly wave. *Ion. Wea. Rev.*, **112**, 313-325.

Leary, C.A., and R.A. Houze, Jr., 1979a: The structure and evolution of convection in a tı pical cloud cluster. *J. Atmos. Sci.*, **36**, 437-457.

Leary, C.A., and R.A. Houze, Jr., 1979b: Melting and evaporation of hydrometeors in precipitation from the anvil clouds of deep tropical convection. *J. Atmos. Sci.*, **36**, 66( 579.

Leary, C.A., A.L. Doggett, IV, and G.M. Jurica, 1993: Navigational Uncertainties in the TOGA COARE shipboard radar data: Implications for echo locations and Doppler velocities. Report to the TOGA COARE International Project Office, 20pp. and Appendix (236pp.).

LeMone, M.A., and E.J. Zipser, 1980: Cumulonimbus vertical velocity events in GATE. Part I: Diameter, intensity, and mass flux. *J. Atmos. Sci.*, **37**, 2444-2457.

LeMone, M.A., and D.P. Jorgensen, 1991: Precipitation and kinematic structure of an oceanic mesoscale convective system. Part II: Analysis of in-situ data and momentum fluxes. *Mon. Wea. Rev.*, **119**, 2638-2653.

Ligda, M.G.H., 1956: The radar observations of mature prefrontal squall lines in the midwestern United States. *VI Congress of Organisation Scientique et Technique Internationale du Vol a Voile (OSTIV)*, St-Yan, France, 6-14 July, publication IV.

Lin, X., and R.H. Johnson, 1994: Heat and moisture budgets and circulation characteristics of a frontal squall line. *J. Atmos. Sci.*, **51**, 1661-1681.

Lucas, C., E.J. Zipser, and M.A. LeMone, 1994: Vertical velocity in oceanic convection off tropical Australia. *J. Atmos. Sci*, **51**, 3183-3193.

Luo, H., and M. Yanai, 1984: The large-scale circulation and heat sources over the Tibetan Plateau and surrounding areas during the early summer of 1979. Part II: Heat and moisture budgets. *Mon. Wea. Rev.*, **112**, 966-989.

Madden, R.A., and P.R. Julian, 1972: Description of global-scale circulation cells in the tropics with a 40-50-day period. *J. Atmos. Sci.*, **29**, 1109-1123.

Mapes, B., and R.A. Houze Jr., 1993a: An integrated view of the 1987 Australian monsoon and its mesoscale convective systems. II: Vertical structure. *Quart. J. Roy. Meteor. Soc.*, **119**, 733-754

Mapes, B., and R.A. Houze Jr., 1993b: Cloud clusters and superclusters over the oceanic warm pool. *Mon. Wea. Rev.*, **121**, 1398-1415.

Marshall, J.S., and W. Palmer, 1948: The distribution of raindrops with size. *J. Meteorol.*, **5**, 165-166.

Matejka, T., 1993: Concurrent Extended Vertical Velocity Azimuth Display (CEVAD) analysis of single-Doppler radar data. Preprints, *26th Int. Conf. on Radar Meteorology*, Norman, Oklahoma, Amer. Meteor. Soc, 463-465.

Matejka, T., and R.C. Srivastava, 1991: An improved version of the Extended Velocity-Azimuth Display Analysis of single-Doppler radar data. *J. Atmos. Oceanic Technol.*, **8**, 453-466.

May, P.T., 1995: The organisation of convection in the rainbands of tropical cyclone Laurence. *Mon. Wea. Rev.*, submitted.

Mohr, C.G., and L.J. Miller, 1983: CEDRIC - a software package for cartesian space edi ıg, synthesis, and display of radar fields under interactive control. Preprints, *21st Conf. ( Radar Meteorology.*, Edmonton, Alta., Canada. Amer. Meteor. Soc., 559-574.

Newton, C.W., 1950: Structure and mechanism of the prefrontal squall line. *J. Meteor.*, **7** 210-222.

O'Brien, J.J., 1970: Alternative solutions to the classical vertical velocity problem. *J. Appl Meteor.*, **9**, 197-203.

Ogura, Y., and M.T. Liou, 1980: The structure of a midlatitude squall line. *J. Atmos. Sci.* **37**, 553-567.

Orville, R.E., and R.W. Henderson, 1986: Global distribution of midnight lightning: Sept ıber 1977 to August 1978. *Mon. Wea. Rev.*, **114**, 2640-2653.

Petersen, W., 1992: Cloud-to-ground lightning in tropical mesoscale convective systems. I .S. thesis, Dept. of Atmos. Sci., Colorado State Univ., 225pp. [Atmos. Sci. Paper No. 5 3]

Petersen, W.A., R. Cifelli, S.A. Rutledge, and B.F. Smull, 1995: Cloud-to-ground lightn g and the related kinematic structures of two tropical oceanic MCS's: Contrasting cases. Pr ırints, *Conf. on Cloud Phys.*, 75th Annual Meeting, Dallas, Texas, Amer. Meteor. Soc., 55 -558.

Ralph, F.M., 1995: Using radar-measured radial vertical velocities to distinguish precipita ın scattering from clear-air scattering. *J. Atmos. Oceanic Technol.*, **12**, 257-267.

Ralph, F.M., M. Crochet, and S.V. Venkateswaran, 1993: Observations of a mesoscale d ıted gravity wave. *J. Atmos. Sci.*, **50**, 3277-3291.

Ramage, C.S., 1968: Role of a tropical "Maritime Continent" in the atmospheric circulati ı. *Mon. Wea. Rev.*, **96**, 365-370.

Randell, S.C., S.A. Rutledge, R.D. Farley, and J.H. Helsdon, Jr., 1994: A modeling stu on the early electrical development of tropical convection: Continental and oceanic (monsoo storms. *Mon. Wea. Rev.*, **122**, 1852-1877.

Rasmussen, E.N., and S.A. Rutledge, 1993: Squall line evolution. Part I: Kinematic and reflectivity structure. *J. Atmos. Sci.*, **50**, 2584-2606.

Ray, P.S., C.L. Ziegler, and W. Bumgarner, 1980: Single- and multiple-Doppler radar observations of tornadic storms. *Mon. Wea. Rev.*, **108**, 1607-1625.

Rickenbach, T.M., 1995: Rainfall production from the spectrum of convection observed b shipboard radar during TOGA COARE. TOGA COARE. Preprints, *21st Conf. on Hurricanes and Tropical Meteorology*, Miami, Florida, Amer. Meteor. Soc., 116-11 .

Riehl, H., and J.S. Malkus, 1958: On the heat balance in the equatorial trough zone. *Geo tysica*, **6**, 503-538.

Rogers, R.R., W.L. Ecklund, D.A. Carter, K.S. Gage, and S.A. Ethier, 1993: Research applications of a boundary-layer wind profiler. *Bull. Amer. Meteor. Soc.*, **74**, 567-580.

Rosenfeld, D., D.B. Wolff, and D. Atlas, 1993: General probability-matched relations between radar reflectivity and rain rate. *J. Appl. Meteor.*, **32**, 50-72.

Rosenfeld, D., E. Amitai, and D.B. Wolff, 1995a: Classification of rain regimes by the three-dimensional properties of reflectivity fields. *J. Appl. Meteor.*, **34**, 198-211.

Rosenfeld, D., E. Amitai, and D.B. Wolff, 1995b: Improved accuracy of radar WPMM estimated rainfall upon application of objective classification criteria. *J. Appl. Meteor.*, **34**, 212-223.

Rutledge, S.A.,1991: Middle latitude and tropical mesoscale convective systems. *Rev. Geophys. (Supplement)*, **29**, 88-97.

Rutledge, S.A., and R.A. Houze, Jr., 1987: A diagnostic modeling study of the trailing stratiform region of a midlatitude squall line. *J. Atmos. Sci.*, **44**, 2640-2656.

Rutledge, S.A., E.R. Williams, and T.D. Keenan, 1992: The Down Under Doppler and Electricity Experiment (DUNDEE): Overview and preliminary results. *Bull. Amer. Meteor. Soc.*, **73**, 3-16.

Rutledge, S.A., R.A. Houze Jr., M.I. Biggerstaff, and T. Matejka, 1988: The Oklahoma-Kansas mesoscale convective system of 10-11 June 1985: Precipitation structure and single-Doppler radar analysis. *Mon. Wea. Rev.*, **116**, 1409-1430.

Rutledge, S.A., R. Cifelli, C. DeMott, W. Petersen, T. Rickenbach, J. Lutz, R. Bowie, M. Strong, and E. Williams, 1993: The shipboard deployment of the MIT C-band radar during TOGA COARE. Preprints, *26th Int. Conf. on Radar Meteorology*, Norman, Oklahoma, Amer. Meteor. Soc., 371-373.

Sato, T., H. Doji, H. Iwai, I. Kimura, S. Fukao, M. Yamamoto, T. Tsuda and S. Kato, 1990: Computer processing for deriving drop-size distributions and vertical air velocities from VHF Doppler radar spectra. *Radio Sci.*, **25**, 961-973.

Short, D.A., T. Kozu, K. Nakamura, and T.D. Keenan, 1993: On stratiform rain in the tropics. *J. Meteor. Soc. Japan*, submitted.

Simpson, J., R.F. Adler and G.R. North, 1988: A proposed Tropical Rainfall Measuring Mission (TRMM) satellite. *Bull. Amer. Meteor. Soc.*, **69**, 278-295.

Smull, B.F., and R.A. Houze, Jr., 1985: A midlatitude squall line with a trailing region of stratiform rain: Radar and satellite observations. *Mon. Wea. Rev.*, **113**, 117-133.

Smull, B.F., and R.A. Houze, Jr., 1987a: Dual-Doppler radar analysis of a midlatitude squall line with a trailing region of stratiform rain. *J. Atmos. Sci.*, **44**, 2128-2148.

Smull, B.F., and R.A. Houze, Jr., 1987b: Rear inflow in a squall line with trailing stratiform precipitation. *Mon. Wea. Rev.*, **115**, 2869-2889.

Sommeria, G. and J. Testud, 1984: COPT 81: A field experiment designed for the study o dynamics and electrical activity of deep convection in continental tropical regions. *Bu Amer. Meteor. Soc.*, **65**, 4-10.

Srivastava, R.C., T.J. Matejka and T.J. Lorello, 1986: Doppler radar study of the trailing nvil region associated with a squall line. *J. Atmos. Sci.*, **43**, 356-377.

Steiner, M., and R.A. Houze, Jr., 1993: Three-dimensional validation at TRMM ground-t ıth sites: Some early results from Darwin, Australia. Preprints, *26th Int. Conf. on Radar Meteorology*, Norman, Oklahoma, Amer. Meteor. Soc., 417-420.

Szoke, E.J., E.J. Zipser, and D.P. Jorgensen, 1986, A radar study of convective cells in mesoscale systems in GATE. Part I: Vertical profile statistics and comparison with hurricanes. *J. Atmos. Sci.*, **43**, 182-197.

Tao, W.K., J. Simpson, C.H. Sui, B. Ferrier, S. Lang, J. Scala, M.D. Chou, and K. Pic ering, 1993: Heating, moisture, and water budgets of tropical and middle latitude squall line : Comparisons and sensitivity to longwave radiation. *J. Atmos. Sci.*, **50**, 673-690.

Thompson, R.M., Jr., S.W. Payne, E.E. Recker and R.J. Reed, 1979: Structure and pro rties of synoptic-scale wave disturbances in the Intertropical Convergence Zone of the eas rn Atlantic. *J. Atmos. Sci.*, **36**, 53-72.

Wakasugi, K., A. Mizutani, M. Matsuo, S. Fukao, and S. Kato, 1986: A direct method f deriving drop-size distribution and vertical air velocities from VHF Doppler radar sp tra. *J. Atmos. Oceanic Technol.*, **3**, 623-629.

Wakasugi, K., A. Mizutani, M. Matsuo, S. Fukao, and S. Kato, 1987: Further discussion n deriving drop-size distribution and vertical air velocities from VHF Doppler radar sp tra. *J. Atmos. Oceanic Technol.*, **4**, 170-179.

Waldteufel, P., and H. Corbin, 1979: On the analysis of single-Doppler radar data. *J. Ap Meteor.*, **18**, 532-542.

Webster, P.J., and R. Lukas, 1992: TOGA COARE: The Coupled Ocean-Atmosphere R ponse Experiment. *Bull. Amer. Meteor. Soc.*, **73**, 1377-1416.

Williams, E., and N. Renno, 1993: An analysis of the conditional instability of the tropic atmosphere. *Mon. Wea. Rev.*, **121**, 21-36.

Williams, E.R., S.A. Rutledge, S.G. Geotis, N. Renno, E. Rasmussen, and T. Rickenba ı, 1992: A radar and electrical study of tropical "hot towers". *J. Atmos. Sci.*, **49**, 1386-1395.

Willis, P.T., R.A. Black, and F.D. Marks, Jr., 1995: Airborne rain drop size distributio in TOGA COARE. Preprints, *21st Conf. on Hurricanes and Tropical Meteorology*, Mi ni, Florida, Amer. Meteor. Soc., 431-433.

Yanai, M., S. Esbensen and J. H. Chu, 1973: Determination of bulk properties of tropic cloud clusters from large-scale heat and moisture budgets. *J. Atmos. Sci.*, **30**, 611-627.

Yoe, J.G., M.F. Larsen, and E.J. Zipser, 1992: VHF wind-profiler data quality and comparison of methods for deducing horizontal and vertical air motions in a mesoscale convective storm. *J. Atmos. Oceanic Technol.*, **9**, 713-727.

Young, K.C., 1993: *Microphysical Processes in Clouds*. Oxford University Press, 427pp.

Zipser, E.J., 1969: The role of organized unsaturated convective downdrafts in the structure and rapid decay of an equatorial disturbance. *J. Appl. Meteor.*, **8**, 799-814.

Zipser, E.J., and M.A. LeMone, 1980: Cumulonimbus vertical velocity events in GATE. Part II: Synthesis and model core structure. *J. Atmos. Sci.*, **37**, 2458-2469.

Zipser, E.J., and K. Lutz, 1994: The vertical profile of radar reflectivity of convective cells: A strong indicator of storm intensity and lightning probability? *Mon. Wea. Rev.*, **122**, 1751-1759.

Zipser, E.J., R.J. Meitin, and M.A. LeMone, 1981: Mesoscale motion fields in association with a GATE convection band. *J. Atmos. Sci*, **38**, 1725-1750.

## Appendix A

# COMPARISON OF VHF WIND PROFILER AND MICROWAVE RADAR: SCATTERING MECHANISMS AND SAMPLING GEOMETRY

## A1 Review of scattering from clear air and precipitation

In general, the echoing mechanism for the wind profiler and scanning radar depends o the wavelength of the observing system. The reflectivity associated with clear air turbulence sc tter (i.e., Bragg scatter) has a weak dependence on wavelength compared to Rayleigh scattering from precipitation targets as shown below in (A1).

$$\eta_a = 0.38 C_n^2 \lambda^{-1/3} \quad \text{A1a)}$$

$$\eta_p = \frac{\pi^5 |K|^2 Z_e}{\lambda^4} \quad \text{A1b)}$$

In A1, $\eta_a$ is the reflectivity associated with clear air, $\eta_p$ is the reflectivity associated with precipitation, $\lambda$ is wavelength, $C_n^2$ is the refractive index structure parameter, $|K|^2$ is the di lectric constant for water, and $Z_e$ is the effective radar reflectivity factor. (A1) shows that Rayleig h scattering is enhanced at shorter wavelengths compared to Bragg scattering.

Echoing from clear air arises from irregularities in the radio refractive index associat d with small scale turbulence of a scale size equal to half the wavelength of the radar (Gage 1990) Thus, a 50 MHz VHF radar is most sensitive to 3 m size irregularities. In the troposphere, gradi nts in

the refractive index are dominated by water vapor and atmospheric pressure as well as temperature changes. Gossard et al. (1984) has shown that in order to observe atmospheric turbulence, the clear air sensing radar must have a half wavelength greater than $\sim 4.2\, l_o$, where $l_o$ is the inner scale of turbulence. $l_o$ is proportional to the Kolmogorov microscale $\eta_o = (\nu^3/\epsilon)^{1/4}$ where $\nu$ is the kinematic viscosity and $\epsilon$ is the eddy dissipation rate. Since $\nu$ increases with height, longer wavelength radars are needed to observed turbulence in the middle atmosphere (Balsley and Gage 1980).

The wavelength dependence of scattering is commonly combined into an expression which shows the amount of Rayleigh scattering (expressed as the radar reflectivity factor $Z$ in $mm^6\ m^{-3}$) that would produce the same amount of backscattered power as a specified variability in the clear air refractive index ($C_n^2$ in $m^{-2/3}$) as

$$dBZ = 10(\log_{10} C_n^2 + \log_{10} \lambda^{11/3} + 15.13), \qquad \text{(A2)}$$

where $dBZ = 10 \log_{10} Z$ is the reflectivity (Gossard 1988; Rogers et al. 1993; Ralph 1995). Figure A1, taken from Ralph (1995,) shows a plot of $C_n^2$ versus $dBZ$ and identifies typical ranges of radar reflectivity factor $Z$ for which Rayleigh scattering will likely dominate clear air echo returns for different wavelength radars. For $C_n^2$ values of $10^{-15}$-$10^{-13}$ (representative of moderate to severe turbulence in thunderstorms; Chilson et al. 1993), a VHF profiler will have a contribution from both Bragg (clear air) and Rayleigh (precipitation) scattering for reflectivity values ranging from 30-50 (typical of heavy rainfall in a thunderstorm). In contrast, a 5-cm radar is sensitive to Rayleigh scattering from cloud and precipitation targets only for all $dBZ$ values above $\sim$ -28. It is this property of wavelength dependence in scattering that makes VHF profilers an appropriate frequency to retrieve vertical air motions in the presence of precipitation.

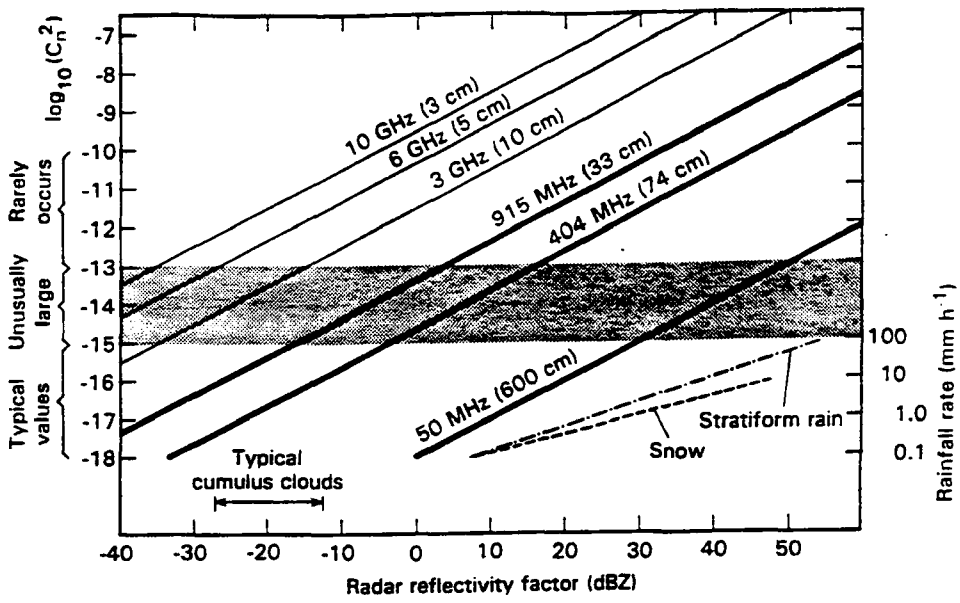


Fig. A1. Diagram for Rayleigh scattering from precipitation targets (expressed in *dBZ*) versus Bragg scattering from clear air (expressed as $\log_{10}C_n^2$) for weather and clear air radars. Lines for clear air (heavy bold) and weather (bold) radars show the amount of Rayleigh scattering that is equivalent to a given amount of Bragg scattering for each radar frequency (wavelength), based on Eq. (A2). The shaded region represents the transition from conditions for which Bragg scattering usually dominates (i.e., weak Rayleigh scattering) to those for which Rayleigh scattering will almost always dominate under normal atmospheric conditions observed outside the convective boundary layer and mantle echoes. *Z-R* relationships for stratiform rain and snow are also shown (from Ralph 1995).

## A2 Sampling geometry of scanning radar and wind profiler platforms

In order to place wind profiler and scanning Doppler radar retrieval results in proper context, it is necessary to examine the sampling dimensions of each instrument. For a vertically pointing wind profiler in a region of relatively small vertical wind shear, the volume of atmosphere sampled by the profiler beam is conical with horizontal dimensions proportional to the profiler beamwidth. Because of the dwell time and averaging process described in Ch. 2, the geometry of the profiler sampling region at any given height becomes elliptical, with increasing eccentricity as the length of the averaging interval increases and/or the convective system advection speed increases. The major axis of the ellipse is parallel to the direction of storm motion (see Fig. A2 and Table A1). Note that the orientation of the ellipse can vary with height in regions containing large vertical shear of the horizontal wind (e.g. in an MCS with intense storm relative flow).

In contrast, the 5-cm radars collected data by scanning the beam through 360° of azimuth over a range of elevation angles. Assuming nearly continuous radar echo coverage around the radar, the sampling volume for any of the single Doppler retrieval techniques is cylindrical, so that at any given height, the sampling area is approximately constant (circular)[8]. For a cylinder with radius 30 km, the total sampling area is $\sim$2800 km$^2$. In contrast, the wind profiler samples only a small fraction of this area at any given height (Table A1). The results in Table A1 indicate that any comparison of kinematic structures between the two platforms will have to account for the large differences in spatial sampling. In this study, the sampling time scales have at least been made similar; nevertheless it must be emphasized that the atmospheric volume sampled by each

---

[8] During the time required to collect a complete volume of radar data (8-10 minutes), the radar sampling region is modified as described above for the wind profiler. However, in the case of the scanning radar, the change in sampling geometry during data collection is relatively small, due to the large region of atmosphere sampled by the radar relative to the storm advection speed (Matejka and Srivastava 1991).

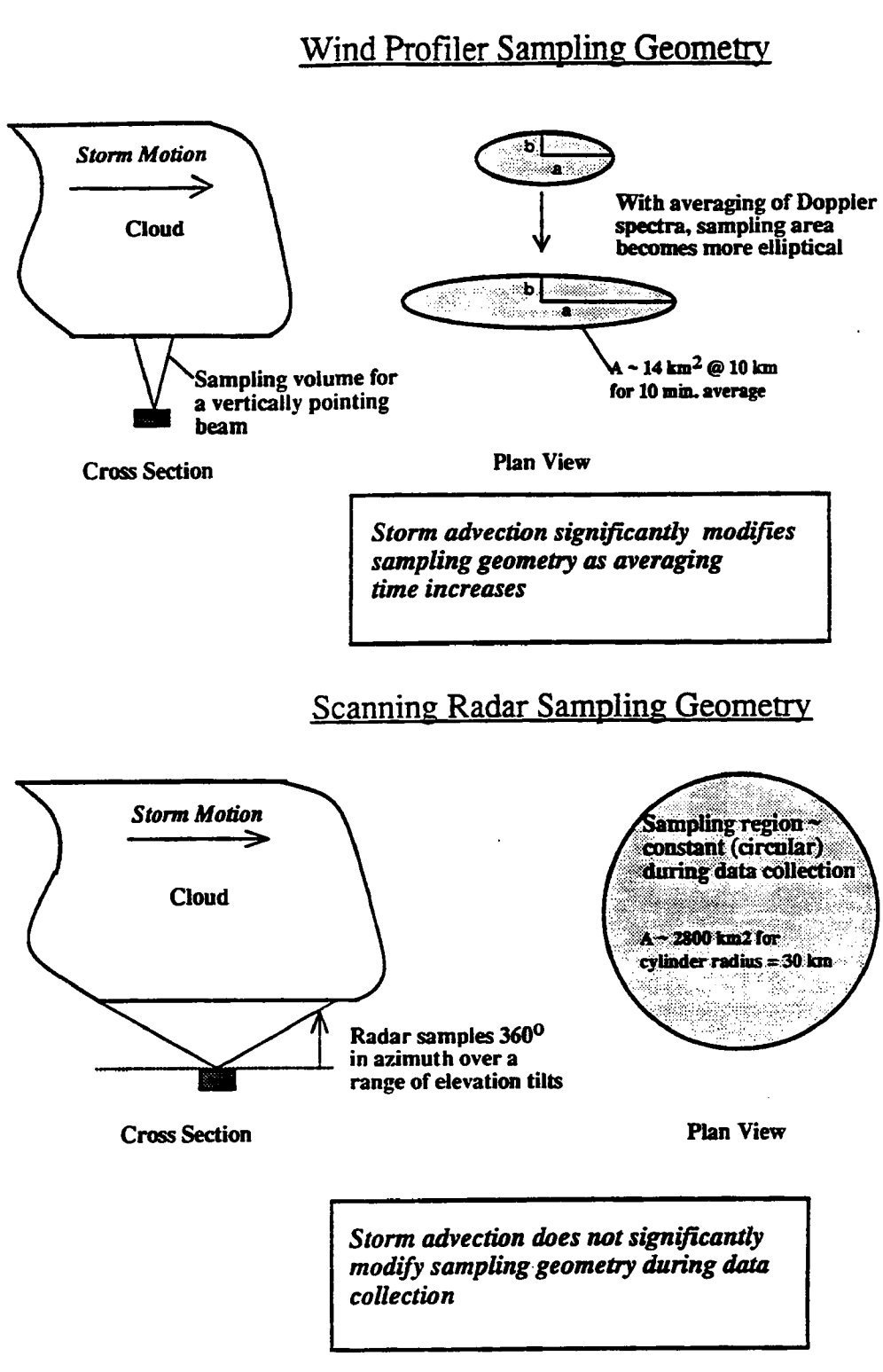


Fig. A2. Schematic diagram showing the sampling geometry and area of the 50 MHz wind profiler (top) and the 5-cm Doppler radars (bottom; from Cifelli et al. 1995).

Table A1. Sampling area calculations for the wind profiler compared to the single Doppler radar. The calculations are performed for an arbitrary height of 10 km and assume a storm speed of 10 $ms^{-1}$ over the profiler [parallel to the major axis (a)]. Note that the profiler area is an ellipse with increasing eccentricity (major axis length) as the averaging time increases (see Fig. A2). It is assumed that the single Doppler sampling domain is approximately cylindrical with a radius of 30 km so that the area at any height is constant (Cifelli et al. 1995).

| Avg. Interval (min) | Major Axis [a] (km) | Minor Axis [b] (km) | Profiler Sampling Area [$\pi$*a*b] ($km^2$) | Radar Sampling Area [$\pi$*$r^2$] ($km^2$) | Fraction of Radar Area (%) |
|---|---|---|---|---|---|
| 5 | 4.6 | 0.6 | 8.7 | 2827 | ~0.3 |
| 10 | 7.6 | 0.6 | 14.3 | 2827 | ~0.5 |
| 15 | 10.6 | 0.6 | 20.0 | 2827 | ~0.7 |
| 30 | 19.6 | 0.6 | 36.9 | 2827 | ~1.3 |
| 100 | 61.6 | 0.6 | 116.1 | 2827 | ~4.1 |

platform is quite distinct, even when the profiler data are averaged over a relatively long sampling period.

For a volume of atmosphere that is sampled by the wind profiler and radar at the same time but different spatial scales, differences in the diagnosed fields may be attributed to some combination of the following:

a. biases in the wind profiler data resulting from contamination of the precipitation component of the Doppler spectra with the turbulence component of the spectra (contamination by precipitation will introduce a negative (downward) bias in the profiler vertical velocity estimates);
b. errors due to the evolution of the divergence and vertical velocity fields during the sampling period;

c. application of an inappropriate top boundary condition for single Doppler retrieval analysis; and

d. non-homogeneities in the horizontal divergence and vertical velocity fields across the analysis domain (differences in the region sampled by the profiler and the single Doppler radars)- the meteorologically significant variability.

As discussed in Ch. 2, clear air Doppler spectra obtained in the MCSs studied herein were susceptible to precipitation contamination in the elevation range of 3.5 to 6.5 km of each MCS. In this altitude range, air motion estimates were shifted over 2 m $s^{-1}$ on average to correct for the effects of precipitation (Cifelli and Rutledge, 1994b). Although the wind profiler vertical motion estimates were adjusted to account for precipitation bias, the possibility that the vertical velocity estimates have considerable error in some of the range gates cannot be entirely ruled out.

In regard to potential errors resulting from the evolution of divergence and vertical motion fields during sampling (see b above), Cifelli and Rutledge (1994b) showed that the wind profiler vertical motion (divergence) fields in the stratiform portions of the convective systems they studied were relatively stable for averaging periods of 5-15 minutes. It was not possible to perform a similar sensitivity study for the scanning radar data since the sampling period was fixed. However, retrievals that could be performed at consecutive (10 minute) intervals showed little difference in the diagnosed profiles, suggesting that the kinematic fields did not evolve appreciably during sampling (at least at spatial scales measured by the radar: 0.5-1.0 km).

Potential error source (c) and the scale-difference effect (d) above are discussed in Appendices B and C and in Cifelli et al. (1995). It is simply noted here that it is difficult to directly compare the kinematic structures diagnosed from each observation platform, not only due

to potential errors in the analysis methods, but also due to the large variability in the wind profiler estimates of vertical motion resulting from small-scale turbulence features.

## Appendix B

## COMPARISON OF HORIZONTAL DIVERGENCE AND VERTICAL MOTION RETRIEVALS FROM SCANNING RADAR AND WIND PROFILER

In this Appendix, a comparison of two single-Doppler techniques and the wind profiler retrieval to analyze vertical motions and horizontal divergence patterns in the stratiform portions of MCSs is provided. The scanning Doppler radar techniques are:

- EVAD (Extended Velocity Azimuth Display; Srivastava et al. 1986; Matejka and Srivastava 1991); and
- CEVAD (Concurrent Extended Velocity Display; Matejka 1993).

In these single-Doppler techniques, the kinematics of the mesoscale velocity field is analyzed. The wind profiler technique, on the other hand, makes a direct measurement of vertical motion (Cifelli and Rutledge 1994b). Both the Doppler radar and the wind profiler techniques require removing the effects of hydrometeor fall speeds. For the Doppler radar methods, these must be separated from the horizontal divergence, which can be integrated to produce an estimate of vertical air motion. For the wind profiler technique, it must be separated from the detected vertical velocity itself (Carter et al. 1991).

Each analysis technique has its strengths and weaknesses. The scanning Doppler radars provide an estimate of the mesoscale wind field within a relatively large volume and in short time. Because the scanning radar techniques are designed to analyze mesoscale flow patterns, the resulting horizontal divergence and vertical air velocity profiles appear smooth compared to those obtained from the wind profiler. However, for the scanning radar analyses to be performed, relatively large volumes filled with echo are required, limiting the situations in which the methods can be applied. The wind profiler, on the other hand, makes measurements over a relatively small spatial domain, enabling this technique to resolve small-scale variations in the vertical motion pattern. Unlike the microwave scanning radars, the profiler technique is also able to obtain these measurements in clear air. The resulting detailed vertical velocity structure is often rather complicated (and possibly noisy if the hydrometeor velocity signal is not easy to remove). Individual profiles may not be representative of the mesoscale flow. However, the mesoscale vertical velocity pattern can be reclaimed by time averaging the wind profiler retrievals (Cifelli et al. 1995). Thus, the wind profiler and scanning radar techniques are complimentary.

Another disadvantage of the scanning radar techniques is that, since they retrieve vertical profiles of horizontal divergence, one or more boundary conditions must be specified before the mass continuity equation can be integrated to produce a profile of vertical air velocity ($w$). These boundary condition assumptions can introduce error, especially in situations where data collection does not extend to a $w=0$ level at the top of the cloud system. Such an effect would result when, for example, Doppler radar data are subject to significant attenuation or when upward motion extends beyond the minimum-detectable echo boundary. The profiler technique, by measuring $w$ directly, avoids the need for specified boundary conditions.

To compare and contrast the EVAD, CEVAD, and profiler techniques, vertical profiles of horizontal divergence and vertical air velocity in several tropical MCSs near Darwin, N.T., Australia that were observed during the DUNDEE were examined and the results interpreted in light of the strengths and weaknesses of the four techniques used (Cifelli et al. 1995). Herein, a brief description of each of the single-Doppler analysis techniques is provided.

## B1. EVAD analysis

The EVAD algorithm consists of two steps:

1) Traditional VAD (Browing and Wexler 1968) analysis, which analyzes horizontal rings of radial velocity data for each elevation cone within a specified vertical cylinder of radar data to determine the mean horizontal wind field; and

2) EVAD analysis which separates the combined effect of divergence and precipitation fall speed from the VAD derived horizontal wind field and calculates divergence, hydrometeor fall speed, hydrometeor terminal fall speed, and vertical velocity as a function of altitude within a specified volume of VAD data.

In VAD, the radar data are divided into horizontal rings centered on the radar and a truncated Fourier series is used to model the radial velocity field $\bar{v}_r$ according to:

$$\bar{v}_r = \sum_{i=1}^{7} a_i f_i(\phi) + \bar{\epsilon} \qquad \text{(B1)}$$

where $f_1 = 1, f_2 = \sin\phi, f_3 = \cos\phi, f_4 = \sin 2\phi, f_5 = \cos 2\phi, f_6 = \sin 3\phi, f_7 = \cos 3\phi$, $\phi$ = azimuth angle, $a_i$ represents the particular Fourier coefficient, and $\bar{\epsilon}$ is the departure of the regression model from the actual observations (Matejka and Srivastava 1991). It is important to note that in the VAD analysis, reliable solutions for the Fourier coefficients ($a_i$) are typically obtained in situations where the wind field is relatively uniform (stratiform as opposed to convective portions of precipitating regions) and nearly complete echo coverage surrounds the radar[9]. In the ideal situation, the wind data are approximately evenly spaced around the radar so that the basis functions $f_i$ in (B1) form an orthogonal set and the regression is not particularly sensitive to departures from the model assumptions (Matejka and Srivastava 1991).

Radar volume scans were scrutinized to determine the suitability of the EVAD technique for each volume of data. A total of 37 retrievals were generated from radar volumes collected in the four MCSs. Within a specific volume of data, radar elevation angles ranged from 1-45° (most of the time) or 1-60° (occasionally). The time required for the radar to complete an individual VAD volume scan was approximately 8-10 minutes.

In order to apply EVAD, it is assumed that both hydrometeor fall speed and divergence are horizontally uniform within a specified vertical layer. The depth of each layer is determined from the radar gate spacing (usually 500 m for the particular radar data used in this study) and is

---

[9] Matejka and Srivastava (1991) recommend that the EVAD technique be applied in situations where the largest azimuthal gap in radar echo coverage surrounding the radar is $\sim \leq 30°$.

constant throughout the EVAD volume. Moreover, it is assumed that there are no significant temporal variations in the wind field during the radar volume sampling period.

For a given height interval containing multiple rings, both particle fall speed and divergence may be determined from a weighted least squares fit independently in each layer (Srivastava et al. 1986; Matejka and Srivastava 1991; Matejka 1993) according to:

$$\frac{2a_0}{r\cos(\alpha)} = D + W_p \frac{2\sin(\alpha)}{r\cos(\alpha)} \tag{B2}$$

where $D$ = horizontal divergence, $W_p$ = hydrometeor vertical velocity ($w$ - $V_t$; $V_t$ is the hydrometeor terminal fall speed), $a_o$ = the VAD estimated zeroth Fourier coefficient, $\alpha$ is the elevation angle of the radar beam, and r is the radius of the analysis domain.

Vertical velocity within the EVAD analysis domain is calculated by integrating the anelastic form of the mass continuity equation. In order to account for errors accumulated in the integration, a variational method similar to that employed by O'Brien (1970) is used to obtain a modified profile of divergence (see equations (21) and (22) of Matejka and Srivastava 1991).

The altitude of the highest echo from one of the three steepest elevation scans analyzed in VAD was utilized as the location of the EVAD top boundary and it was assumed that the vertical velocity at this point was zero. It was also assumed that the vertical velocity was zero at the altitude of the radar (essentially sea level). For the MCSs studied, the EVAD analysis domain radius was set at 30 km, which allowed for considerable overlap in data coverage between the MIT and TOGA radars when both systems were collecting simultaneous data (Fig. 2.1).

## B2 CEVAD analysis

CEVAD is identical to EVAD except for two important aspects. In CEVAD, the solution is obtained by an optimization of (B2) throughout all the layers concurrently, not independently as for EVAD. In addition, the top boundary condition is formulated in terms of hydrometeor terminal fall speed. As we shall see, using terminal fall speed as the top boundary condition can be useful in situations where radar echo does not extend high enough to reliably set a vertical air motion boundary condition at the upper boundary. Because the CEVAD method is formulated with linked adjustments in all the layers, the sensitivity of the solution to the top boundary condition is reduced (Matejka, 1993). The variational adjustment of the divergence profile in CEVAD is incorporated into the concurrent optimization of (B2) rather than imposed subsequently as in EVAD.

Sensitivity analyses were performed on the selection of terminal fall speed values at the upper boundary in all radar volumes using the CEVAD technique. Fall speeds were varied from 0.5 to 2.0 m $s^{-1}$ and, in general, the results were not particularly sensitive to the value selected. Therefore, for comparison purposes, a terminal fall speed value of 1.0 m $s^{-1}$ was chosen as the upper boundary condition in all of the radar volumes analyzed with CEVAD.

## Appendix C

# DESCRIPTION OF TWO EQUATION AND THREE (OR FOUR) EQUATION SYNTHESIS OF MULTIPLE DOPPLER DATA

## C1 Dual-Doppler synthesis from ship data

Dual-Doppler synthesis was performed on one convective system that was sampled by the MIT and TOGA ship radars. A total of 15 volumes were collected over about a 2.5 hour period and analyzed with the two equation solution (Ray et al. 1980) using the CEDRIC (Custom Editing and Display of Reduced Information in Cartesian space; Mohr and Miller 1983) software to recover the three-dimensional wind field properties. The radar data were first interpolated onto a Cartesian grid using a Cressman weighting scheme with a 1.5 km radius of influence in the horizontal and 1.0 km in the vertical (Ray et al. 1980). The grid spacing was specified to be 1 km in the horizontal and 0.5 km in the vertical. In CEDRIC, an iterative procedure is used to retrieve the horizontal wind and diagnose vertical motion as follows:

1) the $U$ and $V$ components of the wind are calculated from the radial wind estimates assuming there is no vertical motion ($w$);
2) horizontal divergence is calculated from the initial $U$ and $V$ estimates;
3) an initial estimate of $w$ is then diagnosed using the anelastic form of the continuity equation;
4) the horizontal wind components ($U,V$) are re-computed;
5) steps 2-5 are performed until the change in $U,V$ is less than the expected measurement error.

For each CEDRIC run, a one-step Leise filter and patching function were applied to the horizontal winds one time after the initial synthesis in order to remove "spikey" data and smooth the resulting wind field. The vertical velocity was set to zero at a distance of 500 m above the highest measured divergence in each grid column. Vertical air motion was calculated by integrating the anelastic form of the mass continuity equation downward from the top boundary condition in order to take advantage of the density weighting and to minimize errors. The convergence criteria was usually achieved in less than four iterations. In the final step of the analysis, a variational adjustment scheme following O'Brien (1970) was used and mass was redistributed through the grid column to account for uncertainties in the divergence estimates.

### C2 Quad-Doppler synthesis from P-3 data

A total of 12 radar volumes collected by the NOAA P-3 radars from three convective events were provided, courtesy of Brad Smull, Dave Jorgensen, and Sharon Lewis of NOAA/NSSL/MRD (Mesoscale Research and Applications Division, National Severe Storms Lab). All of the volumes used in this study were analyzed using the Quad-Doppler technique described by Jorgensen et al. (1996). Briefly, this method takes advantage of the FAST (Fore/Aft Scanning Technique) strategy employed by both P-3 radar aircraft flying along parallel flight tracks. Each data point in the analysis domain is sampled four times by the two radars since the tail-mounted radars scan for and aft of a line perpendicular to the aircraft heading. A linear interpolation was used to transform the radar data from polar to Cartesian coordinates with a horizontal spacing of 1.5 km and a vertical spacing of 1.0 km. A combination of the overdetermined dual and overdetermined triple Doppler solution syntheses were then applied to each data point to calculate the horizontal wind, depending on which method produced the least error (Jorgensen et al. 1996). The triple solution was applied at echo top to calculate the echo-top

particle motion $W_p$, which was then used to derive the echo top vertical air motion $w$ ($= V_t + W_p$). In principle, the fourth radial velocity measurement is not needed in the analysis; however, it was found to reduce errors in the estimate of $W_p$. The major advantage to this sort of scanning strategy and the resulting synthesis of radar data is that $W_p$ can be measured directly, allowing for a more reliable estimate of $w$ at radar echo top compared to assuming $w = 0$ (Jorgensen et al. 1996).

Jorgensen et al (1996) noted that the overdetermined synthesis procedure (e.g., quad-Doppler sampling) can produce vertical air motions that are over 50% larger compared to the dual-Doppler sampling produced from one radar alone due to the better estimate of $w$ at the radar echo top (as opposed to assigning $w = 0$). The effect was most noticeable in the upper regions of the cloud, since both the two equation and four equation solutions apply a $w = 0$ constraint at the bottom boundary. LeMone and Jorgensen (1991) and Cifelli et al. (1995) have observed similar situations where the diagnosed vertical air motion field has been underestimated due to inadequate measurements of upper level divergence and assuming $w = 0$ at the radar echo top.

## Appendix D

## DARWIN RAINFALL STATISTICS

### D1 Rain gauge results for each MCS

This appendix lists rainfall statistics from each reporting gauge for each MCS event. The location of the Darwin rain gauge network relative to the TOGA radar for the 1989-1990 and 1990-1991 wet seasons is provided in Table D1. Summaries of the partitioned rainfall fraction from each gauge are shown in Tables D2-D14. Individual rain traces for each event analyzed in this study are shown in Figs. D1-D13.

Table D1. Location of AWS Rain Gauge Network Relative to TOGA Radar.

| Station ID | Distance (km) | Azimuth (°) | x (km east) | y (km north) |
|---|---|---|---|---|
| ANN | 96 | 122 | 81 | -51 |
| BATC | 67 | 171 | 10 | 66 |
| BATH | 83 | 336 | -34 | 76 |
| BEL | 34 | 188 | -5 | -34 |
| BER | 0 | 0 | 0 | 0 |
| CPF | 124 | 308 | -98 | 76 |
| CHAN | 118 | 228 | -88 | -79 |
| CHA | 33 | 278 | -33 | 5 |
| DWA | 7 | 304 | -6 | 4 |

| | | | | |
|---|---|---|---|---|
| DWD | 42 | 173 | 5 | -42 |
| DUM | 63 | 251 | -60 | -21 |
| GAR | 130 | 335 | -55 | 118 |
| GOO | 97 | 150 | 48 | -84 |
| GUNC | 35 | 17 | 10 | 33 |
| GUNP | 27 | 28 | 13 | 24 |
| HUM | 43 | 113 | 40 | -17 |
| KOO | 28 | 75 | 27 | 7 |
| LAB | 87 | 213 | -47 | -73 |
| LEP | 13 | 344 | -4 | 12 |
| LIT | 119 | 204 | -48 | -109 |
| MAN | 18 | 275 | -18 | 2 |
| McM | 19 | 119 | 17 | -9 |
| MtB | 89 | 165 | 23 | -86 |
| NOO | 22 | 138 | 15 | -16 |
| PIC | 77 | 356 | -5 | 77 |
| PTS | 91 | 99 | 90 | -14 |
| SNA | 118 | 346 | -29 | 114 |
| SOU | 32 | 176 | 2 | -32 |
| SCP | 97 | 83 | 96 | 12 |
| WOO | 59 | 81 | 58 | 9 |

Table D2. Partitioned rainfall summaries for the 891205 MCS.

| **Station ID** | **Convective Rain (mm)** | **Stratiform Rain (mm)** | **Ratio: Convective / Stratiform Rain** |
|---|---|---|---|
| ANN | 10.4 | 0.2 | 0.98 |
| BATC | 1.0 | 2.2 | 0.31 |
| BATH | 8.8 | 0.6 | 0.94 |

| | | | |
|---|---|---|---|
| BEL | 11.4 | 21.8 | 0.34 |
| BER | 22.2 | 2.8 | 0.89 |
| CPF | | | |
| CHAN | | | |
| CHA | 16.8 | 0.6 | 0.97 |
| DWA | 10.8 | 1.2 | 0.90 |
| DWD | 2.0 | 2.8 | 0.42 |
| DUM | | | |
| GAR | | | |
| GOO | | | |
| GUNC | 10.6 | 0.4 | 0.96 |
| GUNP | 4.8 | 0.4 | 0.92 |
| HUM | 22.8 | 4.6 | 0.83 |
| KOO | 5.4 | 0.6 | 0.90 |
| LAB | 4.6 | 7.8 | 0.37 |
| LEP | 16.4 | 5.6 | 0.75 |
| LIT | | | |
| MAN | 7.2 | 1.4 | 0.84 |
| McM | 36.0 | 5.8 | 0.86 |
| MtB | 0.0 | 0.2 | 0.00 |
| NOO | 57.6 | 11.4 | 0.83 |
| PIC | | | |
| PTS | 7.6 | 0.6 | 0.93 |
| SNA | | | |
| SOU | 32.6 | 8.2 | 0.80 |
| SCP | 0.8 | 0.4 | 0.67 |
| WOO | 8.4 | 0.0 | 1.00 |

Table D3. Partitioned rainfall summaries for the 900110 MCS.

| Station ID | Convective Rain (mm) | Stratiform Rain (mm) | Ratio: Convective / Stratiform Rain |
|---|---|---|---|
| ANN | 4.2 | 2.6 | 0.62 |
| BATC | 6.2 | 5.4 | 0.53 |
| BATH | 40.6 | 1.8 | 0.96 |
| BEL | 25.6 | 5.8 | 0.82 |
| BER | 13.6 | 0.4 | 0.97 |
| CPF | | | |
| CHAN | 2.6 | 5.8 | 0.31 |
| CHA | 0.2 | 0.8 | 0.20 |
| DWA | 11.4 | 0.8 | 0.93 |
| DWD | 29.8 | 7.0 | 0.81 |
| DUM | | | |
| GAR | 6.8 | 0.2 | 0.97 |
| GOO | 51.4 | 9.8 | 0.84 |
| GUNC | 39.6 | 1.6 | 0.96 |
| GUNP | 19.8 | 0.6 | 0.97 |
| HUM | 0.0 | 0.2 | 0.00 |
| KOO | 37.2 | 5.8 | 0.87 |
| LAB | 3.6 | 3.4 | 0.51 |
| LEP | | | |
| LIT | | | |
| MAN | 1.6 | 1.0 | 0.62 |
| McM | 34.8 | 2.0 | 0.95 |
| MtB | | | |
| NOO | 25.0 | 9.8 | 0.72 |
| PIC | 2.8 | 1.0 | 0.74 |

| | | | |
|---|---|---|---|
| PTS | 2.0 | 2.6 | 0.43 |
| SNA | | | |
| SOU | 50.0 | 24.6 | 0.67 |
| SCP | 4.4 | 0.8 | 0.85 |
| WOO | 23.0 | 5.2 | 0.82 |

Table D4. Partitioned rainfall summaries for the 900112 MCS.

| **Station ID** | **Convective Rain (mm)** | **Stratiform Rain (mm)** | **Ratio: Convective / Stratiform Rain** |
|---|---|---|---|
| ANN | 0.2 | 0.4 | 0.33 |
| BATC | 23.4 | 6.4 | 0.79 |
| BATH | 11.8 | 4.2 | 0.74 |
| BEL | 6.0 | 6.0 | 0.50 |
| BER | | | |
| CPF | | | |
| CHAN | 0.0 | 1.2 | 0.00 |
| CHA | 6.6 | 1.4 | 0.83 |
| DWA | 1.6 | 7.4 | 0.18 |
| DWD | 4.6 | 4.8 | 0.49 |
| DUM | | | |
| GAR | 43.6 | 2.4 | 0.95 |
| GOO | 21.4 | 2.0 | 0.91 |
| GUNC | 9.8 | 2.0 | 0.83 |
| GUNP | 28.4 | 2.2 | 0.93 |
| HUM | 9.2 | 5.6 | 0.62 |
| KOO | 8.8 | 3.2 | 0.73 |
| LAB | 6.8 | 5.2 | 0.57 |
| LEP | 11.2 | 2.6 | 0.81 |

| | | | |
|---|---|---|---|
| LIT | 1.2 | 0.8 | 0.60 |
| MAN | 3.8 | 2.4 | 0.61 |
| McM | 4.6 | 4.8 | 0.49 |
| MtB | | | |
| NOO | 3.0 | 5.2 | 0.37 |
| PIC | 38.2 | 1.6 | 0.96 |
| PTS | 1.6 | 2.8 | 0.36 |
| SNA | | | |
| SOU | 0.4 | 0.4 | 0.50 |
| SCP | 0.4 | 3.0 | 0.12 |
| WOO | 26.8 | 0.8 | 0.97 |

Table D5. Partitioned rainfall summaries for the 900118 MCS.

| **Station ID** | **Convective Rain (mm)** | **Stratiform Rain (mm)** | **Ratio: Convective / Stratiform Rain** |
|---|---|---|---|
| ANN | | | |
| BATC | 7.8 | 0.0 | 1.00 |
| BATH | 0.4 | 0.0 | 1.00 |
| BEL | 0.2 | 6.2 | 0.03 |
| BER | 15.8 | 0.2 | 0.99 |
| CPF | | | |
| CHAN | | | |
| CHA | 39.0 | 2.6 | 0.94 |
| DWA | 5.0 | 5.4 | 0.48 |
| DWD | 5.8 | 0.4 | 0.94 |
| DUM | 13.6 | 17.8 | 0.43 |
| GAR | | | |
| GOO | 11.0 | 0.0 | 1.00 |

| | | | |
|---|---|---|---|
| GUNC | 35.2 | 1.8 | 0.95 |
| GUNP | 45.2 | 3.4 | 0.93 |
| HUM | 6.0 | 0.0 | 1.00 |
| KOO | 23.2 | 0.8 | 0.97 |
| LAB | | | |
| LEP | 6.2 | 0.0 | 1.00 |
| LIT | | | |
| MAN | 28.0 | 0.0 | 1.00 |
| McM | 20.8 | 1.2 | 0.95 |
| MtB | | | |
| NOO | 0.2 | 0.0 | 1.00 |
| PIC | 1.8 | 0.0 | 1.00 |
| PTS | | | |
| SNA | | | |
| SOU | 13.6 | 2.2 | 0.86 |
| SCP | | | |
| WOO | 10.4 | 13.8 | 0.43 |

Table D6. Partitioned rainfall summaries for the 900122 MCS.

| **Station ID** | **Convective Rain (mm)** | **Stratiform Rain (mm)** | **Ratio: Convective / Stratiform Rain** |
|---|---|---|---|
| ANN | 0 | 0.2 | 0.00 |
| BATC | 24.2 | 0.0 | 1.00 |
| BATH | 5.6 | 0.8 | 0.88 |
| BEL | 19.6 | 1.0 | 0.95 |
| BER | 13.2 | 1.8 | 0.88 |
| CPF | | | |
| CHAN | | | |

| | | | |
|---|---|---|---|
| CHA | 8.0 | 1.2 | 0.87 |
| DWA | 29.0 | 2.2 | 0.93 |
| DWD | 13.8 | 4.0 | 0.78 |
| DUM | 1.6 | 0.4 | 0.80 |
| GAR | | | |
| GOO | 0.0 | 0.8 | 0.00 |
| GUNC | 2.0 | 5.2 | 0.28 |
| GUNP | | | |
| HUM | 25.6 | 2.2 | 0.92 |
| KOO | 3.8 | 1.8 | 0.68 |
| LAB | 0.0 | 0.2 | 0.00 |
| LEP | | | |
| LIT | | | |
| MAN | 19.2 | 0.6 | 0.97 |
| McM | | | |
| MtB | | | |
| NOO | 8.8 | 1.2 | 0.88 |
| PIC | 0.8 | 1.0 | 0.44 |
| PTS | | | |
| SNA | | | |
| SOU | 25.4 | 0.6 | 0.98 |
| SCP | 19.4 | 7.4 | 0.72 |
| WOO | 31.6 | 4.0 | 0.89 |

Table D7. Partitioned rainfall summaries for the 900128 MCS.

| **Station ID** | **Convective Rain (mm)** | **Stratiform Rain (mm)** | **Ratio: Convective / Stratiform Rain** |
|---|---|---|---|
| ANN | 28.4 | 0.2 | 0.99 |

| | | | |
|---|---|---|---|
| BATC | 10.0 | 2.6 | 0.79 |
| BATH | 0.4 | 2.0 | 0.17 |
| BEL | 13.0 | 2.8 | 0.82 |
| BER | 1.4 | 4.8 | 0.23 |
| CPF | 5.0 | 0.4 | 0.93 |
| CHAN | 0.0 | 0.2 | 0.00 |
| CHA | 5.0 | 2.6 | 0.66 |
| DWA | 0.0 | 4.2 | 0.00 |
| DWD | 10.0 | 3.2 | 0.76 |
| DUM | 15.0 | 3.4 | 0.82 |
| GAR | | | |
| GOO | 2.4 | 0.8 | 0.75 |
| GUNC | 5.6 | 6.0 | 0.48 |
| GUNP | 6.8 | 4.8 | 0.59 |
| HUM | 31.2 | 7.8 | 0.80 |
| KOO | 2.2 | 4.2 | 0.34 |
| LAB | 22.2 | 0.0 | 1.00 |
| LEP | | | |
| LIT | | | |
| MAN | 0.4 | 3.0 | 0.12 |
| McM | | | |
| MtB | 2.0 | 2.2 | 0.48 |
| NOO | 3.8 | 5.4 | 0.41 |
| PIC | 3.4 | 8.2 | 0.29 |
| PTS | 8.8 | 7.2 | 0.55 |
| SNA | | | |
| SOU | | | |
| SCP | 26.6 | 1.8 | 0.94 |
| WOO | 34.6 | 3.8 | 0.90 |

Table D8. Partitioned rainfall summaries for the 901121 MCS.

| Station ID | Convective Rain (mm) | Stratiform Rain (mm) | Ratio: Convective / Stratiform Rain |
|---|---|---|---|
| ANN | 47.2 | 4.0 | 0.92 |
| BATC | 30.4 | 0.6 | 0.98 |
| BATH | 0.0 | 0.2 | 0.00 |
| BEL | 25.4 | 1.0 | 0.96 |
| BER | 20.0 | 0.6 | 0.97 |
| CPF | | | |
| CHAN | 0.4 | 0.8 | 0.33 |
| CHA | | | |
| DWA | | | |
| DWD | 11.0 | 1.8 | 0.86 |
| DUM | | | |
| GAR | | | |
| GOO | 14.0 | 2.2 | 0.86 |
| GUNC | | | |
| GUNP | | | |
| HUM | 10.0 | 4.0 | 0.71 |
| KOO | 9.6 | 1.4 | 0.87 |
| LAB | | | |
| LEP | | | |
| LIT | 1.2 | 3.2 | 0.27 |
| MAN | 11.6 | 0.0 | 1.00 |
| McM | 3.2 | 0.6 | 0.84 |
| MtB | | | |
| NOO | | | |
| PIC | | | |

| | | | |
|---|---|---|---|
| PTS | | | |
| SNA | | | |
| SOU | | | |
| SCP | 20.6 | 1.4 | 0.94 |
| WOO | 0.8 | 2.2 | 0.27 |

Table D9. Partitioned rainfall summaries for the 901210 MCS.

| **Station ID** | **Convective Rain (mm)** | **Stratiform Rain (mm)** | **Ratio: Convective / Stratiform Rain** |
|---|---|---|---|
| ANN | | | |
| BATC | 3.8 | 1.2 | 0.76 |
| BATH | 8.8 | 7.8 | 0.53 |
| BEL | 13.6 | 9.0 | 0.60 |
| BER | 41.6 | 2.4 | 0.95 |
| CPF | | | |
| CHAN | 8.0 | 17.2 | 0.32 |
| CHA | 2.4 | 4.2 | 0.36 |
| DWA | | | |
| DWD | 2.2 | 3.6 | 0.38 |
| DUM | 33.4 | 15.8 | 0.68 |
| GAR | 6.2 | 3.4 | 0.65 |
| GOO | 3.0 | 0.2 | 0.94 |
| GUNC | | | |
| GUNP | 10.6 | 5.4 | 0.66 |
| HUM | 8.0 | 1.0 | 0.89 |
| KOO | 11.4 | 2.0 | 0.85 |
| LAB | 31.6 | 10.4 | 0.75 |
| LEP | | | |

| | | | |
|---|---|---|---|
| LIT | 3.8 | 13.2 | 0.22 |
| MAN | 43.0 | 4.8 | 0.90 |
| McM | 6.6 | 2.8 | 0.70 |
| MtB | | | |
| NOO | | | |
| PIC | 18.4 | 5.4 | 0.77 |
| PTS | | | |
| SNA | 24.0 | 7.4 | 0.76 |
| SOU | | | |
| SCP | 0.0 | 0.4 | 0.00 |
| WOO | 0.6 | 0.4 | 0.60 |

Table D10. Partitioned rainfall summaries for the 901212 MCS.

| **Station ID** | **Convective Rain (mm)** | **Stratiform Rain (mm)** | **Ratio: Convective / Stratiform Rain** |
|---|---|---|---|
| ANN | 1.6 | 0.4 | 0.80 |
| BATC | 18.0 | 7.6 | 0.70 |
| BATH | 3.2 | 7.0 | 0.31 |
| BEL | 28.8 | 24.8 | 0.54 |
| BER | 13.0 | 2.6 | 0.83 |
| CPF | | | |
| CHAN | 37.6 | 21.2 | 0.64 |
| CHA | 3.2 | 18.4 | 0.15 |
| DWA | | | |
| DWD | 26.4 | 6.0 | 0.81 |
| DUM | 24.2 | 12.2 | 0.66 |
| GAR | 100.0 | 29.6 | 0.77 |
| GOO | 2.4 | 1.6 | 0.60 |

| | | | |
|---|---|---|---|
| GUNC | | | |
| GUNP | 8.0 | 3.6 | 0.69 |
| HUM | 5.0 | 1.2 | 0.81 |
| KOO | 7.2 | 3.6 | 0.67 |
| LAB | 31.8 | 54.0 | 0.37 |
| LEP | 30.8 | 27.2 | 0.53 |
| LIT | | | |
| MAN | 23.8 | 1.6 | 0.94 |
| McM | 11.0 | 0.4 | 0.96 |
| MtB | | | |
| NOO | | | |
| PIC | 8.8 | 5.0 | 0.64 |
| PTS | | | |
| SNA | 34.4 | 11.2 | 0.75 |
| SOU | | | |
| SCP | 6.4 | 1.8 | 0.78 |
| WOO | 0.6 | 4.8 | 0.11 |

Table D11. Partitioned rainfall summaries for the 901215 MCS.

| **Station ID** | **Convective Rain (mm)** | **Stratiform Rain (mm)** | **Ratio: Convective / Stratiform Rain** |
|---|---|---|---|
| ANN | 2 | 3.6 | 0.36 |
| BATC | 14.2 | 6.4 | 0.69 |
| BATH | | | |
| BEL | 9.4 | 4.8 | 0.66 |
| BER | 21.2 | 3.2 | 0.87 |
| CPF | | | |
| CHAN | 4.2 | 0.4 | 0.91 |

| | | | |
|---|---|---|---|
| CHA | 7.4 | 0.2 | 0.97 |
| DWA | | | |
| DWD | 9.2 | 3.6 | 0.72 |
| DUM | | | |
| GAR | | | |
| GOO | 2.4 | 1.2 | 0.67 |
| GUNC | | | |
| GUNP | 1.4 | 1.8 | 0.44 |
| HUM | 19.2 | 4.6 | 0.81 |
| KOO | 5.6 | 3.0 | 0.65 |
| LAB | 0.2 | 0.8 | 0.20 |
| LEP | | | |
| LIT | 11.8 | 0.0 | 1.00 |
| MAN | 12.2 | 0.4 | 0.97 |
| McM | 25.0 | 5.0 | 0.83 |
| MtB | | | |
| NOO | | | |
| PIC | | | |
| PTS | | | |
| SNA | 0.2 | 0.0 | 1.00 |
| SOU | | | |
| SCP | 6.6 | 2.4 | 0.73 |
| WOO | 15.4 | 2.4 | 0.87 |

Table D12. Partitioned rainfall summaries for the 910109 MCS.

| **Station ID** | **Convective Rain (mm)** | **Stratiform Rain (mm)** | **Ratio: Convective / Stratiform Rain** |
|---|---|---|---|
| ANN | 15 | 6.4 | 0.70 |

| | | | |
|---|---|---|---|
| BATC | 14.2 | 3.0 | 0.83 |
| BATH | 3.2 | 1.6 | 0.67 |
| BEL | 63.4 | 16.2 | 0.80 |
| BER | 71.6 | 17.0 | 0.81 |
| CPF | | | |
| CHAN | 1.2 | 16.4 | 0.07 |
| CHA | 52.6 | 16.0 | 0.77 |
| DWA | | | |
| DWD | 13.6 | 17.4 | 0.44 |
| DUM | 64.6 | 49.4 | 0.57 |
| GAR | 16.6 | 7.2 | 0.70 |
| GOO | 15.8 | 25.4 | 0.38 |
| GUNC | | | |
| GUNP | 29.8 | 10.4 | 0.74 |
| HUM | | | |
| KOO | | | |
| LAB | 64.2 | 5.0 | 0.93 |
| LEP | | | |
| LIT | 0.2 | 18.6 | 0.01 |
| MAN | | | |
| McM | 16.0 | 17.4 | 0.48 |
| MtB | 42.2 | 28.6 | 0.60 |
| NOO | | | |
| PIC | 3.8 | 1.6 | 0.70 |
| PTS | | | |
| SNA | | | |
| SOU | | | |
| SCP | 6.4 | 6.4 | 0.50 |
| WOO | 27.4 | 13.2 | 0.67 |

Table D13. Partitioned rainfall summaries for the 910129 MCS.

| Station ID | Convective Rain (mm) | Stratiform Rain (mm) | Ratio: Convective / Stratiform Rain |
|---|---|---|---|
| ANN | 0 | 0.6 | 0.00 |
| BATC | 20.4 | 4.6 | 0.82 |
| BATH | 5.8 | 8.2 | 0.41 |
| BEL | 10.0 | 4.4 | 0.69 |
| BER | 16.4 | 3.4 | 0.83 |
| CPF | | | |
| CHAN | | | |
| CHA | 5.8 | 13.0 | 0.31 |
| DWA | | | |
| DWD | 4.2 | 4.8 | 0.47 |
| DUM | 16.0 | 2.8 | 0.85 |
| GAR | 10.4 | 2.0 | 0.84 |
| GOO | 2.2 | 1.8 | 0.55 |
| GUNC | | | |
| GUNP | 9.6 | 4.4 | 0.69 |
| HUM | 5.8 | 6.8 | 0.46 |
| KOO | | | |
| LAB | | | |
| LEP | | | |
| LIT | 13.4 | 1.6 | 0.89 |
| MAN | | | |
| McM | 15.2 | 7.0 | 0.68 |
| MtB | 1.2 | 3.2 | 0.27 |
| NOO | | | |
| PIC | 8.2 | 4.6 | 0.64 |

| | | | |
|---|---|---|---|
| PTS | | | |
| SNA | | | |
| SOU | | | |
| SCP | 7.8 | 2.0 | 0.80 |
| WOO | 10.0 | 1.4 | 0.88 |

Table D14. Partitioned rainfall summaries for the 910130 MCS.

| **Station ID** | **Convective Rain (mm)** | **Stratiform Rain (mm)** | **Ratio: Convective / Stratiform Rain** |
|---|---|---|---|
| ANN | 6.6 | 2.2 | 0.75 |
| BATC | 3.0 | 1.4 | 0.68 |
| BATH | 12.4 | 1.0 | 0.93 |
| BEL | 14.8 | 7.2 | 0.67 |
| BER | | | |
| CPF | | | |
| CHAN | | | |
| CHA | 0.8 | 24.6 | 0.03 |
| DWA | | | |
| DWD | 15.4 | 3.6 | 0.81 |
| DUM | 35.4 | 8.6 | 0.80 |
| GAR | 34.6 | 9.6 | 0.78 |
| GOO | 6.0 | 1.4 | 0.81 |
| GUNC | | | |
| GUNP | 15.6 | 1.8 | 0.90 |
| HUM | 6.6 | 6.0 | 0.52 |
| KOO | | | |
| LAB | | | |
| LEP | | | |

| | | | |
|---|---|---|---|
| LIT | 16.0 | 2.8 | 0.85 |
| MAN | | | |
| McM | 21.8 | 2.4 | 0.90 |
| MtB | 9.6 | 7.8 | 0.55 |
| NOO | | | |
| PIC | 19.2 | 3.0 | 0.86 |
| PTS | | | |
| SNA | | | |
| SOU | | | |
| SCP | 21.8 | 1.0 | 0.96 |
| WOO | 20.8 | 2.2 | 0.90 |

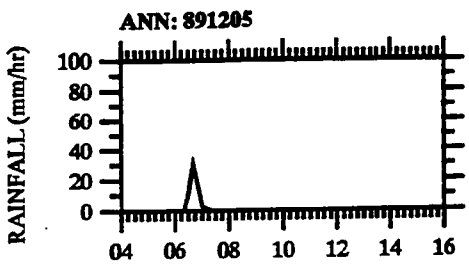
ANN: 891205
RAINFALL (mm/hr)
100
80
60
40
20
0
04 06 08 10 12 14 16

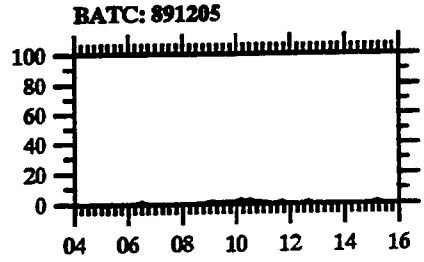
BATC: 891205
100
80
60
40
20
0
04 06 08 10 12 14 16

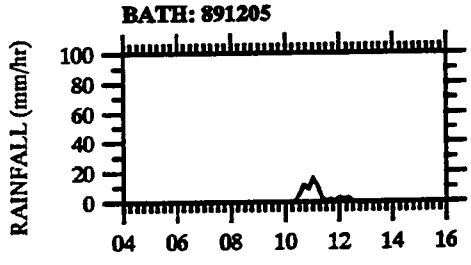
BATH: 891205
RAINFALL (mm/hr)
100
80
60
40
20
0
04 06 08 10 12 14 16

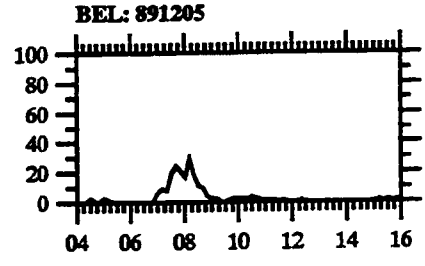
BEL: 891205
100
80
60
40
20
0
04 06 08 10 12 14 16

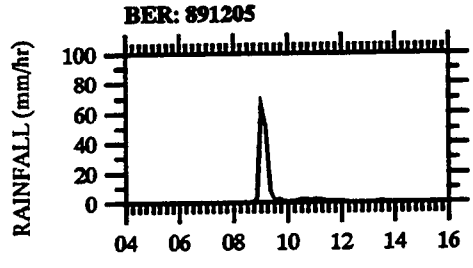
BER: 891205
RAINFALL (mm/hr)
100
80
60
40
20
0
04 06 08 10 12 14 16

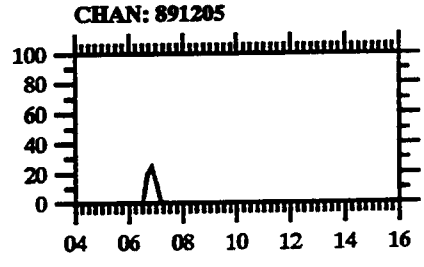
CHAN: 891205
100
80
60
40
20
0
04 06 08 10 12 14 16

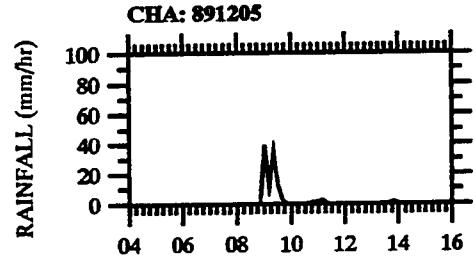
CHA: 891205
RAINFALL (mm/hr)
100
80
60
40
20
0
04 06 08 10 12 14 16

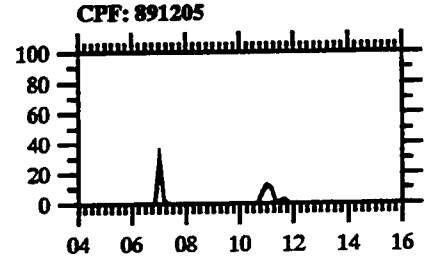
CPF: 891205
100
80
60
40
20
0
04 06 08 10 12 14 16

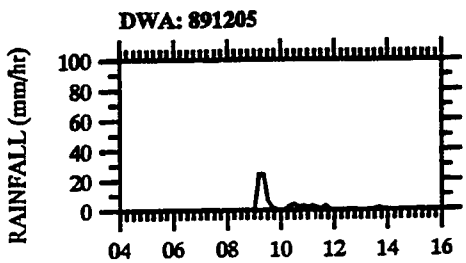
DWA: 891205
RAINFALL (mm/hr)
100
80
60
40
20
0
04 06 08 10 12 14 16

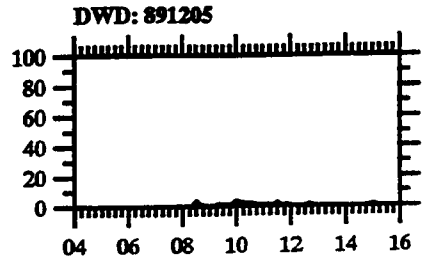
DWD: 891205
100
80
60
40
20
0
04 06 08 10 12 14 16

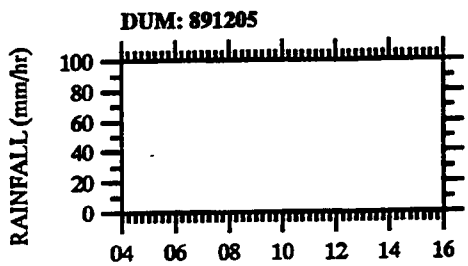
DUM: 891205
RAINFALL (mm/hr)
100
80
60
40
20
0
04 06 08 10 12 14 16

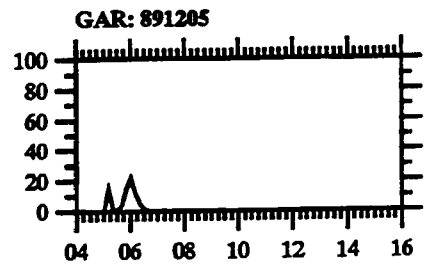
GAR: 891205
100
80
60
40
20
0
04 06 08 10 12 14 16

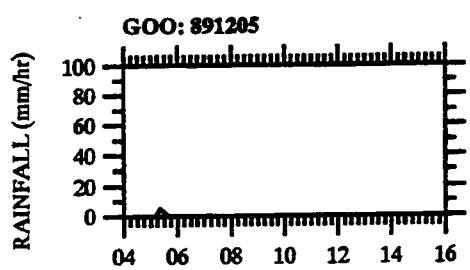
GOO: 891205
RAINFALL (mm/hr)
100
80
60
40
20
0
04 06 08 10 12 14 16

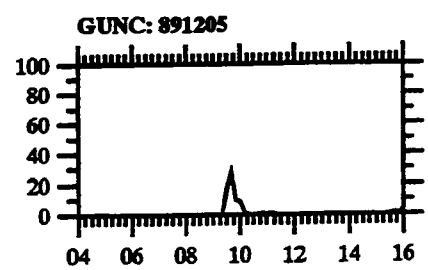
GUNC: 891205
100
80
60
40
20
0
04 06 08 10 12 14 16

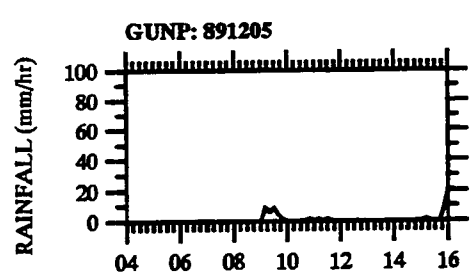
GUNP: 891205
RAINFALL (mm/hr)
100
80
60
40
20
0
04 06 08 10 12 14 16

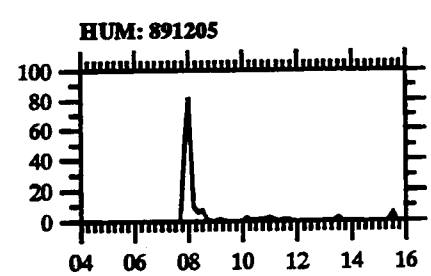
HUM: 891205
100
80
60
40
20
0
04 06 08 10 12 14 16

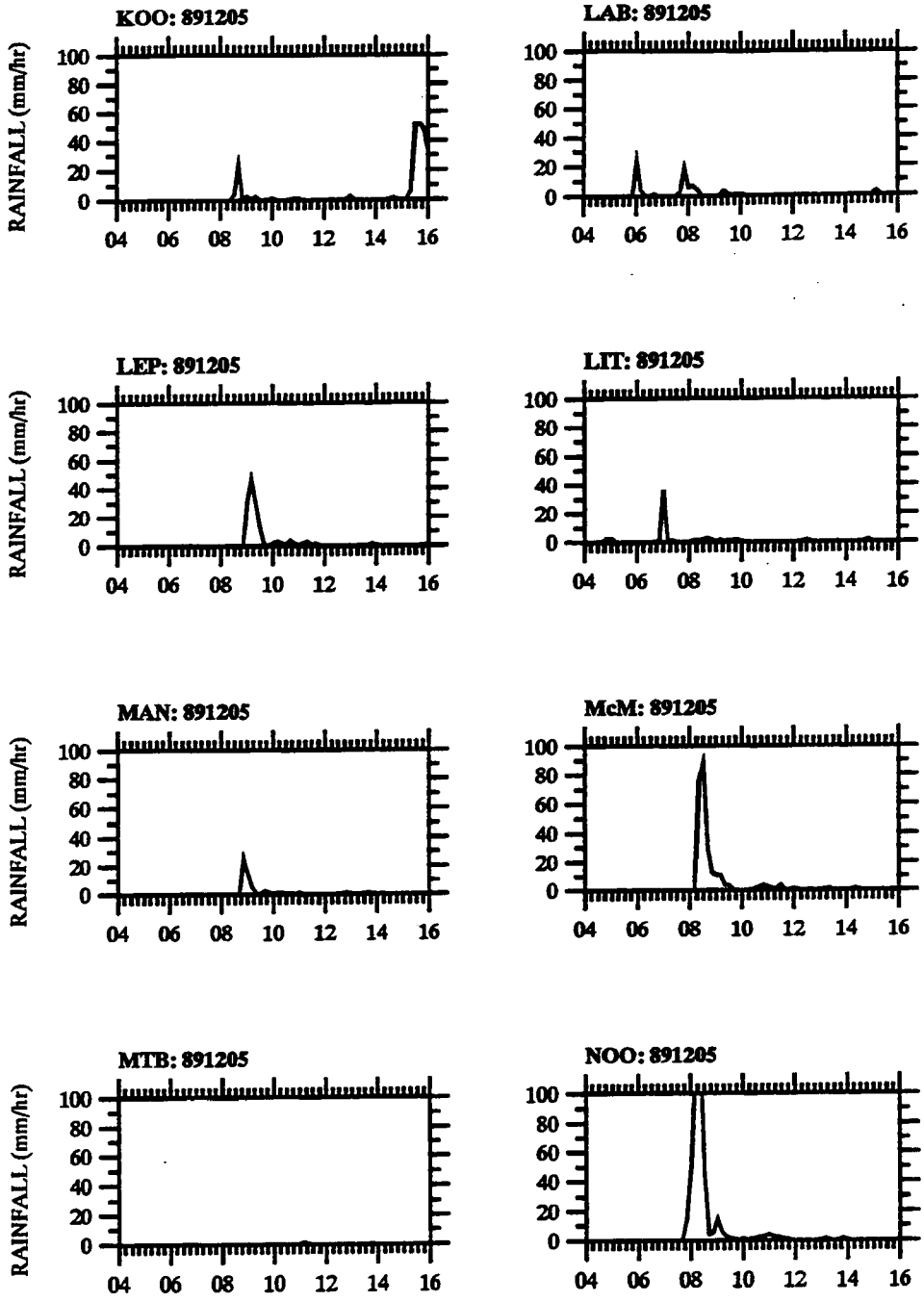
KOO: 891205
LAB: 891205
LEP: 891205
LIT: 891205
MAN: 891205
McM: 891205
MTB: 891205
NOO: 891205
RAINFALL (mm/hr)
0
20
40
60
80
100
04
06
08
10
12
14
16

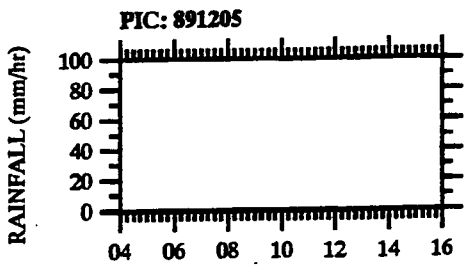
PIC: 891205
RAINFALL (mm/hr)
100
80
60
40
20
0
04 06 08 10 12 14 16

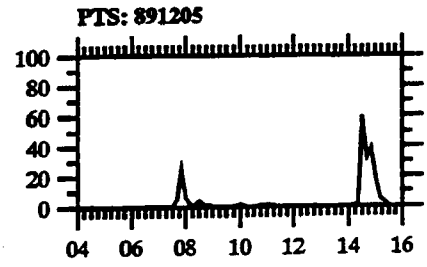
PTS: 891205
100
80
60
40
20
0
04 06 08 10 12 14 16

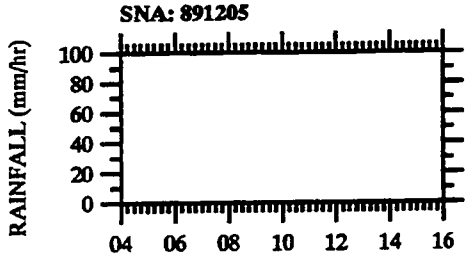
SNA: 891205
RAINFALL (mm/hr)
100
80
60
40
20
0
04 06 08 10 12 14 16

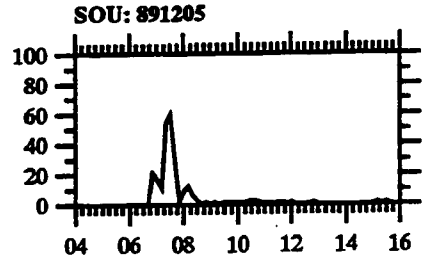
SOU: 891205
100
80
60
40
20
0
04 06 08 10 12 14 16

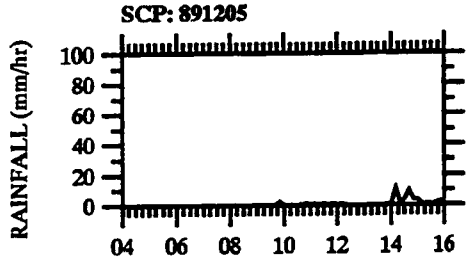
SCP: 891205
RAINFALL (mm/hr)
100
80
60
40
20
0
04 06 08 10 12 14 16

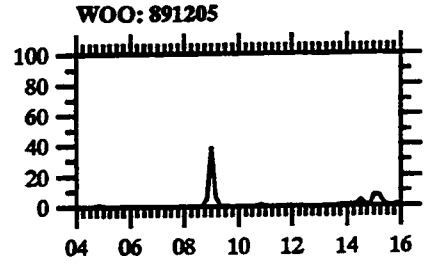
WOO: 891205
100
80
60
40
20
0
04 06 08 10 12 14 16

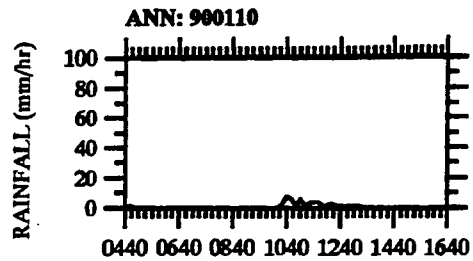
ANN: 900110
RAINFALL (mm/hr)
100
80
60
40
20
0
0440 0640 0840 1040 1240 1440 1640

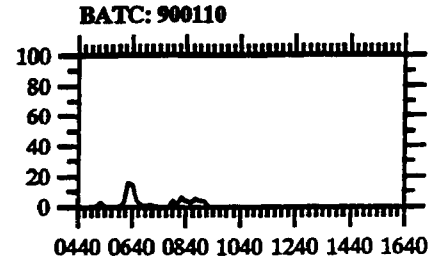
BATC: 900110
100
80
60
40
20
0
0440 0640 0840 1040 1240 1440 1640

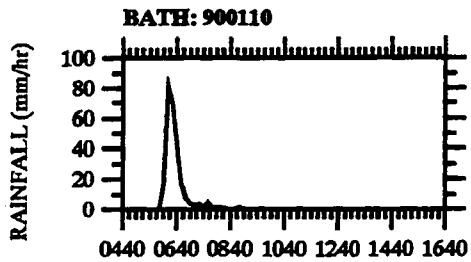
BATH: 900110
RAINFALL (mm/hr)
100
80
60
40
20
0
0440 0640 0840 1040 1240 1440 1640

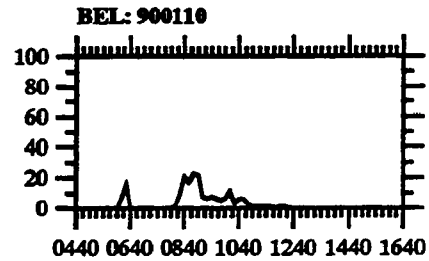
BEL: 900110
100
80
60
40
20
0
0440 0640 0840 1040 1240 1440 1640

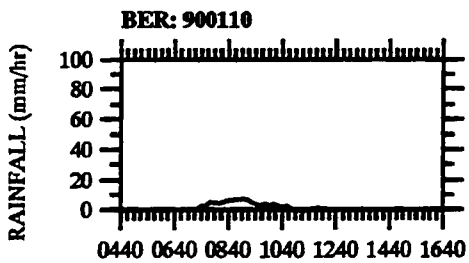
BER: 900110
RAINFALL (mm/hr)
100
80
60
40
20
0
0440 0640 0840 1040 1240 1440 1640

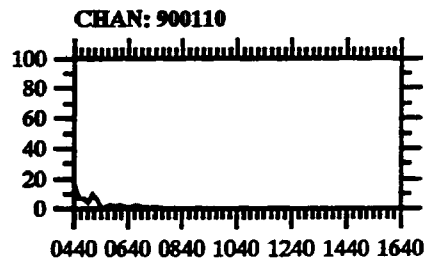
CHAN: 900110
100
80
60
40
20
0
0440 0640 0840 1040 1240 1440 1640

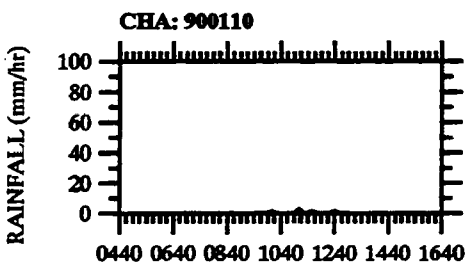
CHA: 900110
RAINFALL (mm/hr)
100
80
60
40
20
0
0440 0640 0840 1040 1240 1440 1640

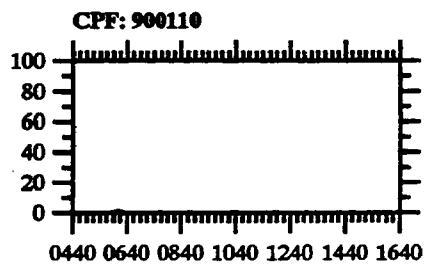
CPF: 900110
100
80
60
40
20
0
0440 0640 0840 1040 1240 1440 1640

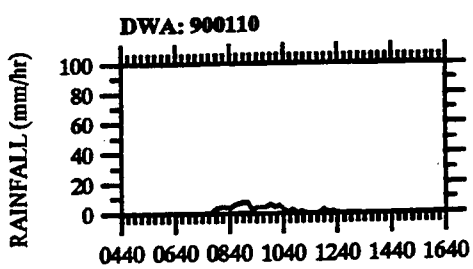
DWA: 900110
RAINFALL (mm/hr)
100
80
60
40
20
0
0440 0640 0840 1040 1240 1440 1640

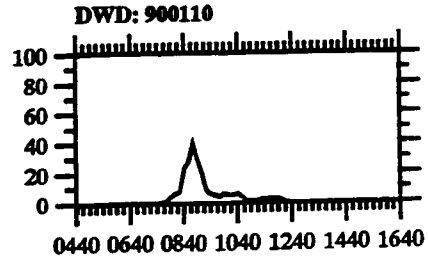
DWD: 900110
100
80
60
40
20
0
0440 0640 0840 1040 1240 1440 1640

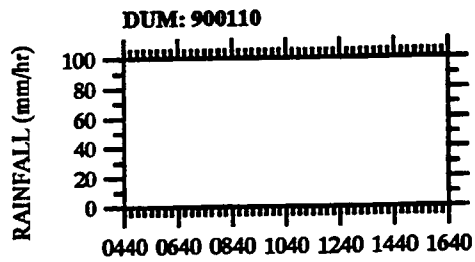
DUM: 900110
RAINFALL (mm/hr)
100
80
60
40
20
0
0440 0640 0840 1040 1240 1440 1640

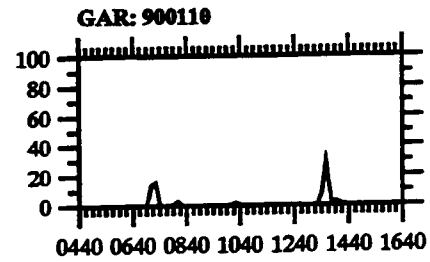
GAR: 900110
100
80
60
40
20
0
0440 0640 0840 1040 1240 1440 1640

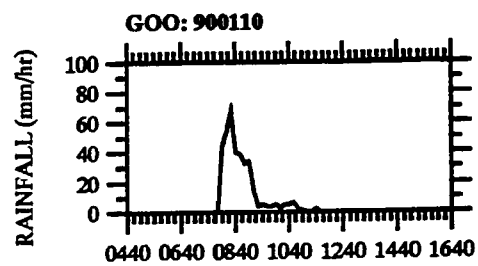
GOO: 900110
RAINFALL (mm/hr)
100
80
60
40
20
0
0440 0640 0840 1040 1240 1440 1640

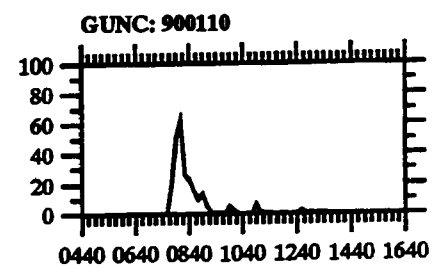
GUNC: 900110
100
80
60
40
20
0
0440 0640 0840 1040 1240 1440 1640

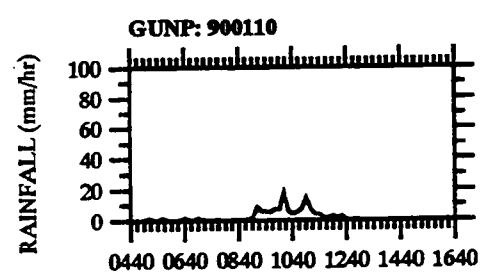
GUNP: 900110
RAINFALL (mm/hr)
100
80
60
40
20
0
0440 0640 0840 1040 1240 1440 1640

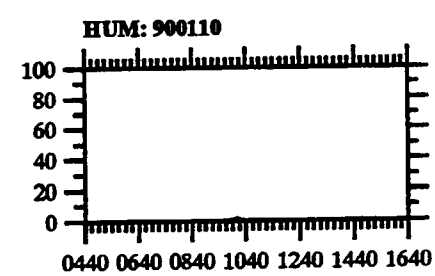
HUM: 900110
100
80
60
40
20
0
0440 0640 0840 1040 1240 1440 1640

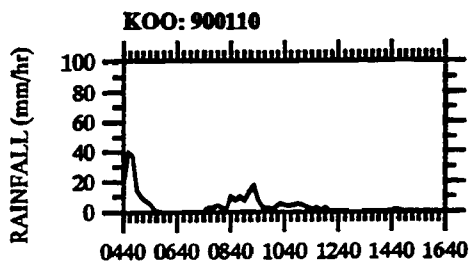
KOO: 900110
RAINFALL (mm/hr)
100
80
60
40
20
0
0440 0640 0840 1040 1240 1440 1640

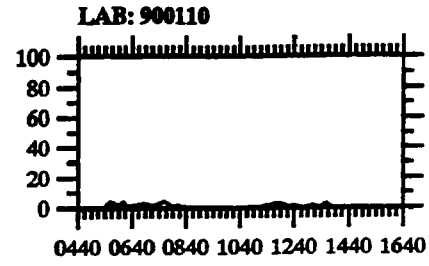
LAB: 900110
100
80
60
40
20
0
0440 0640 0840 1040 1240 1440 1640

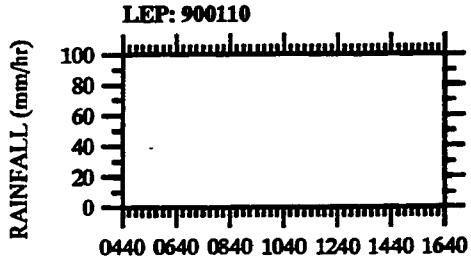
LEP: 900110
RAINFALL (mm/hr)
100
80
60
40
20
0
0440 0640 0840 1040 1240 1440 1640

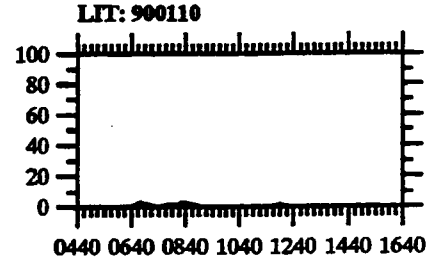
LIT: 900110
100
80
60
40
20
0
0440 0640 0840 1040 1240 1440 1640

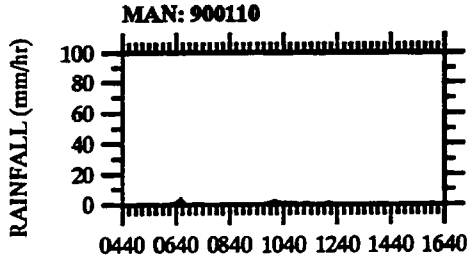
MAN: 900110
RAINFALL (mm/hr)
100
80
60
40
20
0
0440 0640 0840 1040 1240 1440 1640

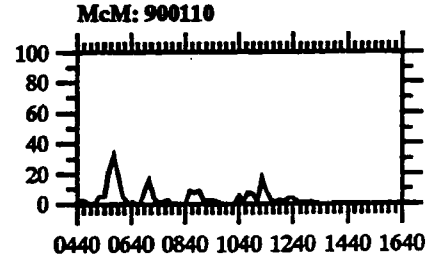
McM: 900110
100
80
60
40
20
0
0440 0640 0840 1040 1240 1440 1640

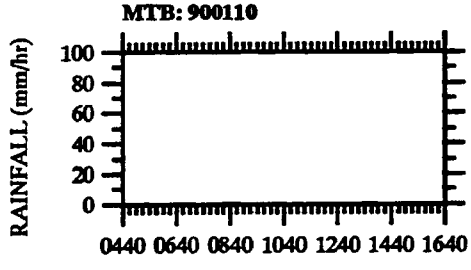
MTB: 900110
RAINFALL (mm/hr)
100
80
60
40
20
0
0440 0640 0840 1040 1240 1440 1640

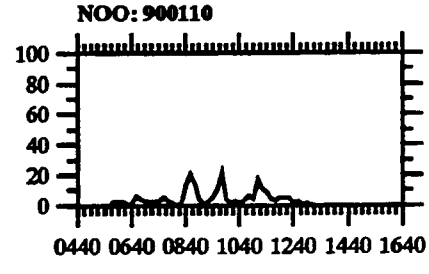
NOO: 900110
100
80
60
40
20
0
0440 0640 0840 1040 1240 1440 1640

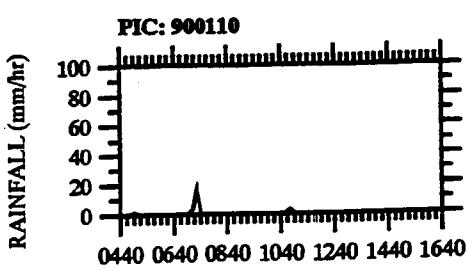
PIC: 900110
RAINFALL (mm/hr)
100
80
60
40
20
0
0440 0640 0840 1040 1240 1440 1640

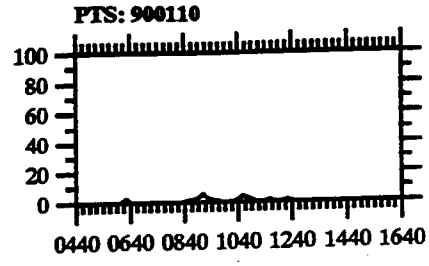
PTS: 900110
100
80
60
40
20
0
0440 0640 0840 1040 1240 1440 1640

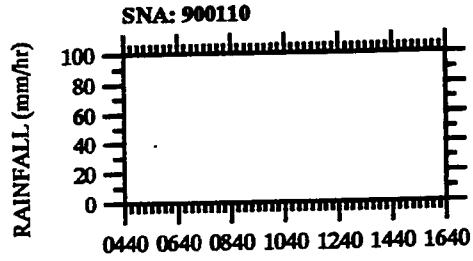
SNA: 900110
RAINFALL (mm/hr)
100
80
60
40
20
0
0440 0640 0840 1040 1240 1440 1640

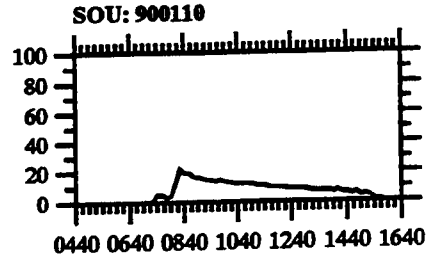
SOU: 900110
100
80
60
40
20
0
0440 0640 0840 1040 1240 1440 1640

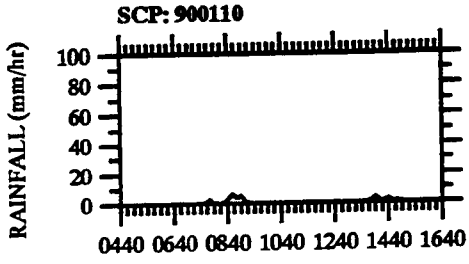
SCP: 900110
RAINFALL (mm/hr)
100
80
60
40
20
0
0440 0640 0840 1040 1240 1440 1640

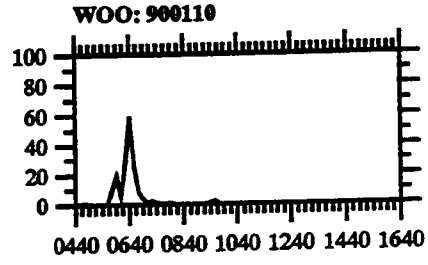
WOO: 900110
100
80
60
40
20
0
0440 0640 0840 1040 1240 1440 1640

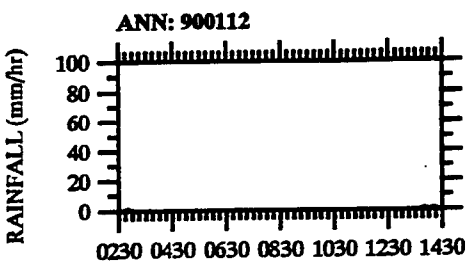
ANN: 900112
RAINFALL (mm/hr)
100
80
60
40
20
0
0230 0430 0630 0830 1030 1230 1430

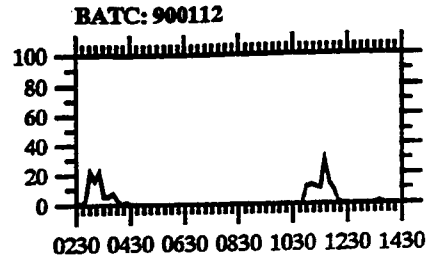
BATC: 900112
100
80
60
40
20
0
0230 0430 0630 0830 1030 1230 1430

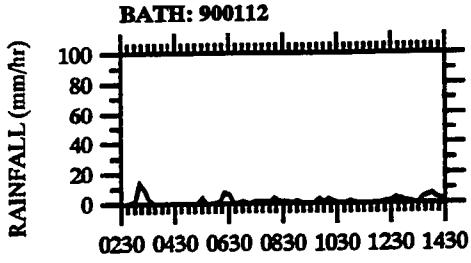
BATH: 900112
RAINFALL (mm/hr)
100
80
60
40
20
0
0230 0430 0630 0830 1030 1230 1430

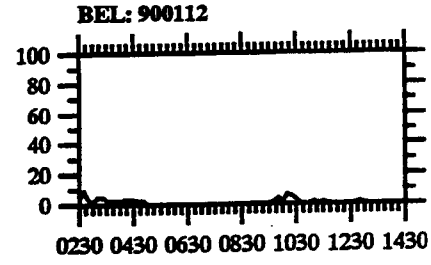
BEL: 900112
100
80
60
40
20
0
0230 0430 0630 0830 1030 1230 1430

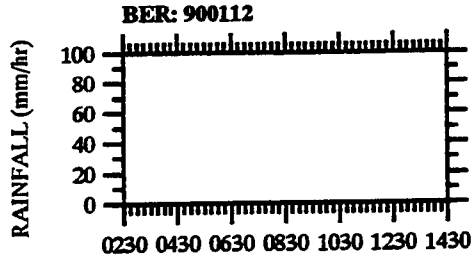
BER: 900112
RAINFALL (mm/hr)
100
80
60
40
20
0
0230 0430 0630 0830 1030 1230 1430

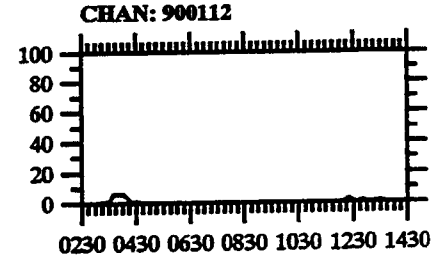
CHAN: 900112
100
80
60
40
20
0
0230 0430 0630 0830 1030 1230 1430

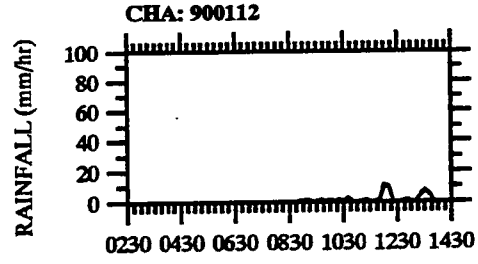
CHA: 900112
RAINFALL (mm/hr)
100
80
60
40
20
0
0230 0430 0630 0830 1030 1230 1430

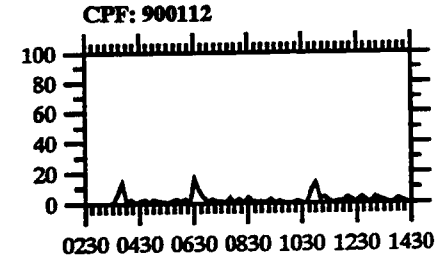
CPF: 900112
100
80
60
40
20
0
0230 0430 0630 0830 1030 1230 1430

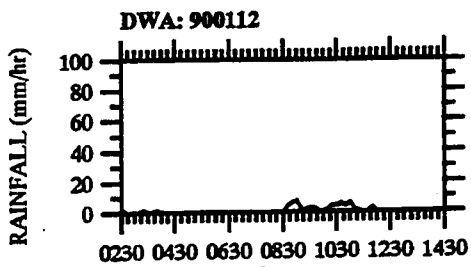
DWA: 900112
RAINFALL (mm/hr)
100
80
60
40
20
0
0230 0430 0630 0830 1030 1230 1430

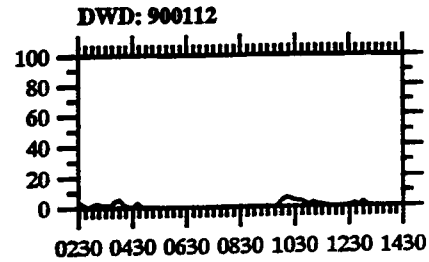
DWD: 900112
100
80
60
40
20
0
0230 0430 0630 0830 1030 1230 1430

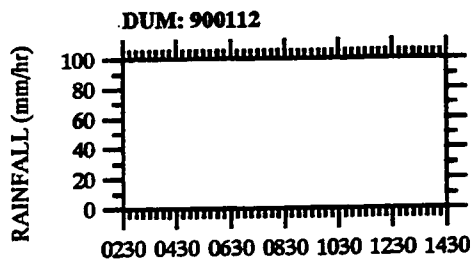
DUM: 900112
RAINFALL (mm/hr)
100
80
60
40
20
0
0230 0430 0630 0830 1030 1230 1430

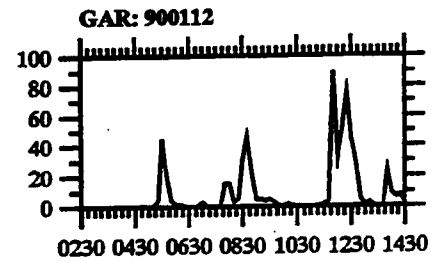
GAR: 900112
100
80
60
40
20
0
0230 0430 0630 0830 1030 1230 1430

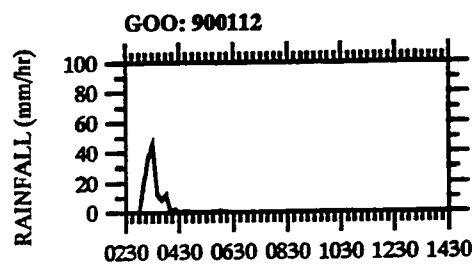
GOO: 900112
RAINFALL (mm/hr)
100
80
60
40
20
0
0230 0430 0630 0830 1030 1230 1430

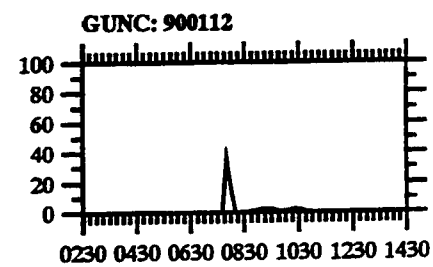
GUNC: 900112
100
80
60
40
20
0
0230 0430 0630 0830 1030 1230 1430

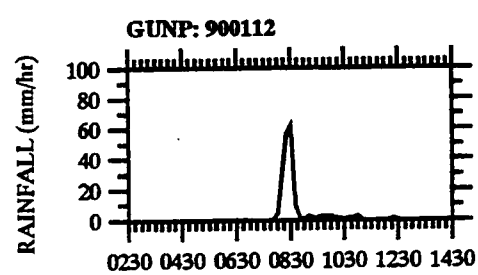
GUNP: 900112
RAINFALL (mm/hr)
100
80
60
40
20
0
0230 0430 0630 0830 1030 1230 1430

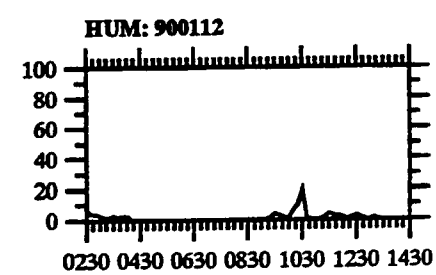
HUM: 900112
100
80
60
40
20
0
0230 0430 0630 0830 1030 1230 1430

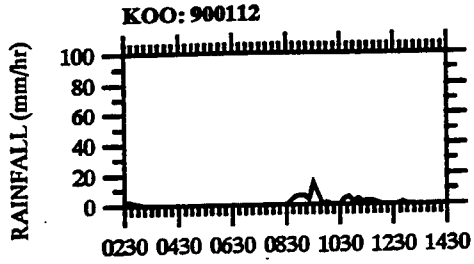
KOO: 900112
RAINFALL (mm/hr)
100
80
60
40
20
0
0230 0430 0630 0830 1030 1230 1430

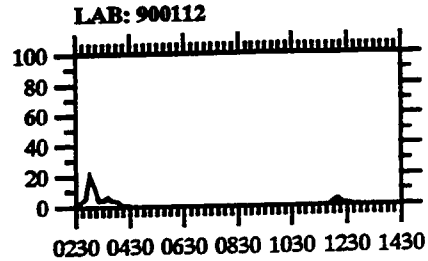
LAB: 900112
100
80
60
40
20
0
0230 0430 0630 0830 1030 1230 1430

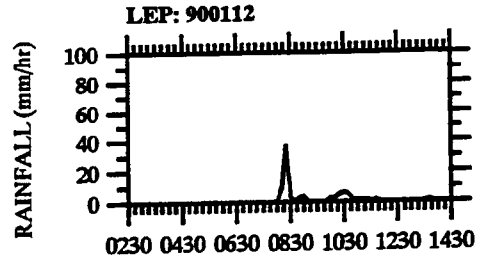
LEP: 900112
RAINFALL (mm/hr)
100
80
60
40
20
0
0230 0430 0630 0830 1030 1230 1430

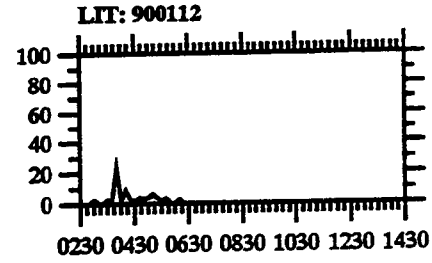
LIT: 900112
100
80
60
40
20
0
0230 0430 0630 0830 1030 1230 1430

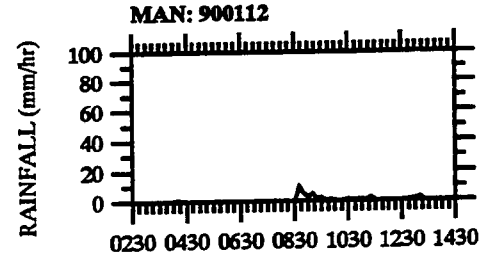
MAN: 900112
RAINFALL (mm/hr)
100
80
60
40
20
0
0230 0430 0630 0830 1030 1230 1430

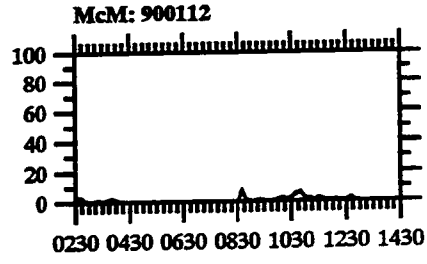
McM: 900112
100
80
60
40
20
0
0230 0430 0630 0830 1030 1230 1430

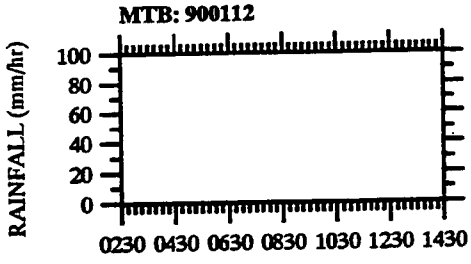
MTB: 900112
RAINFALL (mm/hr)
100
80
60
40
20
0
0230 0430 0630 0830 1030 1230 1430

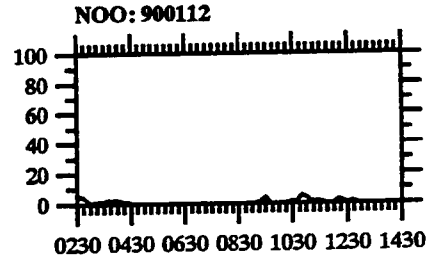
NOO: 900112
100
80
60
40
20
0
0230 0430 0630 0830 1030 1230 1430

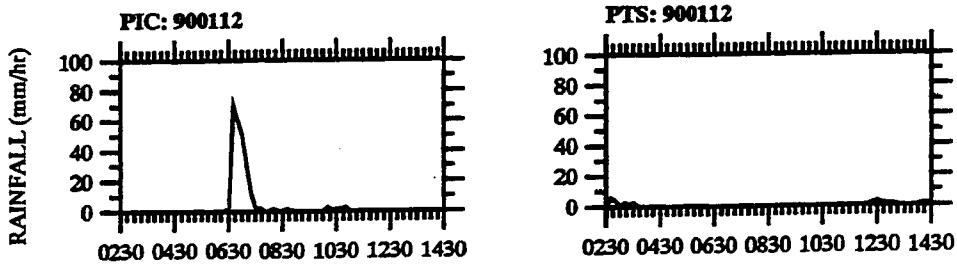
PIC: 900112
RAINFALL (mm/hr)
100
80
60
40
20
0
0230 0430 0630 0830 1030 1230 1430


PTS: 900112
100
80
60
40
20
0
0230 0430 0630 0830 1030 1230 1430

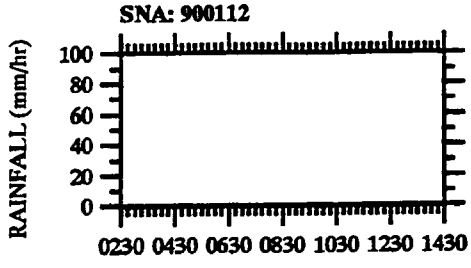
SNA: 900112
RAINFALL (mm/hr)
100
80
60
40
20
0
0230 0430 0630 0830 1030 1230 1430

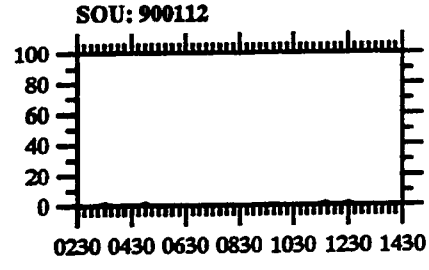
SOU: 900112
100
80
60
40
20
0
0230 0430 0630 0830 1030 1230 1430

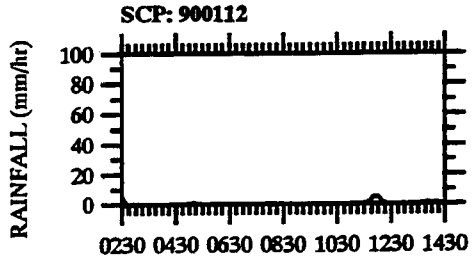
SCP: 900112
RAINFALL (mm/hr)
100
80
60
40
20
0
0230 0430 0630 0830 1030 1230 1430

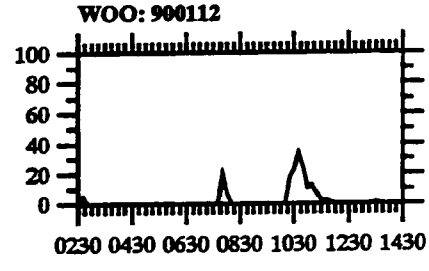
WOO: 900112
100
80
60
40
20
0
0230 0430 0630 0830 1030 1230 1430

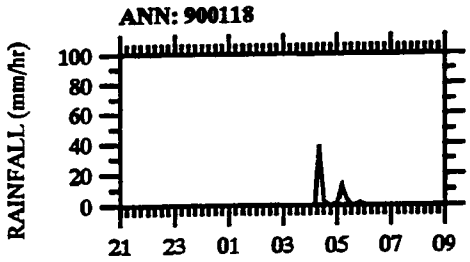
ANN: 900118
RAINFALL (mm/hr)
100
80
60
40
20
0
21 23 01 03 05 07 09

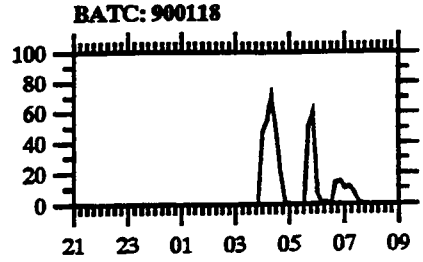
BATC: 900118
100
80
60
40
20
0
21 23 01 03 05 07 09

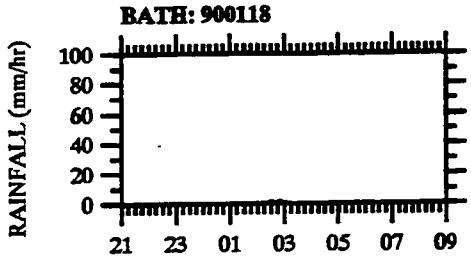
BATH: 900118
RAINFALL (mm/hr)
100
80
60
40
20
0
21 23 01 03 05 07 09

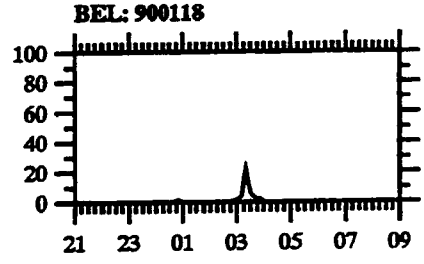
BEL: 900118
100
80
60
40
20
0
21 23 01 03 05 07 09

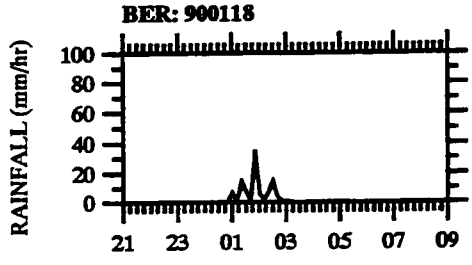
BER: 900118
RAINFALL (mm/hr)
100
80
60
40
20
0
21 23 01 03 05 07 09

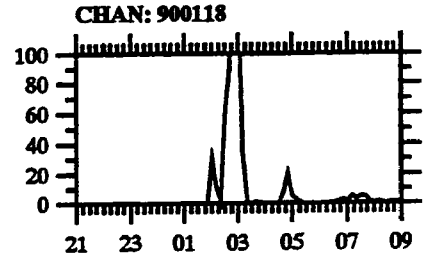
CHAN: 900118
100
80
60
40
20
0
21 23 01 03 05 07 09

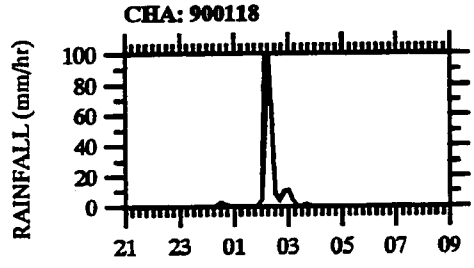
CHA: 900118
RAINFALL (mm/hr)
100
80
60
40
20
0
21 23 01 03 05 07 09

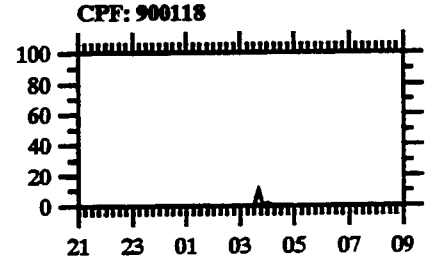
CPF: 900118
100
80
60
40
20
0
21 23 01 03 05 07 09

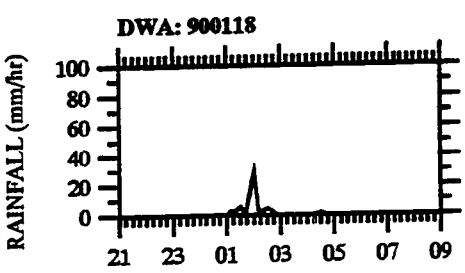
DWA: 900118
RAINFALL (mm/hr)
100
80
60
40
20
0
21 23 01 03 05 07 09

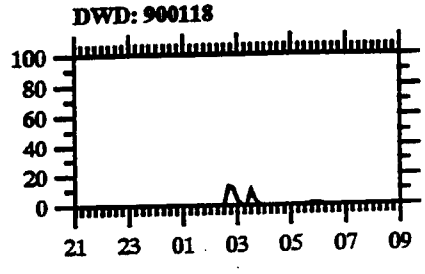
DWD: 900118
100
80
60
40
20
0
21 23 01 03 05 07 09

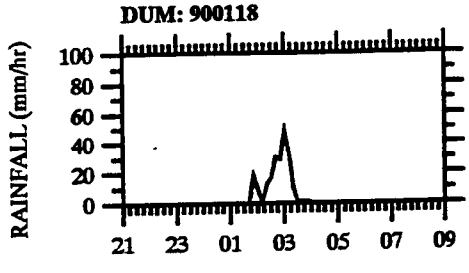
DUM: 900118
RAINFALL (mm/hr)
100
80
60
40
20
0
21 23 01 03 05 07 09

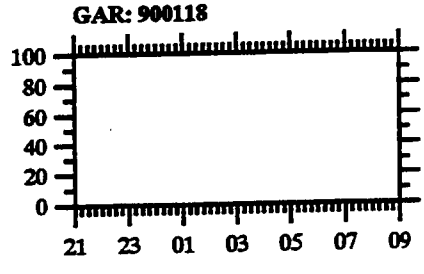
GAR: 900118
100
80
60
40
20
0
21 23 01 03 05 07 09

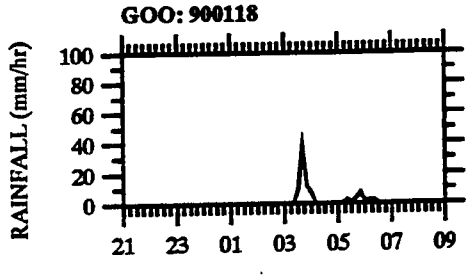
GOO: 900118
RAINFALL (mm/hr)
100
80
60
40
20
0
21 23 01 03 05 07 09

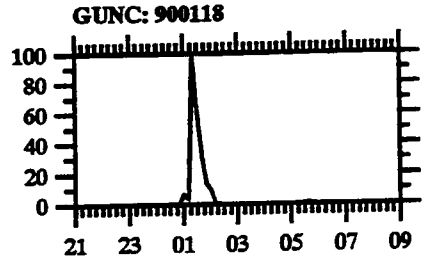
GUNC: 900118
100
80
60
40
20
0
21 23 01 03 05 07 09

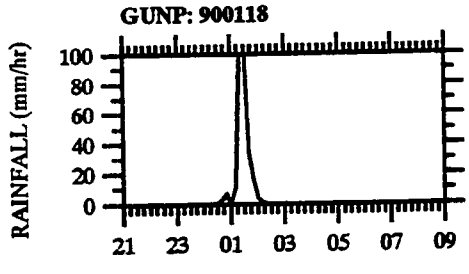
GUNP: 900118
RAINFALL (mm/hr)
100
80
60
40
20
0
21 23 01 03 05 07 09

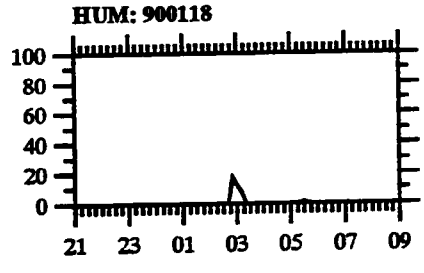
HUM: 900118
100
80
60
40
20
0
21 23 01 03 05 07 09

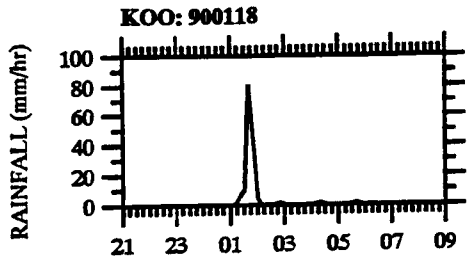
KOO: 900118
RAINFALL (mm/hr)
100
80
60
40
20
0
21 23 01 03 05 07 09

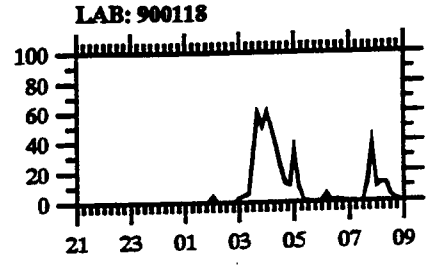
LAB: 900118
100
80
60
40
20
0
21 23 01 03 05 07 09

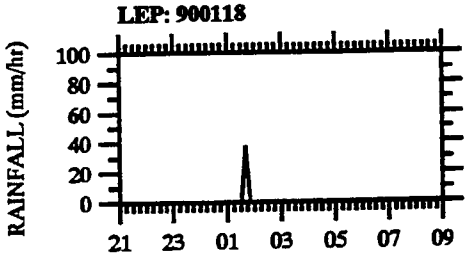
LEP: 900118
RAINFALL (mm/hr)
100
80
60
40
20
0
21 23 01 03 05 07 09

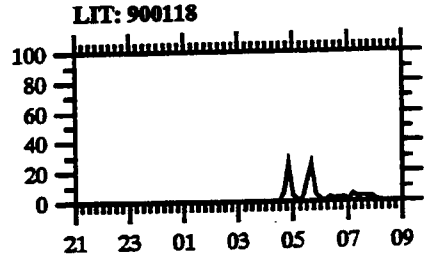
LIT: 900118
100
80
60
40
20
0
21 23 01 03 05 07 09

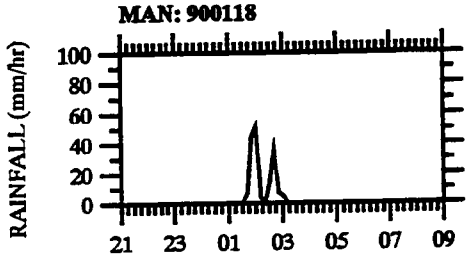
MAN: 900118
RAINFALL (mm/hr)
100
80
60
40
20
0
21 23 01 03 05 07 09

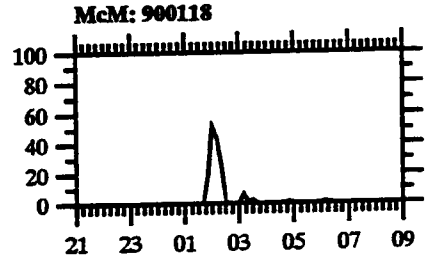
McM: 900118
100
80
60
40
20
0
21 23 01 03 05 07 09

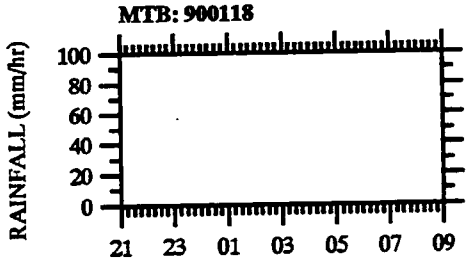
MTB: 900118
RAINFALL (mm/hr)
100
80
60
40
20
0
21 23 01 03 05 07 09

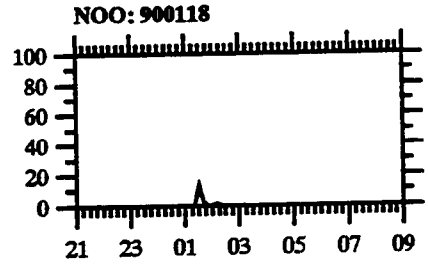
NOO: 900118
100
80
60
40
20
0
21 23 01 03 05 07 09

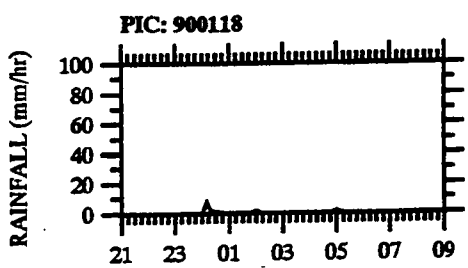
PIC: 900118
RAINFALL (mm/hr)
100
80
60
40
20
0
21 23 01 03 05 07 09

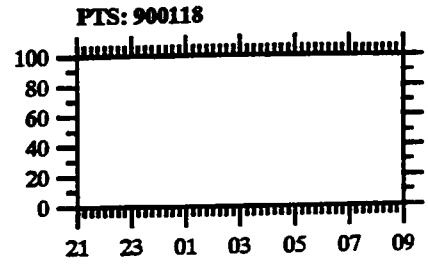
PTS: 900118
100
80
60
40
20
0
21 23 01 03 05 07 09

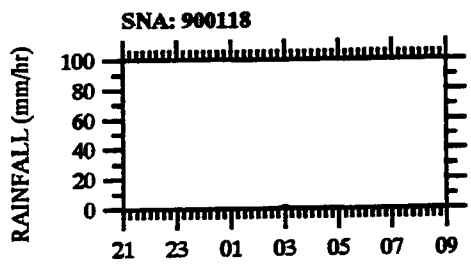
SNA: 900118
RAINFALL (mm/hr)
100
80
60
40
20
0
21 23 01 03 05 07 09

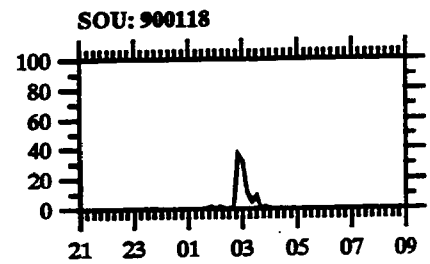
SOU: 900118
100
80
60
40
20
0
21 23 01 03 05 07 09

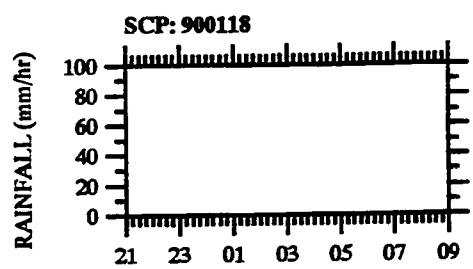
SCP: 900118
RAINFALL (mm/hr)
100
80
60
40
20
0
21 23 01 03 05 07 09

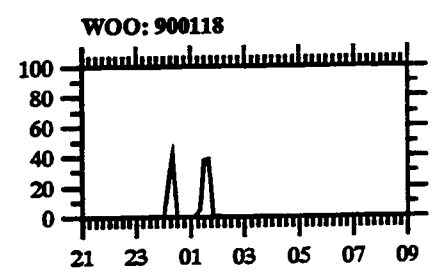
WOO: 900118
100
80
60
40
20
0
21 23 01 03 05 07 09

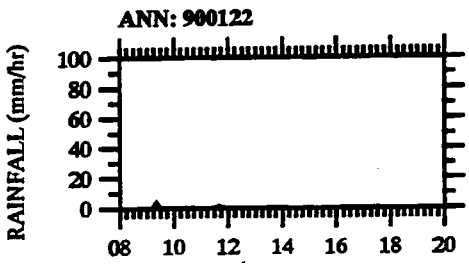
ANN: 900122
RAINFALL (mm/hr)
100
80
60
40
20
0
08 10 12 14 16 18 20

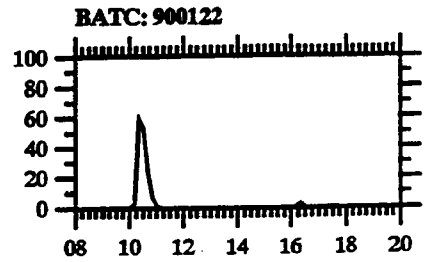
BATC: 900122
100
80
60
40
20
0
08 10 12 14 16 18 20

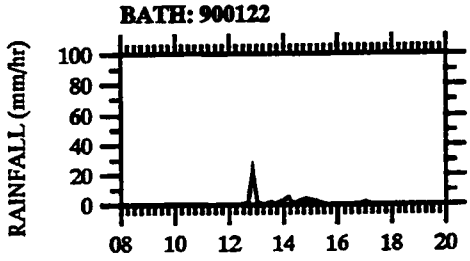
BATH: 900122
RAINFALL (mm/hr)
100
80
60
40
20
0
08 10 12 14 16 18 20

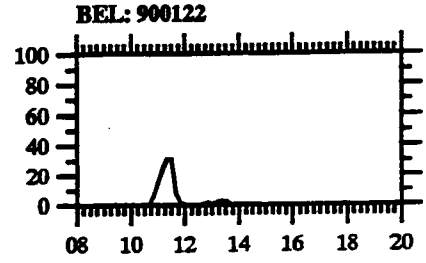
BEL: 900122
100
80
60
40
20
0
08 10 12 14 16 18 20

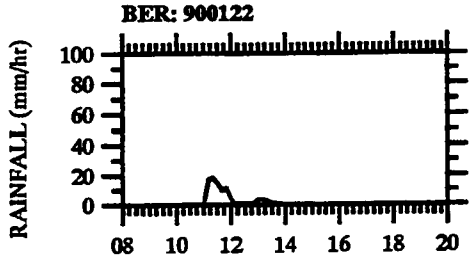
BER: 900122
RAINFALL (mm/hr)
100
80
60
40
20
0
08 10 12 14 16 18 20

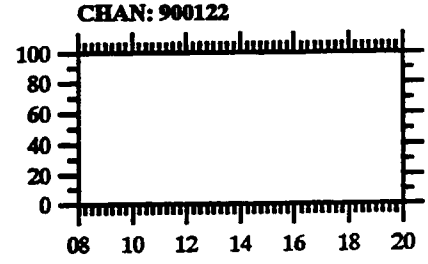
CHAN: 900122
100
80
60
40
20
0
08 10 12 14 16 18 20

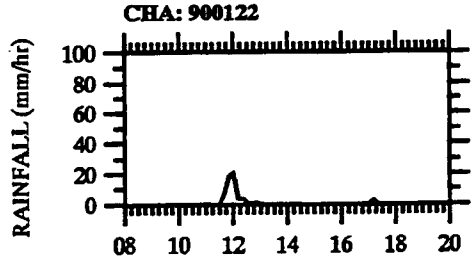
CHA: 900122
RAINFALL (mm/hr)
100
80
60
40
20
0
08 10 12 14 16 18 20

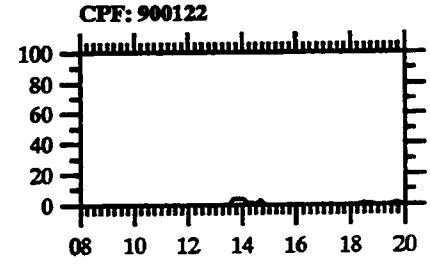
CPF: 900122
100
80
60
40
20
0
08 10 12 14 16 18 20

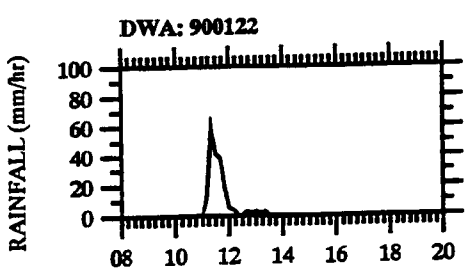
DWA: 900122
RAINFALL (mm/hr)
100
80
60
40
20
0
08 10 12 14 16 18 20

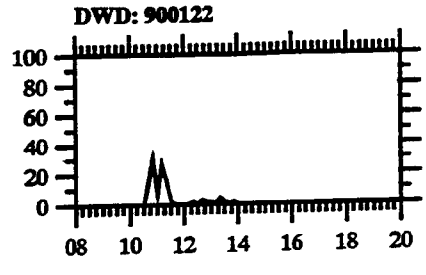
DWD: 900122
100
80
60
40
20
0
08 10 12 14 16 18 20

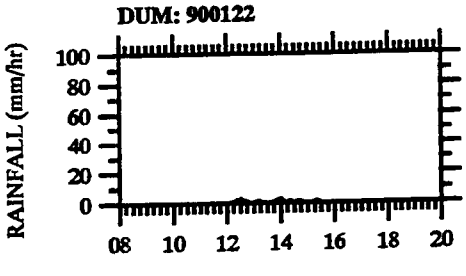
DUM: 900122
RAINFALL (mm/hr)
100
80
60
40
20
0
08 10 12 14 16 18 20

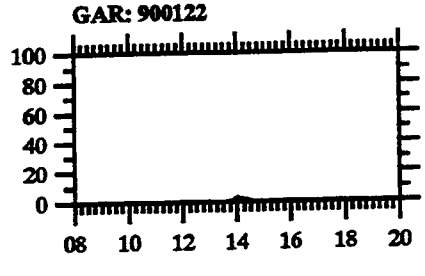
GAR: 900122
100
80
60
40
20
0
08 10 12 14 16 18 20

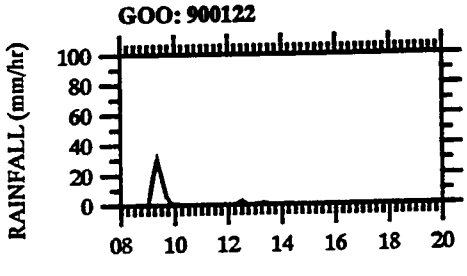
GOO: 900122
RAINFALL (mm/hr)
100
80
60
40
20
0
08 10 12 14 16 18 20

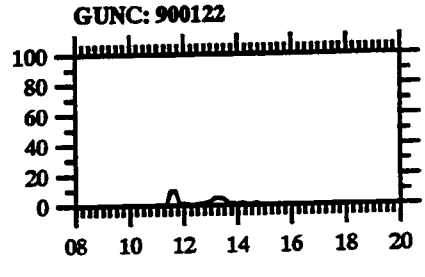
GUNC: 900122
100
80
60
40
20
0
08 10 12 14 16 18 20

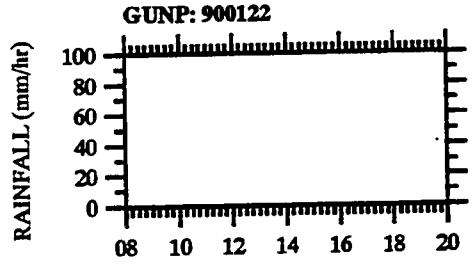
GUNP: 900122
RAINFALL (mm/hr)
100
80
60
40
20
0
08 10 12 14 16 18 20

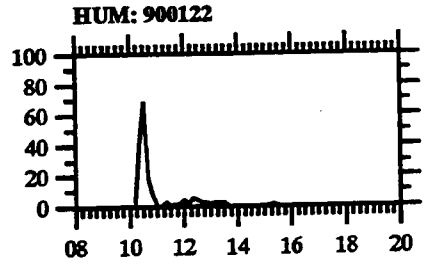
HUM: 900122
100
80
60
40
20
0
08 10 12 14 16 18 20

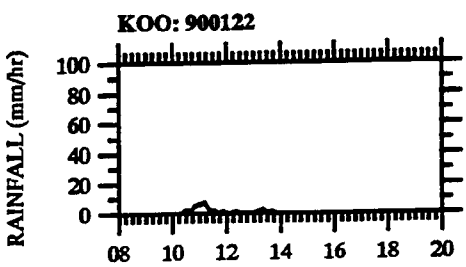
KOO: 900122
RAINFALL (mm/hr)
100
80
60
40
20
0
08 10 12 14 16 18 20

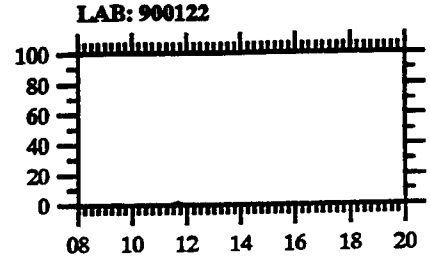
LAB: 900122
100
80
60
40
20
0
08 10 12 14 16 18 20

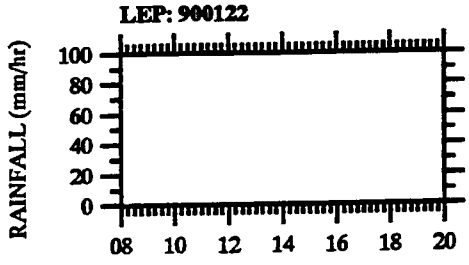
LEP: 900122
RAINFALL (mm/hr)
100
80
60
40
20
0
08 10 12 14 16 18 20

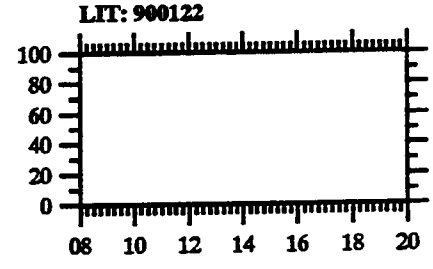
LIT: 900122
100
80
60
40
20
0
08 10 12 14 16 18 20

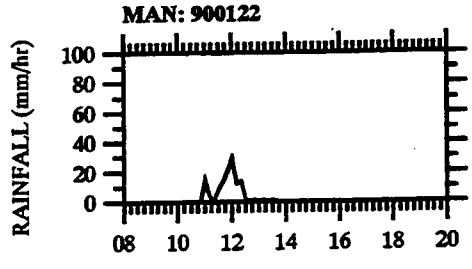
MAN: 900122
RAINFALL (mm/hr)
100
80
60
40
20
0
08 10 12 14 16 18 20

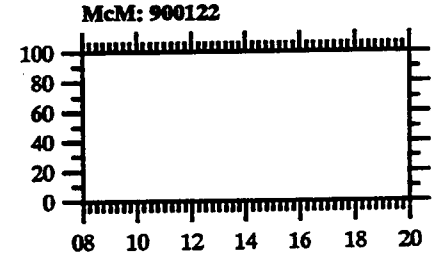
McM: 900122
100
80
60
40
20
0
08 10 12 14 16 18 20

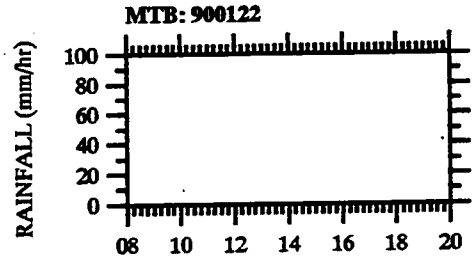
MTB: 900122
RAINFALL (mm/hr)
100
80
60
40
20
0
08 10 12 14 16 18 20

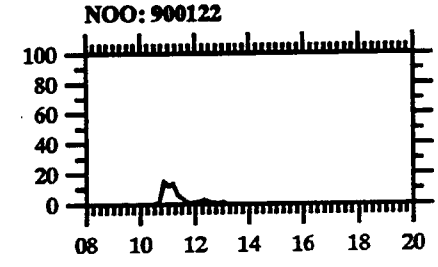
NOO: 900122
100
80
60
40
20
0
08 10 12 14 16 18 20

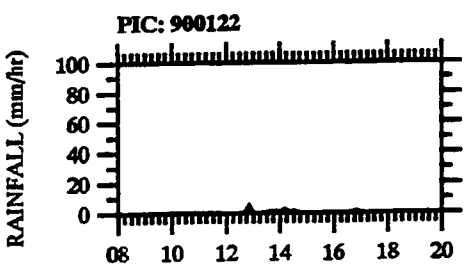
PIC: 900122
RAINFALL (mm/hr)
100
80
60
40
20
0
08 10 12 14 16 18 20

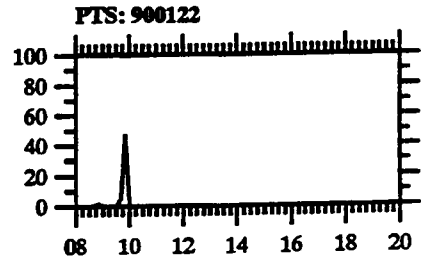
PTS: 900122
100
80
60
40
20
0
08 10 12 14 16 18 20

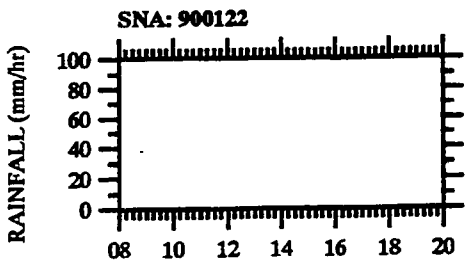
SNA: 900122
RAINFALL (mm/hr)
100
80
60
40
20
0
08 10 12 14 16 18 20

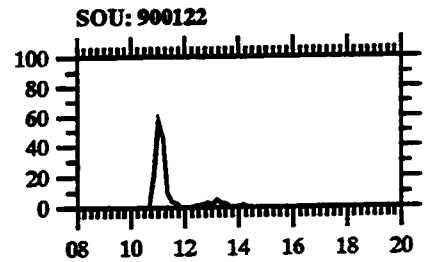
SOU: 900122
100
80
60
40
20
0
08 10 12 14 16 18 20

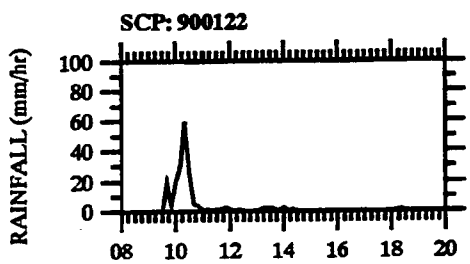
SCP: 900122
RAINFALL (mm/hr)
100
80
60
40
20
0
08 10 12 14 16 18 20

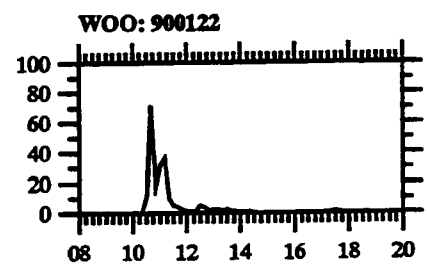
WOO: 900122
100
80
60
40
20
0
08 10 12 14 16 18 20

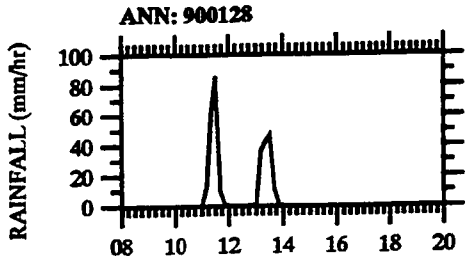
ANN: 900128
RAINFALL (mm/hr)
100
80
60
40
20
0
08 10 12 14 16 18 20

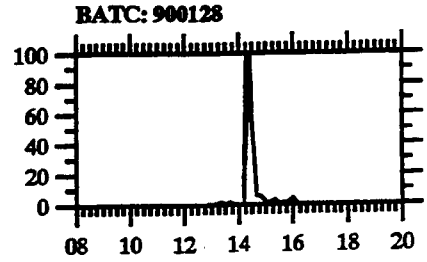
BATC: 900128
100
80
60
40
20
0
08 10 12 14 16 18 20

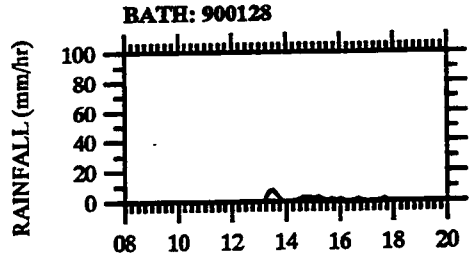
BATH: 900128
RAINFALL (mm/hr)
100
80
60
40
20
0
08 10 12 14 16 18 20

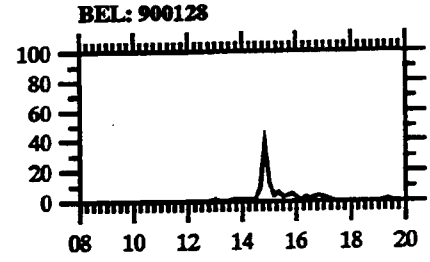
BEL: 900128
100
80
60
40
20
0
08 10 12 14 16 18 20

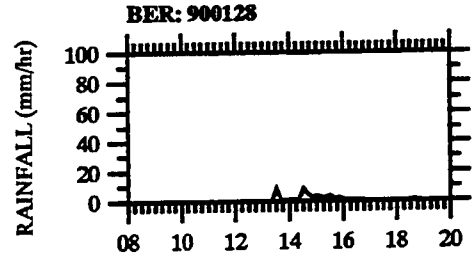
BER: 900128
RAINFALL (mm/hr)
100
80
60
40
20
0
08 10 12 14 16 18 20

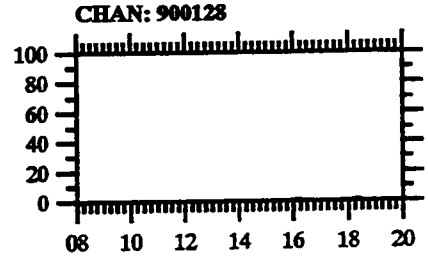
CHAN: 900128
100
80
60
40
20
0
08 10 12 14 16 18 20

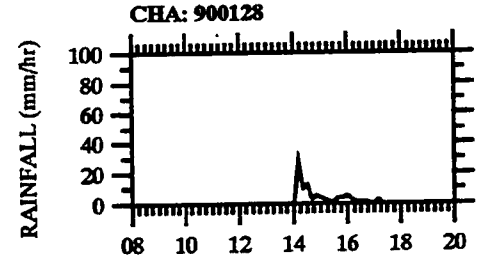
CHA: 900128
RAINFALL (mm/hr)
100
80
60
40
20
0
08 10 12 14 16 18 20

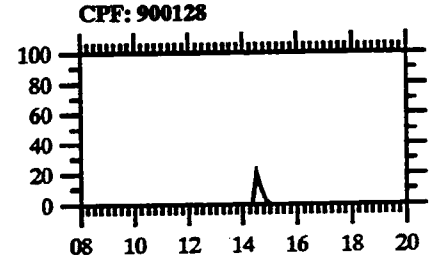
CPF: 900128
100
80
60
40
20
0
08 10 12 14 16 18 20

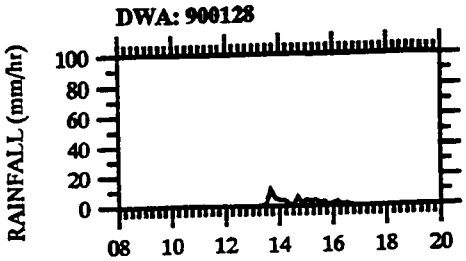
DWA: 900128
RAINFALL (mm/hr)
100
80
60
40
20
0
08 10 12 14 16 18 20

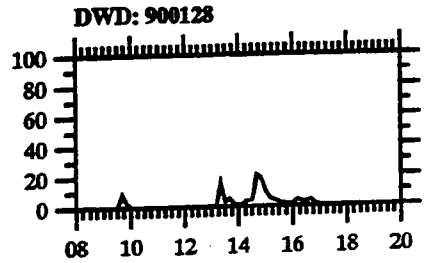
DWD: 900128
100
80
60
40
20
0
08 10 12 14 16 18 20

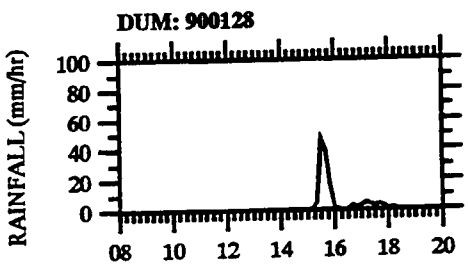
DUM: 900128
RAINFALL (mm/hr)
100
80
60
40
20
0
08 10 12 14 16 18 20

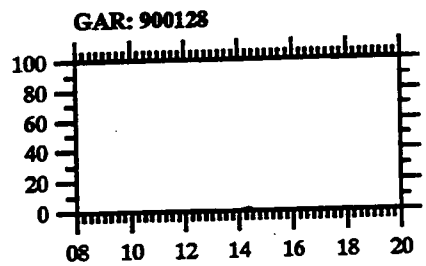
GAR: 900128
100
80
60
40
20
0
08 10 12 14 16 18 20

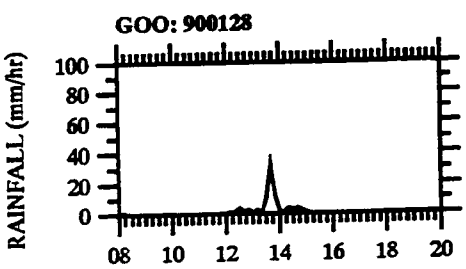
GOO: 900128
RAINFALL (mm/hr)
100
80
60
40
20
0
08 10 12 14 16 18 20

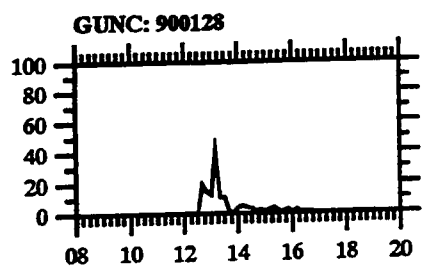
GUNC: 900128
100
80
60
40
20
0
08 10 12 14 16 18 20

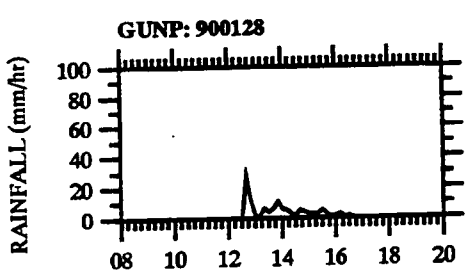
GUNP: 900128
RAINFALL (mm/hr)
100
80
60
40
20
0
08 10 12 14 16 18 20

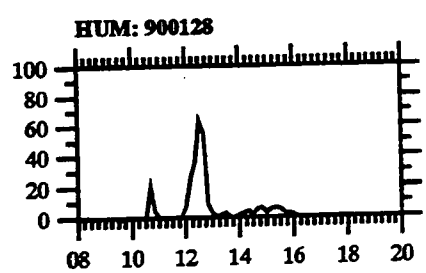
HUM: 900128
100
80
60
40
20
0
08 10 12 14 16 18 20

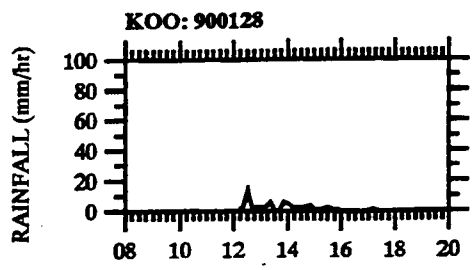
KOO: 900128
RAINFALL (mm/hr)
100
80
60
40
20
0
08 10 12 14 16 18 20

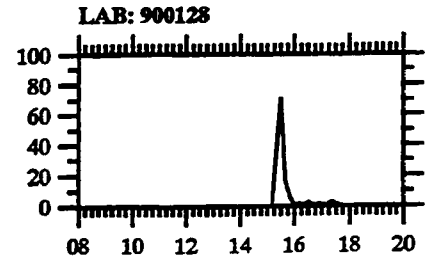
LAB: 900128
100
80
60
40
20
0
08 10 12 14 16 18 20

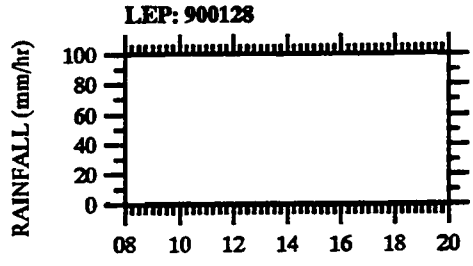
LEP: 900128
RAINFALL (mm/hr)
100
80
60
40
20
0
08 10 12 14 16 18 20

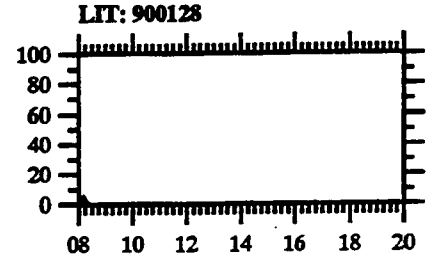
LIT: 900128
100
80
60
40
20
0
08 10 12 14 16 18 20

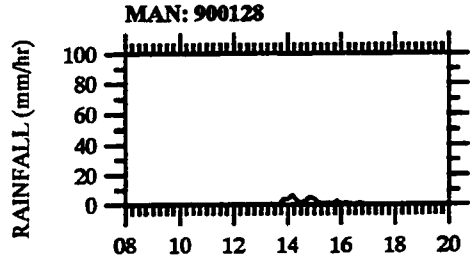
MAN: 900128
RAINFALL (mm/hr)
100
80
60
40
20
0
08 10 12 14 16 18 20

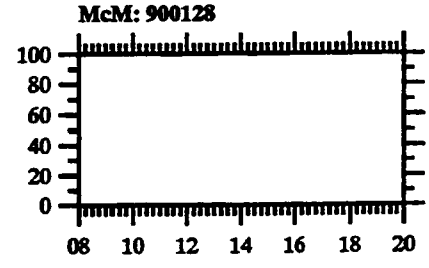
McM: 900128
100
80
60
40
20
0
08 10 12 14 16 18 20

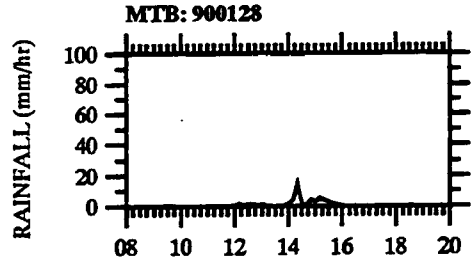
MTB: 900128
RAINFALL (mm/hr)
100
80
60
40
20
0
08 10 12 14 16 18 20

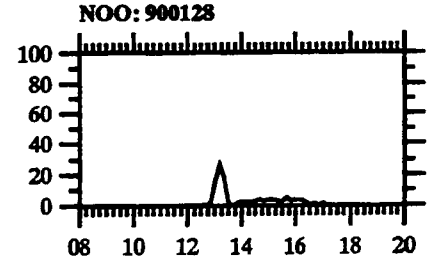
NOO: 900128
100
80
60
40
20
0
08 10 12 14 16 18 20

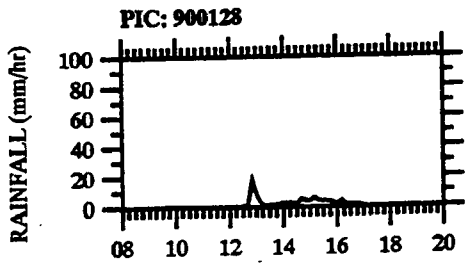
PIC: 900128
RAINFALL (mm/hr)
100
80
60
40
20
0
08 10 12 14 16 18 20

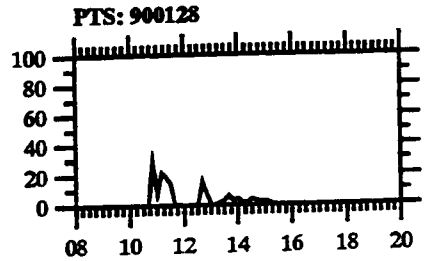
PTS: 900128
100
80
60
40
20
0
08 10 12 14 16 18 20

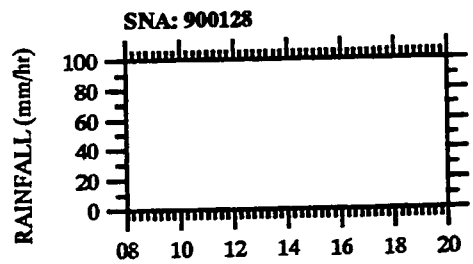
SNA: 900128
RAINFALL (mm/hr)
100
80
60
40
20
0
08 10 12 14 16 18 20

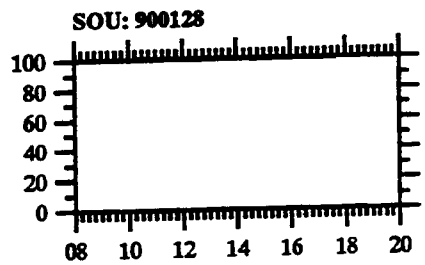
SOU: 900128
100
80
60
40
20
0
08 10 12 14 16 18 20

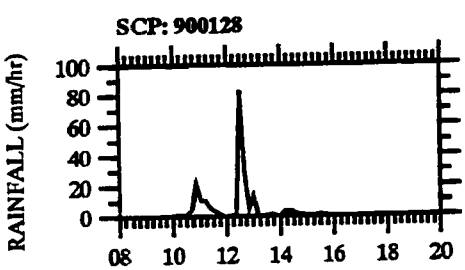
SCP: 900128
RAINFALL (mm/hr)
100
80
60
40
20
0
08 10 12 14 16 18 20

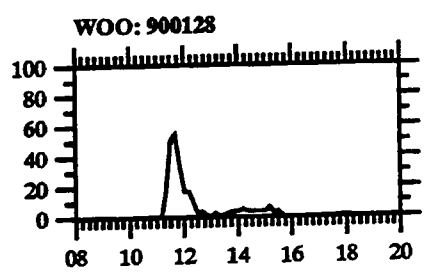
WOO: 900128
100
80
60
40
20
0
08 10 12 14 16 18 20

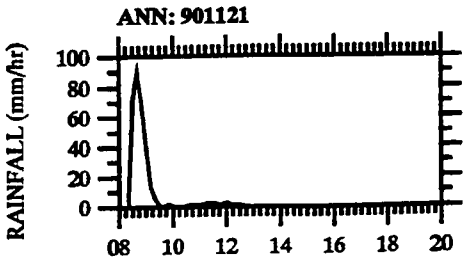
ANN: 901121
RAINFALL (mm/hr)
100
80
60
40
20
0
08 10 12 14 16 18 20

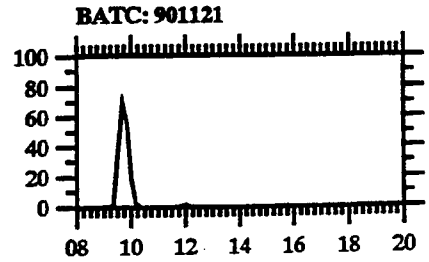
BATC: 901121
100
80
60
40
20
0
08 10 12 14 16 18 20

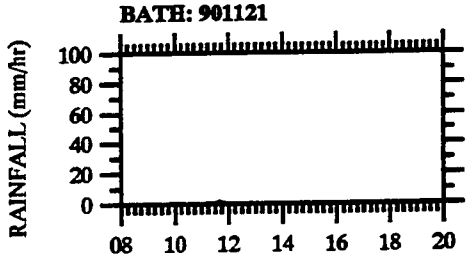
BATH: 901121
RAINFALL (mm/hr)
100
80
60
40
20
0
08 10 12 14 16 18 20

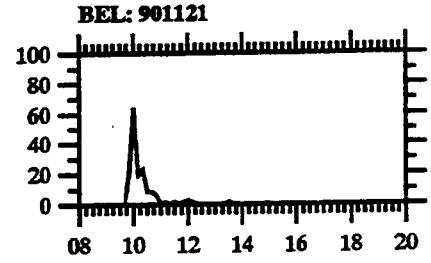
BEL: 901121
100
80
60
40
20
0
08 10 12 14 16 18 20

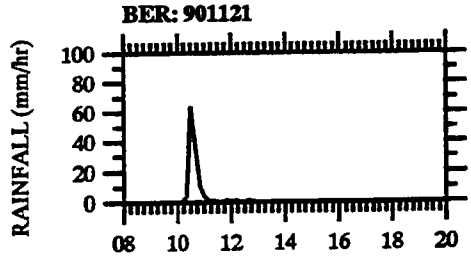
BER: 901121
RAINFALL (mm/hr)
100
80
60
40
20
0
08 10 12 14 16 18 20

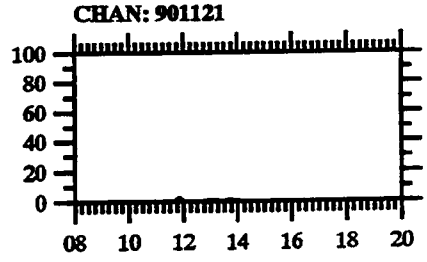
CHAN: 901121
100
80
60
40
20
0
08 10 12 14 16 18 20

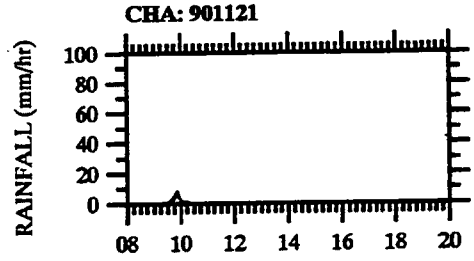
CHA: 901121
RAINFALL (mm/hr)
100
80
60
40
20
0
08 10 12 14 16 18 20

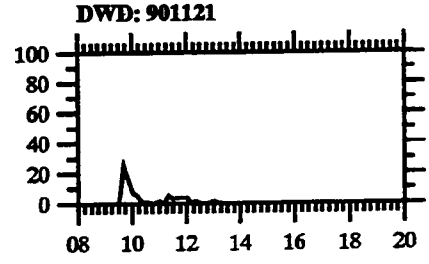
DWD: 901121
100
80
60
40
20
0
08 10 12 14 16 18 20

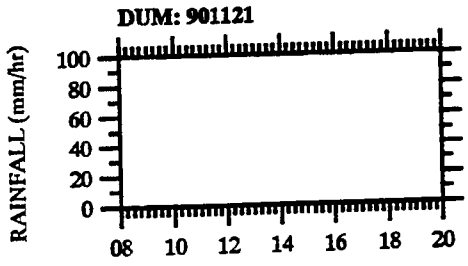
DUM: 901121
RAINFALL (mm/hr)
100
80
60
40
20
0
08 10 12 14 16 18 20

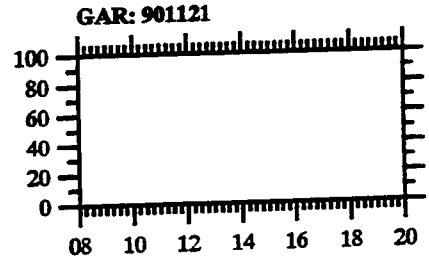
GAR: 901121
100
80
60
40
20
0
08 10 12 14 16 18 20

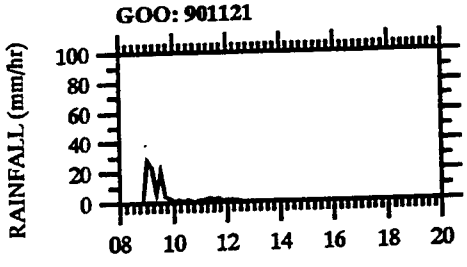
GOO: 901121
RAINFALL (mm/hr)
100
80
60
40
20
0
08 10 12 14 16 18 20

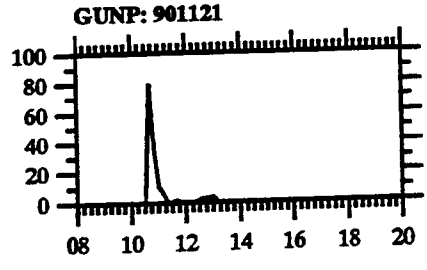
GUNP: 901121
100
80
60
40
20
0
08 10 12 14 16 18 20

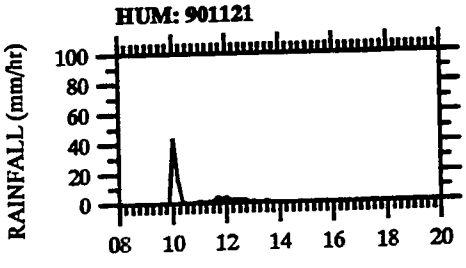
HUM: 901121
RAINFALL (mm/hr)
100
80
60
40
20
0
08 10 12 14 16 18 20

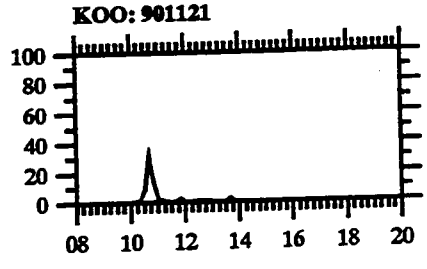
KOO: 901121
100
80
60
40
20
0
08 10 12 14 16 18 20

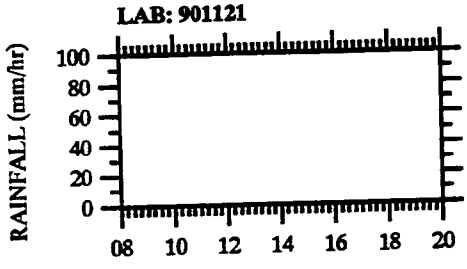
LAB: 901121
RAINFALL (mm/hr)
100
80
60
40
20
0
08 10 12 14 16 18 20


LIT: 901121
100
80
60
40
20
0
08 10 12 14 16 18 20

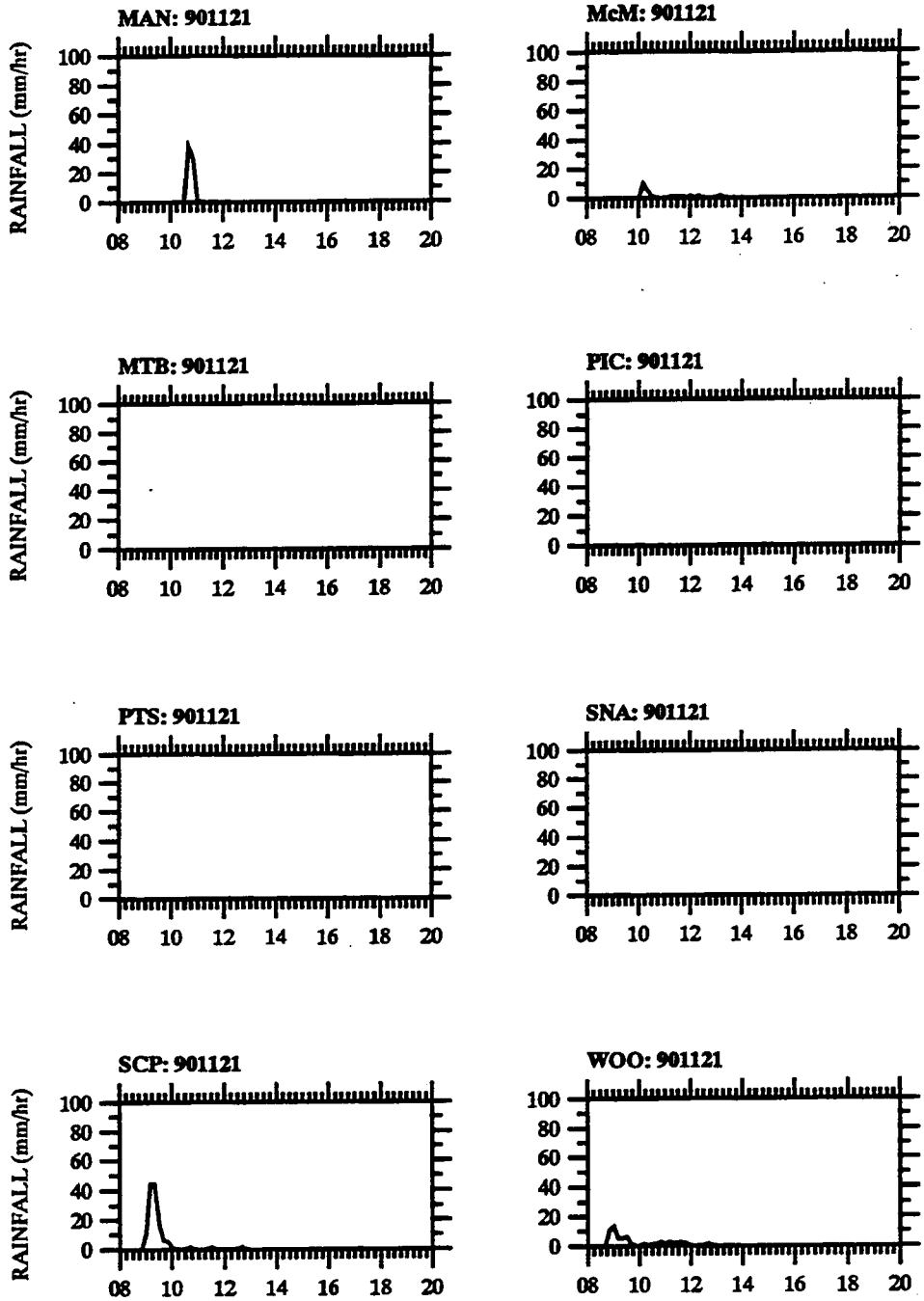
MAN: 901121
McM: 901121
MTB: 901121
PIC: 901121
PTS: 901121
SNA: 901121
SCP: 901121
WOO: 901121
RAINFALL (mm/hr)
0
20
40
60
80
100
08
10
12
14
16
18
20

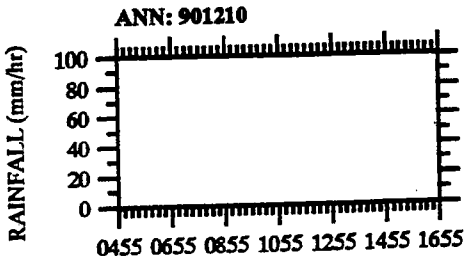
ANN: 901210
RAINFALL (mm/hr)
100
80
60
40
20
0
0455 0655 0855 1055 1255 1455 1655

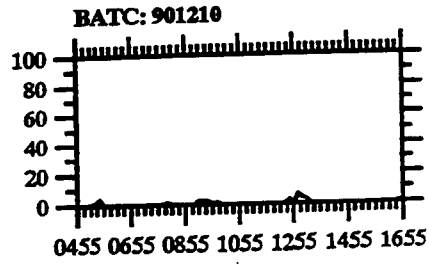
BATC: 901210
100
80
60
40
20
0
0455 0655 0855 1055 1255 1455 1655

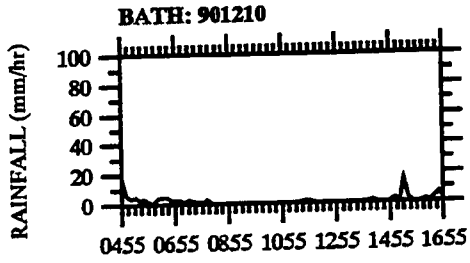
BATH: 901210
RAINFALL (mm/hr)
100
80
60
40
20
0
0455 0655 0855 1055 1255 1455 1655

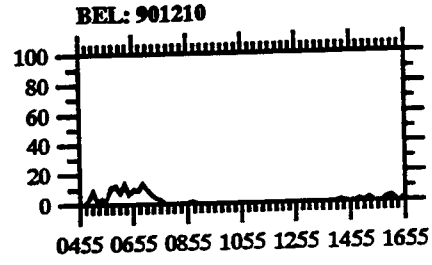
BEL: 901210
100
80
60
40
20
0
0455 0655 0855 1055 1255 1455 1655

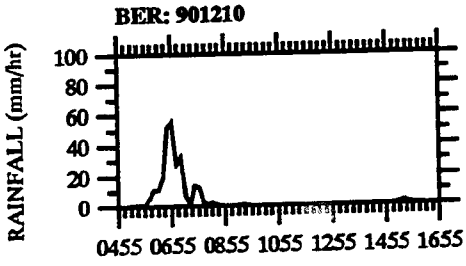
BER: 901210
RAINFALL (mm/hr)
100
80
60
40
20
0
0455 0655 0855 1055 1255 1455 1655

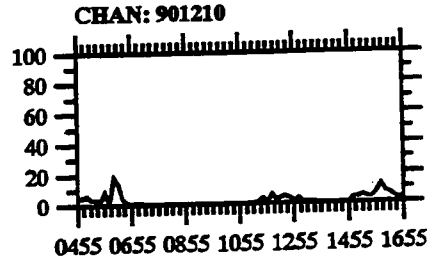
CHAN: 901210
100
80
60
40
20
0
0455 0655 0855 1055 1255 1455 1655

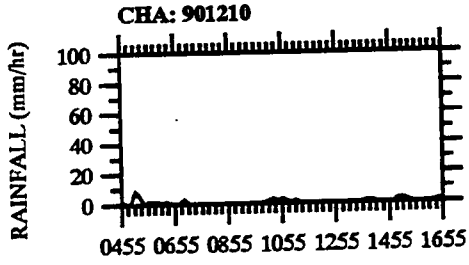
CHA: 901210
RAINFALL (mm/hr)
100
80
60
40
20
0
0455 0655 0855 1055 1255 1455 1655

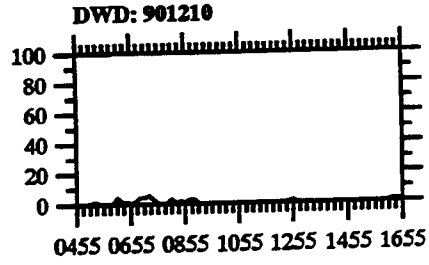
DWD: 901210
100
80
60
40
20
0
0455 0655 0855 1055 1255 1455 1655

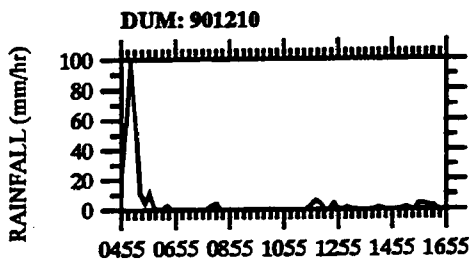
DUM: 901210
RAINFALL (mm/hr)
100
80
60
40
20
0
0455 0655 0855 1055 1255 1455 1655

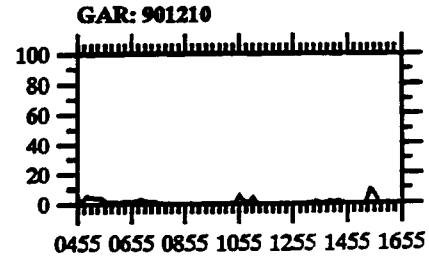
GAR: 901210
100
80
60
40
20
0
0455 0655 0855 1055 1255 1455 1655

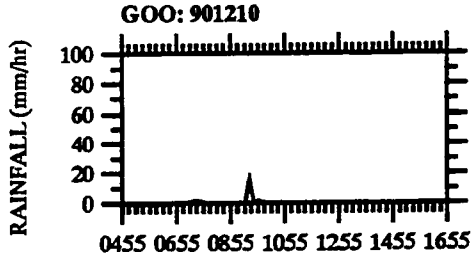
GOO: 901210
RAINFALL (mm/hr)
100
80
60
40
20
0
0455 0655 0855 1055 1255 1455 1655

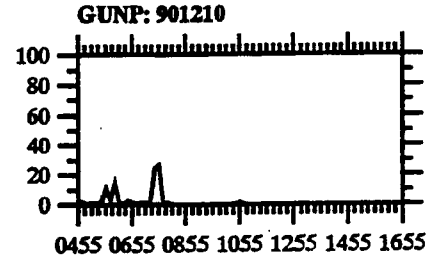
GUNP: 901210
100
80
60
40
20
0
0455 0655 0855 1055 1255 1455 1655

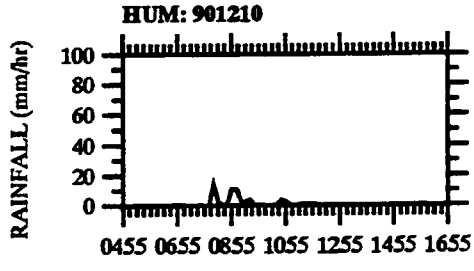
HUM: 901210
RAINFALL (mm/hr)
100
80
60
40
20
0
0455 0655 0855 1055 1255 1455 1655

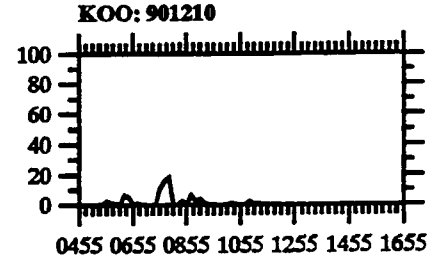
KOO: 901210
100
80
60
40
20
0
0455 0655 0855 1055 1255 1455 1655

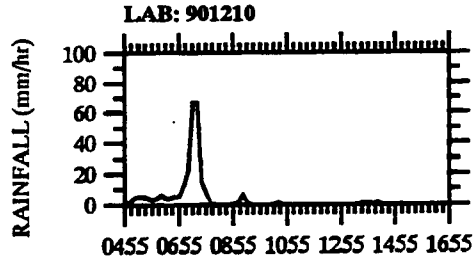
LAB: 901210
RAINFALL (mm/hr)
100
80
60
40
20
0
0455 0655 0855 1055 1255 1455 1655

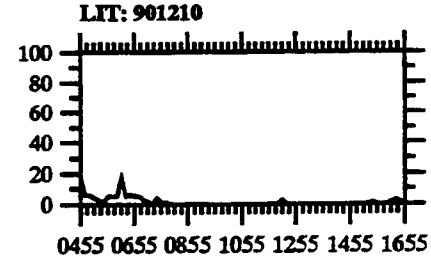
LIT: 901210
100
80
60
40
20
0
0455 0655 0855 1055 1255 1455 1655

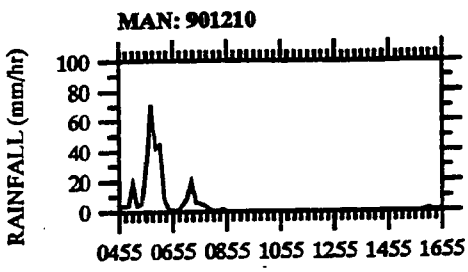
MAN: 901210
RAINFALL (mm/hr)
100
80
60
40
20
0
0455 0655 0855 1055 1255 1455 1655

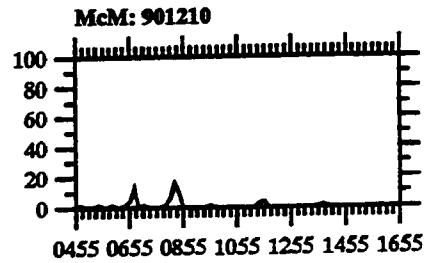
McM: 901210
100
80
60
40
20
0
0455 0655 0855 1055 1255 1455 1655

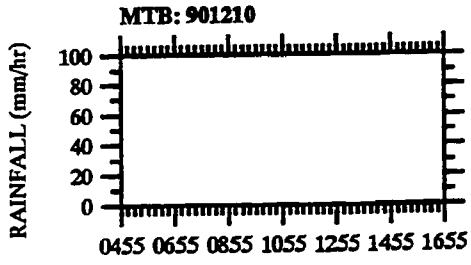
MTB: 901210
RAINFALL (mm/hr)
100
80
60
40
20
0
0455 0655 0855 1055 1255 1455 1655

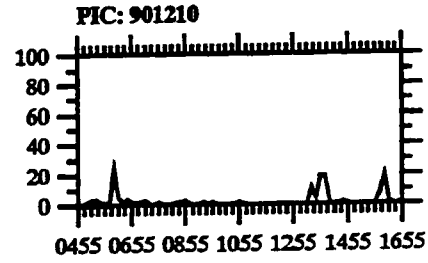
PIC: 901210
100
80
60
40
20
0
0455 0655 0855 1055 1255 1455 1655

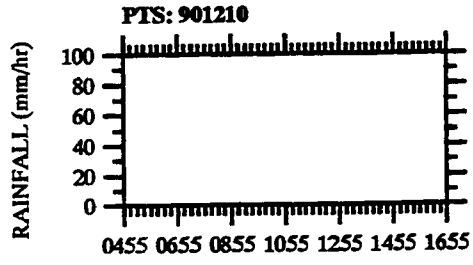
PTS: 901210
RAINFALL (mm/hr)
100
80
60
40
20
0
0455 0655 0855 1055 1255 1455 1655

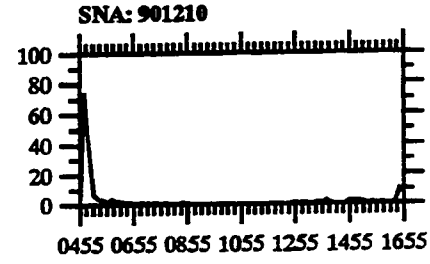
SNA: 901210
100
80
60
40
20
0
0455 0655 0855 1055 1255 1455 1655

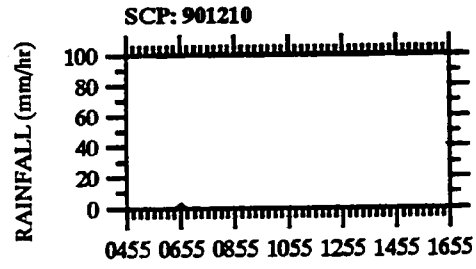
SCP: 901210
RAINFALL (mm/hr)
100
80
60
40
20
0
0455 0655 0855 1055 1255 1455 1655

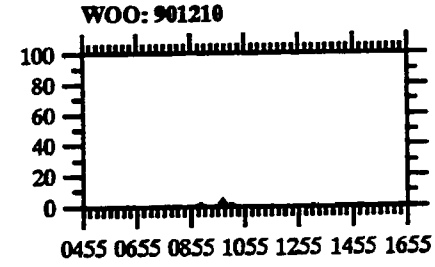
WOO: 901210
100
80
60
40
20
0
0455 0655 0855 1055 1255 1455 1655

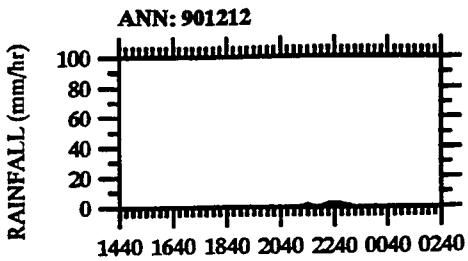
ANN: 901212
RAINFALL (mm/hr)
100
80
60
40
20
0
1440 1640 1840 2040 2240 0040 0240

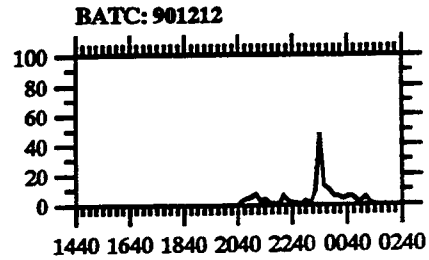
BATC: 901212
100
80
60
40
20
0
1440 1640 1840 2040 2240 0040 0240

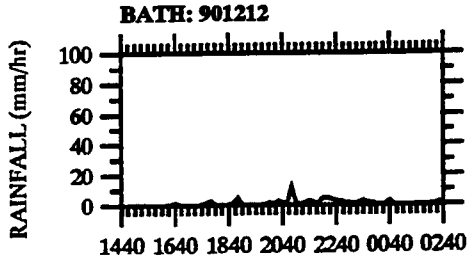
BATH: 901212
RAINFALL (mm/hr)
100
80
60
40
20
0
1440 1640 1840 2040 2240 0040 0240

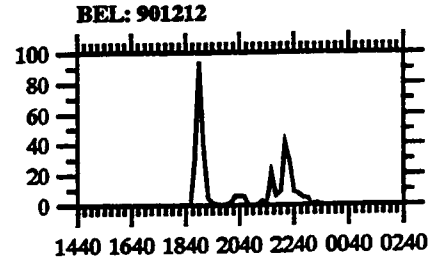
BEL: 901212
100
80
60
40
20
0
1440 1640 1840 2040 2240 0040 0240

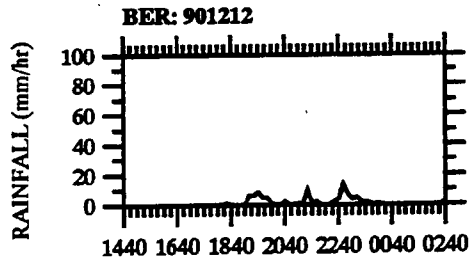
BER: 901212
RAINFALL (mm/hr)
100
80
60
40
20
0
1440 1640 1840 2040 2240 0040 0240

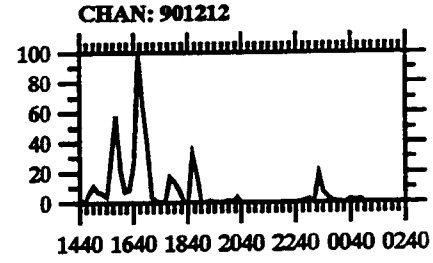
CHAN: 901212
100
80
60
40
20
0
1440 1640 1840 2040 2240 0040 0240

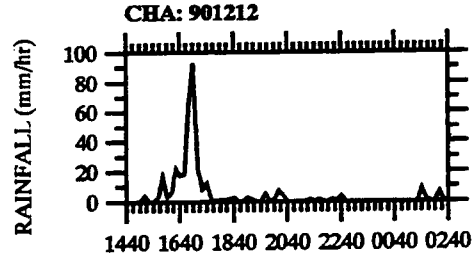
CHA: 901212
RAINFALL (mm/hr)
100
80
60
40
20
0
1440 1640 1840 2040 2240 0040 0240

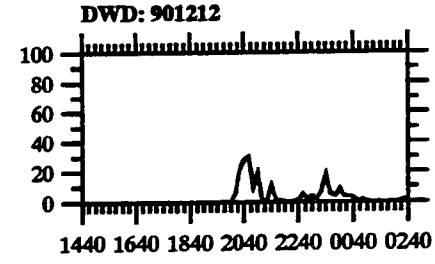
DWD: 901212
100
80
60
40
20
0
1440 1640 1840 2040 2240 0040 0240

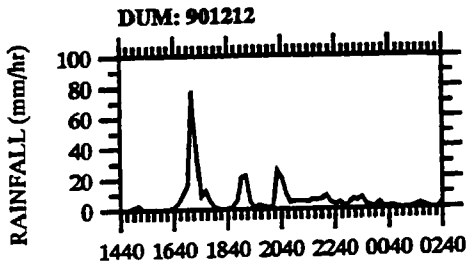
DUM: 901212
RAINFALL (mm/hr)
100
80
60
40
20
0
1440 1640 1840 2040 2240 0040 0240

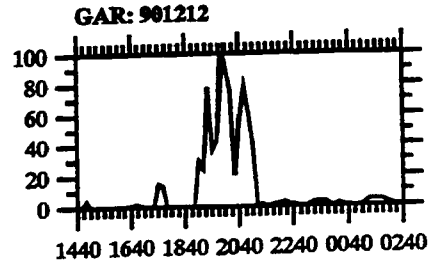
GAR: 901212
100
80
60
40
20
0
1440 1640 1840 2040 2240 0040 0240

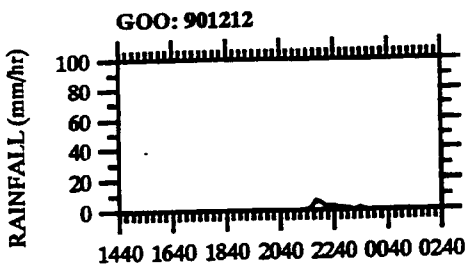
GOO: 901212
RAINFALL (mm/hr)
100
80
60
40
20
0
1440 1640 1840 2040 2240 0040 0240

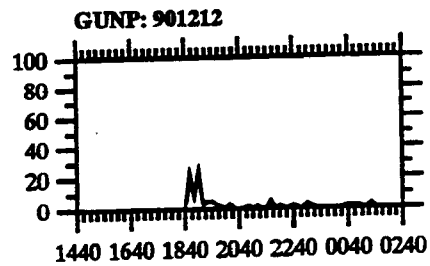
GUNP: 901212
100
80
60
40
20
0
1440 1640 1840 2040 2240 0040 0240

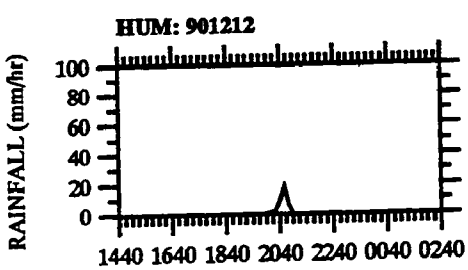
HUM: 901212
RAINFALL (mm/hr)
100
80
60
40
20
0
1440 1640 1840 2040 2240 0040 0240

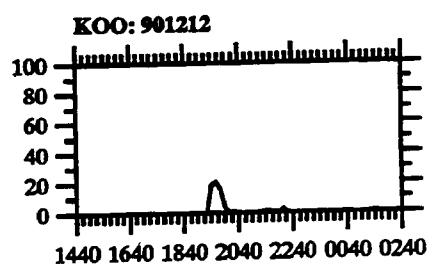
KOO: 901212
100
80
60
40
20
0
1440 1640 1840 2040 2240 0040 0240

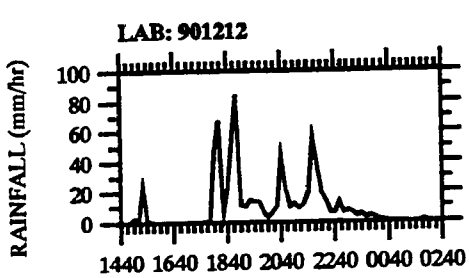
LAB: 901212
RAINFALL (mm/hr)
100
80
60
40
20
0
1440 1640 1840 2040 2240 0040 0240

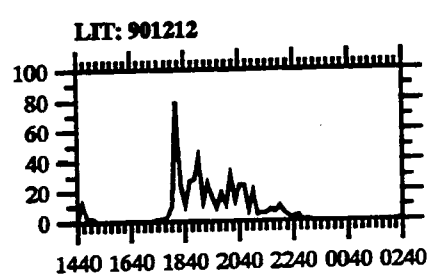
LIT: 901212
100
80
60
40
20
0
1440 1640 1840 2040 2240 0040 0240

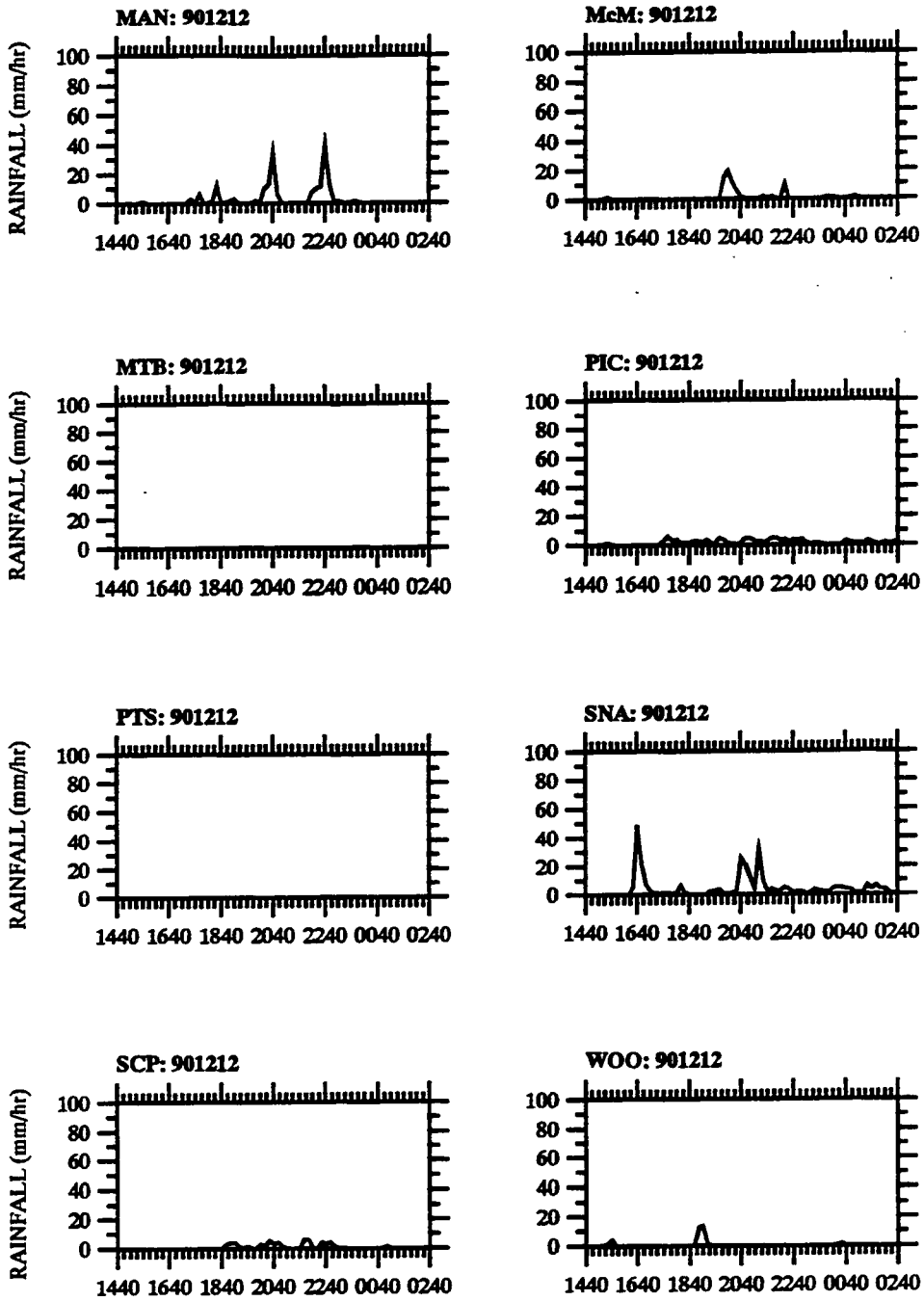
MAN: 901212
McM: 901212
MTB: 901212
PIC: 901212
PTS: 901212
SNA: 901212
SCP: 901212
WOO: 901212
RAINFALL (mm/hr)
100
80
60
40
20
0
1440 1640 1840 2040 2240 0040 0240

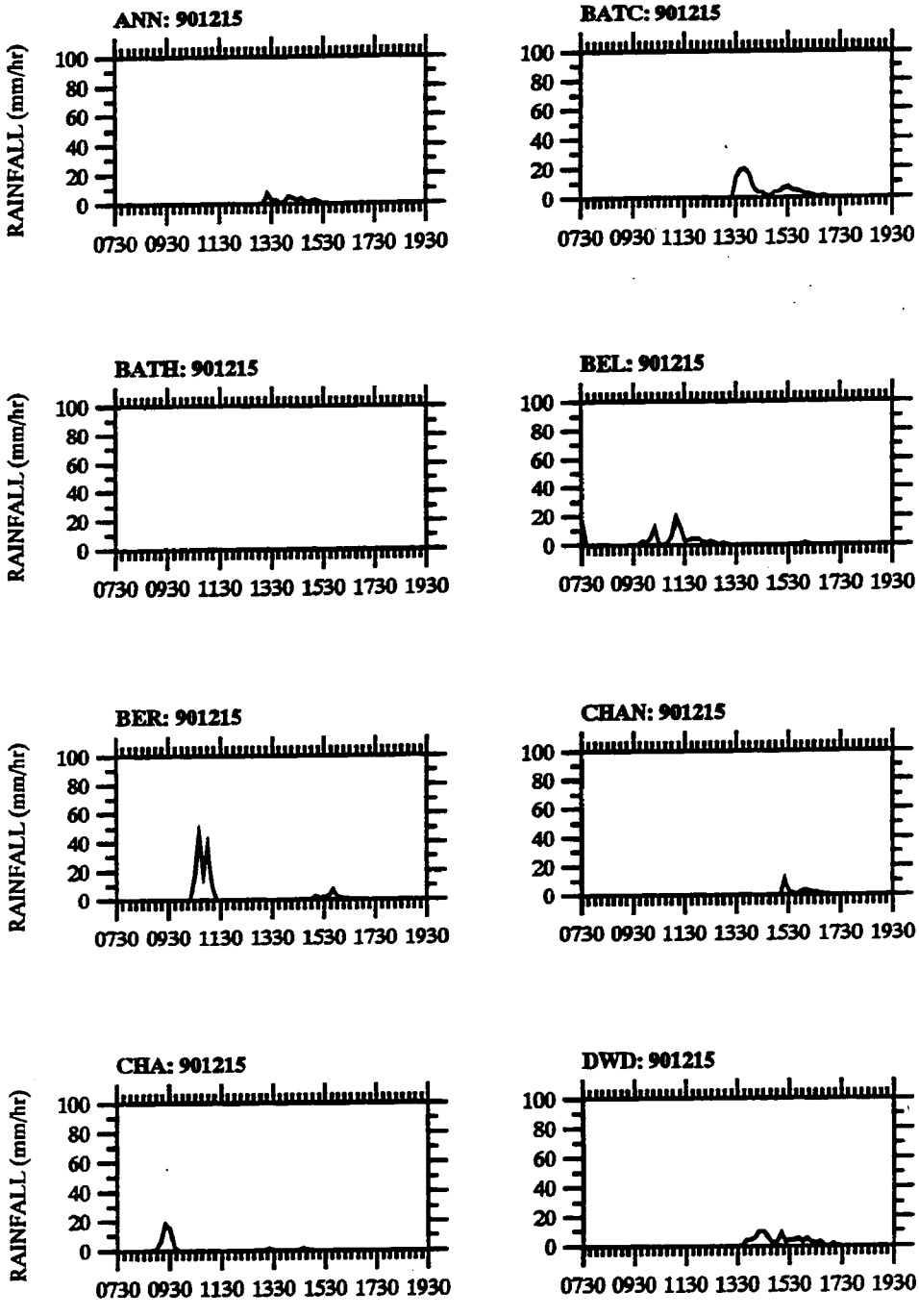
ANN: 901215
BATC: 901215
BATH: 901215
BEL: 901215
BER: 901215
CHAN: 901215
CHA: 901215
DWD: 901215
RAINFALL (mm/hr)
100
80
60
40
20
0
0730 0930 1130 1330 1530 1730 1930

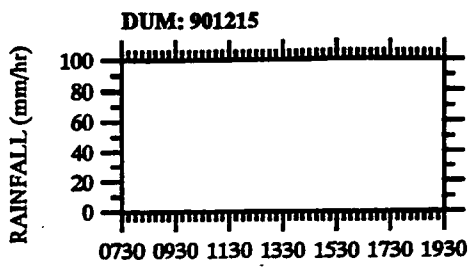
DUM: 901215
RAINFALL (mm/hr)
100
80
60
40
20
0
0730 0930 1130 1330 1530 1730 1930

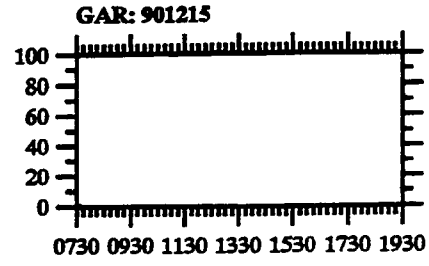
GAR: 901215
100
80
60
40
20
0
0730 0930 1130 1330 1530 1730 1930

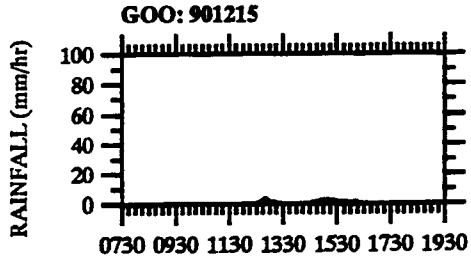
GOO: 901215
RAINFALL (mm/hr)
100
80
60
40
20
0
0730 0930 1130 1330 1530 1730 1930

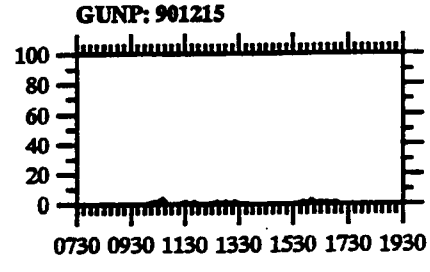
GUNP: 901215
100
80
60
40
20
0
0730 0930 1130 1330 1530 1730 1930

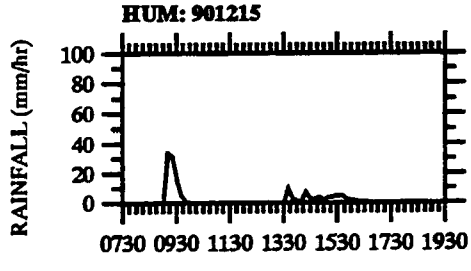
HUM: 901215
RAINFALL (mm/hr)
100
80
60
40
20
0
0730 0930 1130 1330 1530 1730 1930

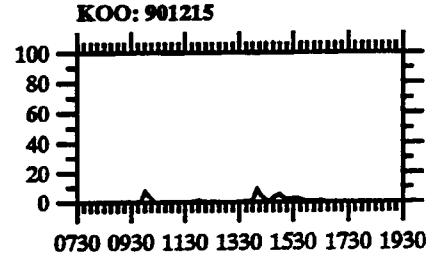
KOO: 901215
100
80
60
40
20
0
0730 0930 1130 1330 1530 1730 1930

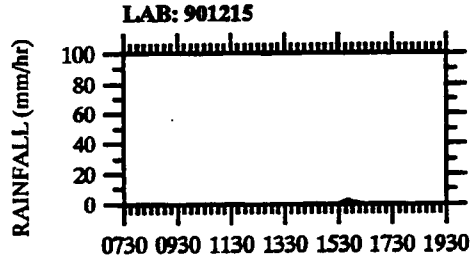
LAB: 901215
RAINFALL (mm/hr)
100
80
60
40
20
0
0730 0930 1130 1330 1530 1730 1930

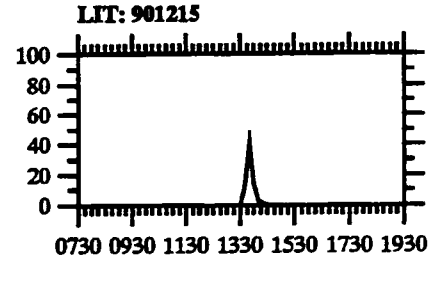
LIT: 901215
100
80
60
40
20
0
0730 0930 1130 1330 1530 1730 1930

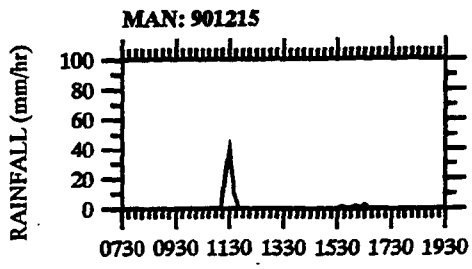
MAN: 901215
RAINFALL (mm/hr)
100
80
60
40
20
0
0730 0930 1130 1330 1530 1730 1930

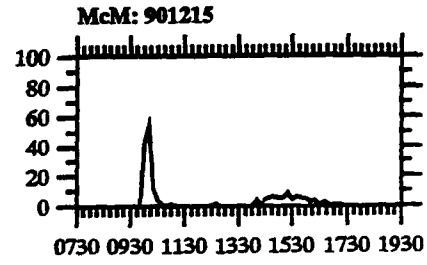
McM: 901215
100
80
60
40
20
0
0730 0930 1130 1330 1530 1730 1930

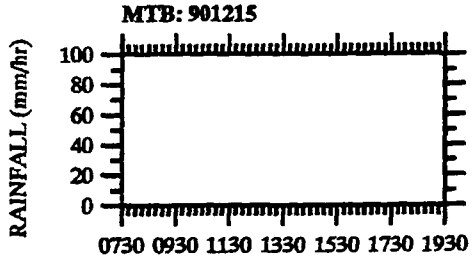
MTB: 901215
RAINFALL (mm/hr)
100
80
60
40
20
0
0730 0930 1130 1330 1530 1730 1930

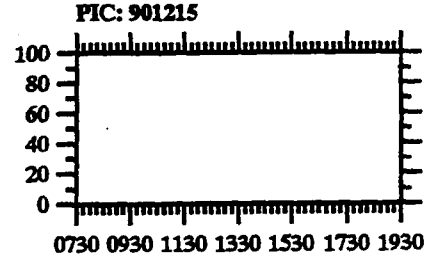
PIC: 901215
100
80
60
40
20
0
0730 0930 1130 1330 1530 1730 1930

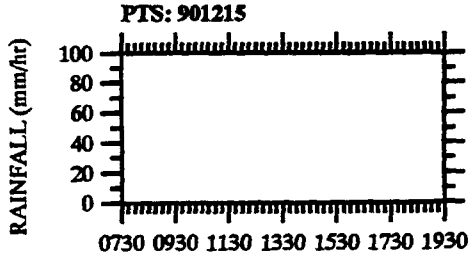
PTS: 901215
RAINFALL (mm/hr)
100
80
60
40
20
0
0730 0930 1130 1330 1530 1730 1930

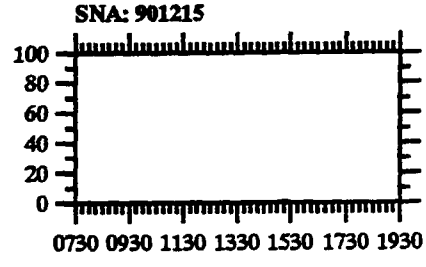
SNA: 901215
100
80
60
40
20
0
0730 0930 1130 1330 1530 1730 1930

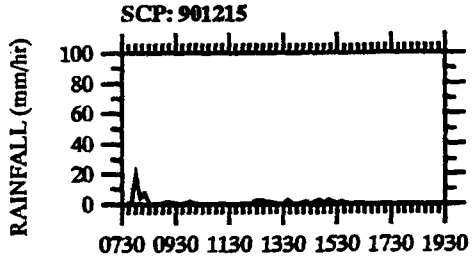
SCP: 901215
RAINFALL (mm/hr)
100
80
60
40
20
0
0730 0930 1130 1330 1530 1730 1930

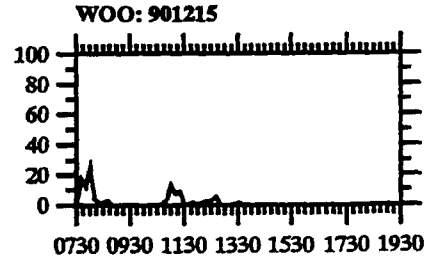
WOO: 901215
100
80
60
40
20
0
0730 0930 1130 1330 1530 1730 1930

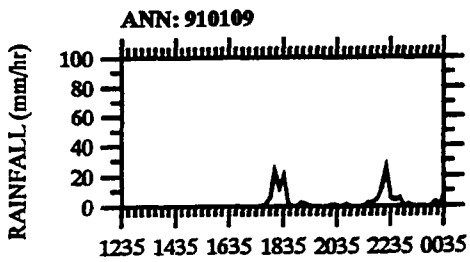
ANN: 910109
RAINFALL (mm/hr)
100
80
60
40
20
0
1235 1435 1635 1835 2035 2235 0035

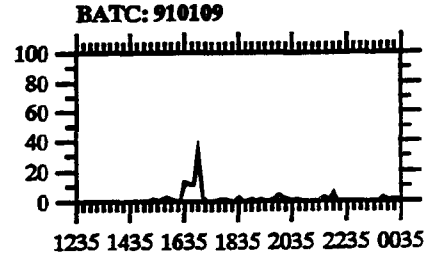
BATC: 910109
100
80
60
40
20
0
1235 1435 1635 1835 2035 2235 0035

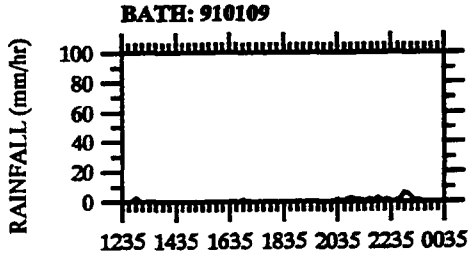
BATH: 910109
RAINFALL (mm/hr)
100
80
60
40
20
0
1235 1435 1635 1835 2035 2235 0035


BEL: 910109
100
80
60
40
20
0
1235 1435 1635 1835 2035 2235 0035

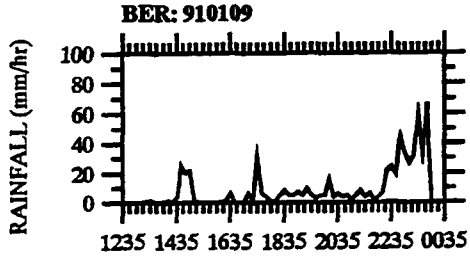
BER: 910109
RAINFALL (mm/hr)
100
80
60
40
20
0
1235 1435 1635 1835 2035 2235 0035

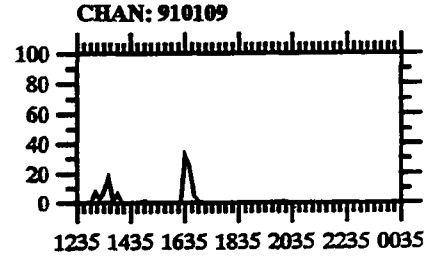
CHAN: 910109
100
80
60
40
20
0
1235 1435 1635 1835 2035 2235 0035

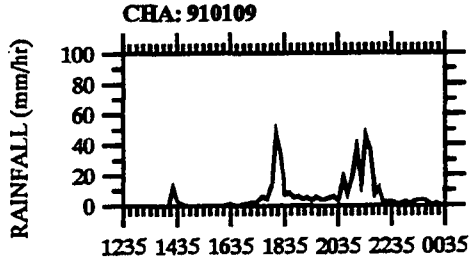
CHA: 910109
RAINFALL (mm/hr)
100
80
60
40
20
0
1235 1435 1635 1835 2035 2235 0035

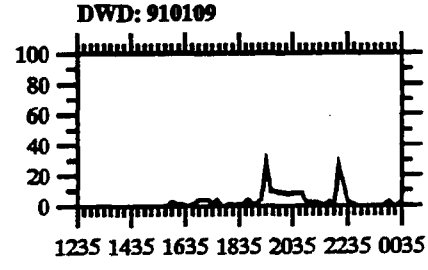
DWD: 910109
100
80
60
40
20
0
1235 1435 1635 1835 2035 2235 0035

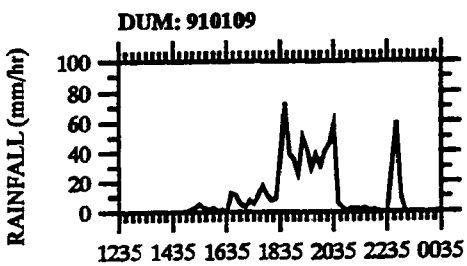
DUM: 910109
RAINFALL (mm/hr)
100
80
60
40
20
0
1235 1435 1635 1835 2035 2235 0035

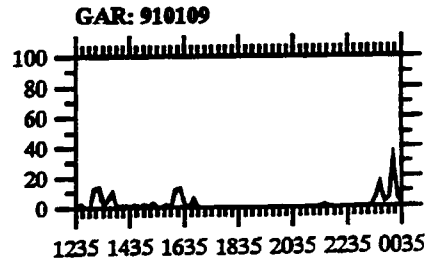
GAR: 910109
100
80
60
40
20
0
1235 1435 1635 1835 2035 2235 0035

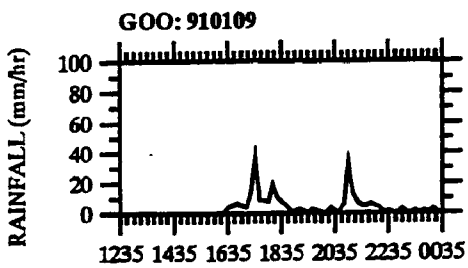
GOO: 910109
RAINFALL (mm/hr)
100
80
60
40
20
0
1235 1435 1635 1835 2035 2235 0035

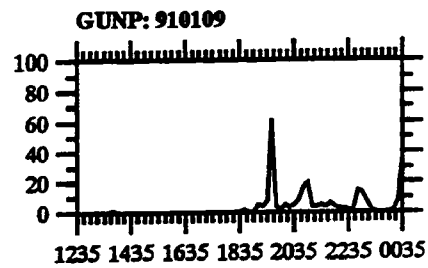
GUNP: 910109
100
80
60
40
20
0
1235 1435 1635 1835 2035 2235 0035

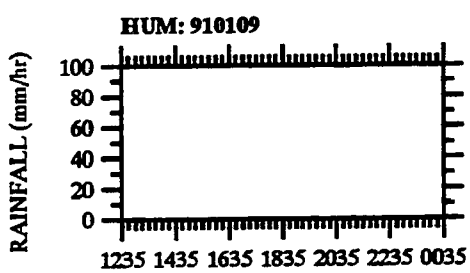
HUM: 910109
RAINFALL (mm/hr)
100
80
60
40
20
0
1235 1435 1635 1835 2035 2235 0035

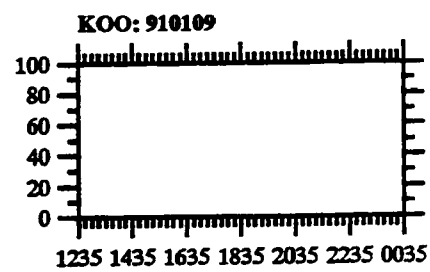
KOO: 910109
100
80
60
40
20
0
1235 1435 1635 1835 2035 2235 0035

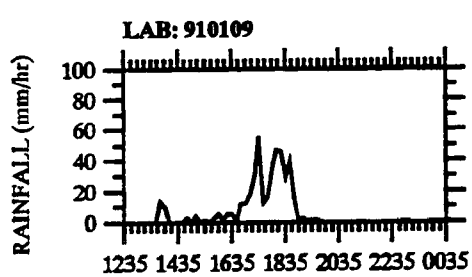
LAB: 910109
RAINFALL (mm/hr)
100
80
60
40
20
0
1235 1435 1635 1835 2035 2235 0035

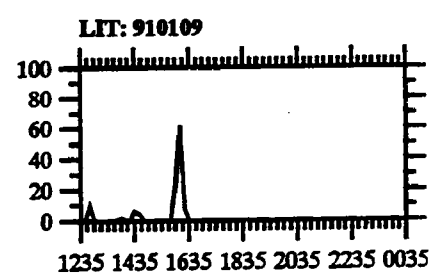
LIT: 910109
100
80
60
40
20
0
1235 1435 1635 1835 2035 2235 0035

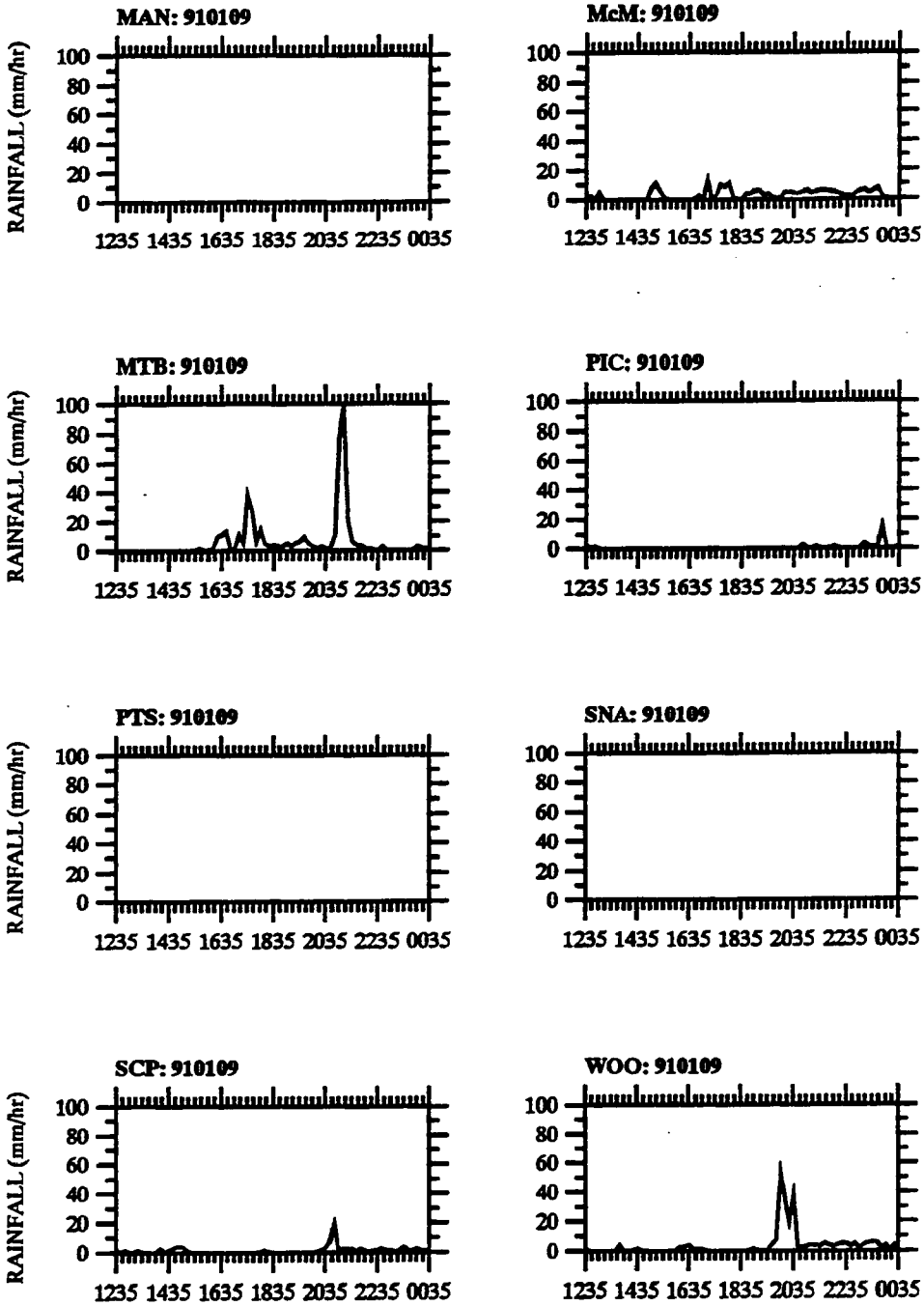
MAN: 910109
McM: 910109
MTB: 910109
PIC: 910109
PTS: 910109
SNA: 910109
SCP: 910109
WOO: 910109
RAINFALL (mm/hr)
100
80
60
40
20
0
1235 1435 1635 1835 2035 2235 0035

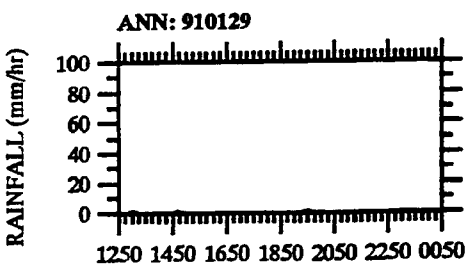
ANN: 910129
RAINFALL (mm/hr)
100
80
60
40
20
0
1250 1450 1650 1850 2050 2250 0050

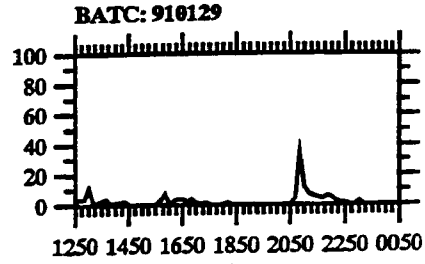
BATC: 910129
100
80
60
40
20
0
1250 1450 1650 1850 2050 2250 0050

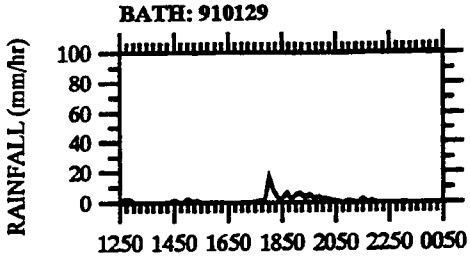
BATH: 910129
RAINFALL (mm/hr)
100
80
60
40
20
0
1250 1450 1650 1850 2050 2250 0050

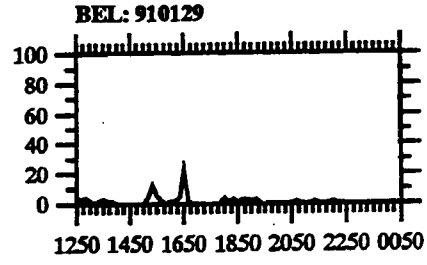
BEL: 910129
100
80
60
40
20
0
1250 1450 1650 1850 2050 2250 0050

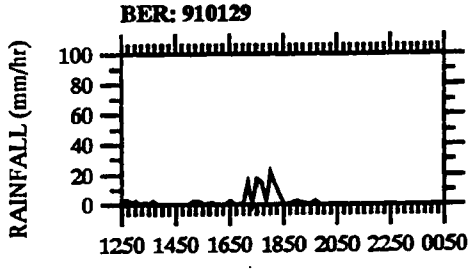
BER: 910129
RAINFALL (mm/hr)
100
80
60
40
20
0
1250 1450 1650 1850 2050 2250 0050

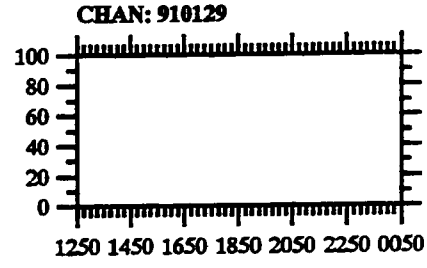
CHAN: 910129
100
80
60
40
20
0
1250 1450 1650 1850 2050 2250 0050

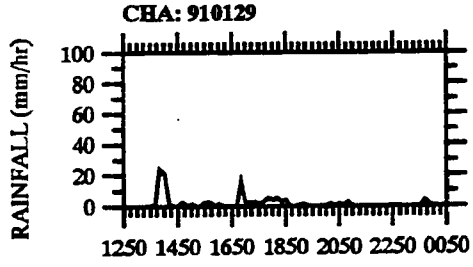
CHA: 910129
RAINFALL (mm/hr)
100
80
60
40
20
0
1250 1450 1650 1850 2050 2250 0050

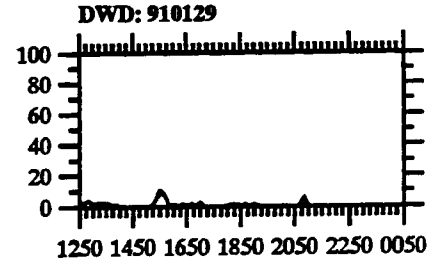
DWD: 910129
100
80
60
40
20
0
1250 1450 1650 1850 2050 2250 0050

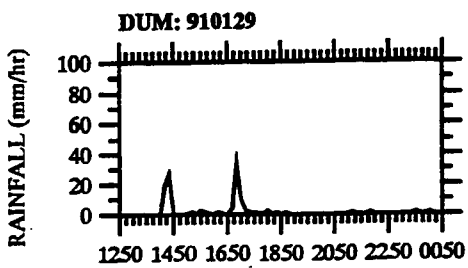
DUM: 910129
RAINFALL (mm/hr)
100
80
60
40
20
0
1250 1450 1650 1850 2050 2250 0050


GAR: 910129
100
80
60
40
20
0
1250 1450 1650 1850 2050 2250 0050

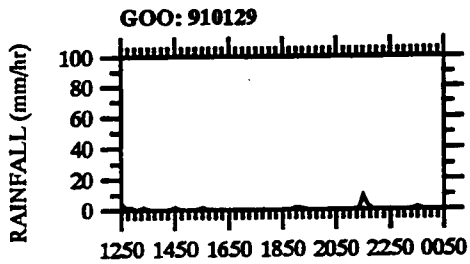
GOO: 910129
RAINFALL (mm/hr)
100
80
60
40
20
0
1250 1450 1650 1850 2050 2250 0050

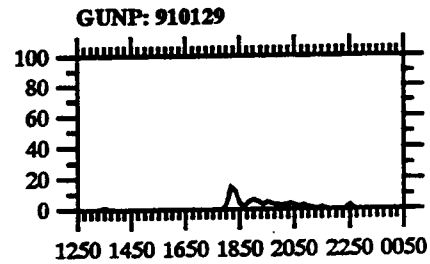
GUNP: 910129
100
80
60
40
20
0
1250 1450 1650 1850 2050 2250 0050

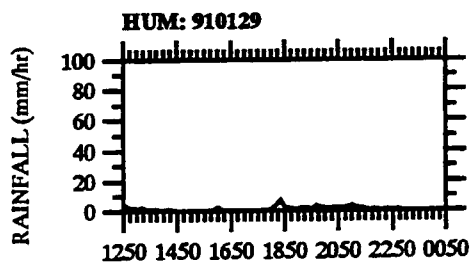
HUM: 910129
RAINFALL (mm/hr)
100
80
60
40
20
0
1250 1450 1650 1850 2050 2250 0050

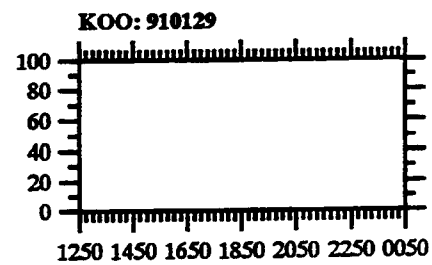
KOO: 910129
100
80
60
40
20
0
1250 1450 1650 1850 2050 2250 0050

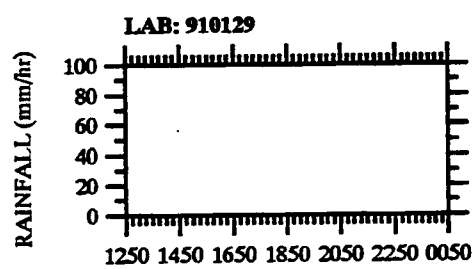
LAB: 910129
RAINFALL (mm/hr)
100
80
60
40
20
0
1250 1450 1650 1850 2050 2250 0050

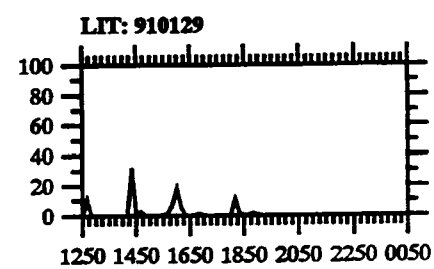
LIT: 910129
100
80
60
40
20
0
1250 1450 1650 1850 2050 2250 0050

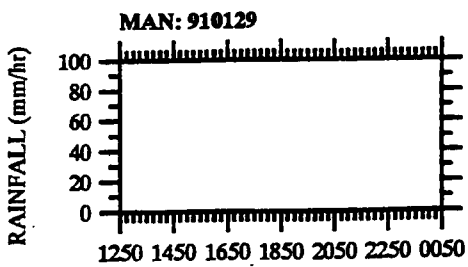
MAN: 910129
RAINFALL (mm/hr)
100
80
60
40
20
0
1250 1450 1650 1850 2050 2250 0050

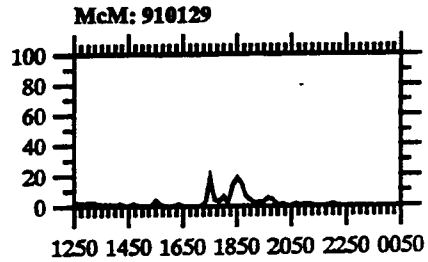
McM: 910129
100
80
60
40
20
0
1250 1450 1650 1850 2050 2250 0050

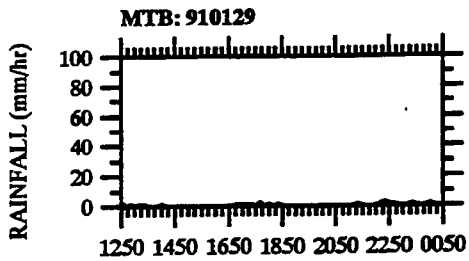
MTB: 910129
RAINFALL (mm/hr)
100
80
60
40
20
0
1250 1450 1650 1850 2050 2250 0050

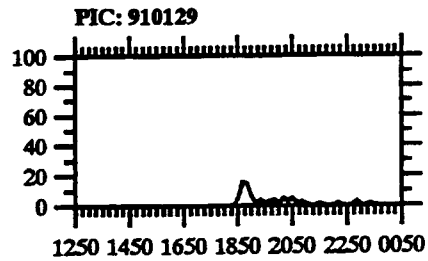
PIC: 910129
100
80
60
40
20
0
1250 1450 1650 1850 2050 2250 0050

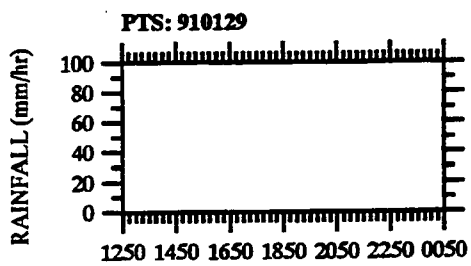
PTS: 910129
RAINFALL (mm/hr)
100
80
60
40
20
0
1250 1450 1650 1850 2050 2250 0050

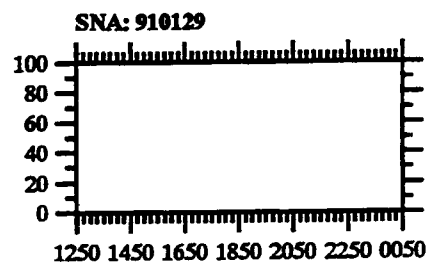
SNA: 910129
100
80
60
40
20
0
1250 1450 1650 1850 2050 2250 0050

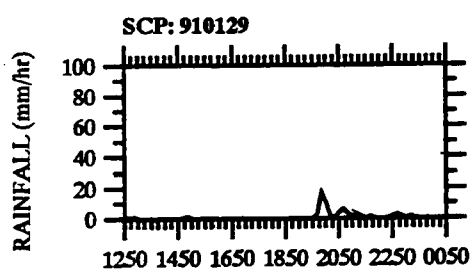
SCP: 910129
RAINFALL (mm/hr)
100
80
60
40
20
0
1250 1450 1650 1850 2050 2250 0050

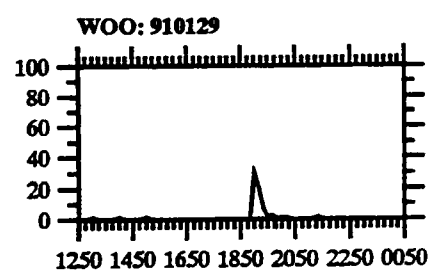
WOO: 910129
100
80
60
40
20
0
1250 1450 1650 1850 2050 2250 0050

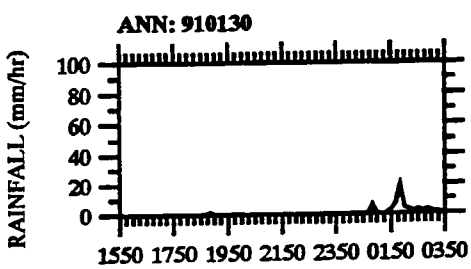
ANN: 910130
RAINFALL (mm/hr)
100
80
60
40
20
0
1550 1750 1950 2150 2350 0150 0350

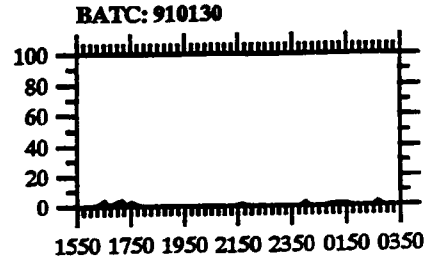
BATC: 910130
100
80
60
40
20
0
1550 1750 1950 2150 2350 0150 0350

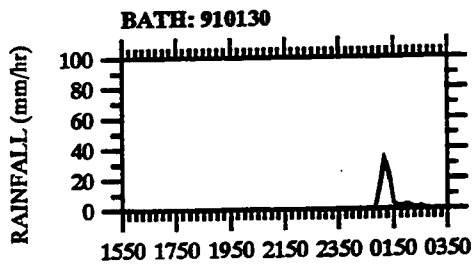
BATH: 910130
RAINFALL (mm/hr)
100
80
60
40
20
0
1550 1750 1950 2150 2350 0150 0350

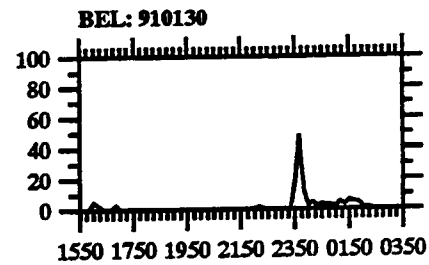
BEL: 910130
100
80
60
40
20
0
1550 1750 1950 2150 2350 0150 0350

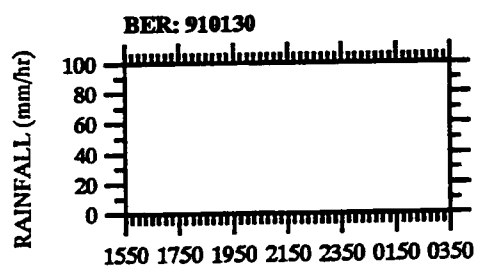
BER: 910130
RAINFALL (mm/hr)
100
80
60
40
20
0
1550 1750 1950 2150 2350 0150 0350

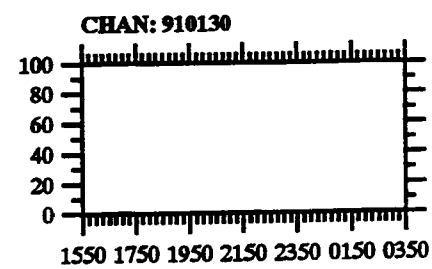
CHAN: 910130
100
80
60
40
20
0
1550 1750 1950 2150 2350 0150 0350

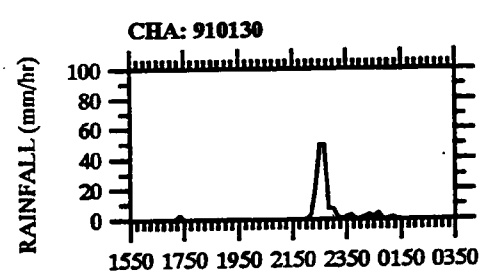
CHA: 910130
RAINFALL (mm/hr)
100
80
60
40
20
0
1550 1750 1950 2150 2350 0150 0350

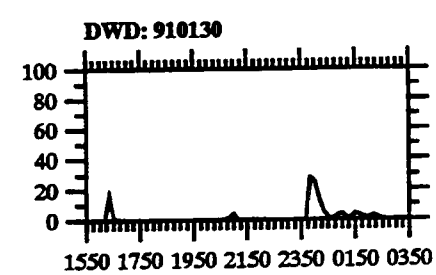
DWD: 910130
100
80
60
40
20
0
1550 1750 1950 2150 2350 0150 0350

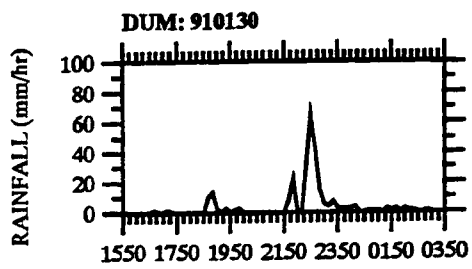
DUM: 910130
RAINFALL (mm/hr)
100
80
60
40
20
0
1550 1750 1950 2150 2350 0150 0350

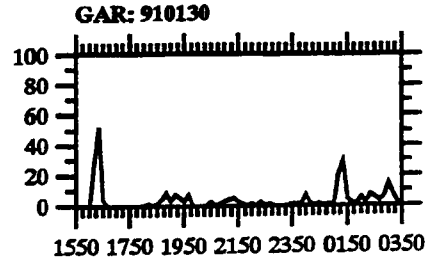
GAR: 910130
100
80
60
40
20
0
1550 1750 1950 2150 2350 0150 0350

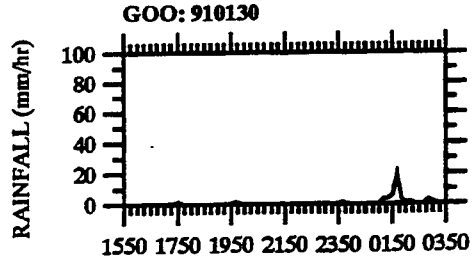
GOO: 910130
RAINFALL (mm/hr)
100
80
60
40
20
0
1550 1750 1950 2150 2350 0150 0350

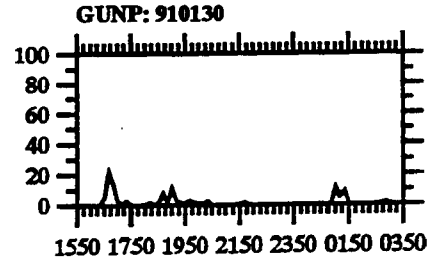
GUNP: 910130
100
80
60
40
20
0
1550 1750 1950 2150 2350 0150 0350

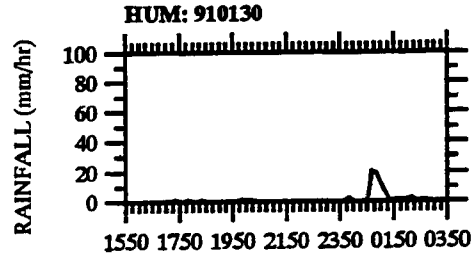
HUM: 910130
RAINFALL (mm/hr)
100
80
60
40
20
0
1550 1750 1950 2150 2350 0150 0350

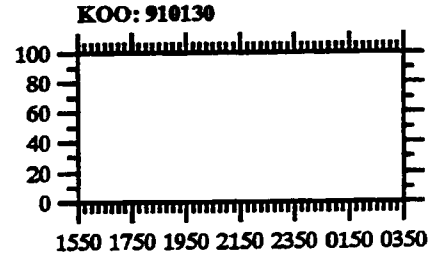
KOO: 910130
100
80
60
40
20
0
1550 1750 1950 2150 2350 0150 0350

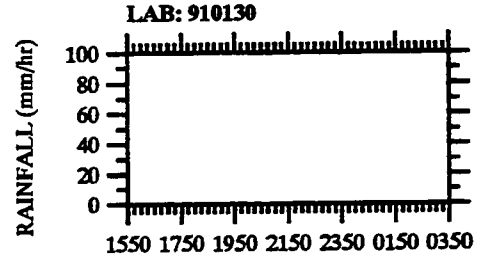
LAB: 910130
RAINFALL (mm/hr)
100
80
60
40
20
0
1550 1750 1950 2150 2350 0150 0350

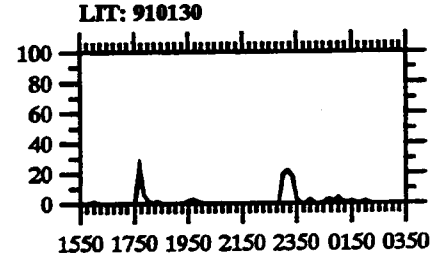
LIT: 910130
100
80
60
40
20
0
1550 1750 1950 2150 2350 0150 0350

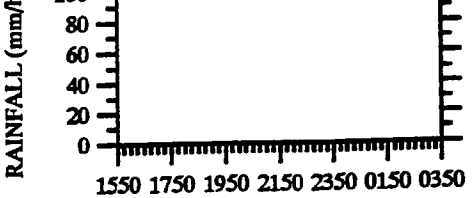
RAINFALL (mm/hr)
100
80
60
40
20
0
1550 1750 1950 2150 2350 0150 0350

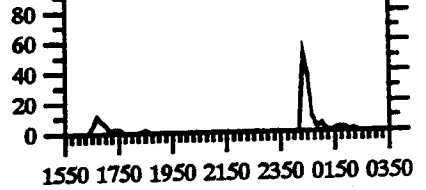
80
60
40
20
0
1550 1750 1950 2150 2350 0150 0350

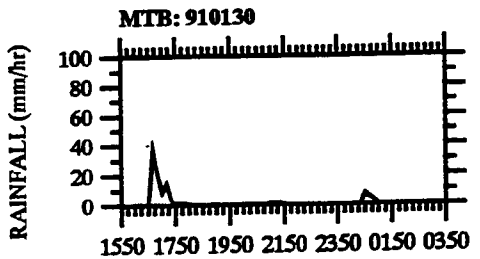
MTB: 910130
RAINFALL (mm/hr)
100
80
60
40
20
0
1550 1750 1950 2150 2350 0150 0350


PIC: 910130
100
80
60
40
20
0
1550 1750 1950 2150 2350 0150 0350

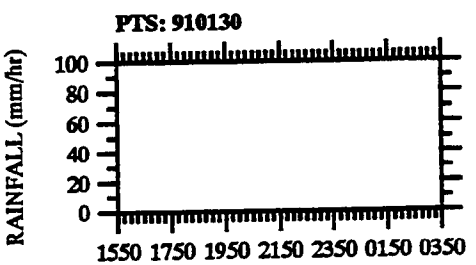
PTS: 910130
RAINFALL (mm/hr)
100
80
60
40
20
0
1550 1750 1950 2150 2350 0150 0350

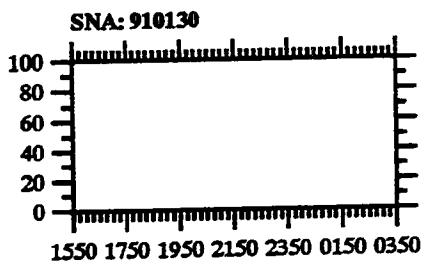
SNA: 910130
100
80
60
40
20
0
1550 1750 1950 2150 2350 0150 0350

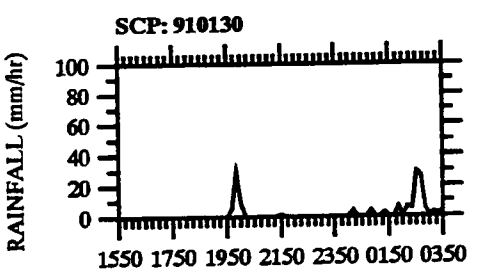
SCP: 910130
RAINFALL (mm/hr)
100
80
60
40
20
0
1550 1750 1950 2150 2350 0150 0350

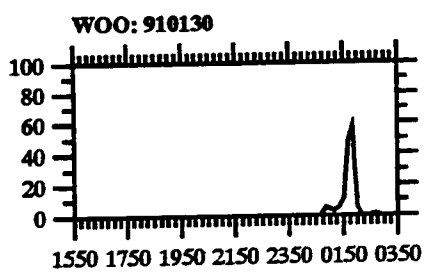
WOO: 910130
100
80
60
40
20
0
1550 1750 1950 2150 2350 0150 0350